UiO : University of Oslo

Lars Musland

Theory and calculations of thermoelectric transport in heterostructures

Thesis submitted for the degree of Philosophiae Doctor

Department of Physics
Faculty of Mathematics and Natural Sciences

2019

Series of dissertations submitted to the
Faculty of Mathematics and Natural Sciences, University of Oslo
No. ⊠⊠⊠⊠

ISSN ⊠⊠⊠⊠⊠⊠⊠⊠

Cover: Hanne Baadsgaard Utigard.
Print production: Reprosentralen, University of Oslo.

Preface

The work behind this thesis was done as a part of the THELMA project, which was a five year long Norwegian effort to research the thermoelectric effect, funded by the Norwegian research council (project number 228854). The thermoelectric effect is a generic term for effects that couple heat and charge transport in materials, and which if sufficiently large, can be utilized to create cooling elements, heat pumps, and even electrical generators without moving parts. My own section of the project was concerned with the thermoelectric properties of heterostructure materials, which have been predicted, and to some extent demonstrated to be beneficial for thermoelectric applications.

The overarching goal of my own project in particular, was the implementation of a general purpose numerical solver capable of simulating heat- and charge transport in heterostructure materials, so that the thermoelectric properties of such materials could be calculated from structural information. While this task is in itself to involved to finish in a single PhD-project, it has served as the overlying motivation for all of my work, which has mostly been focused on laying the ground work for the implementation by studying various formalisms and methods, in order to find the ones most appropriate for the particular problem.

Before starting to implement a solver, one must determine the theoretical formalism in which to formulate the problem, and the method by which to solve the involved equations. The appropriate choices are determined by the accuracy of the results, and by the computational requirements of the calculations. Thus, when selecting a method, one must consider to which extent it results in an accurate solution, how much computation time is required for the calculation, and also whether an unreasonable amount of memory is required. Further, when selecting the theoretical formalism itself, one must consider whether it is theoretically justified for the particular problem, whether it might still give reasonable answers even if this is not the case, and finally, whether there are actually any methods capable of solving the relevant equations within a reasonable amount of time.

My investigation into these questions has taken two separate forms. Partially, it has consisted of a purely theoretical study, where I have studied the literature of the various formalisms, and put some effort into trying to understand the regimes in which they are each justified. Partially, my investigation has also consisted of the implementation of a series of small scale numerical tests, intended to study the computational efficiency of the different methods, and to some extent also to study whether there are notable differences between results of the different formalisms. The latter point concerns in particular differences between the semiclassical Boltzmann equation and approaches based on quantum transport.

Finally, having determined that the NEGF formalism is as an accurate

starting point for these calculations, and that most methods for solving the equations involved are to computationally demanding, I have spent some time trying to develop a method to speed up the solution of these equations by utilizing Monte Carlo calculations

Acknowledgments

First of all, I would like to thank Espen-Flage Larsen, Joakim Bergli and Øystein Prytz for accepting the task of being my supervisors during my work as a PhD student, and for always providing as much support and help as they have been able to. Particularly I would like to thank Espen, with whom I have had the largest cooperation during this work, and who always remains positive, even when things are not working as well as planned.

I would also like to thank the remainder of my colleagues and fellow students at the structure physics group at the University of Oslo, for providing a highly enjoyable environment in which to write a PhD thesis, and for many interesting discussions and entertaining Friday evenings.

Finally, I would like to thank my parents, my grand parents, my sister, the remainder of my family, and my friends for always being supportive.

Lars Musland
Oslo, May 2019

Contents

Chapter 1

Introduction

1.1 Thermoelectric effects, and thermoelectric transport coefficients

The thermoelectric effect, is a generic term for effects that couple the two major transport modes in materials: transport of heat, and transport of electrical charge. To understand the meaning of this, imagine some device, or material slab connected to two contacts, between which there is a voltage difference V, and a temperature difference ΔT. In the commonly presented picture, the flow of heat and charge are independent, meaning that the electrical current I is found from Ohm's law

$$V = RI, \tag{1.1}$$

R being the resistance of the device, while the heat current q is found from the law of heat conduction as

$$q = k\Delta T, \tag{1.2}$$

k being the heat conductance, or thermal conductance. However, in almost all materials there is a small amount of coupling between these transport modes, meaning that voltages can induce heat currents, while temperature gradients can induce electrical currents. Thus, more generally, one must make a modification to Ohm's law as

$$V = RI - \alpha\Delta T, \tag{1.3}$$

where α is known as the Seebeck coefficient. Similarly, the law of heat conduction must also be generalized, and is typically written as

$$q = k\Delta T + \Pi I, \tag{1.4}$$

where Π is referred to as the Peltier coefficient.

With these generalizations, we can identify two important effects. First, a temperature difference may induce currents or voltages. This is referred to as the Seebeck effect. In open circuit conditions, where no current is allowed to flow, the Seebeck effect will induce a voltage $V = -\alpha\Delta T$. Secondly, even in the absence of a temperature difference, there may still be a heat flow $q = \Pi I$. If two devices with different Peltier coefficients are connected, the heat flow q will not be conserved, and accordingly this effect can be used to create heat sources and heat sinks. This is known as the Peltier effect.

The coefficients R, k, α and Π are referred to as transport coefficients. In this thesis I will in particular refer to k, α and Π as thermoelectric transport coefficients, while the purely electrical case will usually be considered separately. One

can also define transport coefficients as material properties. At the macroscopic scale, one may define coefficients $\overleftrightarrow{\sigma}$, $\overleftrightarrow{\alpha}$, $\overleftrightarrow{\kappa}$ and $\overleftrightarrow{\pi}$, such that the relations

$$\boldsymbol{j} = -\overleftrightarrow{\sigma}\left(\boldsymbol{\nabla} V + \overleftrightarrow{\alpha}\boldsymbol{\nabla} T\right) \quad \text{and,} \tag{1.5}$$

$$\boldsymbol{\phi}_Q = -\overleftrightarrow{\kappa}\boldsymbol{\nabla} T + \overleftrightarrow{\pi}\boldsymbol{j}, \tag{1.6}$$

apply at each point of the device. Here $\boldsymbol{j}$ and $\boldsymbol{\phi}_Q$ are respectively the electrical current density and the heat flux density, while $\boldsymbol{\nabla}$ denotes the gradient operation. T and V denotes temperature and voltage as before. The coefficients $\overleftrightarrow{\sigma}$, $\overleftrightarrow{\alpha}$, $\overleftrightarrow{\kappa}$ and $\overleftrightarrow{\pi}$ are material properties, and are respectively referred to as the electrical conductivity, Seebeck coefficient, thermal conductivity and Peltier coefficient of the material. In general these quantities are not scalar, but tensors. This means they correspond to general linear transformations, which can be represented as matrices.

Another thermoelectric effect which is sometimes mentioned, is the Thomson effect, which can be stated as

$$\dot{q} = \boldsymbol{j} \cdot \overleftrightarrow{\mathcal{K}}\boldsymbol{\nabla} T, \tag{1.7}$$

where $\dot{q}$ is the local rate of heat generation, and $\overleftrightarrow{\mathcal{K}}$ is the Thomson coefficient. However, the Thomson effect is a second order effect, and can be derived from the thermoelectric relations presented above. In fact, it can be regarded as a continuum limit of the Peltier effect, and one can show that

$$\overleftrightarrow{\mathcal{K}} = T\frac{\partial \overleftrightarrow{\alpha}}{\partial T}, \tag{1.8}$$

although we will not do that here.

The thermal conductivity and conductance are typically decomposed in two contributions as $\overleftrightarrow{\kappa} = \overleftrightarrow{\kappa}_e + \overleftrightarrow{\kappa}_l$ and $k = k_e + k_l$, where subscripts e and l respectively denotes contributions to the heat flux from electrons and from lattice vibrations. The electron contribution κ_e is intimately related to the electronic conductivity σ, and one defines a coefficient of proportionality $L = \kappa_e/\sigma T$, which is known as the Lorenz coefficient. One can also define a device Lorenz coefficient as $L = Rk_e/T$. In metals the Lorenz coefficient usually has a value approximately equal to $2.44 \cdot 10^{-8}\,\mathrm{V}^2/\mathrm{K}^2$ [9].

1.2 Applications of the thermoelectric effect

One of the most common applications of the thermoelectric effect today, is the use of Peltier elements, which are electrical devices that utilize the Peltier effect to transport heat from one side of the device to the other. Peltier elements are usually made use of for cooling purposes, but in principle they can also be used as heat pumps. However, as of yet their low efficiency is limiting the latter application.

While Peltier elements can not compete with compressor based technologies in terms of efficiency, they have several other advantages. First of all, they

have no moving parts, which means they are noiseless, and have an extremely long durability, requiring as good as no maintenance. Secondly, they have an extremely short response time, meaning that the cooling rate can be adjusted almost instantaneously. The latter fact is highly advantageous in those cooling applications where the temperature must be kept close to some specific value. This is the main application of Peltier elements today.

The Seebeck effect is also made use of in a few technological applications. First of all, many heat sensors and temperature measurement devices make use of the Seebeck effect, since temperature differences can be read off as voltages. This is probably the application of the Seebeck effect that has the biggest consequence in our daily lives. However, an application which is perhaps more interesting, is that the Seebeck effect can be used to construct electrical generators without moving parts. However, just like thermoelectric heat pumps, such thermoelectric generators are limited by their low efficiency. Because of this, their application is restricted to niche cases. An example of such niche cases would be space probes, where the absence of maintenance requirements trumps any efficiency concern.

The efficiency of thermoelectric heat pumps and generators are both determined by a single device parameter

$$ZT = \frac{\alpha \Pi}{Rk} = \frac{\alpha^2}{Rk} T, \tag{1.9}$$

which is known as the figure of merit. The equivalence of the two expressions will be shown later. The efficiency of a thermoelectric generator in particular, is given by the formula

$$\eta = \frac{\chi - 1}{\chi + T_1/T_2} \eta_C, \tag{1.10}$$

where $\chi = \sqrt{ZT + 1}$, T_1 and T_2 are respectively the temperatures on the cold and hot sides of the device, and η_C is the Carnot efficiency $\eta_C = 1 - T_1/T_2$, which is the maximal possible efficiency of a heat engine. In the limit $ZT \to \infty$, we can approximate the efficiency formula as $\eta = \left(1 - 1/\sqrt{ZT}\right) \eta_C$. Thus, the efficiency approaches η_C as ZT is increased, but very slowly.

In addition to the device figure of merit ZT, one defines a similar material figure of merit

$$zT = \frac{\sigma \alpha^2}{\kappa} T, \tag{1.11}$$

where the transport coefficients and material parameters are assumed to either be scalar, or referring to a single well defined direction in the material. The device figure of merit ZT will often lie close to the smallest value of zT in the materials from which the device is constructed, so accordingly the material figure of merit zT is a crucial parameter when choosing materials for thermoelectric applications.

1.3 Heterostructure materials, and related nomenclature

As can to some extent be discerned from the name, a heterostructure material is defined as a material where different sections of the material have different compositions or structure, and where this variation occurs at a mesoscopic size scale (nm-μm range). Thus, the composition or structure of the material varies as a function of position. An important special case is that of quasi-one-dimensional heterostructures, which are particularly important since in an attempt to limit the scope of the project, all of my work has been limited to such structures. The term quasi-one-dimensional simply means that all of the mesoscale structural variation occurs along a single dimension, while the material is homogeneous along the two remaining dimensions. Thus, one can introduce a coordinate system xyz such that the composition and structure of the material depends only on the z-coordinate, and is independent of x and y.

A particularly important subclass of quasi-one-dimensional heterostructures is made up by the superlattices. A superlattice is a quasi-one-dimensional heterostructure which is periodic also in the direction of mesoscale variation. Thus, in the coordinate system introduced above, there is some distance d such that the material composition at coordinate (x, y, z) is always the same as at coordinate $(x, y, z + d)$. In my work, the smallest possible value of d will be referred to as the superlattice period. In order for the material to classify as an actual heterostructure, and not as some bulk material, the superlattice period should be at least a few nanometers. In addition, the literature often reserves the term superlattice to structures where the period is quite small, typically no longer than a few tens of nm. However, as there is not really any good term for quasi-one-dimensional heterostructures in the more general case, I will in fact use the term superlattice also when the period is arbitrarily large.

Since a superlattice is periodic along all three dimensions, it can be constructed as a repeating pattern of a single small block of material. This block will be referred to as the supercell, and sometimes as the superlattice supercell. The term unit cell on the other hand, will in this work be reserved for the unit cells of the underlying materials from which the heterostructure is composed. For instance, in a superlattice consisting of repeating layers of HgTe and CdTe, the term unit cell will always refer to the unit cell of HgTe or CdTe, and never to the supercell of the superlattice.

In the simplest configuration, a superlattice consists simply of a repeating pattern of two different layer types, with differing composition or structure. Often the material in the two layers will also have differing electron band edges. If electron transport occurs in the conduction band, the layers with higher conduction band minima is typically referred to as barriers, while the layers with lower band minima are referred to as wells. The difference between the two conduction band minima is called the barrier height. If electron transport occurs in the valence band, one will often adopt the opposite convention, where the layers with lower valence band maxima are referred to as barriers.

A second important subclass of quasi-one-dimensional heterostructures that should be introduced, is the thin film. A thin film consists of a mesoscopically

dimensioned layer suspended between two macroscopic bulk regions. The thin layer must have a composition or structure different from both bulk regions, and may or may not also contain internal variations. In addition, one or both bulk regions may consist of vacuum.

1.4 Advantages of heterostructuring for thermoelectric applications

There are multiple reasons why heterostructures are interesting for thermoelectric applications. One important effect, which has already been utilized with considerable success, is the fact that including structures at a mesoscopic size scale will typically reduce the mean free path of phonons in the material. Since phonons carry heat but not charge, they will in most cases contribute only to κ_l and k_l, and not to the other transport coefficients introduced above. An exception to this occurs in the presence of phonon drag effects, which are normally ignored in standard materials. In the absence of such effects, it is then easy to see that the material figure of merit

$$zT = \frac{\sigma\alpha^2}{\kappa_e + \kappa_l}T \tag{1.12}$$

can only be positively impacted by the reduction of phonon transport.

Another important consequence of heterostructuring a material, is an effect known as energy filtering, where electrons are freely moving only when their energy lies in some limited range, and where the motion of electrons outside of this range is inhibited. For instance, by including small barriers consisting of materials with higher conduction band minima, the motion of conduction band electrons would be inhibited in the range below the barrier height. Earlier work has predicted energy filtering to have a positive impact on a central trade-off in thermoelectric materials: As a function of doping concentration, the conductivity of the material tends to increase, much as would be expected, but the Seebeck coefficient of the material tends to drop. Thus, since the figure of merit is proportional both to σ and α^2, there is a trade-off between these coefficients when selecting the optimal doping concentration. Energy filtering has been predicted to reduce this trade-off, which means the product $\sigma\alpha^2$ is increased at the optimum.

In addition, some work has indicated that energy filtering may also reduce the Lorenz coefficient. Writing the figure of merit as

$$zT = \frac{\alpha^2}{L}\left(1 + \frac{\kappa_l}{\kappa_e}\right)^{-1} \tag{1.13}$$

shows that this would also be highly beneficial.

These were the effects that motivated our research project to spend some resources on studyin heterostructure materials, and in particular to begin preparatory work to implement a transport solver capable of calculating the thermo-

electric transport coeeficients of such materials. The latter task has served as motivation for all work presented in this thesis.

1.5 Outline of the thesis

This thesis is divided into two major parts. Part I provides an overview of some of the most important formalisms of transport theory, while Part II provides a presentation and discussion of my own work. The order in which these parts are read is not important, as long as the reader is prepared to accept that part II references a few topics in part I. Published works, and work submitted for publication are included at the end of part II.

Chapter 2, the first chapter of part I, is an introduction to the Landauer-Büttiker theory of transport. I open with this subject, since it is in a sense the simplest transport formalism. Also, it provides a conceptually simple and intuitive way of thinking about transport in general. However, while always useful as a conceptual tool, the Landauer-Büttiker theory is not very useful for making quantitative predictions, except when the transport problem can be regarded as ballistic, i.e. free from scattering. Various scattering models can be included in the theory, but these will always either be phenomenological or taken from another formalism.

In order to rigorously obtain predictions where scattering is included, it is better to make use of formalisms derived from first principles. Such formalisms are the subject of the remaining four chapters of part I. Chapter 3 deals with the path integral, or field integral, which is the most general of the formalisms, since it is in fact equivalent to the many particle Schrödinger equation. While rarely directly applicable in practice, the field integral forms an important theoretical starting point, from which most of the remaining theory is derived.

Chapter 4 deals with transport in the linear regime, i.e. the regime where perturbations are small enough for all responses to be simple linear functions of the stimuli. This is an important topic in thermoelectric theory, since at least those thermoelectric applications that are thermally driven will almost always be in the linear regime. Some of the expressions in Chapter 4 are derived from the field integral, but the most important ones, known as the Kubo relations, are derived using the standard Hilbert space operator formalism. Some discussion is also provided for how to convert these expressions into field integrals.

Chapter 5 deals with the perturbative expansion of the field integral. The discussion is limited to the fermionic sector, and to the expansion of two-point correlation functions. We accordingly end up with the Non-equilibrium Green's function, or NEGF formalism, which is the first of the rigorous formalisms that is practically applicable to any major extent. However, application requires additional approximations, which may or may not be severe, depending on the particular problem. Conveniently, transport expressions in the NEGF formalism can be formulated in a language similar to that of the Landauer-Büttiker theory.

The final chapter of part I, Chapter 6, discusses two remaining, and very important transport formalisms. First, by introducing a Markov approximation

to the NEGF formalism, we end up with the master equation approach. Secondly, by introducing an additional assumption of slow spatial variations, we obtain the semiclassical Boltzmann equation, which is probably the most commonly applied of all transport formalisms. I also discuss the multi band version of the Boltzmann equation, which must be justified in a somewhat different manner than the single band version. While not particularly important in bulk systems, the last point may be of major importance when modeling superlattices.

Part I serves three different purposes in the thesis. Firstly, it serves as a reference for many of the theories and equations I have already applied in my work. Thus, part II will commonly make reference to equations and discussions in part I, but mostly to Chapters 2, 5 and 6. A second purpose served by part I, is as a useful overview and work of reference for future work. This applies particularly to Chapters 4 and 6, the subjects of which I have in retrospect realized would have been a better starting point for my own work than the NEGF formalism. This will be more thoroughly discussed later. In any case, these subjects should be useful for future improvements of my implementations, and Chapters 4 and 6 serve as useful references.

The third and final purpose served by part I, is as a documentation of the more theoretical and self serving work I have done during my PhD. In the process of determining the formalism most appropriate for my implementations, I have spent a considerable time reviewing various literature, and on trying to understand the various formalisms, their ranges of applicability, and how they all relate to each other. Part I documents this work, and presents an overview of what I have learned and understood from it.

The more practical aspects of my work are presented in Part II, which is divided into two chapters. Chapter 7 serves as an introduction to this part of my work. There, I discuss the motivation behind my work, our path towards determining the formalism and method of our implementation, our overall progress towards this implementation, and finally how the papers included at the end fit into this picture.

Chapter 8 contains a discussion of various sub-projects that did not result in the submission of a manuscript, as well as some additional results related to the topic of our third paper, Paper III. Section 8.1 describes some experiments with the Boltzmann Monte Carlo method, which was the first method of transport calculations I pursued. Monte Carlo methods are methods where the desired calculation is performed by averaging a set of random results. In particular, the Boltzmann Monte Carlo method obtains a solution to the Boltzmann equation by explicitly simulating the movement of particles, according to physical forces acting upon them, and a sequence of random scattering events. Per today, this is the most efficient method to solve the Boltzmann equation under general conditions.

Sections 8.2 and 8.3 are both concerned with methods for reducing the computational burden associated with the solution of the NEGF equations. Section 8.2 in particular, is concerned with the calculation of the retarded Green's function, a demanding task which must be performed multiple times during a transport calculation. While we eventually landed on the RGF method[6] as the

most efficient method for doing these calculations, Section 8.2 investigates an alternative based on perturbation theory.

Section 8.3 is concerned with a NEGF Monte Carlo method. Motivated by the success of the Boltzmann Monte Carlo method, we have attempted to develop a Monte Carlo method which solves the NEGF equations. This method is the subject of our third paper, Paper III, and Section 8.2 merely includes some additional results, which were omitted from the paper.

Finally, Chapter 9 contains an overview of what I consider to be the most important conclusions I have arrived at during my work.

Part I

An overview of selected topics from transport theory, relevant to the calculation of thermoelectric coefficients

Chapter 2

The Landauer-Büttiker theory of transport

In this chapter, I give an introduction to transport theory, in the form of Landauer-Büttiker theory, which is a very intuitive conceptualization of transport. It is just as useful for conceptualizing semiclassical transport as quantum transport[7, 22, 17]. However, the theory is purely phenomenological, and it is also most useful when scattering is assumed elastic. Thus, for predictive calculations, more rigorous formalisms are required.

2.1 Landauer-Büttiker expressions

2.1.1 Derivation

Consider some electronic device or material sample S, and a set $\{p\}$ of leads connected to S. For each lead p we define the direction pointing away from S as the positive z axis. We assume that p is translationally invariant along the z axis with some period a, and we ignore many particle interactions in the leads. Electron motion in the leads is then determined by the Schrödinger equation

$$\hat{H}\psi(\boldsymbol{x}) = E\psi(\boldsymbol{x}), \tag{2.1}$$

here in its time independent form. Here $\hat{H}$ is the Hamiltonian operator, $\psi(\boldsymbol{x})$ is the wave function, and E is the energy. From Bloch's theorem[11] it follows that the solutions can be written as

$$\psi(\boldsymbol{x}) = \psi_m(k, \boldsymbol{x}) = \phi_m(k, \boldsymbol{x})e^{ikz}, \text{ with} \tag{2.2}$$

$$E = E_m(k). \tag{2.3}$$

Such Bloch states are discussed more thoroughly in Section 6.3.1. The index m refers to the transversal mode of the lead, and the functions $\phi_m(k, \boldsymbol{x})$ are periodic in z.

In the Landauer-Büttiker formalism, the system S is dealt with entirely in terms of a transmission function $\mathcal{T}$, which describes probabilities of transfer between different leads and energies. As we shall see, all the physics relevant to electronic transport calculations is captured by the transmission function. The formalism is not concerned with exactly how $\mathcal{T}$ is to be calculated, so this must be extracted from one of the formalisms to be described below. The following derivation follows Datta[7].

In the most general version of the formalism, the transmission function takes the form $\mathcal{T}_{qp}^{nm}(E, E')$, which is defined as the probability that an electron entering

S from lead p, with energy E and in transversal mode n, exits in lead q, with energy E' and in transversal mode m. However, in reality the Landauer-Büttiker formalism is rarely useful unless the scattering mechanism in S is elastic, so that the exiting energy E' must equal the incoming energy E. In that case the transmission function simplifies to $\mathcal{T}_{qp}^{nm}(E)$, which is defined as before, except that the electron now also exits with energy E.

Consider the total electron flux Φ_q in lead q. This can be separated in two contribution classes: the incoming contributions from lead q itself, and the outgoing contributions having been transmitted through S from all leads p. Thus, the total electron flux in q can be written

$$\Phi_q = \sum_{nk} \Phi_q^n(k) - \sum_{pmnk} \mathcal{T}_{qp}^{nm}(E_m(k))\Phi_p^n(k), \tag{2.4}$$

where the sum is only over values of k with negative flux (moving towards S).

We assume each lead to be internally close to equilibrium, and well described by a chemical potential μ_p and a temperature T_p. Since electrons are fermions their occupation is described by the Fermi function[7, 11]

$$f_p(E) = \frac{1}{e^{\beta_p(E-\mu_p)}+1}. \tag{2.5}$$

If the leads are assumed to have length L, the density of electrons in some state $\psi_m(k, \boldsymbol{x})$ will be $f(E_m(k))/L$, and if the group velocity

$$v_m(k) = \frac{1}{\hbar}\frac{\mathrm{d}E}{\mathrm{d}k}, \tag{2.6}$$

of the state is negative, then the flux hitting S from that state will be $|\Phi_p^m(k)| = f(E_m(k))|v_m(k)|/L$.

For a continuing flux to make sense, we must take the limit $L \to \infty$. (2.4) then becomes

$$\begin{aligned}
\Phi_q &= \sum_n \int \frac{\mathrm{d}k}{2\pi} f_q(E_n(k))v_n(k) - \sum_{pmn} \int \frac{\mathrm{d}k}{2\pi} \mathcal{T}_{qp}^{nm}(E_m(k))f_p(E_m(k))v_m(k) \\
&= \sum_n \int \frac{\mathrm{d}k}{2\pi}\frac{1}{\hbar}\frac{\mathrm{d}E}{\mathrm{d}k} f_q(E_n(k)) - \sum_{pmn} \int \frac{\mathrm{d}k}{2\pi}\frac{1}{\hbar}\frac{\mathrm{d}E}{\mathrm{d}k} \mathcal{T}_{qp}^{nm}(E_m(k))f_p(E_m(k)) \\
&= -\frac{1}{h}\sum_n \int \mathrm{d}E\, f_q(E) + \frac{1}{h}\sum_{pmn} \int \mathrm{d}E\, \mathcal{T}_{qp}^{nm}(E) f_p(E).
\end{aligned} \tag{2.7}$$

In the last expression, the indexes m and n no longer represents only the transversal modes, but possibly also a discrete set of values k where the bands intersect the energy E, and where $v(k)$ is positive.

The total probability of moving from a mode n to any new mode in any lead must be one, so

$$\sum_{pm} \mathcal{T}_{pq}^{mn}(E) = 1. \tag{2.8}$$

Inserting this in (2.7), we get

$$\Phi_q = \frac{1}{h}\sum_{pmn}\int \mathrm{d}E\left(\mathcal{T}_{qp}^{nm}(E)f_p(E) - \mathcal{T}_{pq}^{mn}(E)f_q(E)\right). \tag{2.9}$$

At this point we rewrite the expressions in terms of $i(E)$, the flux contribution from energy E, meaning that

$$\Phi_q = \int \mathrm{d}E\, i_q(E). \tag{2.10}$$

The current in lead q is then

$$I_q = -e\Phi_q = -e\int \mathrm{d}E\, i_q(E), \tag{2.11}$$

where e is the elementary charge. Since the energy flux contribution from energy E must be $Ei(E)$, we can also calculate the total heat flux in lead q as

$$q_q = \int \mathrm{d}E\,(E-\mu_q) i_q(E). \tag{2.12}$$

A more detailed argument for why this is the case is given in Section 3.4.3.

From (2.9) we can express $i_q(E)$ as

$$i_q(E) = \frac{1}{h}\sum_p \left(\bar{\mathcal{T}}_{qp}(E)f_p(E) - \bar{\mathcal{T}}_{pq}(E)f_q(E)\right) \text{ where,} \tag{2.13}$$

$$\bar{\mathcal{T}}_{qp}(E) = \sum_{mn}\mathcal{T}_{qp}^{nm}(E). \tag{2.14}$$

Using more sophisticated formalisms, one can show that under certain conditions

$$\sum_p \bar{\mathcal{T}}_{pq}(E) = \sum_p \bar{\mathcal{T}}_{qp}(E), \tag{2.15}$$

as is done for instance in the appendix of our third paper, Paper III. Inserting this in (2.13), we finally find

$$i_q(E) = \frac{1}{h}\sum_p \bar{\mathcal{T}}_{qp}(E)\left(f_p(E) - f_q(E)\right). \tag{2.16}$$

2.1.2 Linear limit and Landauer formula

In the linear limit, the currents I_q are linear in the lead voltages $V_{pq} = V_p - V_q$. We define the conductances G_{qp} through the relation $I_q = \sum_p G_{qp}V_{pq}$. Let us expand (2.16) to the first order in the potential differences $\Delta\mu_p = \mu_p - \mu$, where μ is the equilibrium potential. We get

$$i_q(E) = \frac{1}{h}\sum_p \bar{\mathcal{T}}_{qp}(E)\frac{\partial f}{\partial \mu}(E)(\Delta\mu_p - \Delta\mu_q) = \frac{1}{h}\sum_p \bar{\mathcal{T}}_{qp}(E)\mathrm{Th}(E)\Delta\mu_{pq}, \tag{2.17}$$

where $\Delta\mu_{pq} = \mu_p - \mu_q = \Delta\mu_p - \Delta\mu_q$, and

$$\mathrm{Th}(E) = -\frac{\partial f}{\partial E}(E) = \frac{\beta}{4\cosh^2 \beta(E-\mu)/2}. \tag{2.18}$$

Inserting (2.17) in (2.11), and utilizing the fact that $\Delta\mu_{qp} = -eV_{qp}$, we get

$$I_q = \frac{e^2}{h}\sum_p \int \mathrm{d}E\, \bar{\mathcal{T}}_{qp}(E)\mathrm{Th}(E)V_{pq}. \tag{2.19}$$

Thus, from the definition of G_{qp},

$$G_{qp} = \frac{e^2}{h}\int \mathrm{d}E\, \bar{\mathcal{T}}_{qp}(E)\mathrm{Th}(E). \tag{2.20}$$

A particularly important special case is that of a device S with only two leads. In that case there is only one conductance $G = G_{12} = G_{21}$, and one transmission function $\bar{\mathcal{T}}(E) = \bar{\mathcal{T}}_{12}(E) = \bar{\mathcal{T}}_{21}(E)$. The relation between G and $\bar{\mathcal{T}}$ is found by removing the indices p and q from (2.20). Clearly, by (1.1) $R = 1/G$. An interesting limit is obtained for $T \to 0$. The function $\mathrm{Th}(E)$ then becomes a delta function, and we get

$$G = \frac{e^2}{h}\bar{\mathcal{T}}(\mu). \tag{2.21}$$

If scattering in S can be ignored, then $\mathcal{T}_{12}^{mn} \sim \delta_{mn}$, and (2.21) becomes

$$G = \frac{2e^2}{h}M, \tag{2.22}$$

where the factor of 2 comes from spin degeneracy, and M is the number of transversal modes per lead and spin. (2.22) is the well known Landauer formula for the quantization of conductance[7, 15].

2.1.3 Thermoelectric coefficients

Following for instance Ref. [17], we can also find linear expressions for currents due to temperature differences $\Delta T_{pq} = T_p - T_q$. Expanding (2.16) to the first order in $\Delta T_p = T_p - T$, we get

$$i_q(E) = -\frac{1}{h}\sum_p \bar{\mathcal{T}}_{qp}(E)\frac{\partial f}{\partial \beta}(E)\frac{\Delta T_p - \Delta T_q}{T^2} = \frac{1}{hT}\sum_p \bar{\mathcal{T}}_{qp}(E)\mathrm{Th}(E)(E-\mu)\Delta T_{pq}. \tag{2.23}$$

Thus, we find from (2.11) that we can write $I_q = \sum_p A_{qp}\Delta T_{pq}$, where

$$A_{qp} = -\frac{e}{hT}\int \mathrm{d}E\, \bar{\mathcal{T}}_{qp}(E)\mathrm{Th}(E)(E-\mu). \tag{2.24}$$

In a situation where there are both voltage and temperature differences between the leads, the lead currents will be $I_q = \sum_p (G_{qp}V_{pq} + A_{qp}\Delta T_{pq})$. Similarly, we can write the lead heat currents as $q_q = \sum_p (B_{qp}V_{pq} + C_{qp}\Delta T_{pq})$. Inserting (2.17) and (2.23) in (2.12), it is easy to see that

$$B_{qp} = -\frac{e}{h}\int \mathrm{d}E\, \bar{\mathcal{T}}_{qp}(E)\mathrm{Th}(E)(E-\mu), \text{ and} \tag{2.25}$$

$$C_{qp} = \frac{1}{hT}\int \mathrm{d}E\, \bar{\mathcal{T}}_{qp}(E)\mathrm{Th}(E)(E-\mu)^2. \tag{2.26}$$

If we limit the situation to two leads, the relations above simplify to $I = GV + A\Delta T$ and $q = BV + C\Delta T$, which are merely reexpressions of the relations (1.3) and (1.4). A, B and C are found by removing the indices p and q from (2.24) to (2.26). Expressions for the thermoelectric transport coefficients α and k_e are most easily obtained by considering the special case where the current $I = 0$. We then have $GV + A\Delta T = 0$, which can be solved to find the voltage $V = -\alpha\Delta T$, with $\alpha = A/G$. Further, the heat current becomes $q = -B\alpha\Delta T + C\Delta T = k_e\Delta T$, with $k_e = C - B\alpha$. Finally considering the heat flux in the general case, we see that it can be written $k_e\Delta T + \Pi I$, with $\Pi = B/G$. Comparing (2.24) to (2.25), we also find $\Pi = \alpha T$.

Summarizing, we have obtained the expressions

$$\alpha = A/G, \tag{2.27}$$

$$k_e = C - AB/G, \quad \text{and} \tag{2.28}$$

$$\Pi = B/G = \alpha T, \tag{2.29}$$

allowing us to rewrite the expressions for I and q as

$$I = G(V + \alpha\Delta T), \text{ and} \tag{2.30}$$

$$q = k\Delta T + \Pi I, \tag{2.31}$$

in agreement with (1.3) and (1.4).

The Seebeck coefficient α can be rewritten in an interesting way by introducing the probability distribution

$$P(E) = \frac{e^2}{hG}\bar{\mathcal{T}}(E)\mathrm{Th}(E). \tag{2.32}$$

This function is positive, and integrates to 1 by (2.20). From (2.24), we get

$$\alpha = \frac{A}{G} = -\frac{e}{hGT}\int \mathrm{d}E\, \bar{\mathcal{T}}(E)\mathrm{Th}(E)(E-\mu) = -\frac{1}{eT}\langle E-\mu\rangle = -\frac{k_B}{e}\langle\chi\rangle, \tag{2.33}$$

where the brackets denote the expectation value with respect to the probability distribution P, k_B is the Boltzmann constant, and the dimensionless quantity $\chi = \beta(E-\mu)$.

As mentioned, the electronic heat conductance k_e is often expressed as $k_e = GLT$, where L is the Lorenz number or Lorenz coefficient. L can also be expressed in terms of P and χ, as

$$L = \frac{C - B\alpha}{GT} = \frac{1}{hGT^2}\int \mathrm{d}E\,\bar{\mathcal{T}}(E)\mathrm{Th}(E)(E-\mu)^2 - \frac{\Pi\alpha}{T} \tag{2.34}$$
$$= \frac{\left\langle (E-\mu)^2 \right\rangle}{e^2T^2} - \alpha^2 = \frac{k_B^2}{e^2}\left\langle \chi^2 \right\rangle - \frac{k_B^2}{e^2}\langle\chi\rangle^2 = \frac{k_B^2}{e^2}\left\langle \left(\chi - \langle\chi\rangle\right)^2 \right\rangle = \frac{k_B^2}{e^2}\mathrm{Var}\,\chi,$$

where Var denotes variance taken with respect to P.

In a metallic system we can approximate $\bar{\mathcal{T}}(E)$ as constant over an energy range of a few k_BT. Thus, $P(E) \approx \mathrm{Th}(E)$, and we can calculate L explicitly. since $\mathrm{Th}(E)$ is a symmetric function, $\langle\chi\rangle = 0$. Accordingly

$$\mathrm{Var}\,\chi = \int \mathrm{d}E\,\mathrm{Th}(E)\chi^2 = \int \mathrm{d}\chi\,\frac{\chi^2}{4\cosh^2\chi/2} = \frac{\pi^2}{3}, \tag{2.35}$$

which is found by contour integrating the function $z^3/4/\cosh^2 z/2$ around the rectangle $[-\infty,\infty]\times[0,2\pi i]$. By (2.34) we find

$$L = \frac{\pi^2 k_B^2}{3e^2} = 2.44\cdot 10^{-8}\,\mathrm{V}^2/\mathrm{K}^2, \tag{2.36}$$

the standard value of the Lorenz number[9].

2.2 Discussion of the leads

In the previous section, drastic approximations were introduced in the physics of the leads. They were assumed to be infinitely long and perfectly periodic, and they were assumed to be free of scattering, so that the electrons are described by a single particle Hamiltonian.

Traditionally, these approximations are justified by the assumption that the leads are highly conductive compared to the device S [7]. If this is the case, then most of the changes in μ and T will happen inside S, so that the leads are close to equilibrium. In addition, the leads will then only give minor contributions to the resistance, and to other measurable properties of the combined system. This means that the physics of the leads will not significantly affect measurable quantities, so that whether or not the leads are described realistically becomes irrelevant.

If the assumption that most of the restiance resides in S does not hold, then the leads of the previous section can be considered a purely theoretical tool. That is, instead of taking the leads to be the real physical leads, we instead include these physical leads in the description of S itself. The leads of the previous section are then merely theoretical abstractions that we use to create non-equilibrium conditions in the theoretical description of S, and to pick up the resulting currents. In the same way as an experimenter will choose the physical leads in the most convenient way in order to do his measurements, theorists may choose these theoretical leads in as convenient a manner as possible. This is done by keeping the lead physics maximally simple.

2.3 Coherent and incoherent regimes

In this section we briefly discuss the behavior of the transmission functions $\mathcal{T}(E)$. To do this in the general case requires a more sophisticated formalism, but we can produce some meaningful results in two simplified regimes. These are the coherent and incoherent regimes, which are determined by how the transport length scale compares to the coherence or phase relaxation length L_ϕ [7]. Coherent transport occurs over length scales much shorter than L_ϕ, and is characterized by carriers taking on the character of classical waves. Incoherent transport occurs over length scales much larger than L_ϕ, and is characterized by carriers taking on a character more like classical particles.

2.3.1 Incoherent regime

In the incoherent regime, interference effects due to the wavelike nature of particles can be ignored. We can then think of the particles as classical, and describe their motion using simple probabilities. Consider a device S with two leads, and bisect it in two parts A and B, A being closer to lead 1 and B closer to lead 2. Assume we know the transmission coefficients of each part to be $\mathcal{T}_A$ and $\mathcal{T}_B$ respectively, and that transport occurs in a single mode in each part.

Then, again following Datta[7], we can find the transmission function of S by the following considerations: Assume lead 1 contains a flux Φ^+ of particles moving towards A, and a flux Φ^- moving away from A. Assume further that at the boundary between parts A and B, there is a flux Φ_A^+ entering B from A, and a flux Φ_A^- entering A from B. Clearly these fluxes are related by the transmission function of A, so that

$$\Phi_A^+ = \mathcal{T}_A\Phi^+ + \mathcal{R}_A\Phi_A^-, \text{ and} \tag{2.37}$$

$$\Phi^- = \mathcal{T}_A\Phi_A^- + \mathcal{R}_A\Phi^+. \tag{2.38}$$

Here the reflection coefficient $\mathcal{R}$ is given by $\mathcal{R} = 1 - \mathcal{T}$. Solving (2.38) for Φ_A^- we get

$$\Phi_A^- = \frac{1}{\mathcal{T}_A}\Phi^- - \frac{\mathcal{R}_A}{\mathcal{T}_A}\Phi^+, \tag{2.39}$$

and inserting that in (2.37) we get

$$\Phi_A^+ = \mathcal{T}_A\Phi^+ + \frac{\mathcal{R}_A}{\mathcal{T}_A}\Phi^- - \frac{\mathcal{R}_A^2}{\mathcal{T}_A}\Phi^+. \tag{2.40}$$

This can be conveniently written in matrix form as

$$\begin{bmatrix}\Phi_A^+\\ \Phi_A^-\end{bmatrix} = \begin{bmatrix}\mathcal{T}_A - \mathcal{R}_A^2/\mathcal{T}_A & \mathcal{R}_A/\mathcal{T}_A\\ -\mathcal{R}_A/\mathcal{T}_A & 1/\mathcal{T}_A\end{bmatrix}\begin{bmatrix}\Phi^+\\ \Phi^-\end{bmatrix}. \tag{2.41}$$

Consider now the fluxes in lead 2. We refer to the flux exiting B as Φ_B^+, and the flux moving toward B as Φ_B^-. Clearly these fluxes are related to the fluxes

Φ_A^+ and Φ_A^- in a manor completely analogous to the above relations, and we thus get

$$\begin{bmatrix} \Phi_B^+ \\ \Phi_B^- \end{bmatrix} = \begin{bmatrix} \mathcal{T}_B - \mathcal{R}_B^2/\mathcal{T}_B & \mathcal{R}_B/\mathcal{T}_B \\ -\mathcal{R}_B/\mathcal{T}_B & 1/\mathcal{T}_B \end{bmatrix} \begin{bmatrix} \Phi_A^+ \\ \Phi_A^- \end{bmatrix}. \tag{2.42}$$

Combining (2.41) and (2.42) we get

$$\begin{bmatrix} \Phi_B^+ \\ \Phi_B^- \end{bmatrix} = \begin{bmatrix} \mathcal{T}_A - \mathcal{R}_A^2/\mathcal{T}_A & \mathcal{R}_A/\mathcal{T}_A \\ -\mathcal{R}_A/\mathcal{T}_A & 1/\mathcal{T}_A \end{bmatrix} \begin{bmatrix} \mathcal{T}_B - \mathcal{R}_B^2/\mathcal{T}_B & \mathcal{R}_B/\mathcal{T}_B \\ -\mathcal{R}_B/\mathcal{T}_B & 1/\mathcal{T}_B \end{bmatrix} \begin{bmatrix} \Phi^+ \\ \Phi^- \end{bmatrix}, \tag{2.43}$$

and since considerations similar to those above could also have been made for the entire device S with transmission $\mathcal{T}$, we must in fact have

$$\begin{bmatrix} \mathcal{T} - \mathcal{R}^2/\mathcal{T} & \mathcal{R}/\mathcal{T} \\ -\mathcal{R}/\mathcal{T} & 1/\mathcal{T} \end{bmatrix} = \begin{bmatrix} \mathcal{T}_A - \mathcal{R}_A^2/\mathcal{T}_A & \mathcal{R}_A/\mathcal{T}_A \\ -\mathcal{R}_A/\mathcal{T}_A & 1/\mathcal{T}_A \end{bmatrix} \begin{bmatrix} \mathcal{T}_B - \mathcal{R}_B^2/\mathcal{T}_B & \mathcal{R}_B/\mathcal{T}_B \\ -\mathcal{R}_B/\mathcal{T}_B & 1/\mathcal{T}_B \end{bmatrix}. \tag{2.44}$$

The relations above are easily generalized to a case where we divide S into a sequence of parts $S_1 \cdots S_N$. Since the fluxes on the boundaries are in each case given by expression similar to (2.41), (2.44) generalizes to

$$\begin{bmatrix} \mathcal{T} - \mathcal{R}^2/\mathcal{T} & \mathcal{R}/\mathcal{T} \\ -\mathcal{R}/\mathcal{T} & 1/\mathcal{T} \end{bmatrix} = \prod_{n=1}^{N} \begin{bmatrix} \mathcal{T}_n - \mathcal{R}_n^2/\mathcal{T}_n & \mathcal{R}_n/\mathcal{T}_n \\ -\mathcal{R}_n/\mathcal{T}_n & 1/\mathcal{T}_n \end{bmatrix}. \tag{2.45}$$

In fact, evaluating the lower right corner of the matrix product in (2.44), we get

$$\frac{1}{\mathcal{T}} = -\frac{\mathcal{R}_A\mathcal{R}_B}{\mathcal{T}_A\mathcal{T}_B} + \frac{1}{\mathcal{T}_A\mathcal{T}_B} = \frac{1-(1-\mathcal{T}_A)(1-\mathcal{T}_B)}{\mathcal{T}_A\mathcal{T}_B} = \frac{1}{\mathcal{T}_A} + \frac{1}{\mathcal{T}_B} - 1, \tag{2.46}$$

and by a simple argument of induction it is easy to see that this generalizes to the case of (2.45) as

$$\frac{1}{\mathcal{T}} - 1 = \sum_{n=1}^{N} \left(\frac{1}{\mathcal{T}_n} - 1 \right). \tag{2.47}$$

In particular, if S is divided into N identical pieces, all having transmission $\mathcal{T}_1$ and length L_1, then

$$\frac{1}{\mathcal{T}} - 1 = N \left(\frac{1}{\mathcal{T}_1} - 1 \right). \tag{2.48}$$

We define the back scattering mean free path λ as

$$\lambda = \frac{L_1}{1/\mathcal{T}_1 - 1} = \frac{\mathcal{T}_1 L_1}{1-\mathcal{T}_1}. \tag{2.49}$$

Note that by (2.48) this is the ratio of two quantities both proportional to N. Thus, if we rather than L_1 and $\mathcal{T}_1$, insert the transmission and length of some

larger set of N parts, (2.49) gives the same value of λ. Accordingly, λ is to some extent independent of the subdivision of S. However, this is only true as long as the lengths $L_1 \gg L_\phi$. Using (2.49), we can write (2.48) as

$$\mathcal{T} = \frac{\lambda}{\lambda + L}, \tag{2.50}$$

in agreement with the literature[7, 22, 17].

2.3.2 Coherent regime

In the coherent regime, we can not think of electrons as classical particles, but we can think of them as classical waves. Consider the same situation as above, where S is subdivided in two parts A and B. The fluxes Φ^+, Φ^-, Φ_A^+, Φ_A^-, Φ_B^+ and Φ_B^- are then associated with amplitudes ϕ^+, ϕ^-, ϕ_A^+, ϕ_A^-, ϕ_B^+ and ϕ_B^-, where in each case $\Phi = |\phi|^2$. The flux amplitudes entering and exiting a subsystem are linearly related, and we can thus write their relationship in a manor similar to (2.37) and (2.38), as[7]

$$\phi_A^+ = t_A^+ \phi^+ + r_A^+ \phi_A^-, \text{ and} \tag{2.51}$$
$$\phi^- = t_A^- \phi_A^- + r_A^- \phi^+, \tag{2.52}$$

where $|t_A^+|^2 = |t_A^-|^2 = \mathcal{T}_A$ and $|r_A^+|^2 = |r_A^-|^2 = \mathcal{R}_A$. Completely analogously to the incoherent case, these equations can also be written in matrix form as

$$\begin{bmatrix} \phi_A^+ \\ \phi_A^- \end{bmatrix} = \begin{bmatrix} t_A^+ - r_A^+ r_A^- / t_A^- & r_A^+ / t_A^- \\ -r_A^- / t_A^- & 1/t_A^- \end{bmatrix} \begin{bmatrix} \phi^+ \\ \phi^- \end{bmatrix}, \tag{2.53}$$

and similarly for ϕ_B^+ and ϕ_B^-. Thus, (2.43) also has an analogous version in the coherent case, as

$$\begin{bmatrix} \phi_B^+ \\ \phi_B^- \end{bmatrix} = \begin{bmatrix} t_A^+ - r_A^+ r_A^- / t_A^- & r_A^+ / t_A^- \\ -r_A^- / t_A^- & 1/t_A^- \end{bmatrix} \begin{bmatrix} t_B^+ - r_B^+ r_B^- / t_B^- & r_B^+ / t_B^- \\ -r_B^- / t_B^- & 1/t_B^- \end{bmatrix} \begin{bmatrix} \phi^+ \\ \phi^- \end{bmatrix}, \tag{2.54}$$

and in fact, in the general case we get an equation analogous to (2.45) as

$$\begin{bmatrix} t^+ - r^+ r^- / t^- & r^+ / t^- \\ -r^- / t^- & 1/t^- \end{bmatrix} = \prod_{n=1}^{N} \begin{bmatrix} t_n^+ - r_n^+ r_n^- / t_n^- & r_n^+ / t_n^- \\ -r_n^- / t_n^- & 1/t_n^- \end{bmatrix}. \tag{2.55}$$

In the special case where all the parts $S_1 \cdots S_N$ are identical, this simplifies to

$$\begin{bmatrix} t^+ - r^+ r^- / t^- & r^+ / t^- \\ -r^- / t^- & 1/t^- \end{bmatrix} = \begin{bmatrix} t_1^+ - r_1^+ r_1^- / t_1^- & r_1^+ / t_1^- \\ -r_1^- / t_1^- & 1/t_1^- \end{bmatrix}^N. \tag{2.56}$$

The matrices in this expression are sometimes referred to as transfer matrices.

2.4 Macroscopic devices

Landauer formalism is usually applied to the study of transport in the microscopic regime. However, following Ref. [17], we can also use it to form a reasonable picture of transport in macroscopic devices. Consider a macroscopic device S with two leads. Assume both S and the leads to be composed of a crystalline material, thus being repetitions of some fundamental cell. In a macroscopic system, boundary conditions have relatively small effects, and we may thus assume periodic boundary conditions in the directions orthogonal to the leads. Then the transversal modes m may be indexed by the transversal component of the Bloch vector, $\boldsymbol{k}_\perp$. Thus, we may write (2.14) as

$$\bar{\mathcal{T}}(E) = 2 \sum_{\boldsymbol{k}_\perp \boldsymbol{k}'_\perp} \mathcal{T}^{\boldsymbol{k}_\perp \boldsymbol{k}'_\perp}(E), \tag{2.57}$$

where the additional factor of 2 comes from spin degeneracy. Let us simplify the expression by making the unjustified assumption that $\mathcal{T}^{\boldsymbol{k}_\perp \boldsymbol{k}'_\perp}(E) \sim \delta_{\boldsymbol{k}_\perp \boldsymbol{k}'_\perp}$. Then

$$\bar{\mathcal{T}}(E) = 2 \sum_{\boldsymbol{k}_\perp} \mathcal{T}^{\boldsymbol{k}_\perp}(E) \approx \frac{2A}{(2\pi)^2} \int \mathrm{d}\boldsymbol{k}_\perp \, \mathcal{T}(\boldsymbol{k}_\perp, E), \tag{2.58}$$

where A is the cross sectional area of S and the leads, and where we have used the macroscopic size to justify switching to an integral.

Since S is macroscopic, we are definitely in the incoherent regime, and since S is also periodic we may thus substitute $\mathcal{T}$ from (2.50). However, in the macroscopic regime we also have $L \gg \lambda$, so that in fact we may take $\mathcal{T} \approx \lambda / L$. Inserting this in (2.58) we get

$$\bar{\mathcal{T}}(E) = \frac{2A}{L} \int \frac{\mathrm{d}\boldsymbol{k}_\perp}{(2\pi)^2} \lambda(\boldsymbol{k}_\perp, E). \tag{2.59}$$

Inserting (2.59) in (2.20), we get

$$G = \frac{A}{L} \frac{2e^2}{h} \int \frac{\mathrm{d}\boldsymbol{k}_\perp}{(2\pi)^2} \int \mathrm{d}E \, \lambda(\boldsymbol{k}_\perp, E) \mathrm{Th}(E). \tag{2.60}$$

Similar expressions can be obtained also for the transport coefficients A B and C.

We also know that for macroscopic devices, the conductance should be $G = A\sigma / L$, where σ is the conductivity. Comparing this with (2.60), we get

$$\sigma = \frac{2e^2}{h} \int \frac{\mathrm{d}\boldsymbol{k}_\perp}{(2\pi)^2} \int \mathrm{d}E \, \lambda(\boldsymbol{k}_\perp, E) \mathrm{Th}(E), \tag{2.61}$$

which is an expression that is independent of the dimensions of the device. Intuitively, this relation should hold at least approximately also beyond the approximation $\mathcal{T}^{\boldsymbol{k}_\perp \boldsymbol{k}'_\perp}(E) \sim \delta_{\boldsymbol{k}_\perp \boldsymbol{k}'_\perp}$, but then with more complex expressions for

the back scattering mean free path λ. In fact, it is not hard to see that (2.61) is equivalent to the relaxation time approximation of the Boltzmann equation[17].

The Seebeck and Lorenz coefficients can still be found from (2.33) and (2.34), but with the probability P replaced with

$$P(E) = \frac{2e^2}{\sigma h} \int \frac{\mathrm{d}\boldsymbol{k}_\perp}{(2\pi)^2} \lambda(\boldsymbol{k}_\perp, E) \mathrm{Th}(E). \tag{2.62}$$

These expressions are then also independent of device dimensions, and should be regarded as approximate estimates of the material coefficients.

Chapter 3

The Non-equilibrium field integral

This chapter contains a derivation of transport expressions within the formalism of field-integrals or path-integrals. The theory is mostly taken from Ref. [2]. In Section 3.1 we introduce and derive the general field integral, while in Section 3.2 we specialize to transport calculations in a device of the type described in the previous chapter. In Section 3.3 we integrate over the lead degrees of freedom to obtain a description in terms of the system S alone. Finally, in Section 3.4 we derive expressions for the expectation values of electrical current and the heat current.

3.1 General field integral

Consider any quantum system S, and any observable A. In general, the state of S is described by a density operator ρ, and the expectation value of A is given by the expression[21, 18] $\langle A\rangle = \operatorname{Tr}\hat{A}\rho$. In particular, the expectation value at time t is $\langle A(t)\rangle = \operatorname{Tr}\hat{A}\rho(t)$, where

$$\rho(t) = U(t,t_0)\rho_0 U^\dagger(t,t_0). \tag{3.1}$$

Here $\rho_0 = \rho(t_0)$ represents the state at time t_0 and $U(t,t_0)$ is the propagator, or evolution operator[21], evolving the state from t_0 to t. The propagator satisfies the Schrödinger equation

$$\hbar i\frac{\mathrm{d}}{\mathrm{d}t}U(t,t_0) = \hat{H}(t)U(t,t_0), \tag{3.2}$$

where $\hat{H}$ is the Hamiltonian. If $\hat{H}$ is not time dependent, then U depends only on the difference between the time arguments, and we can write $U(t,t_0) = U(t-t_0)$. The propagator $U(t)$ satisfies[21]

$$U(-t) = U^\dagger(t), \qquad \text{and} \tag{3.3}$$

$$U(t+t') = U(t)U(t'). \tag{3.4}$$

Still assuming a time independent Hamiltonian, the general expression for $\langle A\rangle$ becomes

$$\begin{aligned}\langle A(t)\rangle &= \operatorname{Tr}\hat{A}\,U(t-t_0)\rho_0 U^\dagger(t-t_0) \\ &= \operatorname{Tr}U^\dagger(t-t_0)\hat{A}U(t-t_0)\rho_0 \\ &= \operatorname{Tr}\hat{A}(t)\rho_0,\end{aligned} \tag{3.5}$$

where we have defined $\hat{A}(t) = U^\dagger(t-t_0)\hat{A}U(t-t_0)$. Generalizing this expression, we define

$$\langle \hat{A}_1(t_1)\hat{A}_2(t_2)\cdots\hat{A}_n(t_n)\rangle = \operatorname{Tr}\hat{A}_1(t_1)\hat{A}_2(t_2)\cdots\hat{A}_n(t_t)\rho_0, \tag{3.6}$$

where $\hat{A}_k(t) = U^\dagger(t-t_0)\hat{A}_k U(t-t_0)$. In particular, we define the two time correlation function $\langle \hat{A}(t)\hat{B}(t')\rangle = \mathrm{Tr}\,\hat{A}(t)\hat{B}(t')\rho_0$. We adopt the convention of writing these expectation values with hats over the observables, in order to distinguish them from another type of expectation value to be introduced below.

3.1.1 Field integral expression for the propagator

A detailed derivation of the field integral is given in Ref. [2], where Chapters 3 and 4 deal with the field integral in imaginary time, and a generalization to real time is briefly covered in chapter 11. Here we will only cover the gist of the argument.

Making use of (3.4) and defining $\Delta t = (t_f - t_0)/N$, we can write $U(t_f - t_0)$ as

$$U(t_f - t_0) = U(\Delta t)^N. \tag{3.7}$$

For $N \to \infty$, Δt becomes arbitrarily small, and accordingly we can obtain an approximate solution of (3.2) as

$$U(\Delta t) \approx I - \frac{i}{\hbar}\hat{H}\Delta t. \tag{3.8}$$

Inserting this in (3.7) we get

$$U(t_f - t_0) \approx \left(I - \frac{i}{\hbar}\hat{H}\Delta t\right)^N. \tag{3.9}$$

We assume that the system S consists of a set of bosonic fields that we denote $\hat{\phi}$, and a set of fermionic fields that we denote $\hat{\psi}$. We introduce single particle bases $\{i\}$ and $\{j\}$ for the fields $\hat{\phi}$, and $\hat{\psi}$ respectively, and write the corresponding field operators as $\hat{\phi}_i$ and $\hat{\psi}_j$. Finally, we organize these operators in vectors $\hat{\boldsymbol{\phi}} = [\hat{\phi}_i]$ and $\hat{\boldsymbol{\psi}} = [\hat{\psi}_j]$.

The identity operator of the system can then be written as[2]

$$I = \int \mathrm{d}(\boldsymbol{\phi},\boldsymbol{\psi}) e^{-|\boldsymbol{\phi}|^2 - \bar{\boldsymbol{\psi}}\boldsymbol{\psi}} |\boldsymbol{\phi},\boldsymbol{\psi}\rangle\langle\boldsymbol{\phi},\bar{\boldsymbol{\psi}}|, \tag{3.10}$$

where we have introduced coherent states

$$|\boldsymbol{\phi},\boldsymbol{\psi}\rangle = e^{\hat{\boldsymbol{\phi}}^\dagger\boldsymbol{\phi} + \hat{\boldsymbol{\psi}}^\dagger\boldsymbol{\psi}}|0\rangle, \tag{3.11}$$

and defined the integration measure $\mathrm{d}(\boldsymbol{\phi},\boldsymbol{\psi})$ as

$$\int \mathrm{d}(\boldsymbol{\phi},\boldsymbol{\psi}) = \iint \frac{\mathbf{d}\boldsymbol{\phi}^\dagger \mathbf{d}\boldsymbol{\phi}}{\pi^d} \iint \mathbf{d}\bar{\boldsymbol{\psi}}\mathbf{d}\boldsymbol{\psi} = \iint \prod_i \frac{\mathrm{d}\phi_i^\star \mathrm{d}\phi_i}{\pi} \iint \prod_j \mathrm{d}\bar{\psi}_j \mathrm{d}\psi_j \tag{3.12}$$

In these expressions ψ_j and $\bar{\psi}_j$ are Grassmann numbers[2].

We insert $N+1$ identity operators on the form of (3.10) in (3.9), such that there is one identity operator on each side of each factor $(I - i\hat{H}\Delta t/\hbar)$. Further, we assume that the Hamiltonian of the system is expressed on normal ordered form as

$$\hat{H} = H(\hat{\boldsymbol{\phi}}^\dagger, \hat{\boldsymbol{\phi}}, \hat{\boldsymbol{\psi}}^\dagger, \hat{\boldsymbol{\psi}}), \tag{3.13}$$

where H is an analytic function, and the operators are ordered such that $\hat{\phi}_i$ and $\hat{\psi}_j$ are always to the right of the adjoint fields. The benefit of the coherent state representation is that $\hat{\phi}_i|\boldsymbol{\phi},\boldsymbol{\psi}\rangle = \phi_i|\boldsymbol{\phi},\boldsymbol{\psi}\rangle$ and $\hat{\psi}_j|\boldsymbol{\phi},\boldsymbol{\psi}\rangle = \psi_j|\boldsymbol{\phi},\boldsymbol{\psi}\rangle$. Thus, since the Hamiltonian is normal ordered, we have

$$\begin{aligned}\langle \boldsymbol{\phi}, \bar{\boldsymbol{\psi}}| \left(I - \frac{i}{\hbar}\hat{H}\Delta t\right)|\boldsymbol{\phi}', \boldsymbol{\psi}\rangle &= \left(1 - \frac{i}{\hbar}H(\boldsymbol{\phi}^\dagger, \boldsymbol{\phi}', \bar{\boldsymbol{\psi}}, \boldsymbol{\psi})\Delta t\right)\langle \boldsymbol{\phi}, \boldsymbol{\psi}|\boldsymbol{\phi}, \boldsymbol{\psi}\rangle \\ &\approx e^{-\frac{i}{\hbar}H(\boldsymbol{\phi}^\dagger, \boldsymbol{\phi}', \bar{\boldsymbol{\psi}}, \boldsymbol{\psi})\Delta t + \boldsymbol{\phi}^\dagger\boldsymbol{\phi}' + \bar{\boldsymbol{\psi}}\boldsymbol{\psi}},\end{aligned} \tag{3.14}$$

where we have also used the formula $\langle \boldsymbol{\phi}, \bar{\boldsymbol{\psi}}|\boldsymbol{\phi}', \boldsymbol{\psi}\rangle = e^{\boldsymbol{\phi}^\dagger\boldsymbol{\phi}' + \bar{\boldsymbol{\psi}}\boldsymbol{\psi}}$ for the inner product of coherent states[2].

Making use of these steps, we can after some rearrangement write (3.9) as

$$U(t_f - t_0) = \int D(\phi, \psi) e^{iS^+[\phi,\psi]/\hbar}|\boldsymbol{\phi}_N, \boldsymbol{\psi}_N\rangle\langle \boldsymbol{\phi}_0, \bar{\boldsymbol{\psi}}_0|, \tag{3.15}$$

where we have defined the field integral

$$\int D(\phi, \psi) = \iint \prod_{n=0}^{N} \mathrm{d}(\boldsymbol{\phi}_n, \boldsymbol{\psi}_n). \tag{3.16}$$

and the action S^+ as

$$\begin{aligned}&\frac{i}{\hbar}S^+[\phi,\psi] = -|\boldsymbol{\phi}_0|^2 - \bar{\boldsymbol{\psi}}_0\boldsymbol{\psi}_0 + \\ &\frac{i}{\hbar}\sum_{n=0}^{N-1}\left\{\hbar i\boldsymbol{\phi}_{n+1}^\dagger(\boldsymbol{\phi}_{n+1} - \boldsymbol{\phi}_n) + \hbar i\bar{\boldsymbol{\psi}}_{n+1}(\boldsymbol{\psi}_{n+1} - \boldsymbol{\psi}_n) - H(\boldsymbol{\phi}_{n+1}^\dagger, \boldsymbol{\phi}_n, \bar{\boldsymbol{\psi}}_{n+1}, \boldsymbol{\psi}_n)\Delta t\right\}.\end{aligned} \tag{3.17}$$

Since we are interested in the limit $\Delta t \to 0$, we can formally approximate the sum as

$$\begin{aligned}&\sum_{n=0}^{N-1}\Delta t\left\{\hbar i\boldsymbol{\phi}_{n+1}^\dagger\tfrac{\boldsymbol{\phi}_{n+1}-\boldsymbol{\phi}_n}{\Delta t} + \hbar i\bar{\boldsymbol{\psi}}_{n+1}\tfrac{\boldsymbol{\psi}_{n+1}-\boldsymbol{\psi}_n}{\Delta t} - H(\boldsymbol{\phi}_{n+1}^\dagger, \boldsymbol{\phi}_n, \bar{\boldsymbol{\psi}}_{n+1}, \boldsymbol{\psi}_n)\right\} \\ &\approx \int_{t_0}^{t_f}\mathrm{d}t\,\left(\hbar i\boldsymbol{\phi}^\dagger\dot{\boldsymbol{\phi}} + \hbar i\bar{\boldsymbol{\psi}}\dot{\boldsymbol{\psi}} - H(\boldsymbol{\phi}^\dagger, \boldsymbol{\phi}, \bar{\boldsymbol{\psi}}, \boldsymbol{\psi})\right),\end{aligned} \tag{3.18}$$

where $\boldsymbol{\phi}_n = \boldsymbol{\phi}(n\Delta t)$ and $\boldsymbol{\psi}_n = \boldsymbol{\psi}(n\Delta t)$. This integral must however be thought of as a purely symbolic notation, since in reality the limit $N \to \infty$ is not

well defined for the field integral expressions above, and since the derivative of Grassmann numbers is in any case not meaningful.

We will also require a field integral expression for $U^\dagger$. Taking the adjoint of (3.9), we get

$$U^\dagger(t_f - t_0) = \left(I + \frac{i}{\hbar}\hat{H}\Delta t\right)^N. \tag{3.19}$$

then simply repeating the argument above, we eventually end up with the expression

$$U^\dagger(t_f - t_0) = \int D(\phi,\psi) e^{iS^-[\phi,\psi]/\hbar} |\boldsymbol{\phi}_0, \boldsymbol{\psi}_0\rangle\langle\boldsymbol{\phi}_N, \bar{\boldsymbol{\psi}}_N|, \tag{3.20}$$

where the action S^- is given by

$$\frac{i}{\hbar}S^-[\phi,\psi] = -|\boldsymbol{\phi}_N|^2 - \bar{\boldsymbol{\psi}}_N\boldsymbol{\psi}_N \tag{3.21}$$
$$-\frac{i}{\hbar}\sum_{n=0}^{N-1}\left\{\hbar i\boldsymbol{\phi}_n^\dagger(\boldsymbol{\phi}_{n+1} - \boldsymbol{\phi}_n) + \hbar i\bar{\boldsymbol{\psi}}_n(\boldsymbol{\psi}_{n+1} - \boldsymbol{\psi}_n) - H(\boldsymbol{\phi}_n^\dagger, \boldsymbol{\phi}_{n+1}, \bar{\boldsymbol{\psi}}_n, \boldsymbol{\psi}_{n+1})\Delta t\right\}.$$

Again, the sum can formally be approximated as

$$\sum_{n=0}^{N-1}\Delta t\left\{\hbar i\boldsymbol{\phi}_n^\dagger\frac{\boldsymbol{\phi}_{n+1} - \boldsymbol{\phi}_n}{\Delta t} + \hbar i\bar{\boldsymbol{\psi}}_n\frac{\boldsymbol{\psi}_{n+1} - \boldsymbol{\psi}_n}{\Delta t} - H(\boldsymbol{\phi}_n^\dagger, \boldsymbol{\phi}_{n+1}, \bar{\boldsymbol{\psi}}_n, \boldsymbol{\psi}_{n+1})\right\}$$
$$\approx \int_{t_0}^{t_f}\mathrm{d}t\,\left(\hbar i\boldsymbol{\phi}^\dagger\dot{\boldsymbol{\phi}} + \hbar i\bar{\boldsymbol{\psi}}\dot{\boldsymbol{\psi}} - H(\boldsymbol{\phi}^\dagger, \boldsymbol{\phi}, \bar{\boldsymbol{\psi}}, \boldsymbol{\psi})\right). \tag{3.22}$$

3.1.2 Field integral expressions for expectation values

Single particle fermionic and bosonic observables respectively take the form

$$\hat{A} = \sum_{ij} A_{ij}\hat{\psi}_i^\dagger\hat{\psi}_j, \text{ and} \tag{3.23}$$

$$\hat{B} = \sum_{ij} B_{ij}\hat{\phi}_i^\dagger\hat{\phi}_j, \tag{3.24}$$

where $A_{ij} = \langle i|\hat{A}|j\rangle$ and $B_{ij} = \langle i|\hat{B}|j\rangle$ for single particle states $|i\rangle$ and $|j\rangle$. Thus, we have

$$\langle A\rangle = \sum_{ij} A_{ij}\langle\hat{\psi}_i^\dagger\hat{\psi}_j\rangle, \tag{3.25}$$

and similarly for the bosonic case. Accordingly, all single particle expectation values can be found by calculating expectation values on the form $\langle\hat{\psi}_i^\dagger\hat{\psi}_j\rangle$ and $\langle\hat{\phi}_i^\dagger\hat{\phi}_j\rangle$.

By (3.6) we have

$$\begin{aligned}\langle\hat{\psi}_i^\dagger(t)\hat{\psi}_j(t')\rangle &= \mathrm{Tr}\, U^\dagger(t-t_0)\hat{\psi}_i^\dagger U(t-t_0)U^\dagger(t'-t_0)\hat{\psi}_j U(t'-t_0)\rho_0 \\ &= \mathrm{Tr}\, U^\dagger(t-t_0)\hat{\psi}_i^\dagger U^\dagger(t_f-t)U(t_f-t')\hat{\psi}_j U(t'-t_0)\rho_0 \\ &= \mathrm{Tr}\, U^\dagger(t_f-t_0)U(t_f-t)\hat{\psi}_i^\dagger U(t-t')\hat{\psi}_j U(t'-t_0)\rho_0 \\ &= \mathrm{Tr}\, U^\dagger(t-t_0)\hat{\psi}_i^\dagger U^\dagger(t'-t)\hat{\psi}_j U^\dagger(t_f-t')U(t_f-t_0)\rho_0,\end{aligned} \tag{3.26}$$

where we have introduced an arbitrary final time $t_f > t, t'$, and made use of (3.3) and (3.4). The product $U(t_f - t')\hat{\psi}_j U(t' - t_0)$ in the second line can be written as a field integral by the same procedure as in the previous section, where we approximate the propagators as products of linear factors, and then insert $N+1$ identity operators given by (3.10). However, we must take care to place the appropriate identity operator to the right of $\hat{\psi}_j$, so that we can make use of the relation $\hat{\psi}_j|\boldsymbol{\phi},\boldsymbol{\psi}\rangle = \psi_j|\boldsymbol{\phi},\boldsymbol{\psi}\rangle$ to get rid of this operator.

Clearly, we end up with an expression identical to (3.15), except for an additional factor of $\psi_{mj} = \psi_j(t')$. As long as we assume the Hamiltonian to be even in the fermionic fields, this factor can be commuted to the left in the expression, so that we end up with

$$U(t_f - t')\hat{\psi}_j U(t' - t_0) = \int D(\phi,\psi)\psi_j(t')e^{iS^+[\phi,\psi]/\hbar}|\boldsymbol{\phi}_N,\boldsymbol{\psi}_N\rangle\langle\boldsymbol{\phi}_0,\bar{\boldsymbol{\psi}}_0|. \tag{3.27}$$

Proceeding in a precisely analogous manor, we also find the relation

$$U^\dagger(t - t_0)\hat{\psi}_i^\dagger U^\dagger(t_f - t) = \int D(\phi,\psi)\bar{\psi}_i(t)e^{iS^-[\phi,\psi]/\hbar}|\boldsymbol{\phi}_0,\boldsymbol{\psi}_0\rangle\langle\boldsymbol{\phi}_N,\bar{\boldsymbol{\psi}}_N|. \tag{3.28}$$

Inserting (3.27) and (3.28) in the second line of (3.26), we obtain after some rearrangement

$$\langle\hat{\psi}_i^\dagger(t)\hat{\psi}_j(t')\rangle = \int D(+,-)\bar{\psi}_i^-(t)\psi_j^+(t')e^{iS[\phi^+,\psi^+,\phi^-,\psi^-]/\hbar}, \tag{3.29}$$

where we have introduced the short notation

$$\int D(+,-) = \int D(\phi^+,\psi^+,\phi^-,\psi^-) = \int D(\phi^+,\psi^+)\int D(\phi^-,\psi^-), \tag{3.30}$$

as well as the total action S, defined by the expression

$$\begin{aligned}\frac{i}{\hbar}S[\phi^+,\psi^+,\phi^-,\psi^-] = \frac{i}{\hbar}\left(S^+[\phi^+,\psi^+] + S^-[\phi^-,\psi^-]\right) + \boldsymbol{\phi}_N^{-\dagger}\boldsymbol{\phi}_N^+ + \bar{\boldsymbol{\psi}}_N^-\boldsymbol{\psi}_N^+ \\ + \ln\langle\boldsymbol{\phi}_0^+,\bar{\boldsymbol{\psi}}_0^+|\rho_0|\boldsymbol{\phi}_0^-,-\boldsymbol{\psi}_0^-\rangle,\end{aligned} \tag{3.31}$$

where S^+ and S^- are given respectively by (3.17) and (3.21), and where the negative sign in front of $\boldsymbol{\psi}_0^-$ comes from the Grassmann anti-commutation relations.

Motivated by this result, we make the general definition

$$\langle A_1(t_1)\cdots A_n(t_n)\rangle = \int D(+,-)A_1(t_1)\cdots A_n(t_n)e^{iS[\phi^+,\psi^+,\phi^-,\psi^-]/\hbar}, \quad (3.32)$$

which allows us to write (3.29) simply as $\langle\hat{\psi}_i^\dagger(t)\hat{\psi}_j(t')\rangle = \langle\bar{\psi}_i^-(t)\psi_j^+(t')\rangle$. (3.32) defines the general non-equilibrium field integral, also known as the Keldysh field integral.[2]

As long as $t > t'$, we can make use of the same procedure as above to write also the product $U(t_f - t)\hat{\psi}_i^\dagger U(t - t')\hat{\psi}_j U(t' - t_0)$ from the third line of (3.26) as a field integral. Combining the resulting expression with (3.20), we obtain $\langle\hat{\psi}_i^\dagger(t)\hat{\psi}_j(t')\rangle = \langle\bar{\psi}_i^+(t)\psi_j^+(t')\rangle$. Finally, $U^\dagger(t - t_0)\hat{\psi}_i^\dagger U^\dagger(t' - t)\hat{\psi}_j U^\dagger(t_f - t')$ from the fourth line of (3.26) can be written as a field integral in the same manner, as long as we require $t < t'$. Combining the resulting expression with (3.15), we obtain $\langle\hat{\psi}_i^\dagger(t)\hat{\psi}_j(t')\rangle = \langle\bar{\psi}_i^-(t)\psi_j^-(t')\rangle$. Summarizing, we have found the following relations between operator and field integral expectation values:

$$\begin{aligned}\langle\hat{\psi}_i^\dagger(t)\hat{\psi}_j(t')\rangle &= \langle\bar{\psi}_i^-(t)\psi_j^+(t')\rangle \\ &= \langle\bar{\psi}_i^+(t)\psi_j^+(t')\rangle \qquad t > t' \\ &= \langle\bar{\psi}_i^-(t)\psi_j^-(t')\rangle \qquad t < t'.\end{aligned} \quad (3.33)$$

The opposite product $\langle\hat{\psi}_i(t)\hat{\psi}_j^\dagger(t')\rangle$ can be found in a similar fashion, by simply exchanging the operators $\hat{\psi}_j$ and $\hat{\psi}_i^\dagger$ in (3.26), renaming the indices, and then repeating the calculations above. In the end, the results are

$$\begin{aligned}\langle\hat{\psi}_i(t)\hat{\psi}_j^\dagger(t')\rangle &= \langle\psi_i^-(t)\bar{\psi}_j^+(t')\rangle \\ &= \langle\psi_i^+(t)\bar{\psi}_j^+(t')\rangle \qquad t \geq t' \\ &= \langle\psi_i^-(t)\bar{\psi}_j^-(t')\rangle \qquad t \leq t'.\end{aligned} \quad (3.34)$$

Clearly, the same procedure can also be applied to the bosonic expressions. This yields the near identical expressions

$$\begin{aligned}\langle\phi_i^\dagger(t)\phi_j(t')\rangle &= \langle\phi_i^{-\star}(t)\phi_j^+(t')\rangle \\ &= \langle\phi_i^{+\star}(t)\phi_j^+(t')\rangle \qquad t > t' \\ &= \langle\phi_i^{-\star}(t)\phi_j^-(t')\rangle \qquad t < t'\end{aligned} \quad (3.35)$$

$$\begin{aligned}\langle\phi_i(t)\phi_j^\dagger(t')\rangle &= \langle\phi_i^-(t)\phi_j^{+\star}(t')\rangle \\ &= \langle\phi_i^+(t)\phi_j^{+\star}(t')\rangle \qquad t \geq t' \\ &= \langle\phi_i^-(t)\phi_j^{-\star}(t')\rangle \qquad t \leq t'.\end{aligned} \quad (3.36)$$

3.2 Transport field integral

3.2.1 Definition of the model

Let us now return to the system described in Section 2.1, where a system S is connected to a set of leads p. We will assume that the degrees of freedom in S

are a bosonic field $\boldsymbol{\phi}$, and fermionic field $\boldsymbol{\psi}$, and that these are controlled by a Hamiltonian on the form of (3.13). We also assume that lead p contains a fermionic field $\boldsymbol{\psi}_p$, and a bosonic field $\boldsymbol{\phi}_p$. Following the discussion of Section 2.2, we take the only purpose of the leads to be to drive S out of equilibrium, and accordingly choose the lead physics from considerations of simplicity rather than realism. Thus, we assume the lead Hamiltonians to be quadratic in the fields, and write the Hamiltonian of lead p as

$$\hat{H}_p = \hat{\boldsymbol{\psi}}_p^\dagger H_p^F \hat{\boldsymbol{\psi}}_p + \hat{\boldsymbol{\phi}}_p^\dagger H_p^B \hat{\boldsymbol{\phi}}_p, \tag{3.37}$$

where H_p^F and H_p^B are matrix representations of the fermionic and bosonic single particle Hamiltonians respectively.

An other simplification we will make, is to assume the leads to be internally in equilibrium at $t = t_0$. This can be justified from an assumption that the leads are not in contact with S before this time. Accordingly, this assumption is more plausible than the one made in Chapter 2, where we assumed the leads to be in equilibrium at all times. The density operator $\rho_p(t_0)$ can then be expressed as[18]

$$\rho_p(t_0) = \frac{1}{Z_p} e^{-\beta_p(\hat{H}_p - \mu_p \hat{N}_p^F)}, \tag{3.38}$$

where $T_p = 1/k_B\beta_p$ is the temperature, μ_p the chemical potential of the fermion field, and $\hat{N}_p^F = \hat{\boldsymbol{\psi}}_p^\dagger \hat{\boldsymbol{\psi}}_p$ is the fermion number operator.

We assume that the interactions between the leads and the system S consists of simple single particle hopping, so that the interaction terms are also quadratic in the fields. Thus, we can write the total Hamiltonian as

$$\hat{H} = \hat{H}_S + \sum_p \left(\hat{H}_p + \hat{\boldsymbol{\phi}}_p^\dagger b_p \hat{\boldsymbol{\phi}} + \hat{\boldsymbol{\phi}}^\dagger b_p^\dagger \hat{\boldsymbol{\phi}}_p + \hat{\boldsymbol{\psi}}_p^\dagger t_p \hat{\boldsymbol{\psi}} + \hat{\boldsymbol{\psi}}^\dagger t_p^\dagger \hat{\boldsymbol{\psi}}_p \right), \tag{3.39}$$

where $\hat{H}_S$ is given by (3.13), $\hat{H}_p$ by (3.37), and b_p and t_p are matrices describing single particle hopping between the leads and S, for bosons and fermions respectively.

On the other hand, the total density operator $\rho_0 = \rho(t_0)$ will be assumed to be on the product form

$$\rho_0 = \rho_S(t_0) \prod_p \rho_p(t_0), \tag{3.40}$$

where all the factors are assumed to commute. This form can again be justified from the assumption that the leads are first brought into contact with S at $t = t_0$. While $\rho_p(t_0)$ have been defined above, we still require an expression for $\rho_S(t_0)$, the state of S at $t = t_0$. We are generally interested in stationary properties at times $t \gg t_0$, at which we assume S to have reached a steady state $\rho_S(t)$ which is independent of the initial state. Thus, we can choose $\rho_S(t_0)$ arbitrarily, and we select it for purposes of simplicity as

$$\rho_S(t_0) = |0\rangle\langle 0| = P_S^0, \tag{3.41}$$

i.e. the ground state projection operator acting on S. Accordingly, the full state ρ_0 of (3.40) becomes

$$\rho_0 = \frac{1}{Z} \exp\left(\sum_p -\beta_p (\hat{H}_p - \mu_p \hat{N}_p^F) \right) P_S^0. \tag{3.42}$$

3.2.2 Expression as a field integral

To express the model defined above as a field integral, we must calculate the total action S defined in (3.31). To begin, we collect the component fields $\boldsymbol{\psi}$, $\boldsymbol{\psi}_p$, and so on in total field vectors $\tilde{\boldsymbol{\psi}}$, $\bar{\tilde{\boldsymbol{\psi}}}$ and $\tilde{\boldsymbol{\phi}}$. That is, we define $\tilde{\boldsymbol{\psi}} = [\boldsymbol{\psi}, \cdots \boldsymbol{\psi}_p \cdots]$ and similarly for the other fields. The total action of the system is then given by (3.31), with ψ substituted for $\tilde{\psi}$ and ϕ substituted for $\tilde{\phi}$.

The evaluation of this action is a straight forward task, except for the bracket involving ρ_0. By (3.42) we have

$$\begin{aligned} \ln \langle \tilde{\boldsymbol{\phi}}_0^+, \bar{\tilde{\boldsymbol{\psi}}}_0^+ | \rho_0 | \tilde{\boldsymbol{\phi}}_0^-, -\tilde{\boldsymbol{\psi}}_0^- \rangle = & \sum_p \ln \langle \boldsymbol{\phi}_{p0}^+, \bar{\boldsymbol{\psi}}_{p0}^+ | e^{-\beta_p (\hat{H}_p - \mu_p \hat{N}_p^F)} | \boldsymbol{\phi}_{p0}^-, -\boldsymbol{\psi}_{p0}^- \rangle \\ & + \ln \langle \boldsymbol{\phi}_0^+, \bar{\boldsymbol{\psi}}_0^+ | P_S^0 | \boldsymbol{\phi}_0^-, -\boldsymbol{\psi}_0^- \rangle - \ln Z. \end{aligned} \tag{3.43}$$

From the definition (3.11) of the coherent states, it is easily realized that $\langle \boldsymbol{\phi}_0^+, \bar{\boldsymbol{\psi}}_0^+ | P_S^0 | \boldsymbol{\phi}_0^-, -\boldsymbol{\psi}_0^- \rangle = 1$. To find the remaining terms we will make use of commutation relations of exponential operators. By making use of the fundamental commutation relations of the fermionic and bosonic fields, $[\phi_i, \phi_j^\dagger] = \phi_i \phi_j^\dagger - \phi_j^\dagger \phi_i = \delta_{ij}$ and $\{\psi_i, \psi_j^\dagger\} = \psi_i \psi_j^\dagger + \psi_j^\dagger \psi_i = \delta_{ij}$, together with a Taylor expansion of the exponential, one can show that for any matrix A

$$e^{\boldsymbol{\phi}^\dagger \hat{\boldsymbol{\phi}}} e^{\hat{\boldsymbol{\phi}}^\dagger A \hat{\boldsymbol{\phi}}} = e^{\hat{\boldsymbol{\phi}}^\dagger A \hat{\boldsymbol{\phi}}} e^{\boldsymbol{\phi}^\dagger e^A \hat{\boldsymbol{\phi}}}, \quad \text{and} \tag{3.44}$$

$$e^{\boldsymbol{\psi}^\dagger \hat{\boldsymbol{\psi}}} e^{\hat{\boldsymbol{\psi}}^\dagger A \hat{\boldsymbol{\psi}}} = e^{\hat{\boldsymbol{\psi}}^\dagger A \hat{\boldsymbol{\psi}}} e^{\boldsymbol{\psi}^\dagger e^A \hat{\boldsymbol{\psi}}}. \tag{3.45}$$

These expressions can be used together with the definition of the coherent states (3.11) to rearrange the terms of (3.43) in such a way that the relation $\hat{\psi}_j |\boldsymbol{\phi}, \boldsymbol{\psi}\rangle = \psi_j |\boldsymbol{\phi}, \boldsymbol{\psi}\rangle$ can be used to remove the operators from the expressions. The results is

$$\ln \langle \boldsymbol{\phi}_{p0}^+, \bar{\boldsymbol{\psi}}_{p0}^+ | e^{-\beta_p (\hat{H}_p - \mu_p \hat{N}_p^F)} | \boldsymbol{\phi}_{p0}^-, -\boldsymbol{\psi}_{p0}^- \rangle = \boldsymbol{\phi}_{p0}^{+\dagger} e^{-\beta_p H_p^B} \boldsymbol{\phi}_{p0}^- - \bar{\boldsymbol{\psi}}_{p0}^+ e^{-\beta_p (H_p^F - \mu_p)} \boldsymbol{\psi}_{p0}^-. \tag{3.46}$$

Accordingly, making use of (3.43), (3.31) and (3.39), we can write the total action S as

$$S[\tilde{\phi}^+, \tilde{\psi}^+, \tilde{\phi}^-, \tilde{\psi}^-] = S_S + \sum_p \left(S_p^B + S_p^F \right), \tag{3.47}$$

where

$$\frac{i}{\hbar}S_S[\phi^+,\psi^+,\phi^-,\psi^-] = \frac{i}{\hbar}\left(S^+[\phi^+,\psi^+] + S^-[\phi^-,\psi^-]\right) + \boldsymbol{\phi}_N^{-\dagger}\boldsymbol{\phi}_N^+ + \bar{\boldsymbol{\psi}}_N^-\boldsymbol{\psi}_N^+, \tag{3.48}$$

with S^+ and S^- given respectively by (3.17) and (3.21), and where

$$\frac{i}{\hbar}S_p^B = \frac{i}{\hbar}\left(S_p^{B+} + S_p^{B-}\right) + \boldsymbol{\phi}_{pN}^{-\dagger}\boldsymbol{\phi}_{pN}^+ + \boldsymbol{\phi}_{p0}^{+\dagger}e^{-\beta_p H_p^B}\boldsymbol{\phi}_{p0}^- - \ln Z_p^B, \qquad \text{and} \tag{3.49}$$

$$\frac{i}{\hbar}S_p^F = \frac{i}{\hbar}\left(S_p^{F+} + S_p^{F-}\right) + \bar{\boldsymbol{\psi}}_{pN}^-\boldsymbol{\phi}_{pN}^+ - \bar{\boldsymbol{\psi}}_{p0}^+e^{-\beta_p(H_p^F-\mu_p)}\boldsymbol{\psi}_{p0}^- - \ln Z_p^F, \tag{3.50}$$

with

$$\frac{i}{\hbar}S_p^{B+} = -|\boldsymbol{\phi}_{p0}^+|^2 + \frac{i}{\hbar}\sum_{n=0}^{N-1}\left\{\hbar i\boldsymbol{\phi}_{pn+1}^{+\dagger}(\boldsymbol{\phi}_{pn+1}^+ - \boldsymbol{\phi}_{pn}^+) - \boldsymbol{\phi}_{pn+1}^{+\dagger}H_p^B\boldsymbol{\phi}_{pn}^+\Delta t\right\} \tag{3.51}$$

$$-\frac{i}{\hbar}\sum_{n=0}^{N-1}\left\{\boldsymbol{\phi}_{pn+1}^{+\dagger}b_p\boldsymbol{\phi}_n^+ + \boldsymbol{\phi}_{n+1}^{+\dagger}b_p^\dagger\boldsymbol{\phi}_{pn}^+\right\}\Delta t,$$

$$\frac{i}{\hbar}S_p^{F+} = -\bar{\boldsymbol{\psi}}_{p0}^+\boldsymbol{\psi}_{p0}^+ + \frac{i}{\hbar}\sum_{n=0}^{N-1}\left\{\hbar i\bar{\boldsymbol{\psi}}_{pn+1}^+(\boldsymbol{\psi}_{pn+1}^+ - \boldsymbol{\psi}_{pn}^+) - \bar{\boldsymbol{\psi}}_{pn+1}^+H_p^F\boldsymbol{\psi}_{pn}^+\Delta t\right\} \tag{3.52}$$

$$-\frac{i}{\hbar}\sum_{n=0}^{N-1}\left\{\bar{\boldsymbol{\psi}}_{pn+1}^+t_p\boldsymbol{\psi}_n^+ + \bar{\boldsymbol{\psi}}_{n+1}^+t_p^\dagger\boldsymbol{\psi}_{pn}^+\right\}\Delta t,$$

$$\frac{i}{\hbar}S_p^{B-} = -|\boldsymbol{\phi}_{pN}^-|^2 - \frac{i}{\hbar}\sum_{n=0}^{N-1}\left\{\hbar i\boldsymbol{\phi}_{pn}^{-\dagger}(\boldsymbol{\phi}_{pn+1}^- - \boldsymbol{\phi}_{pn}^-) - \boldsymbol{\phi}_{pn}^{-\dagger}H_p^B\boldsymbol{\phi}_{pn+1}^-\Delta t\right\} \tag{3.53}$$

$$+\frac{i}{\hbar}\sum_{n=0}^{N-1}\left\{\boldsymbol{\phi}_{pn}^{-\dagger}b_p\boldsymbol{\phi}_{n+1}^- + \boldsymbol{\phi}_n^{-\dagger}b_p^\dagger\boldsymbol{\phi}_{pn+1}^-\right\}\Delta t, \qquad \text{and}$$

$$\frac{i}{\hbar}S_p^{F-} = -\bar{\boldsymbol{\psi}}_{pN}^-\boldsymbol{\psi}_{pN}^- - \frac{i}{\hbar}\sum_{n=0}^{N-1}\left\{\hbar i\bar{\boldsymbol{\psi}}_{pn}^-(\boldsymbol{\psi}_{pn+1}^- - \boldsymbol{\psi}_{pn}^-) - \bar{\boldsymbol{\psi}}_{pn}^-H_p^F\boldsymbol{\psi}_{pn+1}^-\Delta t\right\} \tag{3.54}$$

$$+\frac{i}{\hbar}\sum_{n=0}^{N-1}\left\{\bar{\boldsymbol{\psi}}_{pn}^-t_p\boldsymbol{\psi}_{n+1}^- + \bar{\boldsymbol{\psi}}_n^-t_p^\dagger\boldsymbol{\psi}_{pn+1}^-\right\}\Delta t.$$

3.3 Integration over the leads

Combining (3.32) and (3.47), and making use of the facts that S_S contains no terms from the leads, and S_p^B and S_p^F no terms from the other leads q, we can

reexpress a general expectation value $\langle A[\phi,\psi]\rangle$ of fields in S as

$$\langle A\rangle = \int D(+,-)A[\phi,\psi]e^{iS_S/\hbar}\prod_p \int D(\phi_p^+,\phi_p^-)e^{iS_p^B/\hbar}\int D(\psi_p^+,\psi_p^-)e^{iS_p^F/\hbar}, \tag{3.55}$$

so that the lead sections of the integral can be performed separately. By (3.49)-(3.54), the lead actions S_p^B and S_p^F are quadratic in the fields, so accordingly, these integrals can be performed using Gaussian integration.

Introducing a total field vector $\boldsymbol{\phi}_p = [\boldsymbol{\phi}_{p0}^+ \cdots \boldsymbol{\phi}_{pN}^+, \boldsymbol{\phi}_{p0}^- \cdots \boldsymbol{\phi}_{pN}^-]$ and similar for the other fields, the lead actions can be expressed as

$$S_p^B = \boldsymbol{\phi}_p^\dagger A_p \boldsymbol{\phi}_p + \boldsymbol{\phi}_p^\dagger B_p \boldsymbol{\phi} + \boldsymbol{\phi}^\dagger B_p^\dagger \boldsymbol{\phi}_p + \hbar i \ln Z_p^B, \quad \text{and} \tag{3.56}$$

$$S_p^F = \bar{\boldsymbol{\psi}}_p C_p \boldsymbol{\psi}_p + \bar{\boldsymbol{\psi}}_p T_p \boldsymbol{\psi} + \bar{\boldsymbol{\psi}} T_p^\dagger \boldsymbol{\psi}_p + \hbar i \ln Z_p^F, \tag{3.57}$$

where A_p, B_p, C_p and T_p are appropriate matrices. Making use of Gaussian integration rules found for instance in Altland and Simons[2], we find

$$\int D(\phi_p^+,\phi_p^-)e^{iS_p^B/\hbar} = \frac{\hbar i}{Z_p^B}\det A_p^{-1} e^{-i\boldsymbol{\phi}^\dagger B_p^\dagger A_p^{-1} B_p \boldsymbol{\phi}/\hbar}, \quad \text{and} \tag{3.58}$$

$$\int D(\psi_p^+,\psi_p^-)e^{iS_p^F/\hbar} = \frac{1}{\hbar i Z_p^F}\det C_p\, e^{-i\bar{\boldsymbol{\psi}} T_p^\dagger C_p^{-1} T_p \boldsymbol{\psi}/\hbar}. \tag{3.59}$$

Further, the prefactors of these expressions must in fact equal 1. To see this, consider isolated lead systems, respectively with total Hamiltonians $\hat{H} = \hat{\boldsymbol{\phi}}_p^\dagger H_p^B \hat{\boldsymbol{\phi}}_p$ and $\hat{H} = \hat{\boldsymbol{\psi}}_p^\dagger H_p^F \hat{\boldsymbol{\psi}}_p$. It should be clear that the actions of these systems are given respectively by (3.49) and (3.50), but excluding the terms involving the matrices b_p and t_p. Thus, these actions can be written $S = \boldsymbol{\phi}_p^\dagger A_p \boldsymbol{\phi}_p$ and $S = \bar{\boldsymbol{\psi}}_p C_p \boldsymbol{\psi}_p$ respectively. Applying (3.32) to these systems, and again making use of Gaussian integration rules, we find

$$1 = \langle 1\rangle = \frac{\hbar i}{Z_p^B}\det A_p^{-1} = \frac{1}{\hbar i Z_p^F}\det C_p. \tag{3.60}$$

Thus, making use of (3.58) and (3.59), we can express (3.55) as

$$\langle A\rangle = \int D(+,-)A[\phi,\psi]e^{iS^{\text{eff}}[\phi,\psi]/\hbar}, \tag{3.61}$$

where the effective action S^{eff} is given by

$$S^{\text{eff}}[\phi,\psi] = S_S + \sum_p \left(S_p^{B,\text{eff}} + S_p^{F,\text{eff}}\right), \quad \text{with} \tag{3.62}$$

$$S_p^{B,\text{eff}} = -\boldsymbol{\phi}^\dagger B_p^\dagger D_p B_p \boldsymbol{\phi}, \quad \text{and} \tag{3.63}$$

$$S_p^{F,\text{eff}} = -\bar{\boldsymbol{\psi}} T_p^\dagger G_p T_p \boldsymbol{\psi}. \tag{3.64}$$

where we have defined $D_p = A_p^{-1}$ and $G_p = C_p^{-1}$.

3.3.1 Green's functions

Following Altland and Simons[2], expressions for D_p and G_p could be obtained by direct inversion of the matrices A_p and C_p. However, as we will see D_p and G_p are related to certain operator expectation values, which are in fact easier to calculate. Consider again the isolated lead systems with actions $\boldsymbol{\phi}_p^\dagger A_p \boldsymbol{\phi}_p$ and $\bar{\boldsymbol{\psi}}_p C_p \boldsymbol{\psi}_p$. Once again making use of (3.32) and laws of Gaussian integrals, we have

$$\langle \boldsymbol{\phi}_p \boldsymbol{\phi}_p^\dagger \rangle = \frac{1}{Z_p^B} \iint \frac{\mathbf{d}\boldsymbol{\phi}_p^\dagger \mathbf{d}\boldsymbol{\phi}_p}{\pi^{2Nd}} \boldsymbol{\phi}_p \boldsymbol{\phi}_p^\dagger e^{-\boldsymbol{\phi}_p^\dagger A_p \boldsymbol{\phi}_p / \hbar i} = i\hbar A_p^{-1} = i\hbar D_p, \quad \text{and} \tag{3.65}$$

$$\langle \boldsymbol{\psi}_p \bar{\boldsymbol{\psi}}_p \rangle = \frac{1}{Z_p^F} \iint \mathbf{d}\bar{\boldsymbol{\psi}}_p \mathbf{d}\boldsymbol{\psi}_p \boldsymbol{\psi}_p \bar{\boldsymbol{\psi}}_p e^{-\bar{\boldsymbol{\psi}}_p C_p \boldsymbol{\psi}_p / \hbar i} = i\hbar C_p^{-1} = i\hbar G_p. \tag{3.66}$$

Accordingly, the matrices D_p and G_p describe correlations between the various fields in the leads. In the literature, these objects are often referred to as Green's functions[2, 15, 7]. When dealing with more general systems, where the action need not be quadratic, we define the Green's functions directly through the relations $i\hbar D = \langle \boldsymbol{\phi}\boldsymbol{\phi}^\dagger \rangle$ and $i\hbar G = \langle \boldsymbol{\psi}\bar{\boldsymbol{\psi}} \rangle$. It is convenient to decompose these matrices into four sectors in the following manner:

$$\boldsymbol{\phi}^\dagger D \boldsymbol{\phi} = \begin{bmatrix} \boldsymbol{\phi}^{+\dagger} & \boldsymbol{\phi}^{-\dagger} \end{bmatrix} \begin{bmatrix} D^t & D^< \\ D^> & D^{\bar{t}} \end{bmatrix} \begin{bmatrix} \boldsymbol{\phi}^+ \\ \boldsymbol{\phi}^- \end{bmatrix}, \quad \text{and} \tag{3.67}$$

$$\bar{\boldsymbol{\psi}} G \boldsymbol{\psi} = \begin{bmatrix} \bar{\boldsymbol{\psi}}^+ & \bar{\boldsymbol{\psi}}^- \end{bmatrix} \begin{bmatrix} G^t & G^< \\ G^> & G^{\bar{t}} \end{bmatrix} \begin{bmatrix} \boldsymbol{\psi}^+ \\ \boldsymbol{\psi}^- \end{bmatrix}, \tag{3.68}$$

where $\boldsymbol{\phi}^+ = [\boldsymbol{\phi}_0^+ \cdots \boldsymbol{\phi}_N^+]$, $\boldsymbol{\phi}^- = [\boldsymbol{\phi}_0^- \cdots \boldsymbol{\phi}_N^-]$, and similar for the fermionic fields. Writing out the definitions in terms of the component matrices, we have

$$i\hbar D^t(t,t') = i\hbar D^t_{nm} = \langle \boldsymbol{\phi}^+(t) \boldsymbol{\phi}^{+\dagger}(t') \rangle, \tag{3.69}$$

$$i\hbar D^<(t,t') = i\hbar D^<_{nm} = \langle \boldsymbol{\phi}^+(t) \boldsymbol{\phi}^{-\dagger}(t') \rangle, \tag{3.70}$$

$$i\hbar D^>(t,t') = i\hbar D^>_{nm} = \langle \boldsymbol{\phi}^-(t) \boldsymbol{\phi}^{+\dagger}(t') \rangle, \tag{3.71}$$

$$i\hbar D^{\bar{t}}(t,t') = i\hbar D^{\bar{t}}_{nm} = \langle \boldsymbol{\phi}^-(t) \boldsymbol{\phi}^{-\dagger}(t') \rangle, \tag{3.72}$$

where $t = n\Delta t$ and $t' = m\Delta t$. Similarly, for the fermionic fields we have

$$i\hbar G^t(t,t') = i\hbar G^t_{nm} = \langle \boldsymbol{\psi}^+(t) \bar{\boldsymbol{\psi}}^+(t') \rangle, \tag{3.73}$$

$$i\hbar G^<(t,t') = i\hbar G^<_{nm} = \langle \boldsymbol{\psi}^+(t) \bar{\boldsymbol{\psi}}^-(t') \rangle, \tag{3.74}$$

$$i\hbar G^>(t,t') = i\hbar G^>_{nm} = \langle \boldsymbol{\psi}^-(t) \bar{\boldsymbol{\psi}}^+(t') \rangle, \tag{3.75}$$

$$i\hbar G^{\bar{t}}(t,t') = i\hbar G^{\bar{t}}_{nm} = \langle \boldsymbol{\psi}^-(t) \bar{\boldsymbol{\psi}}^-(t') \rangle. \tag{3.76}$$

Making use of (3.35) and (3.36), we can reexpress the bosonic Green's

functions in terms of operator expectation values as

$$D^{>}_{ij}(t,t') = -i\langle\hat{\phi}_i(t)\hat{\phi}^{\dagger}_j(t')\rangle/\hbar, \tag{3.77}$$

$$D^{<}_{ij}(t,t') = -i\langle\hat{\phi}^{\dagger}_j(t')\hat{\phi}_i(t)\rangle/\hbar, \tag{3.78}$$

$$D^{t}(t,t') = D^{>}(t,t')\theta(t-t') + D^{<}(t,t')\theta(t'-t-\Delta t), \quad \text{and} \tag{3.79}$$

$$D^{\bar{t}}(t,t') = D^{<}(t,t')\theta(t-t'-\Delta t) + D^{>}(t,t')\theta(t'-t), \tag{3.80}$$

where $\theta(t)$ is a step function such that $\theta(t) = 1$ for $t \geq 0$, and $\theta(t) = 0$ for $t < 0$. For the corresponding fermionic Green's functions, we find using (3.33) and (3.34)

$$G^{>}_{ij}(t,t') = -i\langle\hat{\psi}_i(t)\hat{\psi}^{\dagger}_j(t')\rangle/\hbar, \tag{3.81}$$

$$G^{<}_{ij}(t,t') = i\langle\hat{\psi}^{\dagger}_j(t')\hat{\psi}_i(t)\rangle/\hbar, \tag{3.82}$$

$$G^{t}(t,t') = G^{>}(t,t')\theta(t-t') + G^{<}(t,t')\theta(t'-t-\Delta t), \quad \text{and} \tag{3.83}$$

$$G^{\bar{t}}(t,t') = G^{<}(t,t')\theta(t-t'-\Delta t) + G^{>}(t,t')\theta(t'-t), \tag{3.84}$$

where the changes of sign are due to anti-commutation of the Grassmann numbers.

There is a connection between the superscript notation of the Green's functions and the relations expressed in (3.77)-(3.84). For instance, $G^{<}$ and $D^{<}$ are equal to G^{t} and D^{t} precisely when $t < t'$, while $G^{>}$ and $D^{>}$ are equal to G^{t} and D^{t} when $t > t'$. Further, examining (3.79) and (3.83), we see that the nonzero term is always the term where the operator with the largest time argument is applied last. Therefore, G^{t} and D^{t} are referred to as time ordered Green's functions. Similarly, examining (3.80) and (3.84), we see that see that the nonzero term is always the term where the operator with the largest time argument is applied first. $G^{\bar{t}}$ and $D^{\bar{t}}$ are therefore referred to as anti-time ordered Green's functions[2, 15].

Expressions for the Green's functions of non-interacting systems like our isolated leads, are easiest to obtain by introducing a diagonal basis of the single particle Hamiltonian. Accordingly, considering some arbitrary non-interacting system with bosonic single particle Hamiltonian H^B, and fermionic single particle Hamiltonian H^F, we introduce a basis of eigenvectors u_i and v_i of H^B and H^F respectively, and write these matrices as

$$H^B = \sum_i E^B_i u_i u^{\dagger}_i, \quad \text{and} \tag{3.85}$$

$$H^F = \sum_i E^F_i v_i v^{\dagger}_i. \tag{3.86}$$

Using these bases, we can express both the propagator $U(t-t')$ and ρ_0 in diagonal form, after which (3.77), (3.78), (3.81) and (3.82) are easy to evaluate.

The details can be found for instance in the book by Jacoboni[15], who derives

$$i\hbar D^{<}(t,t') = \sum_i n(E_i^B) e^{iE_i^B(t'-t)/\hbar} u_i u_i^\dagger, \qquad \text{and} \tag{3.87}$$

$$i\hbar D^{>}(t,t') = \sum_i \left[1 + n(E_i^B)\right] e^{iE_i^B(t'-t)/\hbar} u_i u_i^\dagger, \quad \text{where} \tag{3.88}$$

$$n(E) = \frac{1}{e^{\beta E} - 1}, \tag{3.89}$$

and similarly for the fermionic expressions,

$$i\hbar G^{<}(t,t') = -\sum_i f(E_i^F) e^{iE_i^F(t'-t)/\hbar} v_i v_i^\dagger, \qquad \text{and} \tag{3.90}$$

$$i\hbar G^{>}(t,t') = \sum_i \left[1 - f(E_i^F)\right] e^{iE_i^F(t'-t)/\hbar} v_i v_i^\dagger, \quad \text{where} \tag{3.91}$$

$$f(E) = \frac{1}{1 + e^{\beta(E-\mu)}}. \tag{3.92}$$

Having calculated $D^{>}$, $D^{<}$, $G^{>}$ and $G^{<}$ using these expressions, the time ordered and anti-time ordered Green's functions are easily obtained from (3.79), (3.80), (3.83) and (3.84).

3.3.2 Effective action

In (3.56) and (3.57), the matrices T_p and B_p describe the coupling of the lead fields $\boldsymbol{\phi}_p$ and $\boldsymbol{\psi}_p$ to the system fields $\boldsymbol{\phi}$ and $\boldsymbol{\psi}$. Thus, examining (3.48)-(3.54) we see that T_p and B_p must satisfy

$$\boldsymbol{\phi}_p^\dagger B_p \boldsymbol{\phi} = -\sum_{n=0}^{N-1} \left\{ \boldsymbol{\phi}_{pn+1}^{+\dagger} b_p \boldsymbol{\phi}_n^+ - \boldsymbol{\phi}_{pn}^{-\dagger} b_p \boldsymbol{\phi}_{n+1}^- \right\} \Delta t, \quad \text{and} \tag{3.93}$$

$$\bar{\boldsymbol{\psi}}_p T_p \boldsymbol{\psi} = -\sum_{n=0}^{N-1} \left\{ \bar{\boldsymbol{\psi}}_{pn+1}^{+} t_p \boldsymbol{\psi}_n^+ - \bar{\boldsymbol{\psi}}_{pn}^{-} t_p \boldsymbol{\psi}_{n+1}^- \right\} \Delta t, \tag{3.94}$$

for any appropriately sized vectors $\boldsymbol{\phi}_p^\dagger$, $\boldsymbol{\phi}$, $\bar{\boldsymbol{\psi}}_p$ and $\boldsymbol{\psi}$, with $\boldsymbol{\phi} = [\boldsymbol{\phi}_1^+ \cdots \boldsymbol{\phi}_N^+, \boldsymbol{\phi}_1^- \cdots \boldsymbol{\phi}_N^-]$ and so on. These expressions, together with the block decompositions (3.67) and (3.68), can be used to rewrite (3.63) and (3.64) as

$$\begin{aligned} S_p^{B,\text{eff}} = -\sum_{n=0}^{N-1}\sum_{m=0}^{N-1} \Big\{ & \boldsymbol{\phi}_n^{+\dagger} b_p^\dagger D_{pn+1,m+1}^t b_p \boldsymbol{\phi}_m^+ - \boldsymbol{\phi}_n^{+\dagger} b_p^\dagger D_{pn+1,m}^{<} b_p \boldsymbol{\phi}_{m+1}^- \\ & - \boldsymbol{\phi}_{n+1}^{-\dagger} b_p^\dagger D_{pn,m+1}^{>} b_p \boldsymbol{\phi}_m^+ + \boldsymbol{\phi}_{n+1}^{-\dagger} b_p^\dagger D_{pn,m}^{\bar{t}} b_p \boldsymbol{\phi}_{m+1}^- \Big\} \Delta t^2 \end{aligned} \tag{3.95}$$

and,

$$\begin{aligned} S_p^{F,\text{eff}} = -\sum_{n=0}^{N-1}\sum_{m=0}^{N-1} \Big\{ & \bar{\boldsymbol{\psi}}_n^{+} t_p^\dagger G_{pn+1,m+1}^t t_p \boldsymbol{\psi}_m^+ - \bar{\boldsymbol{\psi}}_n^{+} t_p^\dagger G_{pn+1,m}^{<} t_p \boldsymbol{\psi}_{m+1}^- \\ & - \bar{\boldsymbol{\psi}}_{n+1}^{-} t_p^\dagger G_{pn,m+1}^{>} t_p \boldsymbol{\psi}_m^+ + \bar{\boldsymbol{\psi}}_{n+1}^{-} t_p^\dagger G_{pn,m}^{\bar{t}} t_p \boldsymbol{\psi}_{m+1}^- \Big\} \Delta t^2. \end{aligned} \tag{3.96}$$

We first consider the terms $\bar{\psi}_n^+ t_p^\dagger G^<_{pn+1,m} t_p \psi^-_{m+1}$ from (3.96). By (3.90) we have

$$\begin{aligned}\hbar i t_p^\dagger G^<_{pnm} t_p = \hbar i t_p^\dagger G_p^<(t,t') t_p &= -\sum_i f_p(E_i^F) e^{iE_i^F(t'-t)/\hbar} t_p^\dagger v_i v_i^\dagger t_p \\ &= -\int \mathrm{d}E f_p(E) e^{iE(t'-t)/\hbar} \sum_i t_p^\dagger v_i v_i^\dagger t_p \, \delta(E - E_i^F).\end{aligned} \tag{3.97}$$

Since the leads are supposed to be macroscopic objects, we now take the limit where the lead size $L_p \to \infty$. The distance between the eigenvalues E_i^F will then approach zero, so that the delta functions in the expression will be distributed with infinite density. In the limit we then obtain a continuous function which we denote

$$\Gamma_p^F(E) = 2\pi \lim_{L_p \to \infty} \sum_i t_p^\dagger v_i v_i^\dagger t_p \, \delta(E - E_i^F). \tag{3.98}$$

Thus, in the limit $L_p \to \infty$ we can write (3.97) as

$$t_p^\dagger G^<_{pnm} t_p = \frac{i}{h} \int \mathrm{d}E f_p(E) \Gamma_p^F(E) e^{iE(m-n)\Delta t/\hbar}. \tag{3.99}$$

Performing the sum over n and m, we find

$$\sum_{n=0}^{N-1} \sum_{m=0}^{N-1} \bar{\psi}_n^+ t_p^\dagger G^<_{pn+1,m} t_p \psi^-_{m+1} = \frac{i}{h\Delta t^2} \int \mathrm{d}E f_p(E) \bar{\boldsymbol{\psi}}^+(E) \Gamma_p^F(E) \boldsymbol{\psi}^-(E), \tag{3.100}$$

where we have defined

$$\boldsymbol{\psi}^+(E) = \sum_{n=0}^{N-1} \Delta t \boldsymbol{\psi}_n^+ e^{iE(n+1)\Delta t/\hbar}, \quad \text{and} \tag{3.101}$$

$$\boldsymbol{\psi}^-(E) = \sum_{n=0}^{N-1} \Delta t \boldsymbol{\psi}_{n+1}^- e^{iEn\Delta t/\hbar}. \tag{3.102}$$

In a similar fashion, using (3.91), we obtain

$$t_p^\dagger G^>_{pnm} t_p = \frac{i}{h} \int \mathrm{d}E [f_p(E) - 1] \Gamma_p^F(E) e^{iE(m-n)\Delta t/\hbar}, \tag{3.103}$$

and

$$\sum_{n=0}^{N-1} \sum_{m=0}^{N-1} \bar{\psi}_{n+1}^- t_p^\dagger G^>_{pn,m+1} t_p \psi_m^+ = \frac{i}{h\Delta t^2} \int \mathrm{d}E \, [f_p(E) - 1] \, \bar{\boldsymbol{\psi}}^-(E) \Gamma_p^F(E) \boldsymbol{\psi}^+(E). \tag{3.104}$$

For the summation of the terms involving G_p^t and $G_p^{\bar{t}}$, it is convenient to make some additional definitions. We define the Fourier transform

$$\Gamma_p^F(t) = \int \mathrm{d}E \, \Gamma_p^F(E) e^{-iEt/\hbar}, \tag{3.105}$$

and the two important functions

$$\Sigma_p^r(t) = -i\tilde{\theta}(t)\Gamma_p^F(t) \quad \text{and,} \tag{3.106}$$

$$\Sigma_p^a(t) = i\tilde{\theta}(-t)\Gamma_p^F(t), \tag{3.107}$$

where the step function $\tilde{\theta}(t)$ differs from the previously defined function $\theta(t)$ only in that $\tilde{\theta}(0) = \frac{1}{2}$. We also define the inverse Fourier transforms

$$\Sigma^r(E) = \frac{1}{2\pi}\int \mathrm{d}E\, \Sigma^r(t)e^{iEt/\hbar} \quad \text{and} \tag{3.108}$$

$$\Sigma^a(E) = \frac{1}{2\pi}\int \mathrm{d}E\, \Sigma^a(t)e^{iEt/\hbar}. \tag{3.109}$$

One can show that in fact

$$\Sigma_p^r(E) = \lim_{\eta\to 0^+}\frac{1}{2\pi}\int \mathrm{d}E' \frac{\Gamma_p^F(E')}{E - E' + i\eta}, \quad \text{while} \tag{3.110}$$

$$\Sigma_p^a(E) = \Sigma_p^r(E)^\dagger = \lim_{\eta\to 0^+}\frac{1}{2\pi}\int \mathrm{d}E' \frac{\Gamma_p^F(E')}{E - E' - i\eta}. \tag{3.111}$$

Now, using (3.83), (3.99), (3.103) and (3.106), we find

$$\begin{aligned} t_p^\dagger G_{pnm}^t t_p &= t_p^\dagger G_{pnm}^< t_p + t_p^\dagger \left(G_{pnm}^> - G_{pnm}^<\right) t_p \theta(n-m) \\ &= \frac{i}{h}\int \mathrm{d}E f_p(E)\Gamma_p^F(E)e^{iE(m-n)\Delta t/\hbar} + \frac{1}{h}\Sigma_p^r(t-t') - \frac{i}{2h}\delta_{nm}t_p^\dagger t_p. \end{aligned} \tag{3.112}$$

Since the last term in this expression is proportional to δ_{nm}, it will upon insertion in (3.96) result in an expression of order $\Delta t^2 \cdot N \sim 1/N$. Thus, since the approximation (3.9) already includes an error of order $1/N$, we are free to remove this term without changing the order of the approximation. Then making use of (3.108), (3.101) and (3.102), we obtain

$$\begin{aligned} &\sum_{n=0}^{N-1}\sum_{m=0}^{N-1} \bar{\boldsymbol{\psi}}_n^+ t_p^\dagger G_{pn+1,m+1}^t t_p \boldsymbol{\psi}_m^+ \\ &= \frac{1}{h\Delta t^2}\int \mathrm{d}E\, \bar{\boldsymbol{\psi}}^+(E)\left[if_p(E)\Gamma_p^F(E) + \Sigma_p^r(E)\right]\boldsymbol{\psi}^+(E). \end{aligned} \tag{3.113}$$

In a completely analogous manner, starting from (3.84), we find

$$\begin{aligned} &\sum_{n=0}^{N-1}\sum_{m=0}^{N-1} \bar{\boldsymbol{\psi}}_{n+1}^- t_p^\dagger G_{pnm}^{\bar{t}} t_p \boldsymbol{\psi}_{m+1}^- \\ &= \frac{1}{h\Delta t^2}\int \mathrm{d}E\, \bar{\boldsymbol{\psi}}^-(E)\left[if_p(E)\Gamma_p^F(E) - \Sigma_p^a(E)\right]\boldsymbol{\psi}^-(E). \end{aligned} \tag{3.114}$$

Then inserting (3.100), (3.104), (3.113) and (3.114) in (3.96), we find that the fermionic component of the effective action can be expressed as

$$\begin{aligned} \frac{i}{\hbar}S_p^{F,\mathrm{eff}} = \frac{1}{h\hbar}\int \mathrm{d}E \big\{ & f_p(E)\left[\bar{\boldsymbol{\psi}}^+(E) - \bar{\boldsymbol{\psi}}^-(E)\right]\Gamma_p^F(E)\left[\boldsymbol{\psi}^+(E) - \boldsymbol{\psi}^-(E)\right] \\ & + \bar{\boldsymbol{\psi}}^-(E)\Gamma_p^F(E)\boldsymbol{\psi}^+(E) - i\bar{\boldsymbol{\psi}}^+(E)\Sigma_p^r(E)\boldsymbol{\psi}^+(E) + i\bar{\boldsymbol{\psi}}^-(E)\Sigma_p^a(E)\boldsymbol{\psi}^-(E)\big\}. \end{aligned} \tag{3.115}$$

Repeating the procedure above with the corresponding bosonic expressions, we also find that the bosonic component of the effective action (3.95) can be expressed as

$$\begin{aligned}\frac{i}{\hbar}S_p^{B,\text{eff}} = \frac{1}{h\hbar}\int \mathrm{d}E \Big\{ &- n_p(E)\,[\boldsymbol{\phi}^+(E) - \boldsymbol{\phi}^-(E)]^\dagger \Gamma_p^B(E)[\boldsymbol{\phi}^+(E) - \boldsymbol{\phi}^-(E)] \\ &+ \boldsymbol{\phi}^-(E)^\dagger \Gamma_p^B(E)\boldsymbol{\phi}^+(E) - i\boldsymbol{\phi}^+(E)^\dagger \Theta_p^r(E)\boldsymbol{\phi}^+(E) \\ &+ i\boldsymbol{\phi}^-(E)^\dagger \Theta_p^a(E)\boldsymbol{\phi}^-(E)\Big\},\end{aligned} \tag{3.116}$$

where we have defined

$$\Gamma_p^B(E) = \lim_{L_p\to\infty} 2\pi \sum_i b_p^\dagger u_i u_i^\dagger b_p\, \delta(E - E_i^B), \tag{3.117}$$

$$\Gamma_p^B(t) = \int \mathrm{d}E\, \Gamma_p^B(E) e^{-iEt/\hbar}, \tag{3.118}$$

$$\Theta_p^r(t) = -i\tilde{\theta}(t)\Gamma_p^B(t), \tag{3.119}$$

$$\Theta_p^a(t) = i\tilde{\theta}(-t)\Gamma_p^B(t), \tag{3.120}$$

$$\Theta^r(E) = \frac{1}{2\pi}\int \mathrm{d}E\, \Theta^r(t) e^{iEt/\hbar}, \tag{3.121}$$

$$\Theta^a(E) = \frac{1}{2\pi}\int \mathrm{d}E\, \Theta^a(t) e^{iEt/\hbar}, \tag{3.122}$$

$$\boldsymbol{\phi}^+(E) = \sum_{n=0}^{N-1} \Delta t \boldsymbol{\phi}_n^+ e^{iE(n+1)\Delta t/\hbar}, \quad \text{and} \tag{3.123}$$

$$\boldsymbol{\phi}^-(E) = \sum_{n=0}^{N-1} \Delta t \boldsymbol{\phi}_{n+1}^- e^{iEn\Delta t/\hbar}. \tag{3.124}$$

3.4 Transport expectation values

3.4.1 Operator expressions

Let Φ_p be the flux of fermions exiting the system S at lead p, and let N_p be the number of fermions in p. Then since N_p can change only by fermions entering or exiting S, we must have $\dot{N}_p = \Phi_p$. Since the lead p is assumed macroscopic, we can identify $N_p = \langle N_p \rangle$, and using (3.5) we get

$$\Phi_p = \frac{\mathrm{d}N_p}{\mathrm{d}t} = \frac{\mathrm{d}}{\mathrm{d}t}\mathrm{Tr}\,\rho_0 \hat{N}_p^F(t) \tag{3.125}$$

Now using (3.2), we have for any observable A

$$\frac{\mathrm{d}}{\mathrm{d}t}\hat{A}(t) = \frac{i}{\hbar}U^\dagger(t-t_0)[\hat{H},\hat{A}]U(t-t_0). \tag{3.126}$$

Applying this to (3.125) we get

$$\Phi_p(t) = i\mathrm{Tr}\,\rho_0 U^\dagger(t-t_0)[\hat{H},\hat{N}_p^F]U(t-t_0)/\hbar. \tag{3.127}$$

Clearly $\hat{N}_p^F$ commutes with the bosonic degrees of freedom, and since $\hat{N}_p^F$ contains only fields from lead p, it also commutes with $\hat{H}_S$, as well as the terms from the other leads. Thus, by (3.39) we have

$$[\hat{H}, \hat{N}_p^F] = [\hat{\boldsymbol{\psi}}_p^\dagger H_p^F \hat{\boldsymbol{\psi}}_p, \hat{N}_p^F] + [\hat{\boldsymbol{\psi}}_p^\dagger t_p \hat{\boldsymbol{\psi}}, \hat{N}_p^F] + [\hat{\boldsymbol{\psi}}^\dagger t_p^\dagger \hat{\boldsymbol{\psi}}_p, \hat{N}_p^F]. \tag{3.128}$$

Making use of some operator algebra, starting with the fundamental commutation relation $\{\psi_i, \psi_j^\dagger\} = \psi_i \psi_j^\dagger + \psi_j^\dagger \psi_i = \delta_{ij}$ and the definiton $\hat{N}_p^F = \hat{\boldsymbol{\psi}}_p^\dagger \hat{\boldsymbol{\psi}}_p$, we find that

$$[\hat{\boldsymbol{\psi}}_p^\dagger H_p^F \hat{\boldsymbol{\psi}}_p, \hat{N}_p^F] = 0, \qquad \text{while,} \tag{3.129}$$

$$[\hat{\boldsymbol{\psi}}_p^\dagger t_p \hat{\boldsymbol{\psi}}, \hat{N}_p^F] = -\hat{\boldsymbol{\psi}}_p^\dagger t_p \hat{\boldsymbol{\psi}}. \tag{3.130}$$

Taking the adjoint of the latter, we also find $[\hat{\boldsymbol{\psi}}^\dagger t_p^\dagger \hat{\boldsymbol{\psi}}_p, \hat{N}_p^F] = -[\hat{N}_p^F, \hat{\boldsymbol{\psi}}^\dagger t_p^\dagger \hat{\boldsymbol{\psi}}_p] = \hat{\boldsymbol{\psi}}^\dagger t_p^\dagger \hat{\boldsymbol{\psi}}_p$. Thus, (3.128) becomes

$$[\hat{H}, \hat{N}_p^F] = \hat{\boldsymbol{\psi}}^\dagger t_p^\dagger \hat{\boldsymbol{\psi}}_p - \hat{\boldsymbol{\psi}}_p^\dagger t_p \hat{\boldsymbol{\psi}}, \tag{3.131}$$

so that (3.127) becomes

$$\Phi_p(t) = -\frac{i}{\hbar} \mathrm{Tr}\, \rho_0 \left(\hat{\boldsymbol{\psi}}_p^\dagger(t) t_p \hat{\boldsymbol{\psi}}(t) - \hat{\boldsymbol{\psi}}^\dagger(t) t_p^\dagger \hat{\boldsymbol{\psi}}_p(t) \right) = \left\langle \hat{\Phi}_p(t) \right\rangle, \tag{3.132}$$

where clearly $\hat{\Phi}_p(t) = -i(\hat{\boldsymbol{\psi}}_p^\dagger(t) t_p \hat{\boldsymbol{\psi}}(t) - \hat{\boldsymbol{\psi}}^\dagger(t) t_p^\dagger \hat{\boldsymbol{\psi}}_p(t))/\hbar$.

Now, let $E_p^F = \hat{\boldsymbol{\psi}}_p^\dagger H_p^F \hat{\boldsymbol{\psi}}_p$ be the total energy associated with fermions in lead p, and let Φ_p^{EF} be the corresponding energy flux entering p from S. Then by an argument similar to the one preceding (3.125), we have

$$\Phi_p^{EF} = \frac{\mathrm{d}E_p^F}{\mathrm{d}t} = \frac{i}{\hbar} \mathrm{Tr}\, \rho_0 U^\dagger(t - t_0) [\hat{H}, \hat{\boldsymbol{\psi}}_p^\dagger H_p^F \hat{\boldsymbol{\psi}}_p] U(t - t_0). \tag{3.133}$$

Again, the term $\hat{\boldsymbol{\psi}}_p^\dagger H_p^F \hat{\boldsymbol{\psi}}_p$ clearly commutes both with bosonic degrees of freedom, as well as with terms that are exclusive to S or to the other leads. Since it also obviously commutes with itself, we obtain by again making use of (3.39) and some operator algebra,

$$[\hat{H}, \hat{\boldsymbol{\psi}}_p^\dagger H_p^F \hat{\boldsymbol{\psi}}_p] = [\hat{\boldsymbol{\psi}}_p^\dagger t_p \hat{\boldsymbol{\psi}} + \hat{\boldsymbol{\psi}}^\dagger t_p^\dagger \hat{\boldsymbol{\psi}}_p, \hat{\boldsymbol{\psi}}_p^\dagger H_p^F \hat{\boldsymbol{\psi}}_p] = -\hat{\boldsymbol{\psi}}_p^\dagger H_p^F t_p \hat{\boldsymbol{\psi}} + \hat{\boldsymbol{\psi}}^\dagger t_p^\dagger H_p^F \hat{\boldsymbol{\psi}}_p. \tag{3.134}$$

Thus, (3.133) becomes

$$\Phi_p^{EF} = -\frac{i}{\hbar} \mathrm{Tr}\, \rho_0 \left(\hat{\boldsymbol{\psi}}_p^\dagger(t) H_p^F t_p \hat{\boldsymbol{\psi}}(t) - \hat{\boldsymbol{\psi}}^\dagger(t) t_p^\dagger H_p^F \hat{\boldsymbol{\psi}}_p(t) \right) = \left\langle \hat{\Phi}_p^{EF}(t) \right\rangle, \tag{3.135}$$

with $\hat{\Phi}_p^{EF}(t) = -i(\hat{\boldsymbol{\psi}}_p^\dagger(t) H_p^F t_p \hat{\boldsymbol{\psi}}(t) - \hat{\boldsymbol{\psi}}^\dagger(t) t_p^\dagger H_p^F \hat{\boldsymbol{\psi}}_p(t))/\hbar$.

Letting $E_p^B = \hat{\phi}_p^\dagger H_p^B \hat{\phi}_p$ be the energy associated with bosons in p, and Φ_p^{EB} the corresponding energy flux, it is clear that Φ_p^{EB} can be obtained by simply repeating the steps above. The result is

$$\begin{aligned}\Phi_p^{EB} = \frac{\mathrm{d}E_p^B}{\mathrm{d}t} &= \frac{i}{\hbar}\mathrm{Tr}\,\rho_0 U^\dagger(t-t_0)[\hat{H}, \hat{\phi}_p^\dagger H_p^B \hat{\phi}_p]U(t-t_0) \\ &= -\frac{i}{\hbar}\mathrm{Tr}\,\rho_0 \left(\hat{\phi}_p^\dagger(t) H_p^B b_p \hat{\phi}(t) - \hat{\phi}^\dagger(t) b_p^\dagger H_p^B \hat{\phi}_p(t)\right) = \left\langle \hat{\Phi}_p^{EB}(t)\right\rangle,\end{aligned} \tag{3.136}$$

with $\hat{\Phi}_p^{EB}(t) = -i(\hat{\phi}_p^\dagger(t) H_p^B b_p \hat{\phi}(t) - \hat{\phi}^\dagger(t) b_p^\dagger H_p^B \hat{\phi}_p(t))/\hbar$. Finally, letting $E_p = E_p^F + E_p^B$ be the total energy of lead p, and Φ_p^E the total energy flux entering p from S, we have

$$\Phi_p^E = \frac{\mathrm{d}E_p}{\mathrm{d}t} = \Phi_p^{EF} + \Phi_p^{EB} = \left\langle \hat{\Phi}_p^E(t)\right\rangle, \tag{3.137}$$

with $\hat{\Phi}_p^E(t) = \hat{\Phi}_p^{EF}(t) + \hat{\Phi}_p^{EB}(t)$.

3.4.2 Field integral expressions

Using the relationship (3.33) between operator and field integral expectation values, we can reexpress (3.132) as

$$\Phi_p(t) = -\frac{i}{\hbar}\left\langle \bar{\boldsymbol{\psi}}_p^-(t) t_p \boldsymbol{\psi}^+(t) - \bar{\boldsymbol{\psi}}^-(t) t_p^\dagger \boldsymbol{\psi}_p^+(t)\right\rangle. \tag{3.138}$$

In order to express this in terms of fields confined within S alone, we will make use of a commonly applied trick where the expectation value is reexpressed as a derivative. Thus, we define the modified action

$$S(x) = S + x(\bar{\boldsymbol{\psi}}^-(t) t_p^\dagger \boldsymbol{\psi}_p^+(t) - \bar{\boldsymbol{\psi}}_p^-(t) t_p \boldsymbol{\psi}^+(t)). \tag{3.139}$$

Making use of (3.32), it is easily verified that we then have

$$\Phi_p(t) = \frac{\mathrm{d}}{\mathrm{d}x}\int D(+,-)\prod_p \int D(\phi_p^+, \phi_p^-)\int D(\psi_p^+, \psi_p^-) e^{iS(x)/\hbar}, \tag{3.140}$$

where we are assuming evaluation at $x = 0$. The modification (3.139) changes the matrix T of (3.94) and its adjoint $T^\dagger$ respectively to $T_p(x)$ and $\tilde{T}_p^\dagger(x)$, where

$$\bar{\boldsymbol{\psi}}_p T_p(x)\boldsymbol{\psi} = \bar{\boldsymbol{\psi}}_p T_p \boldsymbol{\psi} - x\bar{\boldsymbol{\psi}}_p^-(t) t_p \boldsymbol{\psi}^+(t), \quad \text{and} \tag{3.141}$$

$$\bar{\boldsymbol{\psi}}\tilde{T}_p^\dagger(x)\boldsymbol{\psi}_p = \bar{\boldsymbol{\psi}} T_p^\dagger \boldsymbol{\psi}_p + x\bar{\boldsymbol{\psi}}^-(t) t_p^\dagger \boldsymbol{\psi}_p^+(t). \tag{3.142}$$

Repeating the derivation of (3.96) with $T_p(x)$ and $\tilde{T}_p^\dagger(x)$ substituted for T and $T^\dagger$, we obtain the modified effective action

$$\begin{aligned}S^{\mathrm{eff}}(x) = S^{\mathrm{eff}} + x\sum_{n=0}^{N-1}\{&\bar{\boldsymbol{\psi}}_m^- t_p^\dagger G_{pm,n+1}^t t_p \boldsymbol{\psi}_n^+ - \bar{\boldsymbol{\psi}}_m^- t_p^\dagger G_{pmn}^< t_p \boldsymbol{\psi}_{n+1}^- - \\ &\bar{\boldsymbol{\psi}}_n^+ t_p^\dagger G_{pn+1,m}^< t_p \boldsymbol{\psi}_m^+ + \bar{\boldsymbol{\psi}}_{n+1}^- t_p^\dagger G_{pnm}^{\bar{t}} t_p \boldsymbol{\psi}_m^+\}\Delta t + O(x^2),\end{aligned} \tag{3.143}$$

where $m\Delta t = t$. Thus, by (3.140) and (3.61) we have

$$\begin{aligned}\Phi_p(t) &= \frac{\mathrm{d}}{\mathrm{d}x}\int D(+,-)e^{iS^{\mathrm{eff}}(x)/\hbar} \\ &= \frac{i}{\hbar}\sum_{n=0}^{N-1}\Big\langle \bar{\boldsymbol{\psi}}^-_m t_p^\dagger G^t_{pm,n+1} t_p \boldsymbol{\psi}^+_n - \bar{\boldsymbol{\psi}}^-_m t_p^\dagger G^<_{pmn} t_p \boldsymbol{\psi}^-_{n+1} \\ &\qquad - \bar{\boldsymbol{\psi}}^+_n t_p^\dagger G^<_{pn+1,m} t_p \boldsymbol{\psi}^+_m + \bar{\boldsymbol{\psi}}^-_{n+1} t_p^\dagger G^{\bar{t}}_{pnm} t_p \boldsymbol{\psi}^+_m \Big\rangle \Delta t.\end{aligned} \tag{3.144}$$

Now we make use of the assumption that the system will approach steady state conditions over a time scale which is short compared to $t_f - t_0$. $\Phi_p(t)$ will then essentially be independent of t for all times except very close to t_0. Accordingly, we have

$$\begin{aligned}\Phi_p \approx \frac{1}{N}\sum_{m=1}^{N}\Phi_p(t) = \frac{i}{\hbar}\frac{1}{N}\sum_{m=1}^{N}\sum_{n=0}^{N-1}\Big\langle \bar{\boldsymbol{\psi}}^-_m t_p^\dagger G^t_{pm,n+1} t_p \boldsymbol{\psi}^+_n - \bar{\boldsymbol{\psi}}^-_m t_p^\dagger G^<_{pmn} t_p \boldsymbol{\psi}^-_{n+1} \\ - \bar{\boldsymbol{\psi}}^+_n t_p^\dagger G^<_{pn+1,m} t_p \boldsymbol{\psi}^+_m + \bar{\boldsymbol{\psi}}^-_{n+1} t_p^\dagger G^{\bar{t}}_{pnm} t_p \boldsymbol{\psi}^+_m \Big\rangle \Delta t.\end{aligned} \tag{3.145}$$

Adding (3.83) and (3.84) we find the relation

$$G^t_{mn} + G^{\bar{t}}_{mn} = G^>_{mn} + G^<_{mn} + \delta_{mn}(G^>_{mn} - G^<_{mn}). \tag{3.146}$$

Combining this with the definition $i\hbar G = \langle \boldsymbol{\psi}\bar{\boldsymbol{\psi}}\rangle$ we also obtain

$$\begin{aligned}&\Big\langle \bar{\boldsymbol{\psi}}^-_m t_p^\dagger G^<_{pmn} t_p \boldsymbol{\psi}^-_{n+1} + \bar{\boldsymbol{\psi}}^+_m t_p^\dagger G^<_{pmn} t_p \boldsymbol{\psi}^+_{n+1}\Big\rangle \\ &= \Big\langle \bar{\boldsymbol{\psi}}^-_m t_p^\dagger G^<_{pmn} t_p \boldsymbol{\psi}^+_{n+1} + \bar{\boldsymbol{\psi}}^+_m t_p^\dagger G^<_{pmn} t_p \boldsymbol{\psi}^-_{n+1} \\ &\qquad - \delta_{nm}(\bar{\boldsymbol{\psi}}^+_m t_p^\dagger G^<_{pmn} t_p \boldsymbol{\psi}^-_{n+1} - \bar{\boldsymbol{\psi}}^-_m t_p^\dagger G^<_{pmn} t_p \boldsymbol{\psi}^+_{n+1})\Big\rangle\end{aligned} \tag{3.147}$$

Making use of (3.146) applied to the lead Green's functions G_p, (3.147), (3.99) and (3.103), we can after considerable algebra rewrite (3.145) as

$$\begin{aligned}\Phi_p = &-\frac{1}{h\hbar N}\sum_{m=0}^{N-1}\sum_{n=0}^{N-1}\int \mathrm{d}E\,\Big\langle \bar{\boldsymbol{\psi}}^-_{m+1}[2f_p(E)-1]\Gamma^F_p(E)e^{iE(n-m)\Delta t/\hbar}\boldsymbol{\psi}^+_n \\ &- \bar{\boldsymbol{\psi}}^-_{m+1} f_p(E)\Gamma^F_p(E)e^{iE(n-m-2)\Delta t/\hbar}\boldsymbol{\psi}^+_n \\ &- \bar{\boldsymbol{\psi}}^+_m f_p(E)\Gamma^F_p(E)e^{iE(n-m)\Delta t/\hbar}\boldsymbol{\psi}^-_{n+1}\Big\rangle\Delta t - \frac{1}{h\hbar N}\sum_{n=0}^{N-1} X_n \Delta t,\end{aligned} \tag{3.148}$$

where X_n is an expression of order zero in N. Thus, the entire last term is of order $1/N \cdot N \cdot \Delta t \sim 1/N$, and can accordingly be dropped.

Further, as long as the energy range where $\Gamma^F_p(E)$ is nonzero is bounded, replacing the exponentials $e^{iE(n-m)\Delta t/\hbar}$ and $e^{iE(n-m-2)\Delta t/\hbar}$ with unity will also

only introduce an error of order $1/N$. Doing this and making use of (3.101) and (3.102), we obtain after some rearrangement the symmetrical expression

$$\Phi_p = \int \frac{2\pi \mathrm{d}E}{h^2(t_f - t_0)} \Big\langle (1 - f_p(E))\, \bar{\boldsymbol{\psi}}^-(E)\Gamma_p^F(E)\boldsymbol{\psi}^+(E) + f_p(E)\bar{\boldsymbol{\psi}}^+(E)\Gamma_p^F(E)\boldsymbol{\psi}^-(E)\Big\rangle. \tag{3.149}$$

Field integral expressions for energy flux can be found in the same manner. Comparing (3.135) to (3.132), we see that the fermionic energy flux is obtained by simply replacing t_p and $t_p^\dagger$ in (3.139) respectively with $H_p^F t_p$ and $t_p^\dagger H_p^F$. Upon making use of (3.90), (3.91) and (3.98) to rewrite the effective action as an integral over energy, the additional factor of H_p^F simply becomes a factor of E. Thus, the fermionic energy flux can be obtained from (3.149) simply by including this additional factor of E. Accordingly, we have

$$\Phi_p^{EF} = \int \frac{2\pi \mathrm{d}E\, E}{h^2(t_f - t_0)} \Big\langle (1 - f_p(E))\, \bar{\boldsymbol{\psi}}^-(E)\Gamma_p^F(E)\boldsymbol{\psi}^+(E) + f_p(E)\bar{\boldsymbol{\psi}}^+(E)\Gamma_p^F(E)\boldsymbol{\psi}^-(E)\Big\rangle. \tag{3.150}$$

The bosonic energy flux is obtained in a similar manor. Repeating the steps above with the corresponding bosonic expressions, we obtain

$$\Phi_p^{EB} = \int \frac{2\pi \mathrm{d}E\, E}{h^2(t_f - t_0)} \Big\langle (n_p(E) + 1)\, \boldsymbol{\phi}^-(E)^\dagger \Gamma_p^B(E)\boldsymbol{\phi}^+(E) - n_p(E)\boldsymbol{\phi}^+(E)^\dagger\Gamma_p^B(E)\boldsymbol{\phi}^-(E)\Big\rangle. \tag{3.151}$$

3.4.3 Current and heat flux

In the most typical solid state applications, the model can be expressed in terms of two different types of particles: electrons which are fermions and have charge $-e$, with e the elementary charge, and phonons which are bosons and have charge zero. Thus, the electrical currents at the leads are given simply by $I_p = -e\Phi_p$, or by (3.149),

$$I_p = -e \int \frac{2\pi \mathrm{d}E}{h^2(t_f - t_0)} \Big\langle (1 - f_p(E))\, \bar{\boldsymbol{\psi}}^-(E)\Gamma_p^F(E)\boldsymbol{\psi}^+(E) + f_p(E)\bar{\boldsymbol{\psi}}^+(E)\Gamma_p^F(E)\boldsymbol{\psi}^-(E)\Big\rangle. \tag{3.152}$$

To find an expression for the heat flux q_p through lead p, we make use of the following considerations: Since we are assuming stationary conditions except very close to t_0, there will at $t = t_f$ have passed a total energy of $\Delta E_p = \Phi_p^E(t_f - t_0)$ into lead p. This energy can be decomposed as $\Delta E_p = Q + W$, where Q is the transferred heat, and W is electrical work having been done on that lead. If we imagine that the contact between the leads and S is removed at $t = t_f$, then the lead will reequilibrate after this time. Since the lead size $L_p \to \infty$,

the particle and energy content of the lead has only changed by an arbitrarily small fraction, and accordingly it must reequilibrate to the same state it was in before $t = t_0$. Thus, the chemical potential associated with the lead is still μ_p, so that after equilibration the change in electrical energy can be expressed as $\Delta E_{\mathrm{el}} = W = \mu_p \Delta N_p^F = \mu_p \Phi_p (t_0 - t_f)$.

Thus, we have $\Delta E_p = \Phi_p^E (t_f - t_0) = Q + \mu_p \Phi_p (t_0 - t_f)$, and accordingly the stationary heat flux $q_p = Q/(t_f - t_0)$ can be expressed as $q_p = \Phi_p^E - \mu_p \Phi_p$. Using (3.137), (3.150), (3.151) and (3.149) we thus obtain

$$\begin{aligned} q_p = \int \frac{2\pi \mathrm{d}E\, E}{h^2 (t_f - t_0)} \Big\langle\, & (n_p(E) + 1)\, \boldsymbol{\phi}^-(E)^\dagger \Gamma_p^B(E) \boldsymbol{\phi}^+(E) \\ & - n_p(E) \boldsymbol{\phi}^+(E)^\dagger \Gamma_p^B(E) \boldsymbol{\phi}^-(E) \Big\rangle \\ + \int \frac{\mathrm{d}E\, (E - \mu)}{h\hbar (t_f - t_0)} \Big\langle\, & (1 - f_p(E))\, \bar{\boldsymbol{\psi}}^-(E) \Gamma_p^F(E) \boldsymbol{\psi}^+(E) \\ & + f_p(E) \bar{\boldsymbol{\psi}}^+(E) \Gamma_p^F(E) \boldsymbol{\psi}^-(E) \Big\rangle. \end{aligned} \tag{3.153}$$

Chapter 4

The Linear limit and Kubo relations

(3.152) and (3.153) of the previous chapter gives expression for the currents and heat currents of a transport system under very general conditions. These currents are driven by differences between the temperatures and chemical potentials of the leads. In this chapter we will be concerned with the limit where these differences are small, so that the currents can be expressed in terms of first order approximations. In Section 4.1 we find such expressions by directly differentiating the general expressions (3.152) and (3.153). Then, in Section 4.2 we will discuss a particularly elegant set of expressions, known as the Kubo relations, which will be derived using the operator formalism. Translation into field integral expressions is considered in Section 4.3.

4.1 Direct linear limit of the field integral

4.1.1 Conductance

As discussed in Section 2.1.2, we can in the linear transport regime express the lead currents as

$$I_q = \sum_p G_{qp} V_{pq} = \sum_p G_{qp}(V_p - V_q) = \sum_p \tilde{G}_{qp} \Delta V_p, \tag{4.1}$$

where $\Delta V_p = V_p - V$ with V the equilibrium potential, and where we have defined

$$\tilde{G}_{qp} = G_{qp} - \delta_{qp} \sum_r G_{qr}. \tag{4.2}$$

It is clear from (4.1) that we have

$$\tilde{G}_{qp} = \frac{\partial I_q}{\partial V_p} = -e \frac{\partial I_q}{\partial \mu_p}. \tag{4.3}$$

Thus, making use of (3.152) and (3.61), we find that for $q \neq p$

$$\tilde{G}_{qp} = e^2 \int \frac{2\pi \mathrm{d}E}{h^2 (t_f - t_0)} \left\langle X_q(E) \frac{i}{\hbar} \frac{\partial S^{\mathrm{eff}}}{\partial \mu_p} \right\rangle. \tag{4.4}$$

where

$$X_q(E) = (1 - f_q(E))\, \bar{\boldsymbol{\psi}}^-(E) \Gamma_q^F(E) \boldsymbol{\psi}^+(E) + f_q(E) \bar{\boldsymbol{\psi}}^+(E) \Gamma_q^F(E) \boldsymbol{\psi}^-(E). \tag{4.5}$$

Combining (3.62) and (3.115) we see that

$$\frac{i}{\hbar}\frac{\partial S^{\text{eff}}}{\partial \mu_p} = \frac{1}{h\hbar}\int \mathrm{d}E\, Y_p(E) + \frac{i}{\hbar}\frac{\partial S_p^{F,\text{eff}}}{\partial H_p}\frac{\partial H_p}{\partial \mu_p}, \tag{4.6}$$

where

$$Y_p(E) = \mathrm{Th}(E)\,[\bar{\boldsymbol{\psi}}^+(E) - \bar{\boldsymbol{\psi}}^-(E)]\Gamma_p^F(E)[\boldsymbol{\psi}^+(E) - \boldsymbol{\psi}^-(E)], \tag{4.7}$$

with $\mathrm{Th}(E)$ given by (2.18), and where we are allowing for the possibility that the lead Hamiltonian depends on the chemical potential. However, upon inserting (4.6) in (4.4), and making use of (3.61) again, we see that

$$e^2\int \frac{2\pi \mathrm{d}E}{h^2(t_f - t_0)}\left\langle X_q(E)\frac{i}{\hbar}\frac{\partial S_p^{F,\text{eff}}}{\partial H_p}\frac{\partial H_p}{\partial \mu_p}\right\rangle = -e\frac{\partial I_q}{\partial H_p}\frac{\partial H_p}{\partial \mu_p}. \tag{4.8}$$

But I_q is the current in equilibrium, which is always zero. Thus $\partial I_q/\partial H_p = 0$, so that the term above does not contribute to (4.4), which accordingly becomes

$$\tilde{G}_{qp} = e^2\iint \frac{4\pi^2 \mathrm{d}E\,\mathrm{d}E'}{h^4(t_f - t_0)}\big\langle X_q(E)Y_p(E')\big\rangle. \tag{4.9}$$

4.1.2 Thermoelectric coefficients

In the presence of a temperature gradient we have by the discussion of Section 2.1.3

$$I_q = \sum_p A_{qp}\Delta T_{pq} = \sum_p A_{qp}(T_p - T_q) = \sum_p \tilde{A}_{qp}\Delta T_p, \tag{4.10}$$

where $\Delta T_p = T_p - T$ with T the equilibrium temperature, and where similarly to (4.2) we have defined

$$\tilde{A}_{qp} = A_{qp} - \delta_{qp}\sum_r A_{qr}. \tag{4.11}$$

Clearly we have

$$\tilde{A}_{qp} = \frac{\partial I_q}{\partial T_p} = -\frac{1}{k_B T^2}\frac{\partial I_q}{\partial \beta_p}. \tag{4.12}$$

Thus, again assuming $q \neq p$ and using (3.152) and (3.61), we get

$$\tilde{A}_{qp} = \frac{e}{k_B T^2}\int \frac{2\pi \mathrm{d}E}{h^2(t_f - t_0)}\left\langle X_q(E)\frac{i}{\hbar}\frac{\partial S^{\text{eff}}}{\partial \beta_p}\right\rangle. \tag{4.13}$$

Using (3.62), (3.115) and (3.116) we find

$$\frac{i}{\hbar}\frac{\partial S^{\text{eff}}}{\partial \beta_p} = \frac{1}{h\hbar\beta}\int \mathrm{d}E\,\left(E\,Y_p^B(E) - (E-\mu)Y_p(E)\right) + \frac{i}{\hbar}\frac{\partial S_p^{\text{eff}}}{\partial H}\frac{\partial H}{\partial \mu_p}, \tag{4.14}$$

where

$$Y_p^B(E) = \mathrm{Tb}(E)[\boldsymbol{\phi}^+(E) - \boldsymbol{\phi}^-(E)]^\dagger \Gamma_p^B(E)[\boldsymbol{\phi}^+(E) - \boldsymbol{\phi}^-(E)], \tag{4.15}$$

with

$$\mathrm{Tb}(E) = -\frac{\partial n}{\partial E}(E) = \frac{\beta}{4\sinh^2 \beta E/2}. \tag{4.16}$$

The last term in (4.14) does not contribute to the transport coefficient for reasons similar to those given below (4.8). Thus, (4.13) becomes

$$\tilde{A}_{qp} = -\frac{e}{T}\iint \frac{4\pi^2 \mathrm{d}E\,\mathrm{d}E'}{h^4(t_f - t_0)} \left\langle X_q(E)\left[(E'-\mu)Y_p(E') - E'\,Y_p^B(E')\right]\right\rangle. \tag{4.17}$$

Similar to (4.1) and (4.10), the heat flux q_q can be expressed in terms of linear transport coefficients

$$\tilde{B}_{qp} = B_{qp} - \delta_{qp}\sum_r B_{qr} = \frac{\partial q_q}{\partial V_p}, \qquad \text{and} \tag{4.18}$$

$$\tilde{C}_{qp} = C_{qp} - \delta_{qp}\sum_r C_{qr} = \frac{\partial q_q}{\partial T_p}, \tag{4.19}$$

where B_{qp} and C_{qp} are introduced in Section 2.1.3. Expressions for these coefficients can be found by repeating the derivations above, but starting with the heat flux expression (3.153) rather than (3.152). In the end we obtain

$$\tilde{B}_{qp} = -e\iint \frac{4\pi^2 \mathrm{d}E\,\mathrm{d}E'}{h^4(t_f - t_0)} \left\langle \left[(E-\mu)X_q(E) + E\,X_q^B(E)\right] Y_p(E')\right\rangle, \quad \text{and} \tag{4.20}$$

$$\tilde{C}_{qp} = \frac{1}{T}\iint \frac{4\pi^2 \mathrm{d}E\,\mathrm{d}E'}{h^4(t_f - t_0)} \Big\langle \left[(E-\mu)X_q(E) + E\,X_q^B(E)\right] \times \left[(E'-\mu)Y_p(E') - E'\,Y_p^B(E')\right]\Big\rangle, \tag{4.21}$$

where

$$X_q^B(E) = (n_q(E)+1)\,\boldsymbol{\phi}^-(E)^\dagger \Gamma_q^B(E)\boldsymbol{\phi}^+(E) - n_q(E)\boldsymbol{\phi}^+(E)^\dagger \Gamma_q^B(E)\boldsymbol{\phi}^-(E). \tag{4.22}$$

4.2 Kubo relations

The Kubo relations are a particularly elegant set of expressions for the transport coefficients, which express these in terms of correlation functions between the various currents. The relations were obtained by Kubo in two papers dealing with linear response, where the first[19] dealt with mechanical perturbations, and the second[20] with thermodynamic perturbations.

The treatment of mechanical perturbations, i.e. perturbations consisting of an additional term in the Hamiltonian, is a fairly straight forward procedure,

where one simply makes a first order approximation to the equations of motion. However, in the system considered in Section 3.2.1, the currents are not driven by modifications to the Hamiltonian, but by deviation in the state ρ from its equilibrium value. Such thermodynamic perturbations are more difficult to handle in a formal manner, and indeed Kubo based the derivations in his second paper partially on a set of heuristically justified assumptions. An overview of alternative approaches to dealing with thermodynamic perturbations is provided by Zwanzig[31]. Many of the approaches seem to handle the thermodynamic perturbations by replacing it with a mechanical perturbation which is in some sense equivalent. This is also the approach we take below.

4.2.1 Linear response theory of Conductance

In the operator representation, the expectation value of the particle flux is given by (3.132). Combining this with (3.42), and defining the current operator $\hat{I}_q(t) = -e\hat{\Phi}_p(t)$, we can express the electrical current at lead q as

$$I_q(t) = \left\langle \hat{I}_q(t) \right\rangle = \operatorname{Tr} \hat{I}_q(t) P_S^0 \prod_r \frac{1}{Z_r} e^{-\beta_r(\hat{H}_r - \mu_r \hat{N}_r^F)}. \tag{4.23}$$

In order to find the conductance coefficients $\tilde{G}_{qp}$, we could apply (4.3) directly to this expression, taking the derivative with respect to the chemical potentials μ_r. However, this approach turns out not to be so fruitful. Instead, we will make use of the fact that the conductance can also be expressed as

$$\tilde{G}_{qp} = \frac{\partial I_q}{\partial \phi_p} = -e\frac{\partial I_q}{\partial \epsilon_p}, \tag{4.24}$$

where ϕ_p is the electrostatic potential of lead p, and $\epsilon_p = -e\phi_p$. Since the electrostatic potential constitutes a mechanical perturbation, this expression can be handled using standard linear response theory.

Accordingly, we define the perturbed Hamiltonian

$$\hat{H}' = \hat{H} + \sum_p \epsilon_p N_p^F, \tag{4.25}$$

giving rise to a modified propagator $U'(t)$ satisfying $i\hbar\dot{U}' = \hat{H}'U$. Further, we assume that the system is initially in an equilibrium state of the unmodified Hamiltonian $\hat{H}$. Putting this together, we obtain by (4.24)

$$\tilde{G}_{qp} = -e\frac{\partial}{\partial \epsilon_p} \operatorname{Tr} U'(t-t_0)^\dagger \hat{I}_q U'(t-t_0) \frac{1}{Z} e^{-\beta(\hat{H}-\mu\hat{N}^F)}. \tag{4.26}$$

From here, we proceed by making a first order expansion of the propagator $U'(t)$ in the perturbing potential ϵ_p. Details of the procedure are described at multiple locations in the literature[19, 2, 15]. In the end, one obtains

$$\tilde{G}_{qp} = -e\frac{i}{\hbar}\int_{t_0}^{t} \mathrm{d}t' \left\langle [\hat{N}_p^F(t'), \hat{I}_q(t)] \right\rangle. \tag{4.27}$$

Using the fact that in equilibrium correlation functions of this form depend only on time differences, together with the assumption of steady state conditions for $t \gg t_0$, we can modify the limits of the integral to obtain the expression

$$\tilde{G}_{qp} = -e\frac{i}{\hbar}\int_0^\infty \mathrm{d}t \left\langle [\hat{N}_p^F(0), \hat{I}_q(t)] \right\rangle . \tag{4.28}$$

While (4.28) is itself a valid and useful linear response formula, a more symmetric expression can be found by going through some additional steps. The details of these steps are well described by Kubo[19] and by Jacoboni[15], although in Jacoboni's argument some minor modifications must be made to convert from a canonical to a grand canonical ensemble. In the end, one obtains

$$\tilde{G}_{qp} = -\frac{1}{\hbar}\int_0^\infty \mathrm{d}t \int_0^{\hbar\beta} \mathrm{d}\tau \left\langle \hat{I}_p(-i\tau)\hat{I}_q(t) \right\rangle , \tag{4.29}$$

which is the Kubo relation for conductance.

Finally, although the equivalence of the two conductance expressions (4.3) and (4.24) is certainly intuitive, it is instructive to go through an argument showing why this is true. One way of doing that is to consider a situation where both perturbations are applied, in such a way that they are in equilibrium. Thus, we again perturb the Hamiltonian as in (4.25), but this time we assume that the leads are in an equilibrium state of the perturbed Hamiltonian $\hat{H}'$, meaning that

$$\rho(0) = P_S^0 \prod_r \frac{1}{Z_r} e^{-\beta(\hat{H}'_r - \mu\hat{N}_r^F)}. \tag{4.30}$$

Given this state, the leads are all in equilibrium with each other, but initially not with the subsystem S. However, it is reasonable to assume all parts of the system to equilibrate over some finite time scale, so that for large t, $\rho(t)$ will be an equilibrium state. In particular, since the current is always zero in equilibrium, we have for such large t,

$$I_q(t) = \mathrm{Tr}\, U'(t-t_0)^\dagger \hat{I}_q U'(t-t_0) P_S^0 \prod_r \frac{1}{Z_r} e^{-\beta(\hat{H}'_r - \mu\hat{N}_r^F)} = 0. \tag{4.31}$$

Taking the derivative of this expression with respect to ϵ_p, we find

$$\begin{aligned} &\mathrm{Tr}\, \frac{\partial}{\partial\epsilon_p}\left(U'(t-t_0)^\dagger \hat{I}_q U'(t-t_0)\right) P_S^0 \prod_r \frac{1}{Z_r} e^{-\beta(\hat{H}_r - \mu\hat{N}_r^F)} \\ &+\mathrm{Tr}\, U^\dagger(t-t_0)\hat{I}_q U(t-t_0) \frac{\partial}{\partial\epsilon_p} P_S^0 \prod_r \frac{1}{Z_r} e^{-\beta(\hat{H}'_r - \mu\hat{N}_r^F)} = 0. \end{aligned} \tag{4.32}$$

Next, we note that if we set $\epsilon_p = \mu - \mu_p$, then $\hat{H}'_p - \mu\hat{N}_p^F = \hat{H}_p - \mu_p\hat{N}_p^F$. Inserting this in (4.32), we obtain

$$\begin{aligned} &\mathrm{Tr}\, U^\dagger(t-t_0)\hat{I}_q U(t-t_0) \frac{\partial}{\partial\mu_p} P_S^0 \prod_r \frac{1}{Z_r} e^{-\beta(\hat{H}_r - \mu_r\hat{N}_r^F)} \\ &= \mathrm{Tr}\, \frac{\partial}{\partial\epsilon_p}\left(U'(t-t_0)^\dagger \hat{I}_q U'(t-t_0)\right) P_S^0 \prod_r \frac{1}{Z_r} e^{-\beta(\hat{H}_r - \mu\hat{N}_r^F)}. \end{aligned} \tag{4.33}$$

By (4.23) we recognize the first line of this equation as $\partial I_q/\partial \mu_p$. Further, comparing the second line to (4.26), we see that it is almost identical to $\partial I_q/\partial \epsilon_p$, except that the initial state is different. However, at large times t, where we have obtained steady state conditions, it is reasonable to assume that $I_q(t)$ is in fact independent of the initial state, as long as the temperature and chemical potential of the macroscopic leads are the same. Thus, under this assumption (4.33) simply states

$$\frac{\partial I_q}{\partial \mu_p} = \frac{\partial I_q}{\partial \epsilon_p}, \tag{4.34}$$

which justifies the use of (4.24) to calculate conductance.

4.2.2 Thermoelectric coefficients

To calculate the thermoelectric coefficient $\tilde{A}_{qp}$, we would like to repeat the procedure above, where we were able to make use of standard linear response theory since we could rephrase the definition of the transport coefficient in terms of a mechanical perturbation. However, while the electrostatic potential was a clear candidate as a replacement of the electrochemical potential, there is no obvious candidate to replace the temperature differences in (4.10). Thus, we must proceed more formally. In particular, we will want to make an argument similar to that leading from (4.31) to (4.34), which shows the equivalence of the perturbations $\Delta\mu_p$ and ϵ_p.

Examining the argument, we see that the crucial step is the one below (4.32), where we obtain $\hat{H}'_p - \mu\hat{N}_p^F = \hat{H}_p - \mu_p\hat{N}_p^F$. A similar expression involving temperatures can be obtained by defining the mechanical perturbation as one given by the perturbed Hamiltonian

$$\hat{H}' = \hat{H} + \sum_p \delta_p(\hat{H}_p - \mu\hat{N}_p^F). \tag{4.35}$$

We then have $\hat{H}'_p - \mu\hat{N}_p^F = (1+\delta_p)(\hat{H}_p - \mu\hat{N}_p^F)$. Accordingly, setting $\delta_p = \beta_p/\beta - 1$, we get

$$\beta(\hat{H}'_p - \mu\hat{N}_p^F) = \beta_p(\hat{H}_p - \mu\hat{N}_p^F), \tag{4.36}$$

which is precisely on the form we seek.

With this it is a simple matter to repeat the steps from (4.31) to (4.34). We begin by differentiating (4.31) with respect to δ_p, obtaining a parallel to (4.32). Then we insert (4.36), and make use of the relation $\delta_p = \beta_p/\beta - 1$ to reexpress one of the derivatives, obtaining in the end

$$\frac{\partial I_q}{\partial \beta_p} = -\frac{1}{\beta}\frac{\partial I_q}{\partial \delta_p}. \tag{4.37}$$

Then inserting this in (4.12), we see that we can calculate $\tilde{A}_{qp}$ as

$$\tilde{A}_{qp} = \frac{1}{T}\frac{\partial I_q}{\partial \delta_p}. \tag{4.38}$$

Since we have then expressed the coefficient in terms of the mechanical perturbation (4.35), we can again make use of standard linear response theory to derive the Kubo relation

$$\tilde{A}_{qp} = -\frac{1}{\hbar T}\int_0^\infty \mathrm{d}t \int_0^{\hbar\beta} \mathrm{d}\tau \left\langle \hat{q}_p(-i\tau)\hat{I}_q(t)\right\rangle, \tag{4.39}$$

where we have defined $\hat{q}_p(t) = \hat{\Phi}_p^E(t) - \mu_p\hat{\Phi}_p(t)$.

Combining the expression $q_p = \Phi_p^E - \mu_p\Phi_p$ with (3.132), (3.137) and (3.42), we can express the heat flux in lead p as

$$q_q(t) = \langle \hat{q}_q(t)\rangle = \mathrm{Tr}\,\hat{q}_q(t)P_S^0\prod_r \frac{1}{Z_r}e^{-\beta_r(\hat{H}_r-\mu_r\hat{N}_r^F)} \tag{4.40}$$

Kubo relations for the remaining thermoelectric coefficients $\tilde{B}_{qp}$ and $\tilde{C}_{qp}$ can be found from this expression in a manner analogous to what we did above, by reexpressing (4.18) and (4.19) in terms of derivatives with respect to the mechanical perturbations ϵ_p and δ_p. In the end we obtain

$$\tilde{B}_{qp} = -\frac{1}{\hbar}\int_0^\infty \mathrm{d}t \int_0^{\hbar\beta} \mathrm{d}\tau \left\langle \hat{I}_p(-i\tau)\hat{q}_q(t)\right\rangle, \qquad \text{and} \tag{4.41}$$

$$\tilde{C}_{qp} = -\frac{1}{\hbar T}\int_0^\infty \mathrm{d}t \int_0^{\hbar\beta} \mathrm{d}\tau \left\langle \hat{q}_p(-i\tau)\hat{q}_q(t)\right\rangle. \tag{4.42}$$

4.2.3 Bulk expressions

In the case of macroscopic devices one typically does not need to perform an explicit simulation of the device, since the transport coefficients G, A, B etc. can be calculated relatively easily from bulk material coefficients. Thus, we will briefly consider also such bulk coefficients, starting with conductivity. In the absence of thermodynamic gradients, the conductivity $\overleftrightarrow{\sigma}$ is defined through the relation that at macroscopic size scales $\boldsymbol{j} = \overleftrightarrow{\sigma}\boldsymbol{E} = \sum_{ij}\sigma_{ij}E_j\hat{\boldsymbol{e}}_i$, $\boldsymbol{j}$ being the current density and $\boldsymbol{E}$ the electric field. Typically one also considers alternating fields, and so the relation is generalized to $\boldsymbol{j}(\omega) = \overleftrightarrow{\sigma}(\omega)\boldsymbol{E}(\omega)$, where $\boldsymbol{j}(\omega)$ and $\boldsymbol{E}(\omega)$ are respectively the Fourier transforms of $\boldsymbol{j}(t)$ and $\boldsymbol{E}(t)$.

To obtain an expression for $\overleftrightarrow{\sigma}$, we can apply the same linear response technique made use of above. Knowing that $\boldsymbol{E}$ is related to the electrostatic potential ϕ by $\boldsymbol{E} = -\boldsymbol{\nabla}\phi$, we introduce a perturbing potential $\epsilon(\boldsymbol{x},t) = -e\phi(\boldsymbol{x},t)$, coupled to the local number density of electrons $\hat{n}(\boldsymbol{x})$. We then simply repeat the steps leading to (4.29), with some small modifications to account for the temporal and spatial variation of ϵ. Details of the derivation can again be found in the literature[19, 2, 15]. The end result is

$$\sigma_{ij}(\omega) = V\frac{1}{\hbar}\int_0^\infty \mathrm{d}t \int_0^{\hbar\beta} \mathrm{d}\tau \left\langle \bar{\hat{j}}_j(-i\tau)\bar{\hat{j}}_i(t)\right\rangle e^{-i\omega t}, \tag{4.43}$$

where $i, j \in \{x, y, z\}$, V is the volume of some sufficiently large region of material, and $\bar{\hat{\boldsymbol{j}}}$ denotes the current density operator $\hat{\boldsymbol{j}}(x)$ averaged over this region. To obtain the direct current conductivity, we simply insert $\omega = 0$. In that case, (4.43) takes the same form as the Kubo relations considered above.

More generally we have $\boldsymbol{j} = -\overleftrightarrow{\sigma}\boldsymbol{\nabla}V - \overleftrightarrow{\mathcal{A}}\boldsymbol{\nabla}T$, which reduces to $\boldsymbol{j} = \overleftrightarrow{\sigma}\boldsymbol{E}$ when $\boldsymbol{\nabla}T = \boldsymbol{0} = \boldsymbol{\nabla}(V - \phi)$. The thermoelectric tensor $\overleftrightarrow{\mathcal{A}}$ is related to the coefficients $\tilde{A}_{qp}$ in the same way that $\overleftrightarrow{\sigma}$ is related to $\tilde{G}_{qp}$. Since we can reinterpret $\tilde{A}_{qp}$ as describing responses to the mechanical perturbations δ_p of (4.35), the tensor $\overleftrightarrow{\mathcal{A}}$ must also describe responses to gradients in a generalized mechanical potential $\delta(\boldsymbol{x}, t)$, coupled to the local heat density $\hat{h}(\boldsymbol{x}) - \mu\hat{n}(\boldsymbol{x})$, where $\hat{H} = \int \mathrm{d}\boldsymbol{x}\, \hat{h}(\boldsymbol{x})$. Accordingly, we may employ linear response theory in a manor completely analogous to the derivation of (4.43), obtaining

$$\mathcal{A}_{ij} = V\frac{1}{\hbar T}\int_0^\infty \mathrm{d}t \int_0^{\hbar\beta} \mathrm{d}\tau \left\langle \bar{\hat{\phi}}_{Qj}(-i\tau)\bar{\hat{j}}_i(t)\right\rangle, \tag{4.44}$$

where $\boldsymbol{\phi}_Q$ denotes heat flux, and the rest of the notation is as before.

In the linear regime the heat flux $\boldsymbol{\phi}_Q$ can also be expressed in terms of $\boldsymbol{\nabla}T$ and $\boldsymbol{\nabla}V$ as $\boldsymbol{\phi}_Q = -\overleftrightarrow{\mathcal{B}}\boldsymbol{\nabla}V - \overleftrightarrow{\mathcal{C}}\boldsymbol{\nabla}T$. The thermoelectric tensors $\overleftrightarrow{\mathcal{B}}$ and $\overleftrightarrow{\mathcal{C}}$ can be found by arguments similar to those above, and in the end we obtain

$$\mathcal{B}_{ij} = V\frac{1}{\hbar}\int_0^\infty \mathrm{d}t \int_0^{\hbar\beta} \mathrm{d}\tau \left\langle \bar{\hat{j}}_j(-i\tau)\bar{\hat{\phi}}_{Qi}(t)\right\rangle \quad \text{and,} \tag{4.45}$$

$$\mathcal{C}_{ij} = V\frac{1}{\hbar T}\int_0^\infty \mathrm{d}t \int_0^{\hbar\beta} \mathrm{d}\tau \left\langle \bar{\hat{\phi}}_{Qj}(-i\tau)\bar{\hat{\phi}}_{Qi}(t)\right\rangle. \tag{4.46}$$

Expressions similar to (4.43), (4.44), (4.45) and (4.46) were derived by Kubo in his second paper on the Kubo relations[20], as an example of how to treat thermodynamic perturbations. The equations should be compared to (4.29), (4.39), (4.41) and (4.42), which are their device analogs respectively.

In Section 2.1.3 we saw that in a simple two terminal device we could reexpress the current I and the heat current q in terms of new thermoelectric coefficients, as (2.30) and (2.31). In a similar manner, we can reexpress the current density $\boldsymbol{j}$ and the heat flux $\boldsymbol{\phi}_Q$ in terms of new thermoelectric tensors as

$$\boldsymbol{j} = -\overleftrightarrow{\sigma}\left(\boldsymbol{\nabla}V + \overleftrightarrow{\alpha}\boldsymbol{\nabla}T\right) \quad \text{and,} \tag{4.47}$$

$$\boldsymbol{\phi}_Q = -\overleftrightarrow{\kappa}\boldsymbol{\nabla}T + \overleftrightarrow{\pi}\boldsymbol{j}, \tag{4.48}$$

where $\overleftrightarrow{\kappa}$ is referred to as the thermal conductivity, and $\overleftrightarrow{\alpha}$ and $\overleftrightarrow{\pi}$ respectively as the Seebeck and Peltier coefficients. It is a matter of simple algebra to show that

$$\overleftrightarrow{\alpha} = \overleftrightarrow{\sigma}^{-1}\overleftrightarrow{\mathcal{A}}, \tag{4.49}$$

$$\overleftrightarrow{\pi} = \overleftrightarrow{\mathcal{B}}\overleftrightarrow{\sigma}^{-1} \quad \text{and,} \tag{4.50}$$

$$\overleftrightarrow{\kappa} = \overleftrightarrow{\mathcal{C}} - \overleftrightarrow{\mathcal{B}}\overleftrightarrow{\sigma}^{-1}\overleftrightarrow{\mathcal{A}}, \tag{4.51}$$

where the products represent matrix multiplication. These relations generalize the simple two terminal device expressions given by (2.27)-(2.29).

4.2.4 Correlation functions

The linear response expressions derived above all share a common format where some transport coefficient G_{AB} is expressed as

$$G_{AB} = \int_0^\infty \mathrm{d}t \int_0^{\hbar\beta} \mathrm{d}\tau \left\langle \hat{A}(-i\tau)\hat{B}(t) \right\rangle = \iint_R \mathrm{d}z^\star \mathrm{d}z \, C_{AB}(z), \tag{4.52}$$

where $R = \{z : 0 \leq \mathcal{I}m\, z \leq \hbar\beta, 0 \leq \mathcal{R}e\, z < \infty\}$, and where we have defined the mixed time correlation function $C_{AB}(t + i\tau) = \langle \hat{A}(-i\tau)\hat{B}(t)\rangle$. In particular, (4.29), (4.39), (4.41), (4.42), (4.43), (4.44), (4.45) and (4.46) all have this format.

In addition to the mixed time correlation function, we define a real time correlation function C^t_{AB} given by $C^t_{AB}(t) = C_{AB}(t)$ with t real, and an imaginary time correlation function C^τ_{AB} given by $C^\tau_{AB}(\tau) = C_{AB}(i\tau)$ with τ real. It is easily checked that in equilibrium such correlation functions can only depend on time differences, and so we can also express the real time correlation function as $C^t_{AB}(t' - t) = \langle \hat{A}(0)\hat{B}(t' - t)\rangle = \langle \hat{A}(t)\hat{B}(t')\rangle$.

A final correlation function to be introduced, is the spectral correlation function $C^s_{AB}(E)$. To obtain this function, we make use of a tool known as the Lehmann representation[2], in which we express correlation functions in terms of exact eigenstates of the full Hamiltonian $\hat{H}$. Since $\hat{H}$ commutes with $\hat{N}^F$, these operators can be simultaneously diagonalized. Thus, introducing a basis $\{|i\rangle\}$ which diagonalizes both $\hat{H}$ and $\hat{N}^F$, we can rewrite the mixed time correlation function as

$$\begin{aligned}
\langle \hat{A}(-i\tau)\hat{B}(t)\rangle &= \mathrm{Tr}\frac{1}{Z} e^{-\beta(\hat{H}-\mu\hat{N}^F)} e^{\hat{H}\tau/\hbar} \hat{A} e^{-\hat{H}\tau/\hbar} e^{i\hat{H}t/\hbar} \hat{B} e^{-i\hat{H}t/\hbar} \\
&= \frac{1}{Z}\sum_{ij} \langle i|e^{-\beta(\hat{H}-\mu\hat{N}^F)} e^{\hat{H}\tau/\hbar} \hat{A} e^{-\hat{H}\tau/\hbar}|j\rangle \langle j|e^{i\hat{H}t/\hbar} \hat{B} e^{-i\hat{H}t/\hbar}|i\rangle \\
&= \frac{1}{Z}\sum_{ij} A_{ij} B_{ji} e^{-\beta(E_i-\mu N_i^F)+i(E_j-E_i)t/\hbar+(E_i-E_j)\tau/\hbar}.
\end{aligned} \tag{4.53}$$

where $A_{ij} = \langle i|\hat{A}|j\rangle$, $B_{ji} = \langle j|\hat{B}|i\rangle$, and E_i and N_i^F are respectively eigenvalues of $\hat{H}$ and $\hat{N}^F$. If we now define

$$C^s_{AB}(E) = \frac{1}{Z}\sum_{ij} A_{ij} B_{ji} e^{-\beta(E_i-\mu N_i^F)} \delta(E - E_i + E_j), \tag{4.54}$$

we can write (4.53) simply as

$$C_{AB}(t + i\tau) = \int \mathrm{d}E \, C^s_{AB}(E) e^{-iE(t+i\tau)/\hbar}. \tag{4.55}$$

In particular, the real time correlation function $C^t_{AB}(t) = C_{AB}(t)$ is then a Fourier transform of the spectral correlation function $C^s_{AB}(E)$. In the limit

$L_p \to \infty$, where the leads become infinitely large, we again expect the distance between the energy levels E_i to approach zero, and accordingly that $C^s_{AB}(E)$ becomes a continuous function.

In an actual calculation, one will typically obtain estimates of either the real time correlation function C^t_{AB}, its Fourier transform C^s_{AB}, or the imaginary time correlation function C^τ_{AB}. Thus, the transport coefficient G_{AB} can be obtained if we can reexpress (4.52) in terms of these functions. We begin by considering the relationship between G_{AB} and the imaginary time correlation function. Assuming that the spectral function $C^s_{AB}(E)$ is sufficiently well behaved, we have by (4.55)

$$\frac{\partial}{\partial z^\star} C_{AB}(z) = \int \mathrm{d}E\, C_{AB}(E) \frac{\partial}{\partial z^\star} e^{-iEz/\hbar} = 0, \tag{4.56}$$

which means the function $C_{AB}(z)$ is analytic in the entire complex plane. Thus, it must equal its Taylor expansion around any point, and in particular

$$\begin{aligned} C_{AB}(z) &= \sum_{n=0}^{\infty} \frac{1}{n!} \frac{\partial^n}{\partial z^n} C_{AB}(i\hbar\beta/2)(z - i\hbar\beta/2)^n \\ &= \sum_{n=0}^{\infty} \frac{(-i)^n}{n!} \frac{\partial^n}{\partial \tau^n} C^\tau_{AB}(\hbar\beta/2)(z - i\hbar\beta/2)^n. \end{aligned} \tag{4.57}$$

Thus, given perfect knowledge of the imaginary time correlation function $C^\tau_{AB}(\tau)$ in the interval $\tau \in (0, \hbar\beta)$, we can in principle evaluate $C_{AB}(z)$ at any value of z, so that (4.52) can be used to calculate G_{AB}. However, in typical numerical calculations one will not have perfect knowledge of $C^\tau_{AB}(\tau)$, so in practice the continuation of the function to the complex plane can be a difficult task. Some approaches to solving this problem are described in the literature[30].

Next we consider the relationship between G_{AB} and the spectral correlation function $C^s_{AB}(E)$. Since C^s_{AB} is related to C^t_{AB} by a simple Fourier transform, this will also give us the relationship between G_{AB} and the real time correlation function. Making use of (4.55), we can perform the innermost integral of (4.52) to get

$$\int_0^{\hbar\beta} \mathrm{d}\tau\, C_{AB}(t + i\tau) = \hbar\beta \int \mathrm{d}E\, g(\beta E) C^s_{AB}(E) e^{-iEt/\hbar}, \tag{4.58}$$

where we have defined

$$g(x) = \int_0^1 e^{sx} \mathrm{d}s = \begin{cases} \frac{e^x - 1}{x} & \text{for } x \neq 0 \\ 1 & \text{for } x = 0 \end{cases}. \tag{4.59}$$

Defining now the function $\chi_{AB}(E) = \hbar\beta g(\beta E) C^s_{AB}(E)$, and assuming this function to be sufficiently well behaved to exchange limits and integrals, we can

perform the outermost integral of (4.52) as follows:

$$G_{AB} = \int_0^\infty \mathrm{d}t \int \mathrm{d}E \lim_{\eta\to 0} \chi_{AB}(E) e^{-iEt/\hbar - \eta t} \tag{4.60}$$
$$= \lim_{\eta\to 0} \int \mathrm{d}E\, \chi_{AB}(E) \int_0^\infty \mathrm{d}t\, e^{-iEt/\hbar-\eta t} = -\hbar i \lim_{\eta\to 0} \int \mathrm{d}E\, \frac{\chi_{AB}(E)}{E - i\eta}.$$

Further, one can show that for well behaved functions f, we have

$$\lim_{\eta\to 0} \int \mathrm{d}x\, \frac{f(x)}{x - i\eta} = \pi i f(0) + \int \mathrm{d}x \mathbb{P} \frac{1}{x} f(x), \tag{4.61}$$

where $\mathbb{P}$ denotes principal value. Making use of this relation, the definition of χ_{AB}, and (4.59), we can reexpress (4.60) as

$$G_{AB} = \pi\hbar^2 \beta C^s_{AB}(0) - \hbar^2 i \int \mathrm{d}E \mathbb{P} \frac{1}{E^2} (e^{\beta E} - 1) C^s_{AB}(E). \tag{4.62}$$

4.2.5 Symmetries

The correlation functions introduced above obey several important symmetry relations. Using for instance (4.62), we can translate these relations into symmetries of the transport coefficients. Consider first the real time correlation function $C^t_{AB}(t' - t) = \langle \hat{A}(t)\hat{B}(t')\rangle$. We have $C^t_{AB}(t' - t)^\star = \langle \hat{A}(t)\hat{B}(t')\rangle^\star = \langle \hat{B}(t')\hat{A}(t)\rangle = C^t_{BA}(t - t')$. Taking the inverse Fourier transform of this relation, we also find

$$C^s_{AB}(E)^\star = C^s_{BA}(E). \tag{4.63}$$

Further, exchanging A and B as well as the summation indices in (4.54), we get

$$C^s_{BA}(E) = \frac{1}{Z} \sum_{ij} B_{ji} A_{ij} e^{-\beta(E_j - \mu N^F_j)} \delta(E - E_j + E_i). \tag{4.64}$$

Now, in all of the Kubo relations derived above, the operators $\hat{A}$ and $\hat{B}$ were single particle operators, which in particular means they commute with $\hat{N}^F$. Accordingly, we have $A_{ij} e^{\beta\mu N^F_i} = \langle i| e^{\beta\mu\hat{N}^F} \hat{A}|j\rangle = \langle i|\hat{A} e^{\beta\mu\hat{N}^F}|j\rangle = A_{ij} e^{\beta\mu N^F_j}$. Inserting this in (4.64) we find

$$C^s_{BA}(E) = \frac{1}{Z} \sum_{ij} A_{ij} B_{ji} e^{-\beta(E_j - \mu N^F_i)} \delta(-E + E_j - E_i) = e^{-\beta E} C^s_{AB}(-E). \tag{4.65}$$

Combining this with (4.63), we also find

$$e^{\beta E} C^s_{AB}(E) = C^s_{AB}(-E)^\star. \tag{4.66}$$

Inserting (4.66) in (4.62), we obtain after some rearrangement

$$G_{AB} = \pi\hbar^2\beta C^s_{AB}(0) - 2\hbar^2 \int \mathrm{d}E \mathbb{P}\frac{1}{E^2}\mathcal{I}m\, C^s_{AB}(E). \tag{4.67}$$

Since by (4.66) $C_{AB}(0)$ is real, so is G_{AB}. This is as expected since G_{AB} is defined at $\omega = 0$.

Next, we introduce the time reversal operator $\hat{\tau}$ [21]. The defining properties of this operator is that it is conjugate linear, meaning that $\hat{\tau}(c|\psi\rangle) = c^\star\hat{\tau}|\psi\rangle$, that $\hat{\tau}^2 = I$, and finally that $\hat{\tau}$ preserves the position basis, so that $\hat{\tau}\hat{\psi}_i = \hat{\psi}_i\hat{\tau}$ for any single particle state i which is a real combination of position basis states. Importantly, the last fact also means we can construct a basis of many particle states $|j\rangle$ which is preserved by the time reversal operator, meaning that $\hat{\tau}|j\rangle = |j\rangle$.

So let $\{|i\rangle\}$ be such a many particle basis. We have

$$C^t_{AB}(t'-t) = \frac{1}{Z}\mathrm{Tr}\, e^{-\beta(\hat{H}-\mu\hat{N}^F)}e^{i\hat{H}t/\hbar}\hat{A}e^{-i\hat{H}t/\hbar}e^{i\hat{H}t'/\hbar}\hat{B}e^{-i\hat{H}t'/\hbar} = \frac{1}{Z}\sum_i \langle i|\hat{P}|i\rangle, \tag{4.68}$$

where we have defined $\hat{P} = e^{-\beta(\hat{H}-\mu\hat{N}^F)}e^{i\hat{H}t/\hbar}\hat{A}e^{-i\hat{H}t/\hbar}e^{i\hat{H}t'/\hbar}\hat{B}e^{-i\hat{H}t'/\hbar}$. Making use of the time reversal operator, we can rewrite this as

$$\begin{aligned} C^t_{AB}(t'-t) &= \frac{1}{Z}\sum_i \langle i|\hat{\tau}^2\hat{P}\hat{\tau}^2|i\rangle = \frac{1}{Z}\sum_{ij}\langle i|\hat{\tau}\left[|j\rangle\langle j|\hat{\tau}\hat{P}\hat{\tau}|i\rangle\right] \\ &= \frac{1}{Z}\sum_{ij}\langle j|\hat{\tau}\hat{P}\hat{\tau}|i\rangle^\star\langle i|\hat{\tau}|j\rangle = \frac{1}{Z}\sum_i\langle i|\hat{\tau}\hat{P}\hat{\tau}|i\rangle^\star = \frac{1}{Z}\left(\mathrm{Tr}\,\hat{\tau}\hat{P}\hat{\tau}\right)^\star, \end{aligned} \tag{4.69}$$

or alternatively $C^t_{AB}(t'-t)^\star = \mathrm{Tr}\,\hat{\tau}\hat{P}\hat{\tau}/Z$. Now, using the Taylor expansion of the exponential and the properties of $\hat{\tau}$, it is straight forward to show that

$$\hat{\tau}\hat{P}\hat{\tau} = e^{-\beta(\hat{\tau}\hat{H}\hat{\tau}-\mu\hat{\tau}\hat{N}^F\hat{\tau})}e^{-i\hat{\tau}\hat{H}\hat{\tau}t/\hbar}\hat{\tau}\hat{A}\hat{\tau}e^{i\hat{\tau}\hat{H}\hat{\tau}t/\hbar}e^{-i\hat{\tau}\hat{H}\hat{\tau}t'/\hbar}\hat{\tau}\hat{B}\hat{\tau}e^{i\hat{\tau}\hat{H}\hat{\tau}t'/\hbar}. \tag{4.70}$$

Accordingly we must consider how the involved operators change under the time reversal transform $\hat{X} \to \hat{\tau}\hat{X}\hat{\tau}$. We begin by considering the Hamiltonian $\hat{H}$. It can always be decomposed as $\hat{H} = \hat{H}_1 + \hat{H}_2$, where the components $\hat{H}_1$ and $\hat{H}_2$ are respectively symmetric and anti symmetric under the time reversal transform. Indeed, we can simply let $\hat{H}_1 = (\hat{H} + \hat{\tau}\hat{H}\hat{\tau})/2$ and $\hat{H}_2 = (\hat{H} - \hat{\tau}\hat{H}\hat{\tau})/2$. In solid state applications, the anti symmetric component $\hat{H}_2$ must be proportional to an external magnetic field, since an external electric field, as well as any internal force are left unchanged by time reversal.

Thus, it makes sense to generalize the Hamiltonian as $\hat{H}(b) = \hat{H}_1 + b\hat{H}_2$, where b parameterizes the magnetic field strength. In fact, we will include an explicit dependence on the magnetic field in most operators, writing for instance $\hat{A}$ as $\hat{A}(b)$. In particular, we have $\hat{\tau}\hat{H}(b)\hat{\tau} = \hat{H}_1 - b\hat{H}_2 = \hat{H}(-b)$. The effect of the time reversal transform on $\hat{N}^F$ is easily found by expressing the operator in

terms of a preserved single particle basis i. We have $\hat{\tau}\hat{N}^F\hat{\tau} = \sum_i \hat{\tau}\hat{\psi}_i^\dagger\hat{\psi}_i\hat{\tau} = \hat{N}^F$. Combining this with the effect on $\hat{H}$, we can also find the effect on the current operator $\hat{I}_p = -e\hat{\Phi}_p$. By (3.131) and the definition of $\hat{\Phi}_p(t)$ below (3.132), we have

$$\hat{\tau}\hat{I}_p(b)\hat{\tau} = \hat{\tau}(-ei[\hat{H}(b), \hat{N}_p^F]/\hbar)\hat{\tau} = ei[\hat{H}(-b), \hat{N}_p^F]/\hbar = -\hat{I}_p(-b). \tag{4.71}$$

Similar arguments can be applied to the other currents $\hat{q}_p$, $\hat{\boldsymbol{j}}$ and etc., and result in similar expressions. Since the operators $\hat{A}$ and $\hat{B}$ are always picked from these currents, we thus always have $\hat{\tau}\hat{A}(b)\hat{\tau} = -\hat{A}(-b)$ and $\hat{\tau}\hat{B}(b)\hat{\tau} = -\hat{B}(-b)$. Inserting all of this in (4.70), we get

$$\hat{\tau}\hat{P}(b)\hat{\tau} = e^{-\beta(\hat{H}(-b)-\mu\hat{N}^F)}e^{-i\hat{H}(-b)t/\hbar}\hat{A}(-b)e^{i\hat{H}(-b)t/\hbar}e^{-i\hat{H}(-b)t'/\hbar}\hat{B}(-b)e^{i\hat{H}(-b)t'/\hbar}. \tag{4.72}$$

Thus, by (4.69) we have

$$C_{AB}^t(b, t'-t)^\star = \frac{1}{Z}\mathrm{Tr}\,\hat{\tau}\hat{P}(b)\hat{\tau} = C_{AB}^t(-b, t-t'), \tag{4.73}$$

where we have included an explicit dependence on the magnetic field also in the correlation functions. Taking the inverse Fourier transform of this relation, we find

$$C_{AB}^s(b, E)^\star = C_{AB}^s(-b, E). \tag{4.74}$$

Evaluating (4.67) at field strength $-b$, and making use of (4.74) and the reality of $C_{AB}^s(0)$, we find

$$\begin{aligned} G_{AB}(-b) &= \pi\hbar^2\beta C_{AB}^s(-b, 0) - 2\hbar^2\int \mathrm{d}E\mathbb{P}\frac{1}{E^2}\mathcal{I}m\, C_{AB}^s(-b, E) \\ &= \pi\hbar^2\beta C_{AB}^s(b, 0) + 2\hbar^2\int \mathrm{d}E\mathbb{P}\frac{1}{E^2}\mathcal{I}m\, C_{AB}^s(b, E). \end{aligned} \tag{4.75}$$

Thus, we obtain an interpretation of the two terms in (4.67) in terms of how they behave under reversal of the magnetic field: $G_1 = \pi\hbar^2\beta C_{AB}^s(0)$ is invariant, while the term $G_2 = 2\hbar^2\int \mathrm{d}E\mathbb{P}\,\mathcal{I}m\, C_{AB}^s(E)/E^2$ changes sign. In particular this means that at zero magnetic field we must have $G_{AB} = G_1 = \pi\hbar^2\beta C_{AB}^s(0)$.

Finally, combining (4.74) and (4.63), we obtain $C_{BA}(b, E) = C_{AB}(-b, E)$. Inserting this in (4.67), it follows easily that

$$G_{BA}(b) = G_{AB}(-b). \tag{4.76}$$

These important symmetry relations were also derived by Kubo[19]. At zero magnetic field they reduce to $G_{AB} = G_{BA}$, which are the famous Onsager relations[26]. These relations have several important consequences for the thermoelectric transport coefficients introduced above. For instance they imply symmetry of the conductance and conductivity coefficients: $G_{qp} = G_{pq}$, and $\overleftrightarrow{\sigma} = \overleftrightarrow{\sigma}^T$, as well as a relation between the Peltier and Seebeck coefficients, stating $\Pi_{qp} = T\alpha_{pq}$ and $\overleftrightarrow{\pi} = T\overleftrightarrow{\alpha}^T$.

4.3 Four point functions

In the previous section we obtained expressions for transport coefficients in terms of real time and imaginary time correlation functions. In order to evaluate these expressions using the field integral formalism, we must translate the correlation functions into field integral expectation values. We begin by noting that the operators $\hat{A}$ and $\hat{B}$ from the previous section are always single particle operators, and accordingly are always on the form of (3.23), (3.24), or some linear combination of these. Assuming $\hat{A}$ and $\hat{B}$ to involve only fermionic fields, we have

$$\langle \hat{A}\hat{B}\rangle = \sum_{ijkl} A_{ij}B_{kl}\langle \hat{\psi}_i^\dagger \hat{\psi}_j \hat{\psi}_k^\dagger \hat{\psi}_l\rangle. \tag{4.77}$$

The generalization of this expression to include bosonic fields should be obvious. The important point is that the correlation functions of the previous section can always be expressed as a linear combination of correlation functions involving four fields.

4.3.1 Real time correlation functions

The real time correlation function $C^t_{AB}(t-t')$ introduced in Section 4.2.4 will be a linear combination of correlation functions on the form $\langle \hat{\psi}_i^\dagger(t)\hat{\psi}_j(t)\hat{\psi}_k^\dagger(t')\hat{\psi}_l(t')\rangle$, possibly with all or two of the fields operators replaced with boson operators. In order to express these correlation functions as field integrals, we must make a small modification, where we instead calculate $\langle \hat{\psi}_i^\dagger(t)\hat{\psi}_j(t+\Delta t)\hat{\psi}_k^\dagger(t'+\Delta t)\hat{\psi}_l(t')\rangle$. This modification will only introduce an error of order $1/N$.

The modified correlation functions are seen to be very simple generalizations of the expression to the left in (3.26), and can be expressed as a field integrals in a similar manner as that expression. In particular, we generalize the second line to the right in (3.26), expressing the correlation function in terms of two factors $U^\dagger(t-t_0)\hat{\psi}_i^\dagger U(\Delta t)\hat{\psi}_j U^\dagger(t_f-t)$ and $U(t_f-t')\hat{\psi}_k^\dagger U(\Delta t)\hat{\psi}_l U(t'-t_0)$. These can be expressed as field integrals using straight forward generalizations of (3.27) and (3.28) respectively. Putting these expressions together in a manner generalizing (3.29), we obtain

$$\langle \hat{\psi}_i^\dagger(t)\hat{\psi}_j(t)\hat{\psi}_k^\dagger(t')\hat{\psi}_l(t')\rangle \approx \langle \bar{\psi}_i^-(t)\psi_j^-(t+\Delta t)\bar{\psi}_k^+(t'+\Delta t)\psi_l^+(t')\rangle, \tag{4.78}$$

with an error of order $1/N$. Field integral expectations like the one on the right in this expression, which involves four fields, are referred to as four point functions[2].

Another source of error in (4.78) is the fact that the two expectation values are technically defined with different initial states. The operator expectation on the left is defined in the equilibrium state $e^{-\beta(\hat{H}-\mu\hat{N})}/Z$ of the full system, while the field integral expectation value on the right is defined with an initial state given by (3.42). However, as before we make use of our assumption that the

system equilibrates over some finite time scale, and conclude that the different initial states are irrelevant as long as $t, t' \gg t_0$.

By combining (4.78) with (4.77) and (4.67), we can express any transport coefficient G_{AB} in terms of four point functions. In particular, applying this procedure to the transport coefficients $\tilde{G}_{qp}$, $\tilde{A}_{qp}$, $\tilde{B}_{qp}$ and $\tilde{C}_{qp}$ given by (4.29), (4.39), (4.41) and (4.42), we should in principle obtain expressions equivalent to (4.9), (4.17), (4.20) and (4.21). However, this is difficult to show explicitly.

4.3.2 Imaginary time correlation functions

Section 4.2.4 also introduces imaginary time correlation functions, which are defined as $C^\tau_{AB}(\tau) = \langle \hat{A}(-i\tau)\hat{B}(0)\rangle = \mathrm{Tr} e^{-\beta(\hat{H}-\mu\hat{N}^F)} e^{\tau\hat{H}/\hbar}\hat{A}e^{-\tau\hat{H}/\hbar}\hat{B}/Z$. Again making use of the fact that $\hat{N}$ commutes with the single particle operators $\hat{A}$ and $\hat{B}$, and with the Hamiltonian, we can write this as

$$C^\tau_{AB}(\tau) = \frac{1}{Z}\mathrm{Tr}\, e^{-(\hbar\beta-\tau)(\hat{H}-\mu\hat{N}^F)/\hbar}\hat{A}e^{-\tau(\hat{H}-\mu\hat{N}^F)/\hbar}\hat{B} = \frac{1}{Z}\mathrm{Tr}\, Y(\hbar\beta-\tau)\hat{A}Y(\tau)\hat{B}, \tag{4.79}$$

where we have defined the imaginary time evolution operator $Y(\tau) = e^{-\tau(\hat{H}-\mu\hat{N}^F)/\hbar}$. These functions will be linear combinations of correlation function on the form $\mathrm{Tr}\, Y(\hbar\beta-\tau)\hat{\psi}_i^\dagger\hat{\psi}_j Y(\tau)\hat{\psi}_k^\dagger\hat{\psi}_l/Z$, again possibly with some field operators replaced with bosonic fields. Again, we will make a modification with an error of order $1/N$, and replace these functions with $\mathrm{Tr}\, Y(\hbar\beta-\tau)\hat{\psi}_i^\dagger Y(\Delta\tau)\hat{\psi}_j Y(\tau)\hat{\psi}_k^\dagger Y(\Delta\tau)\hat{\psi}_l/Z$, where $\Delta\tau = \hbar\beta/N$.

By introducing the factorization $Y(\tau) = Y(\Delta\tau)^N \approx (I - \tau(\hat{H}-\mu\hat{N}^F)/\hbar)^N$, we see that these expressions can be converted to field integrals by exactly the same technique that we employed in Section 3.1, and in our discussion of real time four point functions above. Going through with the procedure, we eventually end up with the expression

$$\frac{1}{Z}\mathrm{Tr}\, Y(\hbar\beta-\tau)\hat{\psi}_i^\dagger\hat{\psi}_j Y(\tau)\hat{\psi}_k^\dagger\hat{\psi}_l \approx \langle\bar{\psi}_i(\tau+\Delta\tau)\psi_j(\tau)\bar{\psi}_k(\Delta\tau)\psi_l(0)\rangle_\tau, \tag{4.80}$$

where the imaginary time field expectation $\langle\ \rangle_\tau$ is defined through

$$\langle X[\phi,\psi]\rangle_\tau = \frac{1}{Z}\int D(\phi,\psi)X[\phi,\psi]e^{-S^\tau[\phi,\psi]/\hbar} = \frac{\int D(\phi,\psi)X[\phi,\psi]e^{-S^\tau[\phi,\psi]/\hbar}}{\int D(\phi,\psi)\, e^{-S^\tau[\phi,\psi]/\hbar}}, \tag{4.81}$$

with the imaginary time action S^τ given by

$$\begin{aligned} -\frac{1}{\hbar}S^\tau[\phi,\psi] &= -|\boldsymbol{\phi}_0|^2 - \bar{\boldsymbol{\psi}}_0\boldsymbol{\psi}_0 + \boldsymbol{\phi}_N^\dagger\boldsymbol{\phi}_0 - \bar{\boldsymbol{\psi}}_N\boldsymbol{\psi}_0 - \\ &\frac{1}{\hbar}\sum_{n=0}^{N-1}\left\{\hbar\boldsymbol{\phi}_{n+1}^\dagger(\boldsymbol{\phi}_{n+1}-\boldsymbol{\phi}_n) + \hbar\bar{\boldsymbol{\psi}}_{n+1}(\boldsymbol{\psi}_{n+1}-\boldsymbol{\psi}_n) + \Omega(\boldsymbol{\phi}_{n+1}^\dagger,\boldsymbol{\phi}_n,\bar{\boldsymbol{\psi}}_{n+1},\boldsymbol{\psi}_n)\Delta\tau\right\} \\ &\approx -\frac{1}{\hbar}\int_0^{\hbar\beta}\mathrm{d}\tau\,\left(\hbar\boldsymbol{\phi}^\dagger\dot{\boldsymbol{\phi}} + \hbar\bar{\boldsymbol{\psi}}\dot{\boldsymbol{\psi}} + \Omega(\boldsymbol{\phi}^\dagger,\boldsymbol{\phi},\bar{\boldsymbol{\psi}},\boldsymbol{\psi})\right), \end{aligned} \tag{4.82}$$

where $\Omega(\boldsymbol{\phi}^\dagger, \boldsymbol{\phi}, \bar{\boldsymbol{\psi}}, \boldsymbol{\psi}) = H(\boldsymbol{\phi}^\dagger, \boldsymbol{\phi}, \bar{\boldsymbol{\psi}}, \boldsymbol{\psi}) - \mu\bar{\boldsymbol{\psi}}\boldsymbol{\psi}$. Again the integral expression in the final line must be considered a purely symbolic notation.

Using (4.80) and (4.77), any imaginary time correlation function can be expressed as an imaginary time field integral. By the discussion of Section 4.2.4, techniques of analytical continuation can be used to obtain transport coefficients from these correlation functions. Imaginary time field integrals is a major subject of Ref. [2].

Chapter 5

Non-equilibrium Green's functions

In the previous two chapters, we focused on exact expressions for transport coefficients (in the limit $N \to \infty$). In order to evaluate these expressions, one must almost always apply some technique of approximation. One of the most commonly applied approximation schemes, perturbation theory, is the subject of this chapter. We will limit the discussion to the perturbative expansion of Green's functions, and leave the discussion of four point functions to the literature. See for instance the Bethe Salpeter Equation[2]. In addition, we limit the discussion to the fermionic sector.

The derivations of this chapter primarily follows Altland and Simons[2], and to some extent also Jacoboni[15]. On the other hand, much of the notational conventions are taken from Datta[7].

5.1 Perturbative expansion of the field integral

The effective action S^{eff} is given by (3.62), where the sub-terms can be obtained from (3.115), (3.116), (3.48), (3.17) and (3.21). Examining these expressions, we observe that all terms in S^{eff} are quadratic in the fields, except possibly for those stemming from the Hamiltonian $H(\boldsymbol{\phi}^\dagger, \boldsymbol{\phi}, \bar{\boldsymbol{\psi}}, \boldsymbol{\psi})$. Further, by making use of a technique known as the Hubbard Stratonovich transformation [2], we can remove all terms in the Hamiltonian that are of higher order in the fermionic fields, at the cost of introducing additional bosonic fields. Thus, assuming that this technique has been applied, we can write the effective action as

$$S^{\text{eff}}[\phi, \psi] = \boldsymbol{\phi}^\dagger A_0 \boldsymbol{\phi} + \bar{\boldsymbol{\psi}}[C_0 + C(\boldsymbol{\phi})]\boldsymbol{\psi} + S^{B,\text{int}}[\phi], \tag{5.1}$$

where $C(\boldsymbol{\phi})$ contains no constant terms, and where as indicated $S^{B,\text{int}}$ depends only on the bosonic fields, and contains all such terms in the Hamiltonian which are of order higher than quadratic.

We now define $S_0 = \boldsymbol{\phi}^\dagger A_0 \boldsymbol{\phi} + \bar{\boldsymbol{\psi}} C_0 \boldsymbol{\psi}$ and $S^{\text{int}} = S^{B,\text{int}} + \bar{\boldsymbol{\psi}} C(\boldsymbol{\phi})\boldsymbol{\psi}$, so that we can write $S^{\text{eff}} = S_0 + S^{\text{int}}$. From (3.61) we then obtain the expansion

$$\begin{aligned} \langle A \rangle &= \int D(+,-) A[\phi, \psi] e^{iS_0/\hbar} e^{iS^{\text{int}}/\hbar} \\ &= \sum_n \frac{1}{n!} \int D(+,-) A[\phi, \psi] \left(iS^{\text{int}}/\hbar\right)^n e^{iS_0/\hbar}. \end{aligned} \tag{5.2}$$

In particular, the fermionic Green's function G introduced in Section 3.3.1 has the perturbative expansion

$$i\hbar G = \langle \boldsymbol{\psi} \bar{\boldsymbol{\psi}} \rangle = \sum_n \frac{1}{n!} \int D(+,-) \boldsymbol{\psi} \bar{\boldsymbol{\psi}} \left(iS^{\text{int}}/\hbar\right)^n e^{iS_0/\hbar}. \tag{5.3}$$

5.1.1 Unperturbed Green's functions

The first term in the expansion of the Green's function is the Green's function corresponding to the quadratic action S_0. It is referred to as the unperturbed Green's function, and is given by

$$i\hbar g = \langle \boldsymbol{\psi}\bar{\boldsymbol{\psi}}\rangle_0 = \int D(+,-)\boldsymbol{\psi}\bar{\boldsymbol{\psi}}e^{iS_0/\hbar} = \iint \mathbf{d}\bar{\boldsymbol{\psi}}\mathbf{d}\boldsymbol{\psi}\,\boldsymbol{\psi}\bar{\boldsymbol{\psi}}e^{-\bar{\boldsymbol{\psi}}C_0\boldsymbol{\psi}/\hbar i}, \quad \text{and} \tag{5.4}$$

$$i\hbar d = \langle \boldsymbol{\phi}\boldsymbol{\phi}^\dagger\rangle_0 = \int D(+,-)\boldsymbol{\phi}\boldsymbol{\phi}^\dagger e^{iS_0/\hbar} = \iint \mathbf{d}\boldsymbol{\phi}^\dagger\mathbf{d}\boldsymbol{\phi}\,\boldsymbol{\phi}\boldsymbol{\phi}^\dagger e^{-\boldsymbol{\phi}^\dagger A_0\boldsymbol{\phi}/\hbar i}, \tag{5.5}$$

for fermions and bosons respectively. As these expressions are Gaussian integrals, they can be evaluated in the same manner as the lead Green's functions in Section 3.3.1. Completely analogously to (3.65) and (3.66) we simply get $g = C_0^{-1}$ and $d = A_0^{-1}$.

To proceed further we write the matrix C_0 as

$$C_0 = C_S - \sum_p \Sigma_p, \tag{5.6}$$

where $\bar{\boldsymbol{\psi}}C_S\boldsymbol{\psi}$ contains all quadratic fermionic terms of S_S, and $\bar{\boldsymbol{\psi}}\Sigma_p\boldsymbol{\psi} = -S_p^{F,\text{eff}}$. Here S_S and $S_p^{F,\text{eff}}$ are respectively given by (3.48) and (3.115).

Now consider a system identical to the one considered above, but isolated from the leads. By repeating the arguments above, it should be clear that the unperturbed Green's function g_S of this system is given by $g_S = C_S^{-1}$. Further, since g_S is the Green's function of an isolated non-interacting system, it must satisfy (3.90) and (3.91). Thus, let $\hat{\boldsymbol{\psi}}^\dagger H_S^F\boldsymbol{\psi}$ be the quadratic and fermionic sector of the Hamiltonian $\hat{H}_S$ of the system S. Since by (3.41) $T = 0$, we get from (3.90) and (3.91) respectively

$$i\hbar g_S^<(t,t') = 0 \qquad \text{and} \qquad i\hbar g_S^>(t,t') = e^{iH_S^F(t'-t)/\hbar}. \tag{5.7}$$

Inserting this in (3.83) and (3.84), we also find

$$i\hbar g_S^t(t,t') = e^{iH_S^F(t'-t)/\hbar}\theta(t-t') \quad \text{and,} \tag{5.8}$$

$$i\hbar g_S^{\bar{t}}(t,t') = e^{iH_S^F(t'-t)/\hbar}\theta(t'-t). \tag{5.9}$$

Using the relations $g = C_0^{-1}$ and $g_S = C_S^{-1}$, we have by (5.6)

$$g = (C_S - \Sigma_l)^{-1} = (I - g_S\Sigma_l)^{-1}\, g_S, \tag{5.10}$$

where $\Sigma_l = \sum_p \Sigma_p$. Like the Green's functions, the matrices Σ_p are also naturally divided into four sectors. By (3.115), (3.101) and (3.102), we have

$$\Sigma_{p,nm} = \Delta t^2 \frac{i}{h}\int \mathrm{d}E \begin{bmatrix} f_p(E)\Gamma_p^F(E) - i\Sigma_p^r(E) & -f_p(E)\Gamma_p^F(E) \\ (1-f_p(E))\,\Gamma_p^F(E) & f_p(E)\Gamma_p^F(E) + i\Sigma_p^a(E) \end{bmatrix} e^{-i(t-t')E/\hbar}, \tag{5.11}$$

with $t = n\Delta t$ and $t' = m\Delta t$.

5.1.2 Interaction terms and Feynman diagrams

Since the interaction terms in $S^{\text{int}} = S^{B,\text{int}} + \bar{\boldsymbol{\psi}} C(\boldsymbol{\phi})\boldsymbol{\psi}$ stem from the Hamiltonian, we can by (3.48), (3.17) and (3.21) write these terms as

$$S^{B,\text{int}} = \sum_{n=0}^{N-1} \Delta t \left(U(\boldsymbol{\phi}_n^{-\dagger}, \boldsymbol{\phi}_{n+1}^{-}) - U(\boldsymbol{\phi}_{n+1}^{+\dagger}, \boldsymbol{\phi}_n^{+}) \right), \quad \text{and} \tag{5.12}$$

$$\bar{\boldsymbol{\psi}} C(\boldsymbol{\phi}^\dagger, \boldsymbol{\phi})\boldsymbol{\psi} = \sum_{n=0}^{N-1} \Delta t \left(\bar{\boldsymbol{\psi}}_n^{-} V(\boldsymbol{\phi}_n^{-\dagger}, \boldsymbol{\phi}_{n+1}^{-})\boldsymbol{\psi}_{n+1}^{-} - \bar{\boldsymbol{\psi}}_{n+1}^{+} V(\boldsymbol{\phi}_{n+1}^{+\dagger}, \boldsymbol{\phi}_n^{+})\boldsymbol{\psi}_n^{+} \right), \tag{5.13}$$

where U and V are potentials representing the non-quadratic terms in the Hamiltonian. These can be Taylor expanded as

$$U(\boldsymbol{\phi}^\dagger, \boldsymbol{\phi}) = \sum_{n+m>2} \frac{\partial^n \partial^m U}{\partial^n \boldsymbol{\phi}^\dagger \partial^m \boldsymbol{\phi}} \boldsymbol{\phi}_1^\dagger \cdots \boldsymbol{\phi}_n^\dagger \boldsymbol{\phi}_1 \cdots \boldsymbol{\phi}_m, \quad \text{and} \tag{5.14}$$

$$V(\boldsymbol{\phi}^\dagger, \boldsymbol{\phi}) = \sum_{n+m>0} \frac{\partial^n \partial^m V}{\partial^n \boldsymbol{\phi}^\dagger \partial^m \boldsymbol{\phi}} \boldsymbol{\phi}_1^\dagger \cdots \boldsymbol{\phi}_n^\dagger \boldsymbol{\phi}_1 \cdots \boldsymbol{\phi}_m, \tag{5.15}$$

where we made use of the assumption that S^{int} contains no quadratic terms. For reasons of concreteness and simplicity, we will in the following make approximations to the lowest order, and keep only a third order term in U and a linear term in V. In particular, we let

$$U(\boldsymbol{\phi}^\dagger, \boldsymbol{\phi}) = \sum_{ijk} U_{ijk} (\phi_i + \phi_i^\star)(\phi_j + \phi_j^\star)(\phi_k + \phi_k^\star), \quad \text{and} \tag{5.16}$$

$$V_{ij}(\boldsymbol{\phi}^\dagger, \boldsymbol{\phi}) = \sum_{ijk} V_{ij}^k \left(\phi_k + \phi_k^\star\right), \tag{5.17}$$

so that

$$S^{B,\text{int}} = \sum_{n=0}^{N-1} \sum_{ijk} \Delta t U_{ijk} \Big\{ (\phi_{n+1,i}^{-} + \phi_{ni}^{-\star})(\phi_{n+1,j}^{-} + \phi_{nj}^{-\star})(\phi_{n+1,k}^{-} + \phi_{nk}^{-\star}) \tag{5.18}$$
$$- (\phi_{ni}^{+} + \phi_{n+1,i}^{+\star})(\phi_{nj}^{+} + \phi_{n+1,j}^{+\star})(\phi_{nk}^{+} + \phi_{n+1,k}^{+\star}) \Big\},$$

and

$$\bar{\boldsymbol{\psi}} C(\boldsymbol{\phi}^\dagger, \boldsymbol{\phi})\boldsymbol{\psi} = \sum_{n=0}^{N-1} \sum_{ijk} \Delta t V_{ij}^k \times \tag{5.19}$$
$$\left(\bar{\psi}_{in}^{-} \left(\phi_{n+1,k}^{-} + \phi_{nk}^{-\star} \right) \psi_{j,n+1}^{-} - \bar{\psi}_{i,n+1}^{+} \left(\phi_{nk}^{+} + \phi_{n+1,k}^{+\star} \right) \psi_{jn}^{+} \right).$$

Now, by (5.3) we have

$$i\hbar G = \sum_n \frac{i^n}{n! \hbar^n} \left\langle \boldsymbol{\psi} \bar{\boldsymbol{\psi}} \left(S^{B,\text{int}} + \bar{\boldsymbol{\psi}} C(\boldsymbol{\phi}^\dagger, \boldsymbol{\phi})\boldsymbol{\psi} \right)^n \right\rangle_0, \tag{5.20}$$

where $\langle\,\rangle_0$ denotes the field integral expectation with respect to the unperturbed action S_0. Using (5.18) and (5.19) we can express the n'th order expectation as

$$\begin{aligned}&\left\langle \boldsymbol{\psi}\bar{\boldsymbol{\psi}}\left(S^{B,\mathrm{int}}+\bar{\boldsymbol{\psi}}C(\boldsymbol{\phi}^\dagger,\boldsymbol{\phi})\boldsymbol{\psi}\right)^n\right\rangle_0 \\ &=\sum \Delta t^n\, U_{abc}\cdots U_{def}\;V^i_{gh}\cdots V^l_{jk}\left\langle \phi^\star_a\cdots\phi^\star_b\;\phi_c\cdots\phi_d\;\bar\psi_e\psi_f\cdots\bar\psi_g\psi_h\right\rangle_0,\end{aligned} \tag{5.21}$$

where the sum runs over all terms in S^{int} in each of the n factors. The potential factors U_{abc}, V^i_{gh} and so on in this expression must be interpreted as having an additional negative sign if they are coupled to the forward propagating fields ϕ^+ and ψ^+. The field product expectation values in (5.21) are again just Gaussian integrals, and in fact it can be shown that[2]

$$\begin{aligned}&\left\langle \phi^\star_{i_1}\cdots\phi^\star_{i_n}\;\phi_{j_1}\cdots\phi_{j_m}\;\bar\psi_{k_1}\psi_{l_1}\cdots\bar\psi_{k_p}\psi_{l_p}\right\rangle_0 \\ &=\sum_{\sigma^B\sigma^F}(-1)^{\sigma^F}\left\langle\phi^\star_{i_1}\phi_{j_{\sigma^B_1}}\right\rangle_0\cdots\left\langle\phi^\star_{i_n}\phi_{j_{\sigma^B_n}}\right\rangle_0\left\langle\bar\psi_{k_1}\psi_{l_{\sigma^F_1}}\right\rangle_0\cdots\left\langle\bar\psi_{k_p}\psi_{l_{\sigma^F_p}}\right\rangle_0\end{aligned} \tag{5.22}$$

if $n=m$, and zero otherwise. Here σ^B and σ^F denote permutations of respectively n and p elements, and $(-1)^{\sigma^F}$ denotes the sign of the permutation σ^F. Using 5.22 we can express (5.21) as

$$\begin{aligned}&\left\langle \boldsymbol{\psi}\bar{\boldsymbol{\psi}}\left(S^{B,\mathrm{int}}+\bar{\boldsymbol{\psi}}C(\boldsymbol{\phi}^\dagger,\boldsymbol{\phi})\boldsymbol{\psi}\right)^n\right\rangle_0 \\ &=\sum(-1)^{\sigma^F}\Delta t^n\,U_{abc}\cdots U_{def}\;V^i_{gh}\cdots V^l_{jk}\left\langle\phi^\star_a\phi_b\right\rangle_0\cdots\left\langle\phi^\star_c\phi_d\right\rangle_0\left\langle\bar\psi_e\psi_f\right\rangle_0\cdots\left\langle\bar\psi_g\psi_h\right\rangle_0 \\ &=\sum(-1)^{\sigma^F}\Delta t^n\,U_{abc}\cdots U_{def}\;V^i_{gh}\cdots V^l_{jk}\,(i\hbar d_{ba})\cdots(i\hbar d_{dc})\,(-i\hbar g_{fe})\cdots(-i\hbar g_{hg}),\end{aligned} \tag{5.23}$$

where the sum is now also over the permutations σ^B and σ^F. Then inserting this in (5.20), we obtain

$$\begin{aligned}i\hbar G=\sum\frac{(-1)^x\Delta t^n}{\hbar^n n!}\times& \\ iU_{abc}\cdots iU_{def}iV^i_{gh}\cdots iV^l_{jk}(i\hbar d_{ba})\cdots(i\hbar d_{dc})\,(i\hbar g_{fe})\cdots(i\hbar g_{hg}).&\end{aligned} \tag{5.24}$$

The terms of this sum has a useful representation in the form of diagrams/ graphs. Note that each index except for two will be shared between a potential factor and a Green's function. The two remaining indices are the ones stemming from the product $\boldsymbol{\psi}\bar{\boldsymbol{\psi}}$, and accordingly these are not shared by a potential factor. Thus, each term can be represented by a diagram where the lines represent unperturbed Green's functions, and the vertices represent potential factors. The convention is then that indices of vertices are shared with the lines intersecting them. Thus, each vertex must be an intersection of either three boson lines, or two fermion lines and one boson line, and there can only be two line endpoints not intersecting a vertex. These diagrams are know as Feynman diagrams, and are extensively described in the literature[2, 15, 7, 23, 27].

Since all the potential and Green's function factors would be identical, it is easy to see that terms corresponding to the same diagram must have identical

values except possibly for the sign. However, as it turns out even the sign can be determined from the diagram. It is clear that the fermion lines of the diagram must be organized in one path connecting the two free end points of the diagram, and that the remainder of the fermion lines must form a set of loops. In fact, the sign of a term corresponding to some diagram is simply $(-1)^l$, where l is the number of fermion loops in the diagram[15, 23, 27].

Thus, two terms in (5.23) have the same value if their Feynman diagrams are topologically identical, i.e. if they can be made identical by a continuous transformation. Further, as shown for instance by Jacoboni[15], all terms in (5.24) which correspond to Feynman diagrams that are not connected, end up canceling, and can accordingly be omitted from the sum. Finally, it is also shown in the literature[2, 15] that for any connected Feynman diagram with n vertices, there is exactly $n!$ terms in (5.24) which corresponds to that diagram.

Thus, by the previous two paragraphs, we can omit the terms having disconnected diagrams, perform the sums over the $n!$ terms corresponding to the same diagrams, and finally write (5.24) as

$$i\hbar G = \sum (-1)^l \frac{iU_{abc}\Delta t}{\hbar} \cdots \frac{iU_{def}\Delta t}{\hbar} \frac{iV^i_{gh}\Delta t}{\hbar} \cdots \frac{iV^l_{jk}\Delta t}{\hbar} \times (i\hbar d_{ba}) \cdots (i\hbar d_{dc}) (i\hbar g_{fe}) \cdots (i\hbar g_{hg}), \tag{5.25}$$

where the sum runs over all topologically distinct connected Feynman diagrams with two end points, l is the number of fermion loops in each particular diagram, and the potential factors and Green's functions are those represented by the vertices and lines respectively.

5.1.3 Self energy and the Dyson equation

We now define some terminology. A connected diagram is a diagram containing no isolated groups. A free index is an index on a vertex which is not connected to a Green's function line. A free index diagram is a connected diagram which has no free endpoints, but which has two free indices. A reducible diagram is a free index diagram that can be split into two components by removing a single Green's function line, in such a way that there is one of the original free indices on each new component. An irreducible diagram is a free index diagram that is not reducible.

Any diagram in the expansion (5.25) can be turned into a free index diagram by removing the two free endpoint lines. If the result is then a reducible diagram, a single Green's function line can be removed to obtain two components which are both free index diagrams. If any of these components are reducible, a single Green's function can again be removed to split also this component into two new free index diagrams. The process can be continued until one is left with a finite sequence of irreducible diagrams. Thus, the value of any diagram in (5.25) can be written as

$$D = (i\hbar g_{ij}) A_{jk} (i\hbar g_{kl}) B_{lm} \cdots (i\hbar g_{pq}) C_{qr} (i\hbar g_{rs}), \tag{5.26}$$

where A_{jk}, B_{lm}, $C_{qr}\cdots$ represent irreducible diagrams, j, k, l, m, q and r being the free indices. Thus, (5.25) can be written as

$$i\hbar G_{is} = \sum_{n=1}^{\infty} \sum_{A^1 A^2 \cdots A^n} (i\hbar g_{ij}) A^1_{jk} (i\hbar g_{kl}) A^2_{lm} \cdots (i\hbar g_{pq}) A^n_{qr} (i\hbar g_{rs}), \tag{5.27}$$

where the factors A^n_{ij} correspond to irreducible diagrams, and the second sum is over all such. We now define

$$\Sigma_{s,ij} = i\hbar \sum_{A} A_{ij}, \tag{5.28}$$

where the sum is over all irreducible diagrams. We refer to the matrix Σ_s as the scattering self energy, in order to distinguish it from the lead self energies Σ_p. Inserting (5.28) in (5.27), we get

$$i\hbar G_{is} = \sum_{n=1}^{\infty} \sum_{jklm\cdots pqr} i\hbar g_{ij} \Sigma_{s,jk} g_{kl} \Sigma_{s,lm} \cdots g_{pq} \Sigma_{s,qr} g_{rs} = i\hbar \sum_{n=1}^{\infty} \left[g(\Sigma_s g)^{n-1} \right]_{is}, \tag{5.29}$$

which can be reexpressed as

$$G = \sum_{n=0}^{\infty} g(\Sigma_s g)^n = g + g\Sigma_s \sum_{n=0}^{\infty} g(\Sigma_s g)^n = g + g\Sigma_s G. \tag{5.30}$$

This equation is known as the Dyson equation[2, 15]. With some simple rearrangement it can also be expressed as

$$G = (g^{-1} - \Sigma_s)^{-1} \tag{5.31}$$

Defining the total self energy $\Sigma = \Sigma_s + \Sigma_l$, we get by (5.10)

$$G = (C_S - \Sigma_l - \Sigma_s)^{-1} = (g_S^{-1} - \Sigma)^{-1} = (I - g_S\Sigma)^{-1} g_S. \tag{5.32}$$

5.2 The NEGF equations

5.2.1 Dyson equation as a difference equation

Making use of the last expression in (5.32), we can rewrite the Dyson equation as $(I - g_S\Sigma)G = g_S$. If we explicitly include the block structure corresponding to time arguments, this becomes

$$G_{nm} - \sum_{l=0}^{N-1} \sum_{p=0}^{N-1} g_{,Snl} \Sigma_{lp} G_{pm} = g_{S,nm}. \tag{5.33}$$

Making use of (5.7)-(5.9) it is easy to show that $g^{<}_{S,nm} = 0$, $g^{>}_{S,nm} = e^{-iH_S^F \Delta t/\hbar} g^{>}_{S,n-1,m}$, $g^{t}_{S,nm} = e^{-iH_S^F \Delta t/\hbar} g^{t}_{S,n-1,m} - \frac{i}{\hbar}\delta_{nm}$ and $g^{\bar{t}}_{S,nm} = e^{-iH_S^F \Delta t/\hbar} g^{\bar{t}}_{S,n-1,m} + \frac{i}{\hbar}\delta_{n-1,m}$. If we define matrices

$$M = \begin{bmatrix} e^{-iH_S^F \Delta t/\hbar} & 0 \\ 0 & e^{-iH_S^F \Delta t/\hbar} \end{bmatrix}, \quad P = \begin{bmatrix} I & 0 \\ 0 & 0 \end{bmatrix}, \quad \text{and} \quad Q = \begin{bmatrix} 0 & 0 \\ 0 & I \end{bmatrix}, \tag{5.34}$$

these relations can be combined in a single matrix expression as

$$M g_{S,n-1,m} = g_{S,nm} + \frac{i}{\hbar}(P\delta_{nm} - Q\delta_{n-1,m}). \tag{5.35}$$

Now making use of (5.35) and (5.33) to evaluate $MG_{n-1,m} - G_{nm}$, we obtain the difference equation

$$MG_{n-1,m} - G_{nm} - \frac{i}{\hbar}\sum_{l=0}^{N-1}(P\Sigma_{nl} - Q\Sigma_{n-1,l})G_{lm} = \frac{i}{\hbar}(P\delta_{nm} - Q\delta_{n-1,m}). \tag{5.36}$$

Since we are interested in the limit $N \to \infty$, we can expand M to the first order in Δt, to get

$$M \approx I - iH_S^{FF}\Delta t/\hbar, \quad \text{where} \quad H_S^{FF} = \begin{bmatrix} H_S^F & 0 \\ 0 & H_S^F \end{bmatrix}. \tag{5.37}$$

Making use of this approximation, we can rewrite (5.36) as

$$\begin{aligned} \hbar i(G_{nm} - G_{n-1,m}) - \Delta t H_S^{FF} G_{n-1,m} \\ - \sum_{l=0}^{N-1}(P\Sigma_{nl} - Q\Sigma_{n-1,l})G_{lm} = P\delta_{nm} - Q\delta_{n-1,m}. \end{aligned} \tag{5.38}$$

5.2.2 Contributions to the self energy

Now consider the irreducible diagrams contributing to (5.28). These can be divided into two classes depending on whether or not the free indices sit on the same vertex. We will refer to diagrams where the free indices sit on the same vertex as single vertex diagrams, and those where they sit on different vertices as double vertex diagrams. In any single vertex diagram, the remaining index on the free vertex must be attached to a boson line. Analogously to (5.25), one can show that the sum of all connected diagrams with a single free boson end point is $\langle\phi_i\rangle$ or $\langle\phi_i^\star\rangle$ depending on the type of endpoint. Thus, summing over all single vertex diagrams we in fact obtain

$$\frac{i\Delta t}{\hbar}\sum_k V_{ij}^k \langle\phi_k + \phi_k^\star\rangle. \tag{5.39}$$

Examining (5.19) we see that the vertices always couple fields with the same superscript. Also keeping in mind the comment below (5.21), we express (5.39) in matrix form as

$$\frac{i\Delta t}{\hbar}\sum_k \begin{bmatrix} -V_{ij}^k\langle \phi_k^+ + \phi_k^{+\star}\rangle & 0 \\ 0 & V_{ij}^k\langle \phi_k^- + \phi_k^{-\star}\rangle \end{bmatrix}. \tag{5.40}$$

Further, essentially repeating the arguments leading to (3.35), we see that $\langle \phi_k^+\rangle = \langle \hat{\phi}_k\rangle = \langle \phi_k^-\rangle$. Accordingly, we write the sum of all single vertex diagrams as

$$-\frac{i\Delta t}{\hbar}\begin{bmatrix} \delta H^F(t) & 0 \\ 0 & -\delta H^F(t)\end{bmatrix} = -\frac{i\Delta t}{\hbar}(P-Q)\delta H^{FF}(t), \tag{5.41}$$

where

$$\delta H_{ij}^F(t) = \sum_k V_{ij}^k\langle \phi_k^+(t) + \phi_k^{+\star}(t)\rangle = \sum_k V_{ij}^k\langle \phi_k^-(t) + \phi_k^{-\star}(t)\rangle. \tag{5.42}$$

A diagram in the expansion of $\langle \phi_k\rangle$ must contain a free boson line connected to a vertex, connected to some diagram with two end points. Summing over all such diagrams, it should be clear that

$$\langle \phi_k\rangle = \sum_{lmn}(i\hbar d_{kl})U_{lmn}(i\hbar D_{mn}) + \sum_{lmn}(i\hbar d_{kl})V_{mn}^l(i\hbar G_{mn}). \tag{5.43}$$

Now we turn to the double vertex diagrams. Each one of the two free vertices in the diagram is connected to one free fermion line, and one free boson line. Thus, removing the two free vertices we are left with an irreducible diagram containing two free boson end points, and two free fermion end points. Since an analogue of (5.25) applies also to four point functions, we see that these diagrams are precisely the irreducible diagrams occurring in the expansion of the four point function

$$\left\langle \psi_i\bar{\psi}_j(\phi_k+\phi_k^\star)(\phi_l+\phi_l^\star)\right\rangle. \tag{5.44}$$

Accordingly, we denote the sum of all such diagrams $\left\langle \psi_i\bar{\psi}_j(\phi_k+\phi_k^\star)(\phi_l+\phi_l^\star)\right\rangle_{\mathrm{Irr}}$, so that summing over all double vertex diagrams we get

$$\frac{(i\Delta t)^2}{\hbar^2}\sum_{jklm} V_{ij}^kV_{mn}^l\left\langle \psi_j\bar{\psi}_m(\phi_k+\phi_k^\star)(\phi_l+\phi_l^\star)\right\rangle_{\mathrm{Irr}}. \tag{5.45}$$

Again making use of the comment below (5.21), as well as the fact that (5.19) only couples fields with the same superscript, we can express this in matrix form as

$$\frac{(i\Delta t)^2}{\hbar^2}\sum_{jklm} V_{ij}^kV_{mn}^l\begin{bmatrix} \left\langle \psi_j^+\bar{\psi}_m^+x_k^+x_l^+\right\rangle_{\mathrm{Irr}} & -\left\langle \psi_j^+\bar{\psi}_m^-x_k^+x_l^-\right\rangle_{\mathrm{Irr}} \\ -\left\langle \psi_j^-\bar{\psi}_m^+x_k^-x_l^+\right\rangle_{\mathrm{Irr}} & \left\langle \psi_j^-\bar{\psi}_m^-x_k^-x_l^-\right\rangle_{\mathrm{Irr}}\end{bmatrix}, \tag{5.46}$$

where we have defined $x_i(t) = \phi_i(t) + \phi_i^\star(t)$. Accordingly, we write the sum of all double vertex diagrams as

$$-\frac{i\Delta t^2}{\hbar}\Sigma_s(t,t') = -\frac{i\Delta t^2}{\hbar}\begin{bmatrix} \Sigma_s^t(t,t') & -\Sigma_s^<(t,t') \\ -\Sigma_s^>(t,t') & \Sigma_s^{\bar{t}}(t,t') \end{bmatrix}, \quad \text{where} \tag{5.47}$$

$$\Sigma_{s,in}^t(t,t') = -\frac{i}{\hbar}\sum_{jklm} V_{ij}^k V_{mn}^l \left\langle \psi_j^+(t)\bar{\psi}_m^+(t')x_k^+(t)x_l^+(t')\right\rangle_{\text{Irr}}, \tag{5.48}$$

$$\Sigma_{s,in}^<(t,t') = -\frac{i}{\hbar}\sum_{jklm} V_{ij}^k V_{mn}^l \left\langle \psi_j^+(t)\bar{\psi}_m^-(t')x_k^+(t)x_l^-(t')\right\rangle_{\text{Irr}}, \tag{5.49}$$

$$\Sigma_{s,in}^>(t,t') = -\frac{i}{\hbar}\sum_{jklm} V_{ij}^k V_{mn}^l \left\langle \psi_j^-(t)\bar{\psi}_m^+(t')x_k^-(t)x_l^+(t')\right\rangle_{\text{Irr}}, \quad \text{and} \tag{5.50}$$

$$\Sigma_{s,in}^{\bar{t}}(t,t') = -\frac{i}{\hbar}\sum_{jklm} V_{ij}^k V_{mn}^l \left\langle \psi_j^-(t)\bar{\psi}_m^-(t')x_k^-(t)x_l^-(t')\right\rangle_{\text{Irr}}. \tag{5.51}$$

An important approximation to these expressions is the self consistent Born approximation[2], where one makes the approximation

$$\left\langle \psi_j\bar{\psi}_m x_k x_l\right\rangle_{\text{Irr}} \approx \left\langle \psi_j\bar{\psi}_m\right\rangle\left\langle x_k x_l\right\rangle = -\hbar^2 G_{jm}(D_{kl} - D_{lk}^\star). \tag{5.52}$$

This expression can be further approximated by replacing the full Green's functions with the unperturbed ones, so that $\left\langle \psi_j\bar{\psi}_m x_k x_l\right\rangle_{\text{Irr}} \approx -\hbar^2 g_{jm}(d_{kl} - d_{kl}^\star)$. The latter is referred to simply as the Born approximation.

5.2.3 Continuum limit

Now, inserting the sum of all single vertex diagrams (5.41), and the sum of all double vertex diagrams (5.47) in (5.28), we get

$$\Sigma_{s,nm} = \Delta t\,(P-Q)\delta H^{FF}(t)\delta_{nm} + \Delta t^2\Sigma_s(t,t'), \tag{5.53}$$

where $t = n\Delta t$ and $t' = m\Delta t$. Combining this with the definition of the total self energy Σ above (5.32), we have

$$\Sigma_{nm} = \Delta t\,(P-Q)\delta H^{FF}(t)\delta_{nm} + \Delta t^2\Sigma(t,t'), \tag{5.54}$$

where

$$\Sigma(t,t') = \Sigma_s(t,t') + \sum_p \frac{\Sigma_{p,nm}}{\Delta t^2}, \tag{5.55}$$

with Σ_{pnm} given by (5.11). Inserting (5.54) in (5.38), we obtain

$$\begin{aligned} &\hbar i(G_{nm} - G_{n-1,m}) - \Delta t H_S^{FF} G_{n-1,m} \\ &-\Delta t P\delta H^{FF}(n\Delta t)G_{nm} - \Delta t Q\delta H^{FF}(n\Delta t - \Delta t)G_{n-1,m} \\ &-\Delta t^2\sum_{l=0}^{N-1}(P\Sigma(n\Delta t, l\Delta t) - Q\Sigma(n\Delta t - \Delta t, l\Delta t))G_{lm} = P\delta_{nm} - Q\delta_{n-1,m}. \end{aligned} \tag{5.56}$$

Note that the order of this equation is $1/N$, except near $n = m$, where it is of order N^0. So consider the expression $\Delta t P(\delta H^{FF}(n\Delta t)G_{nm} - \delta H^{FF}(n\Delta t - \Delta t)$ $G_{n-1,m})$. Since δH is differentiable as a function of time, and G is differentiable everywhere except at $t = t'$, the expression must be of order $1/N^2$ everywhere except at $n = m$, where it is of order $1/N$. Thus, the expression is always of higher order than (5.56), and so it can be added to the left side of the equation without changing the order of the approximation. Similarly, the expression

$$\Delta t^2 \sum_{l=0}^{N-1} Q(\Sigma(n\Delta t, l\Delta t) - \Sigma(n\Delta t - \Delta t, l\Delta t))G_{lm} \tag{5.57}$$

is also of order $1/N^2$, since Σ is differentiable everywhere except at $t = t'$. Thus, this expression can also be added to the left side of (5.56). Making both of these modifications, we obtain

$$\begin{aligned} &\hbar i(G_{nm} - G_{n-1,m}) - \Delta t H_C^{FF}(n\Delta t - \Delta t)G_{n-1,m} \\ &\qquad -\Delta t^2 \sum_{l=0}^{N-1} (P - Q)\Sigma(n\Delta t, l\Delta t)G_{lm} = P\delta_{nm} - Q\delta_{n-1,m}, \end{aligned} \tag{5.58}$$

where we have defined $H_C^{FF}(t) = H_S^{FF} + \delta H^{FF}(t)$.

Multiplying (5.58) by $(P - Q)/\Delta t$, and then finally taking the continuum limit $\Delta t \to 0$, we obtain the integro-differential equation

$$(P - Q)\left(\hbar i \frac{\partial G}{\partial t}(t, t') - H_C^{FF}(t)G(t, t')\right) - \int_{t_0}^{t_f} \mathrm{d}t''\, \Sigma(t, t'')G(t'', t') = \delta(t - t'), \tag{5.59}$$

If one is to obtain the strictly correct continuum limit of (5.58), one must take care to make the appropriate interpretation of the delta function in this expression. Indeed, adopting the standard interpretation of the delta function will result in slightly modified Green's functions where the step functions θ in (3.83) and (3.84) are replaced with step functions $\tilde{\theta}$, with $\tilde{\theta}(0) = 1/2$ rather than 1. However, since this modification only affects the time ordered and anti time ordered Green's functions at $t = t'$, and since $G^t(t, t)$ and $G^{\bar{t}}(t, t)$ are never used in the calculation of expectation values, this consideration is not so important in practice. Thus, we will in fact make the modification $\theta \to \tilde{\theta}$ to the Green's functions discussed in the remainder of the chapter.

We now assume the existence of a finite correlation time τ such that $\Sigma(t, t') \approx 0$ for $|t - t'| \gg \tau$. This allows us to replace the limits on the integral in (5.59) with $\pm\infty$, thereby obtaining

$$\begin{bmatrix} \hbar i\partial_t - H_C^F(t) & 0 \\ 0 & -\hbar i\partial_t + H_C^F(t) \end{bmatrix} G(t, t') - \int_{-\infty}^{\infty} \mathrm{d}t''\, \Sigma(t, t'')G(t'', t') = \delta(t - t'), \tag{5.60}$$

where we have defined the corrected Hamiltonian $H_C^F(t) = H_S^F + \delta H^F(t)$, and introduced the short notation $\partial_t = \partial/\partial t$. Similar equations can be found in the literature[2, 15].

5.2.4 Energy representation

Now we make use of the assumption that the system approaches a steady state, so that for $t \gg t_0$ all functions depend only on the argument difference $t - t'$. Thus, $H_C^F(t)$ becomes a constant H_C^F, while G and Σ become functions $G(t-t')$ and $\Sigma(t-t')$. We define energy representations of these functions as Fourier transforms, i.e. we let

$$G(E) = \int_{-\infty}^{\infty} \mathrm{d}t\, G(t-t') e^{iE(t-t')/\hbar}, \tag{5.61}$$

while analogous expressions define $\Sigma(E)$, as well as the component functions $\Sigma_p(E)$, $\Sigma^<(E)$, $G^t(E)$ and so on. Making use of the inverse Fourier transform, we can invert these relationships, obtaining

$$G(t-t') = \frac{1}{h} \int_{-\infty}^{\infty} \mathrm{d}E\, G(E) e^{-iE(t-t')/\hbar}, \tag{5.62}$$

and similar for the other functions.

Taking the Fourier transform of (5.55) and making use of the block decompositions of (5.47) and (5.11), we obtain the relationship

$$\Sigma(E) = \begin{bmatrix} \Sigma^t(t,t') & -\Sigma^<(t,t') \\ -\Sigma^>(t,t') & \Sigma^{\bar{t}}(t,t') \end{bmatrix} \tag{5.63}$$

where

$$\Sigma^t(E) = \Sigma_s^t(E) + \sum_p \left(i f_p(E) \Gamma_p^F(E) + \Sigma_p^r(E) \right), \tag{5.64}$$

$$\Sigma^<(E) = \Sigma_s^<(E) + i \sum_p f_p(E) \Gamma_p^F(E) \tag{5.65}$$

$$\Sigma^>(E) = \Sigma_s^>(E) + i \sum_p \left(f_p(E) - 1 \right) \Gamma_p^F(E), \quad \text{and} \tag{5.66}$$

$$\Sigma^{\bar{t}}(E) = \Sigma_s^{\bar{t}}(E) + \sum_p \left(i f_p(E) \Gamma_p^F(E) - \Sigma_p^a(E) \right). \tag{5.67}$$

Finally, inserting the inverse Fourier transform of $\Sigma(E)$ in (5.60), and then Fourier transforming the entire equation, we obtain

$$\begin{bmatrix} E - H_C^F & 0 \\ 0 & -E + H_C^F \end{bmatrix} G(E) - \Sigma(E) G(E) = I, \tag{5.68}$$

the energy representation of the Dyson equation.

5.2.5 Component Green's functions

Making use of (3.81)-(3.84), one easily shows that $G^<(t,t')^\dagger = -G^<(t',t)$, $G^>(t,t')^\dagger = -G^>(t',t)$ and $G^t(t,t')^\dagger = -G^{\bar{t}}(t',t)$. Fourier transforming these

relations, we obtain $G^<(E)^\dagger = -G^<(E)$, $G^>(E)^\dagger = -G^>(E)$, and $G^t(E)^\dagger = -G^{\bar{t}}(E)$. Further, adding (3.83) and (3.84), and keeping in mind the modification $\theta \to \tilde{\theta}$, we get $G^t(t,t') + G^{\bar{t}}(t,t') = G^<(t,t') + G^>(t,t')$. Fourier transforming this we obtain

$$G^t(E) + G^{\bar{t}}(E) = G^<(E) + G^>(E). \tag{5.69}$$

Now we define new Green's functions

$$G^r(E) = G^t(E) - G^<(E), \quad \text{and} \tag{5.70}$$
$$G^a(E) = G^t(E) - G^>(E), \tag{5.71}$$

which we refer to respectively as the retarded and advanced Green's functions. Making use of (5.69) and the other relations of the previous paragraph, we can also express these functions as

$$G^r(E) = G^>(E) - G^{\bar{t}}(E), \qquad \text{and} \tag{5.72}$$
$$G^a(E) = G^<(E) - G^{\bar{t}}(E) = G^r(E)^\dagger. \tag{5.73}$$

Analogously to (5.70) and (5.71), we also define retarded and advanced self energies respectively as

$$\Sigma^r(E) = \Sigma^t(E) - \Sigma^<(E), \quad \text{and} \tag{5.74}$$
$$\Sigma^a(E) = \Sigma^t(E) - \Sigma^>(E). \tag{5.75}$$

Similar expressions define the scattering self energies $\Sigma_s^r(E)$ and $\Sigma_s^a(E)$.

Inserting the block decompositions of G and Σ given by (3.68) and (5.63) in (5.68), we get

$$\begin{bmatrix} E - H_C^F - \Sigma^t(E) & \Sigma^<(E) \\ \Sigma^>(E) & -E + H_C^F - \Sigma^{\bar{t}}(E) \end{bmatrix} \begin{bmatrix} G^t(E) & G^<(E) \\ G^>(E) & G^{\bar{t}}(E) \end{bmatrix} = \begin{bmatrix} I & 0 \\ 0 & I \end{bmatrix}, \tag{5.76}$$

or in terms of the component functions,

$$\big(E - H_C^F - \Sigma^t(E)\big)\, G^t(E) + \Sigma^<(E) G^>(E) = I, \tag{5.77}$$
$$\big(E - H_C^F - \Sigma^t(E)\big)\, G^<(E) + \Sigma^<(E) G^{\bar{t}}(E) = 0, \tag{5.78}$$
$$\Sigma^>(E) G^t(E) + \big(- E + H_C^F - \Sigma^{\bar{t}}(E)\big) G^>(E) = 0, \quad \text{and} \tag{5.79}$$
$$\Sigma^>(E) G^<(E) + \big(- E + H_C^F - \Sigma^{\bar{t}}(E)\big) G^{\bar{t}}(E) = I. \tag{5.80}$$

Subtracting the first two of these equations, and then making use of (5.70), (5.72) and (5.74), we obtain $\big(E - H_C^F - \Sigma^r(E)\big)\, G^r(E) = I$, and upon inverting

$$G^r(E) = \big(E - H_C^F - \Sigma^r(E)\big)^{-1}. \tag{5.81}$$

Similarly, subtracting (5.79) and (5.80), we find $\Big(E - H_C^F + \Sigma^{\bar{t}}(E) - \Sigma^>(E)\Big)\, G^r(E) = I$. Then multiplying on the right by $E - H_C^F - \Sigma^r(E)$ and making use of (5.81) we get

$$\Sigma^r(E) = \Sigma^>(E) - \Sigma^{\bar{t}}(E), \tag{5.82}$$

which in combination with (5.74) yields

$$\Sigma^t(E) + \Sigma^{\bar{t}}(E) = \Sigma^<(E) + \Sigma^>(E). \tag{5.83}$$

Then combining this with (5.75), we also find

$$\Sigma^a(E) = \Sigma^<(E) - \Sigma^{\bar{t}}(E). \tag{5.84}$$

Note that (5.83), (5.82) and (5.84) respectively form analogs of (5.69), (5.72) and (5.73).

Now adding (5.77) and (5.79) and making use of (5.75), (5.84) and (5.71), we get $\left(E - H_C^F - \Sigma^a(E)\right) G^a(E) = I$, and upon inverting

$$G^a(E) = \left(E - H_C^F - \Sigma^a(E)\right)^{-1}. \tag{5.85}$$

By (5.73) we can equate this to the adjoint of (5.81), and upon inverting we get $\Sigma^a(E) = \Sigma^r(E)^\dagger$. Making use of (5.74), (5.84), (5.64)-(5.67) and (3.111) we then also find $\Sigma_s^a(E) = \Sigma_s^r(E)^\dagger$.

Solving (5.74) and (5.73) for $\Sigma^t(E)$ and $G^{\bar{t}}(E)$ respectively, and then inserting the resulting expressions in (5.78), we get $\left(E - H_C^F - \Sigma^r(E)\right) G^<(E) - \Sigma^<(E) G^a(E) = 0$. Then finally multiplying this expression on the left by $G^r(E)$, and making use of (5.81) we obtain

$$G^<(E) = G^r(E)\Sigma^<(E)G^a(E). \tag{5.86}$$

Together with an expression for the self energies, (5.86) and (5.81) are the only equations one needs to solve to find all Green's functions, since the remaining ones are then easily obtained using the relations (5.70)-(5.73). (5.86) and (5.81) are identified as the main NEGF equations by Datta[7].

5.3 The spectral density

Following Datta[7], we define the spectral density $A(E)$ in terms of the Green's functions introduced above as

$$A(E) = i\left(G^r(E) - G^a(E)\right). \tag{5.87}$$

It follows immediately from this definition and (5.73) that $A(E)$ is Hermitian. Further, making use of the definitions (5.70) and (5.71), we can also express the spectral density as

$$A(E) = i\left(G^>(E) - G^<(E)\right). \tag{5.88}$$

Defining

$$\Gamma(E) = i\left(\Sigma^r(E) - \Sigma^a(E)\right), \tag{5.89}$$

we also have the relations

$$A(E) = G^a(E)\Gamma(E)G^r(E) = G^r(E)\Gamma(E)G^a(E), \tag{5.90}$$

derivations of which can be found in the book by Datta[7].

Inserting the Fourier representation (5.61) of the Green's functions in (5.88), we obtain

$$A(E) = \int_{-\infty}^{\infty} A(t-t')e^{iE(t-t')/\hbar}, \tag{5.91}$$

where in general we define

$$A(t,t') = i\left(G^>(t,t') - G^<(t,t')\right). \tag{5.92}$$

Making use of (3.81) and (3.82), we see that

$$A_{ij}(t,t') = \frac{1}{\hbar}\left(\langle\psi_i(t)\bar{\psi}_j(t')\rangle + \langle\psi_j(t')\bar{\psi}_i(t)\rangle\right) = \frac{1}{\hbar}\left\langle\left\{\psi_i(t), \bar{\psi}_j(t')\right\}\right\rangle, \tag{5.93}$$

meaning that $A(t,t')$ is in fact the anti-commutator correlation function of the field operators.

Taking the inverse Fourier transform of (5.91), and making use of the fundamental anti-commutation relations of the field operators, we find

$$\int_{-\infty}^{\infty} \frac{\operatorname{Tr} A(E)}{2\pi}\mathrm{d}E = \sum_i \hbar A_{ii}(t,t) = \sum_i 1 = s^F, \tag{5.94}$$

where s^F is the total number of fermion single particle states. Thus, it is reasonable to identify the quantity $\operatorname{Tr} A(E)/2\pi$ with the contribution to s^F from different energies, i.e. the Density of states. In the literature[15, 7] it is in fact shown that in the absence of many particle interactions

$$\frac{\operatorname{Tr} A(E)}{2\pi} = \sum_i \delta(E - E_i), \tag{5.95}$$

where the sum is over all fermionic single particle states. The quantity on the right is of course the single particle density of states $D(E)$. Accordingly, we regard $\operatorname{Tr} A(E)/2\pi$ as a meaningful generalization of the density of states outside of the single particle approximation, and make the general identification[2] $D(E) = \operatorname{Tr} A(E)/2\pi$. Naturally, the diagonal elements $A_{ii}(E)/2\pi$ are then identified with the projected density of states $D_i(E)$.

Finally, there are some important relations between the various Green's functions in equilibrium. These can be derived by once again making use of the Lehmann representation, as in Section 4.2.4, to obtain equilibrium expressions for $G^<$ and $G^>$. These representations can then be used to find a relationship between the two Green's functions, which can be reexpressed in terms of the

spectral density using (5.88). The details can be found for instance in the book by Jacoboni[15], who derives the equilibrium relation

$$G^<(E) = if(E)A(E), \tag{5.96}$$

where $f(E)$ is the Fermi function defined in (3.92). Multiplying (5.96) by $(E - H_C^F - \Sigma^r(E))$ and $(E - H_C^F - \Sigma^a(E))$ on the left and right respectively, and making use of (5.86) and (5.90), we also obtain the equilibrium relation

$$\Sigma^<(E) = if(E)\Gamma(E). \tag{5.97}$$

5.4 Transport expressions

From (3.152) we see that we can calculate the electrical current from the expectation values $\langle \bar{\psi}_i^-(E)\psi_j^+(E)\rangle$ and $\langle \bar{\psi}_i^+(E)\psi_j^-(E)\rangle$ as

$$I_p = -e\int \frac{2\pi \mathrm{d}E}{h^2(t_f - t_0)} \sum_{ij} \Big(\big(1 - f_p(E)\big)\, \Gamma^F_{pij}(E)\, \langle \bar{\psi}_i^-(E)\psi_j^+(E)\rangle \tag{5.98}$$
$$+ f_p(E)\Gamma^F_{pij}(E)\, \langle \bar{\psi}_i^+(E)\psi_j^-(E)\rangle \Big).$$

By (3.101) and (3.102) we have

$$\langle \bar{\psi}_i^-(E)\psi_j^+(E)\rangle = \sum_{nm} \Delta t^2\, \langle \bar{\psi}^-_{n+1,i}\psi^+_{mj}\rangle\, e^{iE(m-n+1)\Delta t/\hbar}. \tag{5.99}$$

Making use of (3.82) and taking the limit $\Delta t \to 0$ this becomes

$$\begin{aligned}\langle \bar{\psi}_i^-(E)\psi_j^+(E)\rangle &= -i\hbar \int_{t_0}^{t_f} \mathrm{d}t \int_{t_0}^{t_f} \mathrm{d}t'\, G^<_{ji}(t',t) e^{iE(t'-t)/\hbar} \\ &\approx -i\hbar \int_{t_0}^{t_f} \mathrm{d}t \int_{-\infty}^{\infty} \mathrm{d}t'\, G^<_{ji}(t'-t) e^{iE(t'-t)/\hbar} = -i\hbar(t_f - t_0)G^<_{ji}(E),\end{aligned} \tag{5.100}$$

where we have made use of the assumption that $G^<$ has a finite correlation time to replace the innermost integration limits. In a completely analogous manor, from (3.81) we also find

$$\langle \bar{\psi}_i^+(E)\psi_j^-(E)\rangle = -i\hbar(t_f - t_0)G^>_{ji}(E). \tag{5.101}$$

Inserting (5.100) and (5.101) back in (5.98), and then making use of (5.88), we obtain

$$I_p = \frac{ei}{h}\int \mathrm{d}E\, \mathrm{Tr}\, \Gamma^F_p(E)\big(G^<(E) - if_p(E)A(E)\big). \tag{5.102}$$

By (3.153), the heat current q_p can be decomposed into a bosonic (phonon) component q_p^l and a fermionic (electron) component q_p^e such that $q_p = q_p^l + q_p^e$.

Since we are limiting our discussion to the fermionic sector, we will only consider the fermionic component, which can be expressed as

$$q_p^e = \int \frac{2\pi \mathrm{d}E\,(E-\mu)}{h^2(t_f-t_0)} \sum_{ij} \Big((1-f_p(E))\,\Gamma^F_{pij}(E)\,\big\langle \bar{\psi}_i^-(E)\psi_j^+(E)\big\rangle + f_p(E)\Gamma^F_{pij}(E)\,\big\langle \bar{\psi}_i^+(E)\psi_j^-(E)\big\rangle \Big). \tag{5.103}$$

Inserting (5.100) and (5.101) in this expression, we obtain in a manor analogous to the derivation of (5.102)

$$q_p^e = -\frac{i}{h}\int \mathrm{d}E\,(E-\mu)\mathrm{Tr}\,\Gamma_p^F(E)\big(G^<(E) - if_p(E)A(E)\big). \tag{5.104}$$

Comparing (5.102) and (5.104) to (2.11) and (2.12), we see that the expressions for I_p and q_p^e are respectively on the form of (2.11) and (2.12), with the energy resolved particle flux $i_p(E)$ given by

$$i_p(E) = -\frac{i}{h}\mathrm{Tr}\,\Gamma_p^F(E)\big(G^<(E) - if_p(E)A(E)\big). \tag{5.105}$$

This is also the expression presented by Datta[7].

Chapter 6

Markov and semiclassical approximations

In this chapter, we will discuss two remaining important transport formalisms, which are master equations, and the Boltzmann equation. Master equations apply when the dynamics of the model can be regarded Markovian, i.e. when the future development depends only on the current state. Typically a Markovian approximation can be made when the system develops more slowly than some characteristic non-Markovian time scale. The Boltzmann equation on the other hand, will apply when in addition to such slow temporal variations, there are also slow spatial variations, i.e when the system is homogeneous over long length scales.

In Section 6.1 we will make a Markovian approximation to the NEGF equations introduced in the previous chapter, and derive a general nonlinear master equation. The three remaining sections will be devoted to the Boltzmann equation. For this discussion, we will make use of two important tools known as the Wigner transform and the Moyal expansion, which are introduced in Section 6.2. Then, in Section 6.3 we will discuss how these techniques can be generalized, in such a way that they are applicable to a solid state system with multiple bands. Finally, in Section 6.4 we discuss how the Boltzmann equation arises within this context.

6.1 The Markov approximation and the general Master equation

Combining (3.82) with (3.25), we have

$$\langle A\rangle = -i\hbar\sum_{ij} A_{ij}G^<_{ij}(t,t) = -i\hbar \mathrm{Tr}\, AG^<(t,t), \tag{6.1}$$

for any single particle observable A. Thus, the matrix $-i\hbar G^<(t,t)$ plays the role of a single particle density operator $\rho_e(t)$, since we then have $\langle A\rangle = \mathrm{Tr}\, A\rho_e(t)$. An important note however, is that while the trace of the density operator is usually set to one, in this case we instead have $\mathrm{Tr}\,\rho_e = N_f$, the total number of fermions. One could argue that the latter is in any case a more appropriate convention when one is dealing with multiple identical particles.

Thus, we make the identification $\rho_e(t) = -i\hbar G^<(t,t)$, and obtain the derivative

$$\frac{\mathrm{d}\rho_e}{\mathrm{d}t}(t) = -i\hbar\frac{\mathrm{d}}{\mathrm{d}t}\left(G^<(t,t')|_{t=t'}\right) = -i\hbar\left(\frac{\partial}{\partial t}+\frac{\partial}{\partial t'}\right)G^<(t,t')|_{t=t'}. \tag{6.2}$$

Writing out the upper right component of (5.60), we get

$$\left(\hbar i\frac{\partial}{\partial t} - H_C^F(t)\right) G^<(t,t') = \int_{-\infty}^{\infty} dt'' \left(\Sigma^r(t,t'')G^<(t'',t') + \Sigma^<(t,t'')G^a(t'',t')\right), \tag{6.3}$$

where we have made use of the definition (5.74) and the relation (5.73). Taking the adjoint of (6.3), and then interchanging the time arguments, we obtain also an equation involving the other time derivative:

$$\begin{aligned}\hbar i\frac{\partial}{\partial t'}G^<(t,t') + G^<(t,t')H_C^F(t') = \\ - \int_{-\infty}^{\infty} dt'' \left(G^r(t,t'')\Sigma^<(t'',t') + G^<(t,t'')\Sigma^a(t'',t')\right).\end{aligned} \tag{6.4}$$

Here we have made use some relations concerning the adjoint of Green's functions, all of which either appear in the beginning of Section 5.2.5, or are easily obtained from relations appearing there.

Finally adding (6.3) and (6.4), we get by (6.2)

$$\begin{aligned}-\frac{\mathrm{d}\rho_e}{\mathrm{d}t}(t) - \frac{i}{\hbar}[H_C^F(t),\rho_e(t)] = \int_{-\infty}^{\infty} dt'' \left(\Sigma^r(t,t'')G^<(t'',t) - G^<(t,t'')\Sigma^a(t'',t)\right) \\ - \int_{-\infty}^{\infty} dt'' \left(G^r(t,t'')\Sigma^<(t'',t) - \Sigma^<(t,t'')G^a(t'',t)\right).\end{aligned} \tag{6.5}$$

To proceed further, we will once more make use of the assumption that the various Green's functions have finite correlation times τ, and that they are essentially zero whenever the time arguments are further apart than this characteristic time scale, i.e. when $|t-t'| \gg \tau$. We also assume that these correlation times are typically different for the different Green's functions, so that we have separate correlation times $\tau_F^<$, τ_F^r, $\tau_B^<$, τ_B^r and so on, corresponding to the Green's functions $G^<$, G^r, $D^<$, D^r and so on. The Markov approximation is based upon the assumption that the correlation time $\tau_F^<$ of the lesser Green's function $G^<$ is much larger than all other significant time scales. In particular, we then assume $\tau_F^< \gg \tau_B^r$ and $\tau_B^<$. These conditions essentially amount to the assumption that scattering interactions are sufficiently weak.

The important aspect of this assumption, is that Σ^r and Σ^a will only be significantly different from zero in a range where $G^<$ is approximately constant. Thus, on the right hand side of (6.5), we may approximate $G^<(t,t'') \approx G^<(t'',t) \approx G^<(t,t)$. Doing this, we find

$$\int_{-\infty}^{\infty} dt'' \left(\Sigma^r(t,t'')G^<(t'',t) - G^<(t,t'')\Sigma^a(t'',t)\right) \approx R(t)\rho_e(t) + \rho_e(t)R^\dagger(t), \tag{6.6}$$

where we have defined

$$R(t) = -\frac{i}{\hbar}\int_{-\infty}^{\infty} dt'\Sigma^r(t,t'). \tag{6.7}$$

By the discussion in Section 5.1.2 and 5.1.3, the self energies Σ^r and $\Sigma^<$ can be expressed as integrals involving products of the various Green's functions. In these expression also, we can apply the Markov approximation to exchange factors of $G^<$ with a factor of $\rho_e(t)$. Thus, if ρ_e is known at t, the self energy expressions together with (5.81) forms a self contained set of equations which can be solved for $\Sigma^r(t,t')$, $\Sigma^<(t,t')$ and $G^r(t,t')$ without needing any more information about $G^<$. Accordingly, we can express the solutions as functions of ρ_e, so that $\Sigma^r = \Sigma^r(\rho_e, t-t')$, $\Sigma^< = \Sigma^<(\rho_e, t-t')$ and $G^r = G^r(\rho_e, t-t')$. We are here assuming time independent dynamics, so that the solutions must be invariant under time translation. Inserting for instance the expression for Σ^r in (6.7), we have

$$R(t) = -\frac{i}{\hbar}\int_{-\infty}^{\infty} dt' \Sigma^r(\rho_e(t), t-t') = R(\rho_e(t)), \tag{6.8}$$

so that the matrix R is also some function of ρ_e. Likewise, for the last integral in (6.5), we have

$$\begin{aligned}&\int_{-\infty}^{\infty} dt'' \left(G^r(t,t'')\Sigma^<(t'',t) - \Sigma^<(t,t'')G^a(t'',t)\right) \qquad (6.9)\\ &= \int_{-\infty}^{\infty} dt'' \left(G^r(\rho_e, t-t'')\Sigma^<(\rho_e, t''-t) - \Sigma^<(\rho_e, t-t'')G^a(\rho_e, t''-t)\right) = S(\rho_e(t)).\end{aligned}$$

Finally, combining (5.42) and (5.43), we see that we do not need to apply the Markov approximation to the expression for δH^F, since it already only involves $G^<(t,t)$. Accordingly, $H_C^F(t) = H_S^F + \delta H^F(\rho_e) = H_C^F(\rho_e)$, and we can write (6.5) simply as

$$-\frac{\mathrm{d}\rho_e}{\mathrm{d}t} - \frac{i}{\hbar}[H_C^F(\rho_e), \rho_e] = R(\rho_e)\rho_e + \rho_e R^\dagger(\rho_e) - S(\rho_e). \tag{6.10}$$

It makes sense to rewrite this expression by separating out the Hermitian and anti-Hermitian components of the Matrix R. Thus, we write

$$R = \frac{1}{2}\Gamma + \frac{i}{\hbar}\delta H_M^F, \tag{6.11}$$

where Γ and δH_M^F are both Hermitian matrices. Inserting this in (6.10), we finally obtain the general Markovian nonlinear master equation

$$\frac{\mathrm{d}\rho_e}{\mathrm{d}t} = -\frac{i}{\hbar}[H_e(\rho_e), \rho_e] - \frac{1}{2}\left\{\Gamma(\rho_e), \rho_e\right\} + S(\rho_e). \tag{6.12}$$

Here curly brackets denote anti commutation, and

$$H_e(\rho_e) = H_C^F(\rho_e) + \delta H_M^F(\rho_e) = H_S^F + \delta H^F(\rho_e) + \delta H_M^F(\rho_e). \tag{6.13}$$

From (6.7) and (6.11) it should be clear that

$$\delta H_M(\rho_e) = -\frac{1}{2}\int_{-\infty}^{\infty} dt' \left(\Sigma^r(\rho_e, t-t') + \Sigma^a(\rho_e, t'-t)\right), \quad \text{while} \tag{6.14}$$

$$\Gamma(\rho_e) = -\frac{i}{\hbar}\int_{-\infty}^{\infty} dt' \left(\Sigma^r(\rho_e, t-t') - \Sigma^r(\rho_e, t'-t)\right). \tag{6.15}$$

6.2 The Weyl-Wigner transform

6.2.1 Weyl quantization

The subject of this section is the Weyl and Wigner transforms. The introduction of the Weyl transform in particular, can be motivated from the problem of quantization, which concerns how one may transform a function $g(\boldsymbol{x}, \boldsymbol{p})$ defined in classical phase space, into a corresponding Hilbert space operator $\hat{g} = g(\hat{\boldsymbol{x}}, \hat{\boldsymbol{p}})$. Quantization is a simple procedure when the involved function is a simple polynomial where all terms contain only one of the variables $\boldsymbol{x}$ or $\boldsymbol{p}$. One may then simply replace these variables with the corresponding operators, replacing for instance the term $\boldsymbol{p}^2$ with $\hat{\boldsymbol{p}}^2$ and so on. However, if we generalize the situation simply by including cross terms in $\boldsymbol{x}$ and $\boldsymbol{p}$, the problem becomes more complex. Since the operators $\hat{\boldsymbol{x}}$ and $\hat{\boldsymbol{p}}$ do not commute, there will in general be several inequivalent ways to represent such cross terms as operators[14]. And if the function g is not even analytic, the problem becomes even more difficult.

The procedure known as Weyl quantization seeks to resolve these problems by employing a Fourier transform[13]. Taking the Fourier transform of the function g, and then the inverse Fourier transform of the result, we obtain

$$g(\boldsymbol{x}', \boldsymbol{p}') = \frac{1}{(2\pi)^6} \int \mathrm{d}^3\boldsymbol{k} \int \mathrm{d}^3\boldsymbol{r} \int \mathrm{d}^3\boldsymbol{x} \int \mathrm{d}^3\boldsymbol{p}\, g(\boldsymbol{x}, \boldsymbol{p}) e^{i\boldsymbol{k}\cdot(\boldsymbol{x}'-\boldsymbol{x})-i(\boldsymbol{p}'-\boldsymbol{p})\cdot\boldsymbol{r}}. \quad (6.16)$$

From this expression it is a simple matter to obtain a Hilbert space operator $g(\hat{\boldsymbol{x}}, \hat{\boldsymbol{p}})$ by simply substituting $\boldsymbol{x}'$ and $\boldsymbol{p}'$ with $\hat{\boldsymbol{x}}$ and $\hat{\boldsymbol{p}}$. Thus, we obtain the expression

$$\hat{g} = g(\hat{\boldsymbol{x}}, \hat{\boldsymbol{p}}) = \frac{1}{(2\pi)^6} \int \mathrm{d}^3\boldsymbol{k} \int \mathrm{d}^3\boldsymbol{r} \int \mathrm{d}^3\boldsymbol{x} \int \mathrm{d}^3\boldsymbol{p}\, g(\boldsymbol{x}, \boldsymbol{p}) e^{i\boldsymbol{k}\cdot(\hat{\boldsymbol{x}}-\boldsymbol{x})-i(\hat{\boldsymbol{p}}-\boldsymbol{p})\cdot\boldsymbol{r}}, \quad (6.17)$$

which is well defined for any Fourier transformable function g. The operator $\hat{g}$ is referred to as the Weyl transform of the function g.

It will also be convenient to have more direct expressions for the Weyl transform, in terms of the position and momentum bases. To obtain these, we make use of the Baker-Campbell-Hausdorff theorem[15, 24], which states

$$e^{i\boldsymbol{k}\cdot\hat{\boldsymbol{x}}} e^{-i\hat{\boldsymbol{p}}\cdot\boldsymbol{r}} = e^{i\boldsymbol{k}\cdot\hat{\boldsymbol{x}}-i\hat{\boldsymbol{p}}\cdot\boldsymbol{r}+\hbar i\boldsymbol{k}\cdot\boldsymbol{r}/2}, \quad (6.18)$$

to reexpress (6.17) as

$$\hat{g} = \frac{1}{(2\pi)^6} \int \mathrm{d}^3\boldsymbol{k} \int \mathrm{d}^3\boldsymbol{r} \int \mathrm{d}^3\boldsymbol{x} \int \mathrm{d}^3\boldsymbol{p}\, g(\boldsymbol{x}, \boldsymbol{p}) e^{-i\boldsymbol{k}\cdot\hbar\boldsymbol{r}/2} e^{i\boldsymbol{k}\cdot(\hat{\boldsymbol{x}}-\boldsymbol{x})} e^{-i(\hat{\boldsymbol{p}}-\boldsymbol{p})\cdot\boldsymbol{r}}. \quad (6.19)$$

Making use of the position and momentum bases respectively, we have

$$e^{i\boldsymbol{k}\cdot\hat{\boldsymbol{x}}} = \int \mathrm{d}^3\boldsymbol{y}\, e^{i\boldsymbol{k}\cdot\boldsymbol{y}} |\boldsymbol{y}\rangle\langle\boldsymbol{y}|, \qquad \text{and} \quad (6.20)$$

$$e^{-i\hat{\boldsymbol{p}}\cdot\boldsymbol{r}} = \int \mathrm{d}^3\boldsymbol{q}\, e^{-i\boldsymbol{q}\cdot\boldsymbol{r}} |\boldsymbol{q}\rangle\langle\boldsymbol{q}|. \quad (6.21)$$

Inserting (6.20) in (6.19) we obtain after making use of the Fourier representation of the delta function to integrate over $\boldsymbol{k}$ and $\boldsymbol{y}$,

$$\hat{g} = \frac{1}{h^3} \int \mathrm{d}^3\boldsymbol{x}' \int \mathrm{d}^3\boldsymbol{x} \int \mathrm{d}^3\boldsymbol{p}\, g(\boldsymbol{x},\boldsymbol{p}) |\boldsymbol{x}+\boldsymbol{x}'/2\rangle\langle \boldsymbol{x}+\boldsymbol{x}'/2| e^{-i(\hat{\boldsymbol{p}}-\boldsymbol{p})\cdot\boldsymbol{x}'/\hbar}, \quad (6.22)$$

where $\boldsymbol{x}' = \boldsymbol{r}/\hbar$. Making use of the translation formula $e^{i\hat{\boldsymbol{p}}\cdot\boldsymbol{x}'/\hbar}|\boldsymbol{x}\rangle = |\boldsymbol{x}-\boldsymbol{x}'\rangle$, we find in particular $\langle \boldsymbol{x}+\boldsymbol{x}'/2| e^{-i(\hat{\boldsymbol{p}}-\boldsymbol{p})\cdot\boldsymbol{x}'/\hbar} = \langle \boldsymbol{x}-\boldsymbol{x}'/2| e^{i\boldsymbol{p}\cdot\boldsymbol{x}'/\hbar}$. Inserting this back in (6.22), we finally obtain

$$\hat{g} = \frac{1}{h^3} \int \mathrm{d}^3\boldsymbol{x}' \int \mathrm{d}^3\boldsymbol{x} \int \mathrm{d}^3\boldsymbol{p}\, e^{i\boldsymbol{p}\cdot\boldsymbol{x}'/\hbar} g(\boldsymbol{x},\boldsymbol{p}) |\boldsymbol{x}+\boldsymbol{x}'/2\rangle\langle \boldsymbol{x}-\boldsymbol{x}'/2|, \quad (6.23)$$

where the Weyl transform is expressed in terms of the position basis. Instead inserting (6.21) in (6.19), and essentially repeating the steps above, we can also express the Weyl transform in the momentum basis, as

$$\hat{g} = \frac{1}{h^3} \int \mathrm{d}^3\boldsymbol{x} \int \mathrm{d}^3\boldsymbol{p} \int \mathrm{d}^3\boldsymbol{p}'\, e^{-i\boldsymbol{p}'\cdot\boldsymbol{x}/\hbar} g(\boldsymbol{x},\boldsymbol{p}) |\boldsymbol{p}+\boldsymbol{p}'/2\rangle\langle \boldsymbol{p}-\boldsymbol{p}'/2|. \quad (6.24)$$

6.2.2 The Wigner transform, and the Wigner distribution

Starting from (6.23), and making use of the delta function normalization $\langle \boldsymbol{x}|\boldsymbol{x}'\rangle = \delta(\boldsymbol{x}-\boldsymbol{x}')$, as well as the Fourier representation of the delta function, one can show that

$$g(\boldsymbol{x},\boldsymbol{p}) = \int \mathrm{d}^3\boldsymbol{x}'\, e^{-i\boldsymbol{p}\cdot\boldsymbol{x}'/\hbar} \langle \boldsymbol{x}+\boldsymbol{x}'/2|\hat{g}|\boldsymbol{x}-\boldsymbol{x}'/2\rangle. \quad (6.25)$$

Thus, (6.25) gives the inverse of the Weyl transform, which is referred to as the Wigner transform[15]. The Wigner transform can also be expressed in the momentum basis. Indeed, starting from (6.24) we find in a similar manner

$$g(\boldsymbol{x},\boldsymbol{p}) = \int \mathrm{d}^3\boldsymbol{p}'\, e^{i\boldsymbol{p}'\cdot\boldsymbol{x}/\hbar} \langle \boldsymbol{p}+\boldsymbol{p}'/2|\hat{g}|\boldsymbol{p}-\boldsymbol{p}'/2\rangle. \quad (6.26)$$

Clearly, the Wigner transform simplifies significantly if $\hat{g}$ is diagonal in either the position or momentum bases. That is, if $\langle \boldsymbol{x}|\hat{g}|\boldsymbol{x}'\rangle = g(\boldsymbol{x})\delta(\boldsymbol{x}-\boldsymbol{x}')$ or $\langle \boldsymbol{p}|\hat{g}|\boldsymbol{p}'\rangle = g(\boldsymbol{p})\delta(\boldsymbol{p}-\boldsymbol{p}')$. By (6.25) and (6.26), we have respectively in these two cases simply $g(\boldsymbol{x},\boldsymbol{p}) = g(\boldsymbol{x})$ and $g(\boldsymbol{x},\boldsymbol{p}) = g(\boldsymbol{p})$. In particular, since $\langle \boldsymbol{x}|I|\boldsymbol{x}'\rangle = \delta(\boldsymbol{x}-\boldsymbol{x}')$, the Wigner transform of the identity operator is 1.

Assume now that we are given two operators $\hat{A}$ and $\hat{B}$, whose Wigner transforms are respectively $A^W(\boldsymbol{x},\boldsymbol{p})$ and $B^W(\boldsymbol{x},\boldsymbol{p})$. Then making use of (6.23)

and (6.25), we can write the trace of the product of the two operators as

$$\begin{aligned}\operatorname{Tr}\hat{A}\hat{B} &= \operatorname{Tr}\frac{1}{h^3}\int \mathrm{d}^3\boldsymbol{x}'\int \mathrm{d}^3\boldsymbol{x}\int \mathrm{d}^3\boldsymbol{p}\, e^{i\boldsymbol{p}\cdot\boldsymbol{x}'/\hbar}A^W(\boldsymbol{x},\boldsymbol{p})|\boldsymbol{x}+\boldsymbol{x}'/2\rangle\langle\boldsymbol{x}-\boldsymbol{x}'/2|\hat{B}\\ &= \frac{1}{h^3}\int \mathrm{d}^3\boldsymbol{x}\int \mathrm{d}^3\boldsymbol{p}\, A^W(\boldsymbol{x},\boldsymbol{p})\int \mathrm{d}^3\boldsymbol{x}'\, e^{i\boldsymbol{p}\cdot\boldsymbol{x}'/\hbar}\langle\boldsymbol{x}-\boldsymbol{x}'/2|\hat{B}|\boldsymbol{x}+\boldsymbol{x}'/2\rangle\\ &= \frac{1}{h^3}\int \mathrm{d}^3\boldsymbol{x}\int \mathrm{d}^3\boldsymbol{p}\, A^W(\boldsymbol{x},\boldsymbol{p})\int \mathrm{d}^3\boldsymbol{x}'\, e^{-i\boldsymbol{p}\cdot\boldsymbol{x}'/\hbar}\langle\boldsymbol{x}+\boldsymbol{x}'/2|\hat{B}|\boldsymbol{x}-\boldsymbol{x}'/2\rangle\\ &= \frac{1}{h^3}\int \mathrm{d}^3\boldsymbol{x}\int \mathrm{d}^3\boldsymbol{p}\, A^W(\boldsymbol{x},\boldsymbol{p})B^W(\boldsymbol{x},\boldsymbol{p}). \qquad (6.27)\end{aligned}$$

In particular, since the Wigner transform of I is 1, we get the important special case

$$\operatorname{Tr}\hat{A} = \frac{1}{h^3}\int \mathrm{d}^3\boldsymbol{x}\int \mathrm{d}^3\boldsymbol{p}\, A^W(\boldsymbol{x},\boldsymbol{p}). \qquad (6.28)$$

It should also be noted that the Wigner transform preserves the adjoint operation. Indeed, we have

$$\begin{aligned}A^W(\boldsymbol{x},\boldsymbol{p})^\star &= \int \mathrm{d}^3\boldsymbol{x}'\, e^{i\boldsymbol{p}\cdot\boldsymbol{x}'/\hbar}\langle\boldsymbol{x}-\boldsymbol{x}'/2|\hat{A}^\dagger|\boldsymbol{x}+\boldsymbol{x}'/2\rangle \qquad (6.29)\\ &= \int \mathrm{d}^3\boldsymbol{x}'\, e^{-i\boldsymbol{p}\cdot\boldsymbol{x}'/\hbar}\langle\boldsymbol{x}+\boldsymbol{x}'/2|\hat{A}^\dagger|\boldsymbol{x}-\boldsymbol{x}'/2\rangle,\end{aligned}$$

which is the Wigner transform of $\hat{A}^\dagger$.

The Wigner transform of the density operator is referred to as the Wigner distribution, and denoted f^W. That is, we have[15, 29, 25]

$$f^W(\boldsymbol{x},\boldsymbol{p}) = \int \mathrm{d}^3\boldsymbol{x}'\, e^{-i\boldsymbol{p}\cdot\boldsymbol{x}'/\hbar}\langle\boldsymbol{x}+\boldsymbol{x}'/2|\hat{\rho}|\boldsymbol{x}-\boldsymbol{x}'/2\rangle. \qquad (6.30)$$

Since the Wigner transform preserves the adjoint operation, it follows from the Hermiticity of $\hat{\rho}$ that $f^W(\boldsymbol{x},\boldsymbol{p})$ is a real function. However, it does not follow from the positive definiteness of $\hat{\rho}$ that the Wigner distribution is necessarily positive, and in general this is not the case. But in the special cases where $\hat{\rho}$ is diagonal in the position or momentum basis, $f^W(\boldsymbol{x},\boldsymbol{p})$ will be positive, since in those cases we respectively have $f^W(\boldsymbol{x},\boldsymbol{p}) \sim \langle\boldsymbol{x}|\hat{\rho}|\boldsymbol{x}\rangle \geq 0$ and $f^W(\boldsymbol{x},\boldsymbol{p}) \sim \langle\boldsymbol{p}|\hat{\rho}|\boldsymbol{p}\rangle \geq 0$.

From (6.28) together with our choice of normalization $\operatorname{Tr}\hat{\rho} = N_f$, we find

$$\frac{1}{h^3}\int \mathrm{d}^3\boldsymbol{x}\int \mathrm{d}^3\boldsymbol{p}\, f^W(\boldsymbol{x},\boldsymbol{p}) = N_f. \qquad (6.31)$$

Further, by (6.27) we have for any observable A

$$\langle A\rangle = \operatorname{Tr}\hat{\rho}\hat{A} = \frac{1}{h^3}\int \mathrm{d}^3\boldsymbol{x}\int \mathrm{d}^3\boldsymbol{p}\, f^W(\boldsymbol{x},\boldsymbol{p})A^W(\boldsymbol{x},\boldsymbol{p}). \qquad (6.32)$$

Thus, the Wigner function plays the role of a probability distribution in phase space. However, f^W is not fully interpretable as a probability distribution, since as mentioned it does not generally have to be positive.

6.2.3 The Moyal product and the Moyal expansion

In order to express equations of motion for the Wigner distribution, we will need to find the Wigner transform of a product of Weyl transforms. That is, if $\hat{A}$ and $\hat{B}$ are respectively the Weyl transforms of $A(\boldsymbol{x},\boldsymbol{p})$ and $B(\boldsymbol{x},\boldsymbol{p})$, we need an expression for the Wigner transform of $\hat{A}\hat{B}$. This object is referred to as the Moyal product of the functions A and B, and denoted $A\star B$[2, 10, 25]. Making use of (6.23) and (6.25), and then repeated use of the delta function normalization of the position basis and the Fourier representation of the delta function to integrate away the dummy variables, we eventually end up with the integral representation

$$\begin{aligned}&(A\star B)(\boldsymbol{x},\boldsymbol{p}) \qquad (6.33)\\ &=\frac{16}{h^6}\iint \mathrm{d}^3\boldsymbol{y}\mathrm{d}^3\boldsymbol{q}\mathrm{d}^3\boldsymbol{r}\mathrm{d}^3\boldsymbol{q}'\, e^{2i(\boldsymbol{q}'-\boldsymbol{p})\cdot(\boldsymbol{y}-\boldsymbol{x})/\hbar-2i(\boldsymbol{q}-\boldsymbol{p})\cdot(\boldsymbol{r}-\boldsymbol{x})/\hbar}A(\boldsymbol{y},\boldsymbol{q})B(\boldsymbol{r},\boldsymbol{q}')\end{aligned}$$

of the Moyal product. If either both A and B are independent of $\boldsymbol{x}$, or both A and B are independent of $\boldsymbol{p}$, then the Moyal product simplifies to an ordinary product, so that $(A\star B)(\boldsymbol{x},\boldsymbol{p})=A(\boldsymbol{x},\boldsymbol{p})B(\boldsymbol{x},\boldsymbol{p})$.

In a closed system the density matrix obeys the Von Neumann equation

$$\frac{\mathrm{d}\hat{\rho}}{\mathrm{d}t}=-\frac{i}{\hbar}[\hat{H},\hat{\rho}]. \qquad (6.34)$$

Taking the Wigner transform of both sides of this equation, we obtain the equation

$$\frac{\partial f^W}{\partial t}=-\frac{i}{\hbar}(H\star f^W-f^W\star H)=\left\{\left\{H,\,f^W\right\}\right\}, \qquad (6.35)$$

where H is the Wigner transform of the Hamiltonian $\hat{H}$, and we have introduced the Moyal bracket, defined by the expression

$$\{\{A,B\}\}=\frac{A\star B-B\star A}{i\hbar}. \qquad (6.36)$$

If the system instead obeys the master equation (6.12), we obtain the modified equation

$$\frac{\partial f^W}{\partial t}=\left\{\left\{H,\,f^W\right\}\right\}-\frac{1}{2}\left(\Gamma^W\star f^W+f^W\star\Gamma^W\right)+S[f^W], \qquad (6.37)$$

where Γ^W and $S[f^W]$ are respectively the Wigner transforms of the operators Γ and $S(\rho)$ appearing in (6.12).

Systematic approximations to these equations can be obtained by expressing the Moyal product in terms of a differential expansion. To find this expansion, we start by Taylor expanding the functions A and B in $\boldsymbol{x}$:

$$A(\boldsymbol{x}+\boldsymbol{y},\boldsymbol{q})=\sum_{n=0}^{\infty}\frac{1}{n!}\sum_{i_1\cdots i_n}\frac{\partial^n A}{\partial x_{i_1}\cdots\partial x_{i_n}}(\boldsymbol{x},\boldsymbol{q})y_{i_1}y_{i_2}\cdots y_{i_n}, \qquad (6.38)$$

and similarly for B

$$B(\boldsymbol{x}+\boldsymbol{r},\boldsymbol{q}') = \sum_{m=0}^{\infty} \frac{1}{m!} \sum_{i_1 \cdots i_m} \frac{\partial^m B}{\partial x_{i_1} \cdots \partial x_{i_m}}(\boldsymbol{x},\boldsymbol{q}') r_{i_1} r_{i_2} \cdots r_{i_m}. \tag{6.39}$$

At this point it becomes highly simplifying to introduce left acting differential operators. Thus, we define operators $\frac{\overleftarrow{\partial}}{\partial x}$ by the relation

$$f(x)\frac{\overleftarrow{\partial}}{\partial x} = \frac{\partial}{\partial x} f(x). \tag{6.40}$$

To make the distinction as clear as possible, we will in this context also write the ordinary right acting differential operator as $\frac{\overrightarrow{\partial}}{\partial x}$. Thus, for functions $f(x)$ and $g(x)$, we have

$$f(x)\frac{\overleftarrow{\partial}}{\partial x} g(x) = \frac{\partial f}{\partial x}(x) g(x), \qquad \text{while} \tag{6.41}$$

$$f(x)\frac{\overrightarrow{\partial}}{\partial x} g(x) = f(x)\frac{\partial g}{\partial x}(x). \tag{6.42}$$

With these definitions, one can start with (6.38) and verify that

$$e^{2i(\boldsymbol{q}'-\boldsymbol{p})\cdot\boldsymbol{y}/\hbar} A(\boldsymbol{x}+\boldsymbol{y},\boldsymbol{q}) = \sum_{n=0}^{\infty} \frac{1}{n!} A(\boldsymbol{x},\boldsymbol{q}) \left(\frac{i\hbar}{2} \frac{\overleftarrow{\partial}}{\partial \boldsymbol{x}} \cdot \frac{\overrightarrow{\partial}}{\partial \boldsymbol{p}} \right)^n e^{2i(\boldsymbol{q}'-\boldsymbol{p})\cdot\boldsymbol{y}/\hbar}, \tag{6.43}$$

while similarly, one can use (6.39) to verify that

$$e^{-2i(\boldsymbol{q}-\boldsymbol{p})\cdot\boldsymbol{r}/\hbar} B(\boldsymbol{x}+\boldsymbol{r},\boldsymbol{q}') = \sum_{m=0}^{\infty} \frac{1}{m!} e^{-2i(\boldsymbol{q}-\boldsymbol{p})\cdot\boldsymbol{r}/\hbar} \left(-\frac{i\hbar}{2} \frac{\overleftarrow{\partial}}{\partial \boldsymbol{p}} \cdot \frac{\overrightarrow{\partial}}{\partial \boldsymbol{x}} \right)^m B(\boldsymbol{x},\boldsymbol{q}'). \tag{6.44}$$

Inserting both these expressions in (6.33), and then again making use of the Fourier representation of the delta function to perform the remaining integrals, we obtain the differential expansion

$$\begin{aligned} &(A \star B)(\boldsymbol{x},\boldsymbol{p}) \\ &= \sum_{n=0}^{\infty}\sum_{m=0}^{\infty} \frac{1}{n!m!} A(\boldsymbol{x},\boldsymbol{p}) \left(\frac{i\hbar}{2} \frac{\overleftarrow{\partial}}{\partial \boldsymbol{x}} \cdot \frac{\overrightarrow{\partial}}{\partial \boldsymbol{p}} \right)^n \left(-\frac{i\hbar}{2} \frac{\overleftarrow{\partial}}{\partial \boldsymbol{p}} \cdot \frac{\overrightarrow{\partial}}{\partial \boldsymbol{x}} \right)^m B(\boldsymbol{x},\boldsymbol{p}). \end{aligned} \tag{6.45}$$

Reindexing the sum, and using the binomial theorem, we can simplify the expression further as

$$\begin{aligned} &(A \star B)(\boldsymbol{x},\boldsymbol{p}) \\ &= \sum_{N=0}^{\infty} \frac{1}{N!} A(\boldsymbol{x},\boldsymbol{p}) \sum_{m=0}^{N} \binom{N}{m} \left(\frac{i\hbar}{2} \frac{\overleftarrow{\partial}}{\partial \boldsymbol{x}} \cdot \frac{\overrightarrow{\partial}}{\partial \boldsymbol{p}} \right)^{N-m} \left(-\frac{i\hbar}{2} \frac{\overleftarrow{\partial}}{\partial \boldsymbol{p}} \cdot \frac{\overrightarrow{\partial}}{\partial \boldsymbol{x}} \right)^m B(\boldsymbol{x},\boldsymbol{p}) \\ &= \sum_{N=0}^{\infty} \frac{1}{N!} A(\boldsymbol{x},\boldsymbol{p}) \left(\frac{i\hbar}{2} \right)^N \left(\frac{\overleftarrow{\partial}}{\partial \boldsymbol{x}} \cdot \frac{\overrightarrow{\partial}}{\partial \boldsymbol{p}} - \frac{\overleftarrow{\partial}}{\partial \boldsymbol{p}} \cdot \frac{\overrightarrow{\partial}}{\partial \boldsymbol{x}} \right)^N B(\boldsymbol{x},\boldsymbol{p}). \end{aligned} \tag{6.46}$$

Thus, interpreting the exponential function as its Taylor expansion, we have the formal identity

$$A \star B = A \left[\exp \frac{i\hbar}{2} \left(\frac{\overleftarrow{\partial}}{\partial \boldsymbol{x}} \cdot \frac{\overrightarrow{\partial}}{\partial \boldsymbol{p}} - \frac{\overleftarrow{\partial}}{\partial \boldsymbol{p}} \cdot \frac{\overrightarrow{\partial}}{\partial \boldsymbol{x}} \right) \right] B, \tag{6.47}$$

in agreement with typical literature expressions[2]. To save some space we now introduce the short notation $\overleftarrow{\partial}_{\boldsymbol{q}} \overrightarrow{\partial}_{\boldsymbol{r}} = \overrightarrow{\partial}_{\boldsymbol{r}} \overleftarrow{\partial}_{\boldsymbol{q}} = \frac{\overleftarrow{\partial}}{\partial \boldsymbol{q}} \cdot \frac{\overrightarrow{\partial}}{\partial \boldsymbol{r}} = \frac{\overrightarrow{\partial}}{\partial \boldsymbol{r}} \cdot \frac{\overleftarrow{\partial}}{\partial \boldsymbol{q}}$. (6.47) can then be written as $A \star B = A\, e^{\frac{i\hbar}{2}(\overleftarrow{\partial}_{\boldsymbol{x}} \overrightarrow{\partial}_{\boldsymbol{p}} - \overleftarrow{\partial}_{\boldsymbol{p}} \overrightarrow{\partial}_{\boldsymbol{x}})} B$. The reverse Moyal product $B \star A$ can then be evaluated as

$$\begin{aligned} B \star A &= B\, e^{\frac{i\hbar}{2}(\overleftarrow{\partial}_{\boldsymbol{x}} \overrightarrow{\partial}_{\boldsymbol{p}} - \overleftarrow{\partial}_{\boldsymbol{p}} \overrightarrow{\partial}_{\boldsymbol{x}})} A = A\, e^{\frac{i\hbar}{2}(\overrightarrow{\partial}_{\boldsymbol{x}} \overleftarrow{\partial}_{\boldsymbol{p}} - \overrightarrow{\partial}_{\boldsymbol{p}} \overleftarrow{\partial}_{\boldsymbol{x}})} B \\ &= A\, e^{\frac{i\hbar}{2}(\overleftarrow{\partial}_{\boldsymbol{p}} \overrightarrow{\partial}_{\boldsymbol{x}} - \overleftarrow{\partial}_{\boldsymbol{x}} \overrightarrow{\partial}_{\boldsymbol{p}})} B = A\, e^{-\frac{i\hbar}{2}(\overleftarrow{\partial}_{\boldsymbol{x}} \overrightarrow{\partial}_{\boldsymbol{p}} - \overleftarrow{\partial}_{\boldsymbol{p}} \overrightarrow{\partial}_{\boldsymbol{x}})} B. \end{aligned} \tag{6.48}$$

Accordingly, the Moyal bracket of (6.36) can be written as

$$\begin{aligned} \{\{A, B\}\} &= A \frac{e^{\frac{i\hbar}{2}(\overleftarrow{\partial}_{\boldsymbol{x}} \overrightarrow{\partial}_{\boldsymbol{p}} - \overleftarrow{\partial}_{\boldsymbol{p}} \overrightarrow{\partial}_{\boldsymbol{x}})} - e^{-\frac{i\hbar}{2}(\overleftarrow{\partial}_{\boldsymbol{x}} \overrightarrow{\partial}_{\boldsymbol{p}} - \overleftarrow{\partial}_{\boldsymbol{p}} \overrightarrow{\partial}_{\boldsymbol{x}})}}{i\hbar} B \\ &= \frac{2}{\hbar} A \left(\sin \frac{\hbar}{2} (\overleftarrow{\partial}_{\boldsymbol{x}} \overrightarrow{\partial}_{\boldsymbol{p}} - \overleftarrow{\partial}_{\boldsymbol{p}} \overrightarrow{\partial}_{\boldsymbol{x}}) \right) B, \end{aligned} \tag{6.49}$$

where the sine function is also to be interpreted as its Taylor expansion. In particular, the Wigner transformed Von Neumann equation (6.35) then becomes

$$\frac{\partial f}{\partial t}^W = \frac{2}{\hbar} H \left(\sin \frac{\hbar}{2} (\overleftarrow{\partial}_{\boldsymbol{x}} \overrightarrow{\partial}_{\boldsymbol{p}} - \overleftarrow{\partial}_{\boldsymbol{p}} \overrightarrow{\partial}_{\boldsymbol{x}}) \right) f^W. \tag{6.50}$$

The Moyal anti-commutator $A \star B + B \star A$ can be evaluated in a similar manor, yielding

$$\frac{A \star B + B \star A}{2} = A \left(\cos \frac{\hbar}{2} (\overleftarrow{\partial}_{\boldsymbol{x}} \overrightarrow{\partial}_{\boldsymbol{p}} - \overleftarrow{\partial}_{\boldsymbol{p}} \overrightarrow{\partial}_{\boldsymbol{x}}) \right) B, \tag{6.51}$$

and accordingly we can write the Wigner transformed master equation (6.37) as

$$\begin{aligned} \frac{\partial f}{\partial t}^W &= \frac{2}{\hbar} H \Big(\sin \frac{\hbar}{2} (\overleftarrow{\partial}_{\boldsymbol{x}} \overrightarrow{\partial}_{\boldsymbol{p}} - \overleftarrow{\partial}_{\boldsymbol{p}} \overrightarrow{\partial}_{\boldsymbol{x}}) \Big) f^W \\ &\quad - \Gamma^W \Big(\cos \frac{\hbar}{2} (\overleftarrow{\partial}_{\boldsymbol{x}} \overrightarrow{\partial}_{\boldsymbol{p}} - \overleftarrow{\partial}_{\boldsymbol{p}} \overrightarrow{\partial}_{\boldsymbol{x}}) \Big) f^W + S[f^W]. \end{aligned} \tag{6.52}$$

6.3 Multi-band systems

6.3.1 Bloch states, Wannier states and Envelope transformations

The purpose of this section is to generalize the Wigner transform to multi-band systems. This will be done by utilizing a technique known as envelope

transformations or envelope functions, which will seamlessly merge the concept of band structures with the formalism introduced above. Since band structure arises in systems with a periodic potential, we begin by discussing such systems, and some mathematics which naturally arises there.

Consider a single particle in tree dimensions, having the Hamiltonian

$$\hat{H} = \frac{\hat{\boldsymbol{p}}^2}{2m} + V(\hat{\boldsymbol{x}}), \tag{6.53}$$

where $V(\boldsymbol{x})$ is a potential satisfying the periodic conditions

$$V(\boldsymbol{x}) = V(\boldsymbol{x} + \boldsymbol{b}_i), \qquad i \in \{1, 2, 3\}. \tag{6.54}$$

One can then show that the eigenstates $|\psi\rangle$ of the system must themselves satisfy[11]

$$\langle \boldsymbol{x} + \boldsymbol{b}_i | \psi \rangle = e^{i\boldsymbol{k}\cdot\boldsymbol{b}_i} \langle \boldsymbol{x} | \psi \rangle, \qquad i \in \{1, 2, 3\}. \tag{6.55}$$

Such states are known as Bloch states, and the vector $\boldsymbol{k}$ as the vector of Bloch indices, or alternatively, as the crystal momentum. The Bloch states are denoted $|n, \boldsymbol{k}\rangle$, where n is the band index, needed to distinguish different Bloch states with the same crystal momentum.

Starting with a basis of Bloch states, one can define so called Wannier states[2] as

$$|n, \boldsymbol{j}\rangle = \int_B \frac{\mathrm{d}^3\boldsymbol{k}}{\sqrt{V_B}} e^{-i\boldsymbol{k}\cdot\boldsymbol{x}_{\boldsymbol{j}} + i\theta(\boldsymbol{k})} |n, \boldsymbol{k}\rangle, \tag{6.56}$$

where $\boldsymbol{j}$ is a vector of integers, $\boldsymbol{x}_{\boldsymbol{j}} = j_1\boldsymbol{b}_1 + j_2\boldsymbol{b}_2 + j_3\boldsymbol{b}_3$, $B = \{\boldsymbol{k} : |\boldsymbol{k}\cdot\boldsymbol{b}_i| \leq \pi\}$, V_B is the volume of B, and θ is some function of $\boldsymbol{k}$. The definition can be inverted to obtain the relation

$$\frac{1}{\sqrt{V_B}} \sum_{\boldsymbol{j}} e^{i\boldsymbol{k}'\cdot\boldsymbol{x}_{\boldsymbol{j}} - i\theta(\boldsymbol{k}')} |n, \boldsymbol{j}\rangle = \sum_{\boldsymbol{j}} \int_B \frac{\mathrm{d}^3\boldsymbol{k}}{V_B} e^{i(\boldsymbol{k}'-\boldsymbol{k})\cdot\boldsymbol{x}_{\boldsymbol{j}} - i\theta(\boldsymbol{k}') + i\theta(\boldsymbol{k})} |n, \boldsymbol{k}\rangle = |n, \boldsymbol{k}'\rangle. \tag{6.57}$$

Using the defining property of the Bloch states, we find that the Wannier states satisfy the relation

$$\langle \boldsymbol{x} | n, \boldsymbol{j}\rangle = \int_B \frac{\mathrm{d}^3\boldsymbol{k}}{\sqrt{V_B}} e^{-i\boldsymbol{k}\cdot\boldsymbol{x}_{\boldsymbol{j}} + i\theta(\boldsymbol{k}) - i\boldsymbol{k}\cdot\boldsymbol{x}_{\boldsymbol{j}'-\boldsymbol{j}}} \langle \boldsymbol{x} + \boldsymbol{x}_{\boldsymbol{j}'-\boldsymbol{j}} | n, \boldsymbol{k}\rangle = \langle \boldsymbol{x} + \boldsymbol{x}_{\boldsymbol{j}'-\boldsymbol{j}} | n, \boldsymbol{j}'\rangle, \tag{6.58}$$

meaning that different Wannier states of any single band are related by translation.

If we assume the Bloch states to be delta function normalized, so that $\langle n, \boldsymbol{k} | m, \boldsymbol{k}'\rangle = \delta_{nm}\delta(\boldsymbol{k} - \boldsymbol{k}')$ and $I = \sum_n \int_B \mathrm{d}^3\boldsymbol{k}\, |n, \boldsymbol{k}\rangle\langle n, \boldsymbol{k}|$, then making use of (6.56) and its inverse (6.57), it is straight forward to show that

$$I = \sum_{n\boldsymbol{j}} |n, \boldsymbol{j}\rangle\langle n, \boldsymbol{j}|, \tag{6.59}$$

while $\langle n, \boldsymbol{j}'|m, \boldsymbol{j}\rangle = \delta_{nm}\delta_{\boldsymbol{j}\boldsymbol{j}'}$. Thus, the Wannier states form an orthonormal basis. In particular, the fact that they are orthonormal means they must be localized, and accordingly the Wannier state basis is a basis of localized states, which is invariant under translations that respect the periodic symmetry.

Finally, we define envelope operators $\hat{E}_n$ as

$$\hat{E}_n = \hbar^{3/2} \int_B \mathrm{d}^3\boldsymbol{k}\, e^{-i\theta(\boldsymbol{k})} |\hbar\boldsymbol{k}\rangle\langle n, \boldsymbol{k}|, \tag{6.60}$$

where $|\hbar\boldsymbol{k}\rangle$ is the momentum state with momentum $\boldsymbol{p} = \hbar\boldsymbol{k}$. Given a state $|\psi\rangle$, we refer to $\hat{E}_n|\psi\rangle$ as an envelope transformation of $|\psi\rangle$. The functions $\psi_n^E(\boldsymbol{x}) = \langle \boldsymbol{x}|\hat{E}_n|\psi\rangle$ are referred to as envelope functions[4]. These satisfy

$$\psi_n^E(\boldsymbol{x}) = \hbar^{3/2} \int_B \mathrm{d}^3\boldsymbol{k}\, e^{-i\theta(\boldsymbol{k})} \langle \boldsymbol{x}|\hbar\boldsymbol{k}\rangle\langle n, \boldsymbol{k}|\psi\rangle = \int_B \frac{\mathrm{d}^3\boldsymbol{k}}{(2\pi)^{\frac{3}{2}}}\, e^{i\boldsymbol{k}\cdot\boldsymbol{x} - i\theta(\boldsymbol{k})} \langle n, \boldsymbol{k}|\psi\rangle. \tag{6.61}$$

Thus, the envelope functions are in fact Fourier transforms of functions which are zero for $\boldsymbol{k} \notin B$. Crucially, this means that the envelope functions are almost always more smooth than the wave function $\psi(\boldsymbol{x}) = \langle \boldsymbol{x}|\psi\rangle$. Further, we have in particular

$$\psi_n^E(\boldsymbol{x}_{\boldsymbol{j}}) = \int_B \frac{\mathrm{d}^3\boldsymbol{k}}{(2\pi)^{\frac{3}{2}}}\, e^{i\boldsymbol{k}\cdot\boldsymbol{x}_{\boldsymbol{j}} - i\theta(\boldsymbol{k})} \langle n, \boldsymbol{k}|\psi\rangle = \sqrt{\frac{V_B}{2\pi}} \langle n, \boldsymbol{j}|\psi\rangle. \tag{6.62}$$

This tells us both that there is an important relationship between envelope transformations and Wannier states, and by (6.59) also that all information about the wave function is contained in the value of the envelope functions at the discrete set of points $\boldsymbol{x}_{\boldsymbol{j}}$.

It is easily seen that the envelope operators satisfy $\hat{E}_n^\dagger \hat{E}_n = \hat{P}_n$ and $\hat{E}_n \hat{E}_m^\dagger = \delta_{nm}\hat{P}_B$, where $\hat{P}_n$ and $\hat{P}_B$ are projection operators such that $\hat{P}_n|m, \boldsymbol{k}\rangle = \delta_{nm}|m, \boldsymbol{k}\rangle$, while $\hat{P}_B|\boldsymbol{p}\rangle = |\boldsymbol{p}\rangle$ if $\boldsymbol{p}/\hbar \in B$ and zero otherwise. We then also have

$$\sum_n \hat{E}_n^\dagger \hat{E}_n = I. \tag{6.63}$$

Given an operator $\hat{A}$, we refer to $\hat{E}_n \hat{A} \hat{E}_m^\dagger$ as an envelope transformation of $\hat{A}$. Using (6.63) we have

$$\mathrm{Tr}\, \hat{A} = \sum_n \mathrm{Tr}\, \hat{E}_n^\dagger \hat{E}_n \hat{A} = \sum_n \mathrm{Tr}\, \hat{E}_n \hat{A} \hat{E}_n^\dagger. \tag{6.64}$$

Further, we also have

$$\hat{E}_n \hat{A} \hat{B} \hat{E}_m^\dagger = \sum_l \hat{E}_n \hat{A} \hat{E}_l^\dagger \hat{E}_l \hat{B} \hat{E}_m^\dagger. \tag{6.65}$$

Combining (6.64) and (6.65) we get

$$\operatorname{Tr}\hat{A}\hat{B} = \sum_{nm} \operatorname{Tr}\hat{E}_n\hat{A}\hat{E}_m^\dagger\hat{E}_m\hat{B}\hat{E}_n^\dagger \tag{6.66}$$

so that in particular

$$\langle A\rangle = \operatorname{Tr}\hat{A}\hat{\rho} = \sum_{nm} \operatorname{Tr}\hat{E}_n\hat{\rho}\hat{E}_m^\dagger\hat{E}_m\hat{A}\hat{E}_n^\dagger. \tag{6.67}$$

6.3.2 The multi-band Wigner transformation

We now define a multi-band version of the Wigner transform, as the composition of the standard Wigner transform with an envelope transformation. That is, given an operator $\hat{A}$, we combine (6.60) and (6.26), defining

$$\begin{aligned} A^w_{nm}(\boldsymbol{x},\boldsymbol{k}) &= (\hat{E}_n\hat{A}\hat{E}_m^\dagger)^W(\boldsymbol{x},\hbar\boldsymbol{k}) = \int \mathrm{d}^3\boldsymbol{p}'\, e^{i\boldsymbol{p}'\cdot\boldsymbol{x}/\hbar}\langle\hbar\boldsymbol{k}+\boldsymbol{p}'/2|\hat{E}_n\hat{A}\hat{E}_m^\dagger|\hbar\boldsymbol{k}-\boldsymbol{p}'/2\rangle \\ &= 8\iint_{B^2}\mathrm{d}^3\boldsymbol{k}'\mathrm{d}^3\boldsymbol{k}''\, e^{i(\boldsymbol{k}-\boldsymbol{k}'')\cdot\boldsymbol{x}/\hbar}\langle n,\boldsymbol{k}'|\hat{A}|m,\boldsymbol{k}''\rangle\delta(\boldsymbol{k}'+\boldsymbol{k}''-2\boldsymbol{k}). \end{aligned} \tag{6.68}$$

We also define $A^w(\boldsymbol{x},\boldsymbol{k})$ as the matrix with elements $A^w_{nm}(\boldsymbol{x},\boldsymbol{k})$. Similar definitions, as well as analogs to the derivations below, can be found in the literature[3].

Like the standard Wigner transform, the multi-band Wigner transform respects the adjoint operation. Indeed, $(A^\dagger)^w_{nm} = (\hat{E}_n\hat{A}^\dagger\hat{E}_m^\dagger)^W = ((\hat{E}_m\hat{A}\hat{E}_n^\dagger)^\dagger)^W = (\hat{E}_m\hat{A}\hat{E}_n^\dagger)^{W\star} = A^{w\star}_{mn} = (A^{w\dagger})_{nm}$. Further, for $\boldsymbol{k}',\boldsymbol{k}''\in B$ we have $|(\boldsymbol{k}'+\boldsymbol{k}'')\cdot\boldsymbol{b}_i| \le |\boldsymbol{k}'\cdot\boldsymbol{b}_i| + |\boldsymbol{k}'\cdot\boldsymbol{b}_i| \le 2\pi$, so that also $(\boldsymbol{k}'+\boldsymbol{k}'')/2\in B$. Thus, because of the delta function in (6.68), we must have $A^w(\boldsymbol{x},\boldsymbol{k}) = 0$ whenever $\boldsymbol{k}\notin B$. Making use of this together with (6.64) and (6.28), we get

$$\operatorname{Tr}\hat{A} = \sum_n \int \mathrm{d}^3\boldsymbol{x}\int\frac{\mathrm{d}^3\boldsymbol{k}}{(2\pi)^3}\,A^w_{nn}(\boldsymbol{x},\boldsymbol{k}) = \int\mathrm{d}^3\boldsymbol{x}\int_B\frac{\mathrm{d}^3\boldsymbol{k}}{(2\pi)^3}\operatorname{Tr}A^w(\boldsymbol{x},\boldsymbol{k}). \tag{6.69}$$

Similarly, we can combine (6.66) and (6.27) to get

$$\operatorname{Tr}\hat{A}\hat{B} = \int\mathrm{d}^3\boldsymbol{x}\int_B\frac{\mathrm{d}^3\boldsymbol{k}}{(2\pi)^3}\operatorname{Tr}A^w(\boldsymbol{x},\boldsymbol{k})B^w(\boldsymbol{x},\boldsymbol{k}). \tag{6.70}$$

Finally, using (6.65) we have

$$\begin{aligned} (\hat{A}\hat{B})^w_{nm} &= (\hat{E}_n\hat{A}\hat{B}\hat{E}_m)^W = \sum_l(\hat{E}_n\hat{A}\hat{E}_l^\dagger\hat{E}_l\hat{B}\hat{E}_m^\dagger)^W \\ &= \sum_l(\hat{E}_n\hat{A}\hat{E}_l^\dagger)^W\star(\hat{E}_l\hat{B}\hat{E}_m^\dagger)^W = \sum_l A^w_{nl}\star B^w_{lm}. \end{aligned} \tag{6.71}$$

Thus, defining a matrix Moyal product by $(A\star B)_{nm} = \sum_l A_{nl}\star B_{lm}$, we have

$$(\hat{A}\hat{B})^w = A^w\star B^w. \tag{6.72}$$

Making use of the differential expansion (6.47), we can write the matrix Moyal product as

$$(A \star B)_{nm} = \sum_l A_{nl} \star B_{lm} = \sum_l A_{nl} e^{\frac{i}{2}(\overleftarrow{\partial}_{\boldsymbol{x}}\overrightarrow{\partial}_{\boldsymbol{k}} - \overleftarrow{\partial}_{\boldsymbol{k}}\overrightarrow{\partial}_{\boldsymbol{x}})} B_{lm} \tag{6.73}$$
$$= (A\, e^{\frac{i}{2}(\overleftarrow{\partial}_{\boldsymbol{x}}\overrightarrow{\partial}_{\boldsymbol{k}} - \overleftarrow{\partial}_{\boldsymbol{k}}\overrightarrow{\partial}_{\boldsymbol{x}})} B)_{nm}.$$

However, since the ordinary matrix product is not commutative, the matrix Moyal bracket does not take the simple form of (6.49). But under the assumption that both A and B are Hermitian, we can instead write it as

$$\{\{A, B\}\} = \frac{A e^{\frac{i}{2}(\overleftarrow{\partial}_{\boldsymbol{x}}\overrightarrow{\partial}_{\boldsymbol{k}} - \overleftarrow{\partial}_{\boldsymbol{k}}\overrightarrow{\partial}_{\boldsymbol{x}})} B - B e^{\frac{i}{2}(\overleftarrow{\partial}_{\boldsymbol{x}}\overrightarrow{\partial}_{\boldsymbol{k}} - \overleftarrow{\partial}_{\boldsymbol{k}}\overrightarrow{\partial}_{\boldsymbol{x}})} A}{i\hbar} \tag{6.74}$$
$$= \frac{A e^{\frac{i}{2}(\overleftarrow{\partial}_{\boldsymbol{x}}\overrightarrow{\partial}_{\boldsymbol{k}} - \overleftarrow{\partial}_{\boldsymbol{k}}\overrightarrow{\partial}_{\boldsymbol{x}})} B - (A e^{\frac{i}{2}(\overleftarrow{\partial}_{\boldsymbol{x}}\overrightarrow{\partial}_{\boldsymbol{k}} - \overleftarrow{\partial}_{\boldsymbol{k}}\overrightarrow{\partial}_{\boldsymbol{x}})} B)^\dagger}{i\hbar} = \frac{2}{\hbar}\mathcal{I}m\, A e^{\frac{i}{2}(\overleftarrow{\partial}_{\boldsymbol{x}}\overrightarrow{\partial}_{\boldsymbol{k}} - \overleftarrow{\partial}_{\boldsymbol{k}}\overrightarrow{\partial}_{\boldsymbol{x}})} B,$$

where for any matrix X we define $\mathcal{I}m\, X$ as the anti-Hermitian component $(X - X^\dagger)/2i$.

Generalizing the proceedings of Section 6.2.2 in the obvious manor, we define the multi-band Wigner distribution as the multi-band Wigner transform of the density operator:

$$\rho^w_{nm}(\boldsymbol{x}, \boldsymbol{k}) = \int \mathrm{d}^3\boldsymbol{p}'\, e^{i\boldsymbol{p}'\cdot\boldsymbol{x}/\hbar} \langle \hbar\boldsymbol{k} + \boldsymbol{p}'/2 | \hat{E}_n \hat{\rho} \hat{E}^\dagger_m | \hbar\boldsymbol{k} - \boldsymbol{p}'/2 \rangle. \tag{6.75}$$

Since the multi-band Wigner transform respects the adjoint, ρ^w is a Hermitian matrix. Further, by (6.69) and (6.70) we have

$$N_f = \int \mathrm{d}^3\boldsymbol{x} \int_B \frac{\mathrm{d}^3\boldsymbol{k}}{(2\pi)^3} \operatorname{Tr} \rho^w(\boldsymbol{x}, \boldsymbol{k}) \qquad \text{and} \tag{6.76}$$

$$\langle A \rangle = \int \mathrm{d}^3\boldsymbol{x} \int_B \frac{\mathrm{d}^3\boldsymbol{k}}{(2\pi)^3} \operatorname{Tr} \rho^w(\boldsymbol{x}, \boldsymbol{k}) A^w(\boldsymbol{x}, \boldsymbol{k}). \tag{6.77}$$

Taking the multi-band Wigner transform of the Von Neumann equation 6.34, and making use of the fact that both H^w and ρ^w are Hermitian, we find

$$\frac{\partial \rho}{\partial t}^w = \{\{H^w, \rho^w\}\} = \frac{2}{\hbar}\mathcal{I}m\, H^w e^{\frac{i}{2}(\overleftarrow{\partial}_{\boldsymbol{x}}\overrightarrow{\partial}_{\boldsymbol{k}} - \overleftarrow{\partial}_{\boldsymbol{k}}\overrightarrow{\partial}_{\boldsymbol{x}})} \rho^w. \tag{6.78}$$

Applying the same procedure to the Master equation (6.12), we find

$$\frac{\partial \rho}{\partial t}^w = \{\{H^w, \rho^w\}\} - \frac{1}{2}\left(\Gamma^w \star \rho^w + \rho^w \star \Gamma^w\right) + S^w[\rho^w] \tag{6.79}$$
$$= \frac{2}{\hbar}\mathcal{I}m\, H^w e^{\frac{i}{2}(\overleftarrow{\partial}_{\boldsymbol{x}}\overrightarrow{\partial}_{\boldsymbol{k}} - \overleftarrow{\partial}_{\boldsymbol{k}}\overrightarrow{\partial}_{\boldsymbol{x}})} \rho^w - \mathcal{R}e\, \Gamma^w e^{\frac{i}{2}(\overleftarrow{\partial}_{\boldsymbol{x}}\overrightarrow{\partial}_{\boldsymbol{k}} - \overleftarrow{\partial}_{\boldsymbol{k}}\overrightarrow{\partial}_{\boldsymbol{x}})} \rho^w + S^w[\rho^w],$$

where we define $\mathcal{R}e\, X$ as the Hermitian component $(X + X^\dagger)/2$.

6.4 Classical limit and the Boltzmann equation

In the classical limit $\hbar \to 0$, we identify the Wigner distribution $f^W(\boldsymbol{x}, \boldsymbol{p})$ with the classical distribution function $f(\boldsymbol{x}, \boldsymbol{p})$. Taking the limit $\hbar \to 0$ of the Wigner transformed Von Neumann equation (6.50), amounts to keeping only the terms of the differential expansion that are of order zero in $\hbar$. Thus, we obtain the classical Liouville equation

$$\frac{\partial f}{\partial t} = H(\overleftarrow{\partial}_{\boldsymbol{x}} \overrightarrow{\partial}_{\boldsymbol{p}} - \overleftarrow{\partial}_{\boldsymbol{p}} \overrightarrow{\partial}_{\boldsymbol{x}}) f = \frac{\partial H}{\partial \boldsymbol{x}} \cdot \frac{\partial f}{\partial \boldsymbol{p}} - \frac{\partial H}{\partial \boldsymbol{p}} \cdot \frac{\partial f}{\partial \boldsymbol{x}}. \tag{6.80}$$

Applying the same procedure to (6.52), we obtain the Boltzmann equation

$$\frac{\partial f}{\partial t} = \frac{\partial H}{\partial \boldsymbol{x}} \cdot \frac{\partial f}{\partial \boldsymbol{p}} - \frac{\partial H}{\partial \boldsymbol{p}} \cdot \frac{\partial f}{\partial \boldsymbol{x}} - \Gamma f + S[f], \tag{6.81}$$

where Γ^W has also been identified with a classical function Γ.

Since the terms of order zero in $\hbar$ are also the lowest order terms in the differential expansion, the classical limit amounts to an assumption that all functions are slowly varying with $\boldsymbol{x}$ or $\boldsymbol{p}$. Of these, the easiest to justify is slow variations with $\boldsymbol{x}$. However, in a solid state system this assumption is in fact not justified, since the potential has large variations at an atomic size scale. However, we may get around this by first applying a set of envelope transformations, since these will normally smoothen the state, and if appropriately selected, also the potential.

Applying the Wigner transform after such envelope transformations, we are of course actually applying the multi-band Wigner transformation. Thus, when taking the limit of slow variation with $\boldsymbol{x}$, it is more appropriate to start out with (6.79). Keeping only the terms of differential order zero and two, we obtain

$$\begin{aligned} \frac{\partial \rho^w}{\partial t} = & -\frac{i}{\hbar}[H^w, \rho^w] - \frac{1}{2}\{\Gamma^w, \rho^w\} + \frac{1}{\hbar}\mathcal{R}e\, H^w(\overleftarrow{\partial}_{\boldsymbol{x}} \overrightarrow{\partial}_{\boldsymbol{k}} - \overleftarrow{\partial}_{\boldsymbol{k}} \overrightarrow{\partial}_{\boldsymbol{x}})\rho^w \\ & + \frac{1}{\hbar}\mathcal{I}m\, \Gamma^w(\overleftarrow{\partial}_{\boldsymbol{x}} \overrightarrow{\partial}_{\boldsymbol{k}} - \overleftarrow{\partial}_{\boldsymbol{k}} \overrightarrow{\partial}_{\boldsymbol{x}})\rho^w + S^w[\rho^w]. \end{aligned} \tag{6.82}$$

In order to obtain a multi-band version of the Boltzmann equation, we must transform this equation into a corresponding diagonal format. We do this by making use of a first order perturbation argument. Thus, we begin by making the decompositions $H^w = H_0 + \Delta H$, $\Gamma^w = \Gamma_0 + \Delta\Gamma$ and $\rho^w = \rho_0 + \Delta\rho$, where in all cases the matrix with subscript 0 is the diagonal component of the matrix on the left. We also define $S_0[g]$ as the diagonal component of the functional $S^w[g]$. Then defining the functional

$$\begin{aligned} \Lambda[g] = & -\frac{i}{\hbar}[\Delta H, g] - \frac{1}{2}\{\Delta\Gamma, g\} + S^w[g] - S_0[\rho_0] \\ & + \frac{1}{\hbar}\mathcal{R}e\, H^w(\overleftarrow{\partial}_{\boldsymbol{x}} \overrightarrow{\partial}_{\boldsymbol{k}} - \overleftarrow{\partial}_{\boldsymbol{k}} \overrightarrow{\partial}_{\boldsymbol{x}})g + \frac{1}{\hbar}\mathcal{I}m\, \Gamma^w(\overleftarrow{\partial}_{\boldsymbol{x}} \overrightarrow{\partial}_{\boldsymbol{k}} - \overleftarrow{\partial}_{\boldsymbol{k}} \overrightarrow{\partial}_{\boldsymbol{x}})g, \end{aligned} \tag{6.83}$$

we can write (6.82) as

$$\frac{\partial \rho}{\partial t}^{w} = -\frac{i}{\hbar}[H_0, \rho^w] - \frac{1}{2}\{\Gamma_0, \rho^w\} + \Lambda[\rho^w] + S_0[\rho_0]. \tag{6.84}$$

Now we will make the assumption that the magnitude of the functional Λ is in some sense small, and the ansatz that this causes the non-diagonal component $\Delta\rho$ to be small as well. Thus, we can make a linear expansion of $S^w[\rho^w]$ in $\Delta\rho$. Further, since both Λ and $\Delta\rho$ are small, any term in $\Lambda[\rho^w]$ containing $\Delta\rho$ will in fact be second order, and so to the first order we can make the substitution $\Lambda[\rho^w] = \Lambda[\rho_0]$ in (6.84). In particular, for the non-diagonal element ρ_{nm} of ρ^w we then get

$$\frac{\partial \rho_{nm}}{\partial t} = -\frac{i}{\hbar}(E_n - E_m)\rho_{nm} - \frac{1}{2}(\Gamma_n + \Gamma_m)\rho_{nm} + \Lambda[\rho_0]_{nm}, \tag{6.85}$$

where E_n and Γ_n are respectively the elements of the diagonal matrices H_0 and Γ_0. Noting that $\Gamma_n < 0$ would cause an unphysical exponential growth of some ρ_{nm}, we will assume $\Gamma_n > 0$. (6.85) then implies that effects of the initial value of ρ_{nm} will quickly die out, and that we will be left with the long term solution

$$\rho_{nm} = \int_{-\infty}^{t} \mathrm{d}t'\, e^{-\frac{i}{\hbar}(E_n - E_m)(t-t') - \frac{1}{2}(\Gamma_n + \Gamma_m)(t-t')} \Lambda(t')_{nm}, \tag{6.86}$$

where we have defined $\Lambda(t) = \Lambda[\rho_0(t)]$. Assuming that the frequency $(E_n - E_m)/\hbar$ is much faster than the temporal variations of Λ, there will be a significant cancellation between different regions of the integral, and the leading contribution will come from the region $t' \approx t$, where the exponential is decreasing most rapidly. Thus, we may substitute $\Lambda(t') \approx \Lambda(t)$, obtaining

$$\rho_{nm}(t) = \frac{\Lambda(t)_{nm}}{i(E_n - E_m)/\hbar + (\Gamma_n + \Gamma_m)/2}. \tag{6.87}$$

Accordingly, we have verified the ansatz that small values of Λ will cause the non-diagonal component of ρ^w to be small, and we have identified the precise condition as $\hbar\Lambda(t)_{nm} \ll |E_n - E_m|$.

Finally, we turn to the diagonal elements of (6.84). Denoting the diagonal elements of ρ^w as f_n, the diagonal elements of $S[\rho_0]$ as $S_n[\boldsymbol{f}]$, and keeping in mind that we are still making the substitution $\Lambda[\rho^w] = \Lambda[\rho_0]$, we obtain

$$\frac{\partial f_n}{\partial t} = \frac{1}{\hbar}\frac{\partial E_n}{\partial \boldsymbol{x}} \cdot \frac{\partial f_n}{\partial \boldsymbol{k}} - \frac{1}{\hbar}\frac{\partial E_n}{\partial \boldsymbol{k}} \cdot \frac{\partial f_n}{\partial \boldsymbol{x}} - \Gamma_n f_n + S_n[\boldsymbol{f}], \tag{6.88}$$

which is a multi-band generalization of the Boltzmann equation (6.81). It is common to approximate the scattering term $S_n[\boldsymbol{f}]$ as a functional which is linear and local in $\boldsymbol{x}$. Thus, introducing the integral kernel $\Gamma_{nm}(\boldsymbol{k}, \boldsymbol{k}')$, we have[15]

$$S_n[\boldsymbol{f}](\boldsymbol{x}, \boldsymbol{k}) = \sum_m \int \mathrm{d}^3\boldsymbol{k}'\, \Gamma_{nm}(\boldsymbol{k}, \boldsymbol{k}') f_m(\boldsymbol{x}, \boldsymbol{k}'), \tag{6.89}$$

Inserting this in (6.88) and making use of the fact that $\sum_n \iint \mathrm{d}^3\boldsymbol{k}\mathrm{d}^3\boldsymbol{x} f_n(\boldsymbol{x},\boldsymbol{k})$ is constant, and that the integral of the differential terms cancel by Gauss theorem, we find

$$\sum_n \iint \mathrm{d}^3\boldsymbol{k}\mathrm{d}^3\boldsymbol{x} \left(\Gamma_n(\boldsymbol{x},\boldsymbol{k}) - \sum_m \int \mathrm{d}^3\boldsymbol{k}'\, \Gamma_{mn}(\boldsymbol{k}',\boldsymbol{k})\right) f_n(\boldsymbol{x},\boldsymbol{k}) = 0, \tag{6.90}$$

and since this must hold for all distributions f_n, we must have

$$\Gamma_n(\boldsymbol{x},\boldsymbol{k}) = \sum_m \int \mathrm{d}^3\boldsymbol{k}'\, \Gamma_{mn}(\boldsymbol{k}',\boldsymbol{k}). \tag{6.91}$$

Inserting this and (6.89) in (6.88), we obtain

$$\begin{aligned}\frac{\partial f_n}{\partial t} = &\frac{1}{\hbar}\frac{\partial E_n}{\partial \boldsymbol{x}} \cdot \frac{\partial f_n}{\partial \boldsymbol{k}} - \frac{1}{\hbar}\frac{\partial E_n}{\partial \boldsymbol{k}} \cdot \frac{\partial f_n}{\partial \boldsymbol{x}} \\ &+ \sum_m \int \mathrm{d}^3\boldsymbol{k}' \Big(\Gamma_{nm}(\boldsymbol{k},\boldsymbol{k}') f_m(\boldsymbol{x},\boldsymbol{k}') - \Gamma_{mn}(\boldsymbol{k}',\boldsymbol{k}) f_n(\boldsymbol{x},\boldsymbol{k})\Big),\end{aligned} \tag{6.92}$$

which is the standard form of the multi-band Boltzmann equation[15, 11, 22].

Part II

Progress towards the implementation of a general purpose thermoelectric transport solver for heterostructures

Chapter 7

Context of published and submitted works

7.1 Motivation

My work has been motivated by the problem of calculating thermoelectric transport coefficients in nanoscale heterostructures. For most thermoelectric applications, the Boltzmann equation (6.92) is relied upon as the appropriate transport formalism. By the discussion of Section 6.4 this is certainly justified in many bulk systems, since one can then find a single envelope transform which transforms the Hamiltonian into a function that is both diagonal and independent of $\boldsymbol{x}$. Indeed, in the bulk case it would usually be the failure of the Markov approximation which would make the Boltzmann equation inappropriate. In cases where the field strength is very high, there could also be problems with the assumption of slow spatial variations, but this is usually not the case when calculating thermoelectric coefficients, since we are typically interested in the linear regime.

In nanoscale heterostructures however, the situation is different. In the case of a non-periodic heterostructure, there will not exist an envelope transform which makes the Hamiltonian independent of position, even when no field is applied. And since the envelope transformed Hamiltonian will have variations on the nanoscale, the step from (6.79) to (6.82) is not justified, since it assumes slow spatial variations. In the case of a periodic heterostructure such as a superlattice, one will be able to find an envelope transform which makes the Hamiltonian independent of position, so (6.82) should in fact apply. However, if the superlattice period is large, the bands of the structure will be very close in energy, so that the requirement $\Lambda(t)_{nm} \ll |E_n - E_m|$ from below (6.87) may fail. Accordingly, in this case the step from (6.82) to (6.88) is not justified.

Thus, the applicability of the Boltzmann equation to the problem at hand is not guarantied. This can also be argued from the discussion in Section 2.3, by which it seems clear that if the size scale of the heterostructure is gradually increased, there will be a transition from the coherent to the incoherent regime. Clearly, the Boltzmann equation will not be able to pick up this transition, since it is not at all concerned with the coherence of the particles it describes. However, the fact that the Boltzmann equation is not strictly justified, does not by itself guarantee that calculations will deviate significantly from other methods.

Because of this, one of the first questions we wanted to answer, was how big of a difference one can expect between a semiclassical model like the Boltzmann equation, and a more general method. Work by Wacker[28] has shown that there can be a substantial difference between the Boltzmann equation and NEGF

in superlattice transport. However, his work was mostly concerned with high field applications, and not with the linear regime. In terms of the functional Λ, Wacker's work shows that the Boltzmann equation can be expected to fail when the first term of the second line of (6.83) is to large. For thermoelectric applications, where we are typically in the linear regime, this term can be assumed to be arbitrarily small, and so we are more concerned with the terms from the first line of (6.83), particularly those involving Γ and S, which describe scattering.

In order to directly observe whether Wacker's results generalize to the linear regime, we set out to construct a relatively simple transport model, which could be compared to the Boltzmann equation in a straight forward manor. As material system superlattices of Mercury-Cadmium-Telluride was chosen, since this was the system on which we were likely to do the later calculations. As a scattering model, we made use of the Büttiker approximation. This was mostly because this approximation can be implemented in ballistic transport frameworks.

7.2 The Büttiker approximation

Within the NEGF framework, the Büttiker approximation can be considered as an approximation to the scattering self energy Σ_s introduced in (5.47). The approximation is expressed in terms of the Fourier transformed self energy $\Sigma_s(E)$ as

$$\Sigma_s^r(E) = \sum_\phi \Sigma_{s\phi}^r(E), \quad \text{and} \tag{7.1}$$

$$\Sigma_s^<(E) = \sum_\phi i\Gamma_{s\phi}(E) g_\phi(E), \tag{7.2}$$

where $\Gamma_{s\phi} = i(\Sigma_{s\phi}^r - \Sigma_{s\phi}^{r\dagger})$ is positively definite, and $g_\phi(E) \geq 0$. As we discuss to some length in our third paper (Paper III), it seems highly plausible that $\Gamma_s(E) = i(\Sigma_s^r(E) - \Sigma_s^a(E))$ is positively definite, in which case (7.1) is satisfied with $\{\Sigma_{s\phi}^r\}_\phi = \{\Sigma_s^r\}$. Thus, the approximation consists of the the assumption that the lesser scattering self energy can be expressed as (7.2) with the same set of matrices $\Sigma_{s\phi}^r$. In our third paper we consider an important special case of this, namely the one where the self energies $\Sigma_s^r(E)$ and $\Sigma_s^<(E)$ commute at all energies. In that case we may choose $\Sigma_{s\phi}^r = \theta_\phi |\phi\rangle\langle\phi|$, where the vectors $|\phi\rangle$ make up an orthonormal basis of eigenvectors, and θ_ϕ are the corresponding eigenvalues. Since $\Sigma_s^<(E)$ has the same eigenvector expansion, (7.2) follows immediately.

Combining the Büttiker approximation with (5.63)-(5.67), and also making use of (5.74), we see that the total self energies $\Sigma^r(E)$ and $\Sigma^<(E)$ can be written

as

$$\Sigma^r(E) = \sum_\alpha \Sigma^r_\alpha(E), \quad \text{and} \tag{7.3}$$

$$\Sigma^<(E) = \sum_\alpha i\Gamma_\alpha(E) h_\alpha(E), \tag{7.4}$$

where the summation index α runs both over the leads p and the indices ϕ, and where $h_p(E) = f_p(E)$ and $h_\phi(E) = g_\phi(E)$. Thus, we can reinterpret the equations as describing a transport problem without scattering, but with an additional set of "fictitious leads" indexed by ϕ, in which the electrons have arbitrary distributions g_ϕ rather than equilibrium distributions f_ϕ. These fictitious leads are sometimes referred to as Büttiker probes.

Since there is no scattering in the reinterpreted problem, electron motion within the system S can be treated in a coherent framework, while the effects of both the real and fictitious leads can be dealt with by Landauer-Büttiker theory, as discussed in Chapter 2. In fact, it was in precisely that context Büttiker first introduced fictitious leads in order to study the effects of coherence loss in electronic devices[5]. In our case, the fact that we could reinterpret the model as a ballistic problem in this way, meant it could be implemented in the ballistic transport framework Kwant[12, 1].

In order to define a scattering model within the Büttiker approximation, one must specify the self energy operators $\Sigma^r_{s\phi}$, as well as a model of the distribution functions g_ϕ. In our calculations we set $\Sigma^r_{s\phi}(E) = -i\hbar/2\tau \cdot P_\phi$, where τ is a constant relaxation time, and P_ϕ is a projection operator projecting onto a small group of atoms. Further, we let the scatting mechanism be elastic and local, meaning that at each fictitious lead, the energy resolved current $i_\phi(E) = 0$. This latter condition implicitly defines the distribution functions $g_\phi(E)$.

7.3 Discussion of the first two publications

Our first publication (Paper I) is mainly a documentation of calculations we made in order to test our implementation of the Büttiker approximation within Kwant. These tests were done by comparing the calculations to the Boltzmann equation, which we expected to be in agreement with the model in those cases, since the systems were all either bulk or short period super lattices. And indeed, the deviations between the two methods are quite small, and seem to have origins that are understandable. Partially, the deviation originates in the finite value of the scattering time τ, which even in Bulk system will result in small errors. Another major source of discrepancy, is that in order to make the calculations computationally tractable, we had to modify the scattering mechanism, so that the probe operators P_ϕ did not cover every atom. However, we believe that both of these discrepancies are under control, as the Büttiker results seem to converge toward the Boltzmann results when the relevant parameters are adjusted.

In our second publication (Paper II), we compare the Büttiker approximation to the Boltzmann equation in superlattices of longer period, and we also study

the effect of increasing the scattering time. By the discussion above, these are precisely the systems in which we would expect to observe major discrepancies between these two methods. And indeed this is precisely what we observe. In particular, upon increasing the super lattice period, we do observe a clear transition which is not picked up by the Boltzmann equation. In addition to the Boltzmann equation, we also compare these results to a semiclassical model based upon the incoherent transport expressions of Section 2.3.1, and indeed this is in much better agreement with our results at long periods. Accordingly, the observed transition seems to be a coherent-incoherent transition.

Concluding from this, it seems that if our results are to be reliable, we can not base our calculations on the Boltzmann equation, but must make use of a different formalism. It could be argued, as some of our reviewers did, that the scattering mechanism employed in our calculations is somewhat to simple and specialized to make very broad conclusions about this. However, if nothing else, our results at least show that applicability of the Boltzmann equation is not guarantied, and that considerable care must be taken.

7.4 Choice of formalism and method for the general transport framework

Having determined that the Boltzmann equation is not sufficiently general for our purposes, the next step was to find a formalism which is. Considering the discussions of part I, we see that there are at least five different approaches that should be considered. First, one may consider a direct evaluation of the path integral expressions of Chapter 3, with the time discretization size N set to a finite value. Secondly, we could make use of the perturbative NEGF framework, covered in Chapter 5. As a third option, we could calculate the thermoelectric coefficients by using the Kubo relations, or other linear response expressions, as described in Chapter 4. These expressions could also be evaluated directly through path integration, or we could make use of a perturbative expansion of the four point functions. The final option would be to make use of a Markovian master equation, as discussed in Section 6.1.

Let us first consider the question of path integration versus perturbative calculations. Both of these approaches involve approximations. In the path integral approach, the approximation consists of setting a finite value for N, while in the perturbative approach the approximation lies in the fact that we can only include a subset of the infinitely many Feynman diagrams. In the path integral approach, the computational burden increases very fast both with N and with the number of included single particle states. Thus, we are limited by the need to keep these parameters at a small value, which will again severely limit the quantitative accuracy of the method. In addition, it is commonly agreed that such non-perturbative techniques are required mostly in cases involving strong correlations, such as super conductors and fractional quantum hall systems.

Next, let us consider the Markovian master equation approach. This would in a sense be the most natural generalization of the Boltzmann equation, since we

are only modifying the assumptions of coherence between states, while keeping the assumption of Markovian dynamics. However, in many solid state systems the Markovian approximation is not formally justified. Consider the discussion below (6.5). In the case of phonon scattering, the time scale τ_B^r can be estimated from the optical phonon frequency, which typically lies in the range 10^{13}-10^{14} Hz. Thus, we estimate $\tau_B^r \sim 10^{-14}$-10^{-13} s = 10-100 ps. On the other hand, the time scale $\tau_F^<$ satisfies $\tau_F^< \lesssim \tau_p$, the momentum relaxation time. Since τ_p may also often extend into the range 10-100 ps, the condition $\tau_F^< \gg \tau_B^r$ for Markovian dynamics will often not hold. In addition to this, the computational requirements of the master equation approach is very similar to those of the non-Markovian NEGF method, the only difference being that NEGF requires an additional integral over energy.

Considering the discussion of the previous two paragraphs, it seems clear that the most appropriate formalisms are the two perturbative approaches, NEGF together with the perturbative evaluation of the Kubo relations. In choosing between these two methods, we originally concluded that the approach based on the Kubo relations would be best suited, since this is a linear formalism, and we are interested in linear thermoelectric coefficients. However, before being able to make much progress on this approach, we changed our mind and decided to make use of the NEGF formalism. The reason for this was the increased generality of the NEGF method, the fact that it is formulated in terms of Green's functions rather than four point functions, and thus seems easier to handle, and finally that we figured we could in any case calculate the linear transport coefficients by taking a numerical derivative of the currents. However, in retrospect this choice seems to have been a mistake, as will be discussed further in the concluding chapter (Chapter 9).

Having decided to make use of the NEGF formalism, the next step was to select a method by which to solve the NEGF equations (5.81) and (5.86). We quickly discovered that the RGF method[6] is particularly well suited to solve (5.81) in quasi-one-dimensional systems. However, in the presence of scattering, this equation must be solved self consistently with (5.86), and with expressions for the scattering self energies Σ_s^r and $\Sigma_s^<$. In the literature, the approach most commonly applied for this purpose, is to make use of an iterative procedure.

In the general case, the computational scaling of each iteration is $\sim (MN_g)^2$, where M is the dimension of the matrices $G(E)$, and N_g is the size of the integration grid. In a quasi-one-dimensional system $M \sim N_b Z$, where N_b is the number of bands included, and Z is the extent of the system in the z direction. Further, $N_g = N_E N_{kx} N_{ky}$, where N_E, N_{kx} and N_{ky} are respectively the sizes of integration grids over energy, and over the Bloch indices k_x and k_y. Thus, the full scaling of the method is $\sim N_{itt} N_b^2 Z^2 N_E^2 N_{kx}^2 N_{ky}^2$, with N_{itt} being the number of iterations required for convergence. Accordingly, without the introduction of drastic approximations, the solution of (5.81) and (5.86) is a daunting computational task.

We spent some time experimenting with the benchmarked nanoscale transport software NEMO5[8], which contains routines for the iterative solution of (5.81) and (5.86) within the self consistent Born approximation. However, while this

software is probably very well suited for the nanoscale electronic devices for which it is written, it turned out to be difficult to repurpose it for our somewhat different application. In addition, the fact that we required both a large extent in the z direction, as well as a dense integration grid over k_x and k_y, makes the scaling of the iterative approach a big problem.

7.5 Discussion of the third paper

Accordingly, we decided to abandon both our work on NEMO5, and in fact the iterative approach all together. Instead, we decided to focus on Monte Carlo methods, motivated somewhat by the success of such methods in solving the Boltzmann equation (see Section 8.1 below, and Refs. [15, 22]).

Our third paper (Paper III) is concerned with this subject. The paper describes a Monte Carlo algorithm for evaluating the NEGF lead current given by (5.102). We prove formally that under certain conditions, the expectation value of the estimator equals the lead current. In particular, this is under a particular positivity condition which we show to be satisfied in the self consistent Born approximation. Further, the method is exclusively concerned with the solution of (5.86), which must be assumed to satisfy a certain condition of linearity. In order for this linearity condition to be satisfied, $\Sigma_s^<$ must be a linear function of $G^<$, while G^r can not be a function of $G^<$, so that (5.81) and (5.86) can not be coupled. Accordingly, the linearity requirement is a major limitation of the method. We discuss some options for getting around this. In particular, we argue that with appropriate linearization the method is in any case applicable to linear transport, and we show this explicitly in the case of elastic scattering.

On the other hand, the positivity requirement seems to be an absolute requirement of the method. It is presently unclear under what conditions this is fulfilled beyond the self consistent Born approximation, but we do find some heuristic justification for the assumption in the general case, as long as we specialize to stationary transport.

We also perform some numerical tests of the method. In particular, we calculate conductances of a few short nanowires, and use this to estimate the conductivity in the wires. We compare the results to standard methods like the iterative approach, and find the Monte Carlo results to be in agreement with the alternative methods within a few percent. The relative standard deviation of the Monte Carlo results is also about one percent, so this is as expected.

When it comes to the performance of the method, the nanowire system is not the best suited model for testing this. This is because the Monte Carlo method must be expected to be most competitive in systems with a dependence on a crystal momentum $\boldsymbol{k}$, of which there is none in short nanowires. Indeed, part of the reason for employing the Monte Carlo method in the first place, is to avoid the numerically costly integration grid over $\boldsymbol{k}$, which must be employed by iterative methods. We nevertheless decided to do the first calculations on nanowires, since the introduction of a $\boldsymbol{k}$-dependence complicates the implementation, and we felt that the initial tests should be performed with as simple of an implementation

as possible. For the same reason we again made use of Büttikers approximation as the scattering model.

Chapter 8

Results not submitted for publication

In this chapter I present some calculations done during the course of my work, which are either not sufficiently new or have not matured sufficiently far for publication. Nevertheless, they serve as useful illustrations, and may form important elements of a future general transport framework.

In Section 8.1 I describe some experiments with the Boltzmann Monte Carlo method, which was the first method for transport calculations I pursued. Section 8.1.1 includes results obtained using a direct simulation approach, where currents are estimated directly from the flow of particles through a simulated system. Section 8.1.2 includes a few simple tests of a method where Boltzmann Monte Carlo is combined with the Green-Kubo relations, by which linear transport coefficients can be calculated from correlation functions at equilibrium. While the direct method is applied to superlattices, the Green-Kubo method is only tested in a simple bulk system.

In Section 8.3 I discuss some experiments with a method for making the calculation of the retarded Green's function G^r more efficient. This was work performed before we landed on the RGF method as the best suited method for this purpose in quasi-one-dimensional systems. Put shortly, the method treats exactly only those states which have an energy close to the range of interest, and handles the remaining states using a perturbative expansion.

Finally, in Section 8.2 I present some further results of the NEGF Monte Carlo method, which were omitted from our third paper (Paper III) for reasons of brevity. While the paper illustrates the method on a set of thin nanowires, Section 8.2 includes results obtained from simulations of a small quantum dot, and of a thin film.

8.1 Boltzmann Monte Carlo

As discussed above, the Boltzmann equation is only applicable in a fairly limited range when quantitative accuracy is required. However, most of the important physical effects are still at work, so it serves well for illustrative purposes. In fact, two such effects, namely inelastic scattering and a self consistent electrostatic potential, have in this work only been investigated using the Boltzmann Monte Carlo method. In all other calculations presented in this thesis, scattering is assumed elastic, and electrostatic interactions between the charge carriers are ignored.

This is not because these effects are unimportant. As will be shown below, they are in fact very important. Instead, in the case of the NEGF Monte Carlo

calculations, it is simply because there are more fundamental complications and problems that must be solved first. In the case of our calculations using Kwant, these were made almost exclusively for the purpose of investigating the coherent-incoherent transition, and accordingly the introduction of further complications seemed unnecessary.

The Boltzmann Monte Carlo method is well described in the literature[22, 15]. Put shortly, it involves the explicit simulation of particles as they move through a device or material according to the classical equations of motion

$$\frac{\mathrm{d}\boldsymbol{x}}{\mathrm{d}t} = \boldsymbol{v} = \frac{1}{\hbar}\frac{\partial E}{\partial \boldsymbol{k}}, \tag{8.1}$$

$$\frac{\mathrm{d}\boldsymbol{k}}{\mathrm{d}t} = \frac{1}{\hbar}\boldsymbol{F} = -\frac{1}{\hbar}\frac{\partial E}{\partial \boldsymbol{x}}, \tag{8.2}$$

interrupted by random discontinuous transformations of the momentum $\boldsymbol{k}$, occurring with a rate given by the scattering rate $\Gamma(\boldsymbol{k}', \boldsymbol{k})$ from (6.92). In a multi-band simulation, these scattering events may also change the band index. It can be shown that this process results in the simulated particles being distributed according to a probability proportional to the distribution function $f(\boldsymbol{x}, \boldsymbol{k})$ which solves the Boltzmann equation[22, 15]. Thus, the process can be used to estimate any measurable quantity that can be expressed in terms of this distribution function.

8.1.1 Direct approach

In the direct simulation approach, we directly simulate a charge carrier, or a set of charge carriers, moving according to the procedure described above in the presence of an applied field, or other non-equilibrium perturbation. We may either consider a situation like that described in chapters 2 and 3.2, where some electronic device is connected to a set of leads, or we may simulate some bulk/periodic region of material. In the latter case, one will typically implement periodic boundary conditions, where only a single small region of material is simulated, and the charge carriers are instantly transported to the opposite side whenever they hit a boundary of this region.

Currents can be estimated from the rates by which the carriers exits different leads, or from the average velocity of particles at different locations. The spatial distribution of the particles can be used to calculate variations in charge carrier concentration. These variations are used to evaluate an electrostatic potential, which will act back on the charge carriers through (8.2), resulting in a self consistent potential.

The calculations shown below are performed with highly simplifying approximations. The charge carrier bands are assumed parabolic, according to the relation $E = E_0 + U(\boldsymbol{x}) + \frac{\hbar^2}{2m^\star}\boldsymbol{k}^2$, where $U(\boldsymbol{x})$ is the electrostatic potential, E_0 is a material specific band minimum, and $m^\star$ is a material specific effective mass. A single simulation may contain different materials in different regions, and so there may be a spatial dependency in the parameters E_0 and $m^\star$ as well.

Further, the scattering mechanism is also based on a fairly unphysical phenomenological approximation, where the charge carriers are affected by a continuous thermal noise. Thus, rather than introducing discontinuous scattering events, we modify (8.2) to

$$\frac{\mathrm{d}\boldsymbol{k}}{\mathrm{d}t} = \frac{1}{\hbar}\boldsymbol{F} - \gamma\boldsymbol{k} + \frac{1}{\hbar}\sqrt{2\gamma m^\star k_B T}\boldsymbol{\eta}(t), \tag{8.3}$$

where T is the local lattice temperature, and $\boldsymbol{\eta}$ is a stochastic noise term satisfying $\langle \eta_i(t)\eta_j(t')\rangle = \delta_{ij}\delta(t-t')$. It can be shown that in the absence of a force term $\boldsymbol{F}$, the mean square $\langle \boldsymbol{k}^2\rangle$ will satisfy the equation

$$\frac{\mathrm{d}}{\mathrm{d}t}\langle \boldsymbol{k}^2\rangle = \frac{2\gamma}{\hbar^2}\left(3m^\star k_B T - \langle \hbar^2\boldsymbol{k}^2\rangle\right), \tag{8.4}$$

which has the correct equilibrium solution $\langle \frac{\hbar^2\boldsymbol{k}^2}{2m^\star}\rangle = \frac{3}{2}k_B T$.

Finally, the geometries of the simulations are quasi-one-dimensional. Thus, the material composition, electrostatic potential, and temperature varies only along a single direction. As mentioned, the electrostatic potential is calculated self consistently. The temperature on the other hand, is either constant, or varies linearly.

8.1.1.1 IV- and qV-characteristics

Among the most common things to calculate using Boltzmann Monte Carlo simulations, are IV-characteristics, which show how the current I varies with an applied voltage V. The IV-characteristic is an important characteristic of several different electronic devices. In Figure 8.1a we show the IV-characteristic of a superlattice, calculated by the method described above. The simulations were performed with a well thickness of 20, a barrier thickness of 2, and we imposed periodic boundary conditions over a single superlattice period. The effective mass in both layers was set to $m^\star = 1$, the barrier height to $b = E_{0b} - E_{0w} = 2$, and the temperature was set to $k_B T = 1$. The scattering rate parameter γ was set to 0.1. Finally, the solution of the Poisson equation to obtain the self consistent potential makes use of a permittivity of $\epsilon = 1$. The units of these parameters are arbitrary.

Note that the characteristic does not contain a region of negative differential conductivity, which one expects to see in certain high quality superlattices[28, 15]. This is because this classical model is not able to capture such resonant effects. Accordingly, the model is more appropriate when dealing with superlattices of poor quality, or with broad wells, as discussed in our second publication (Paper II).

Instead the superlattice current grows rapidly with the applied field. Starting out an order of magnitude lower than the bulk current, it grows exponentially with increasing V, and eventually approaches the bulk value. This can be understood from the fact that at high fields, the field will excite the particles into a higher state of energy, and so a larger proportion will have energies above

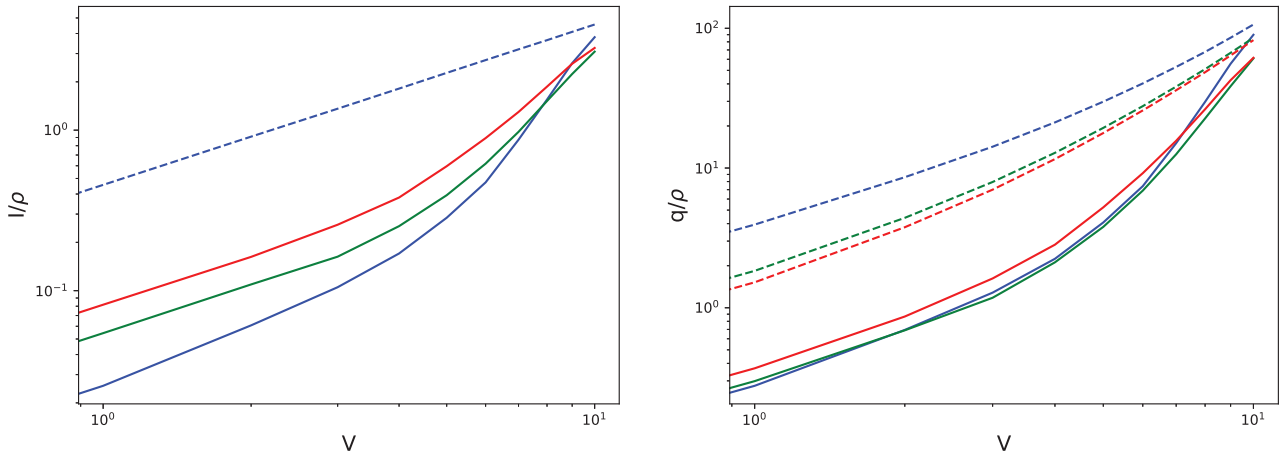

(a) IV-characteristic.

(b) qV-characteristic.

Figure 8.1: IV and qV characteristics of a superlattice heterostructure, according to an incoherent classical transport model. The IV-characteristic in (a) shows how the current I varies with the potential V over a single period. The current is normalized by the charge carrier density ρ. The qV-characteristic in (b) shows instead how the heat current q varies with V. The heat current is also normalized by ρ. Results shown in blue, green and red are respectively calculated with $\rho = 0.01$, $\rho = 1.0$ and $\rho = 2.0$. For comparison, corresponding bulk currents are included as dashed lines. In bulk, the normalized current I/ρ is independent of ρ, so only a single dashed line is shown in (a). All units are arbitrary.

the barrier height, where they are able to contribute to the current. We also see that the superlattice currents lie closer to the bulk values at higher charge carrier concentrations. This is because charge realignment of the superlattice cell will tend to reduce the barrier height. These effects are illustrated in Figure 8.1, which shows more details from the simulations.

In Figure 8.1b we show the qV-characteristic of the same superlattice. Unlike the normalized current, the normalized heat current q/ρ has a dependency on ρ also in bulk. This is because heat is a measure of entropy, and the average entropy per particle decreases with increasing density. In fact, the heat current is calculated as $q = J_E - \mu J$, where J_E is the energy flux, J the particle flux, and $\mu \sim \ln \rho$ is the chemical potential. However, in the superlattice the dependency of q/ρ on ρ is reversed, with q/ρ increasing with the carrier concentration. This is again because charge realignment reduces the barrier height, so that more particles are able to participate in the current. We also observe that unlike I/ρ, q/ρ is a nonlinear function of V also in the bulk case. This is because the field excites the particles to higher energies, so that they carry more heat.

8.1.1.2 Linear transport coefficients

In our work, we are interested in the linear conductivity, and in linear thermoelectric transport coefficients. To calculate such coefficients using the direct

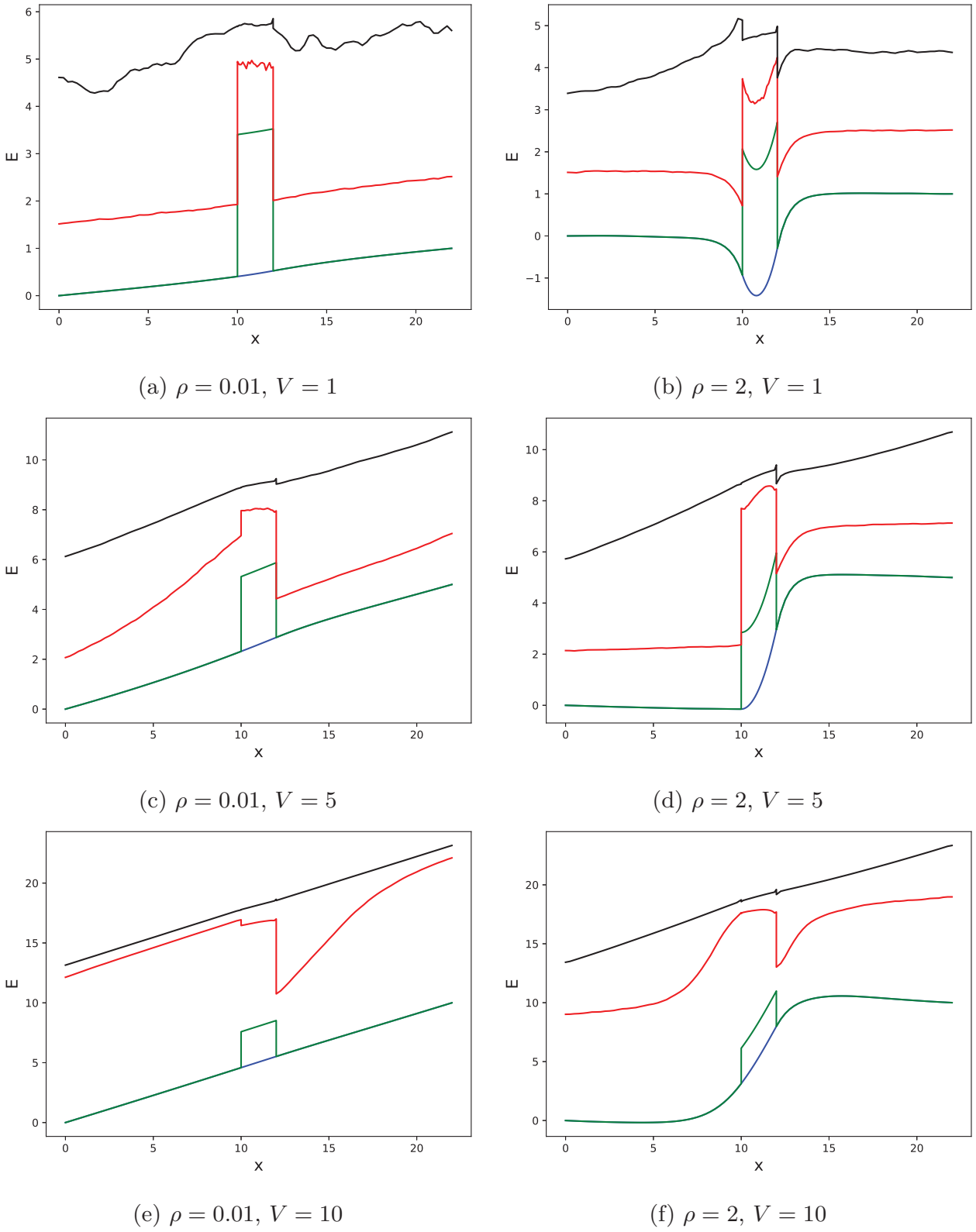

(a) $\rho = 0.01$, $V = 1$

(b) $\rho = 2$, $V = 1$

(c) $\rho = 0.01$, $V = 5$

(d) $\rho = 2$, $V = 5$

(e) $\rho = 0.01$, $V = 10$

(f) $\rho = 2$, $V = 10$

Figure 8.2: Transport through superlattice. x denotes position along direction of transport, ρ is charge carrier concentration, and V is the potential applied over a single period. The electrostatic potential energy is shown in blue, and the conduction band minimum in green. The average particle energy $\langle E \rangle$ is shown in red, while the black curve shows $\langle Ev \rangle / \langle v \rangle$, where v is particle velocity. The irregularities in the black curve at low fields is due to numerical noise. All units are arbitrary.

simulation approach, we apply a small field V, so that we are in the linear regime of the IV- and qV-characteristics of Figure 8.1, and then calculate the linear transport coefficient as response/stimuli. In Figure 8.3, we have calculated the mobility $\mu = \sigma/\rho = I/\rho V$ and the Seebeck coefficient α of a superlattice using this approach. The Seebeck coefficient is found using the relationship $\alpha = \Pi/T$ mentioned at the end of Section 4.2.5, where the Peltier coefficient is calculated as $\Pi = q/I$. The voltage difference V over a single superlattice period was set to $V = 0.5$. Observing Figure 8.1, this should be small enough to be more or less in the linear regime.

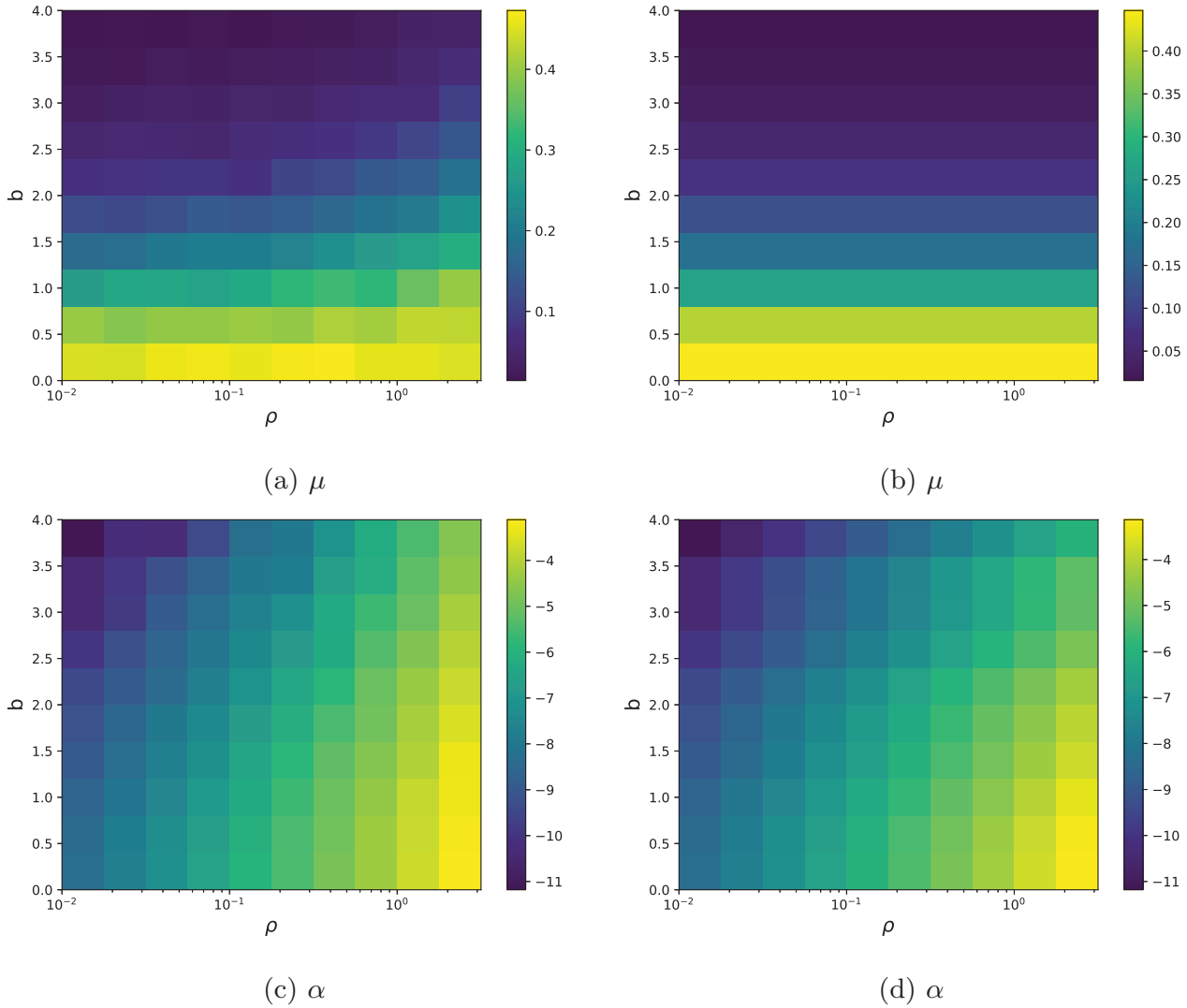

(a) μ (b) μ

(c) α (d) α

Figure 8.3: Mobility μ and Seebeck coefficient α of a superlattice structure, as a function of barrier height b and charge carrier concentration ρ. The figures to the left are calculated with a self consistent Poisson potential, while in the figures to the right no such potential is included. All units are arbitrary.

Figure 8.3 illustrates how the transport coefficients vary with the barrier height b, and with the charge carrier concentration ρ. The other parameters are

set identically as in the previous calculations. We have also included calculations both with and without a self consistent Poisson potential, in order to examine the importance of calculating this field. Observe first that, as expected, the mobility μ decreases rapidly when the barrier height is increased. The largest difference between the calculations with and without self consistent Poisson potential is also observed in the mobility. As expected, in the absence of a self consistent potential, the mobility is independent of ρ, but when such a potential is included, μ tends to fall of more slowly with b at high values of ρ. Again, this is because charge realignment tends to reduce the effective barrier height, as illustrated in Figure 8.2b.

The Seebeck coefficient α tends to increase in absolute value both as the barrier height b is increased, and as the charge carrier density ρ is decreased. The reason why $|\alpha|$ increases with b can again be understood from Figure 8.2. Since $q \sim \langle Ev \rangle$ and $I \sim \langle v \rangle$, we have $\alpha \sim q/I \sim \langle Ev \rangle / \langle v \rangle$, which is included as a black curve in Figure 8.2. As illustrated by the figure, this curve is forced to pass above the barrier.

Some difference can be observed between the calculations with and without self consistent Poisson potential also in the Seebeck coefficient, although the effect is less visible than it is for the mobility. In particular, at the highest values of ρ and b, α is increased from about -6 to about -5 when a self consistent potential is included. In the absence of a self consistent potential, the dependency of α on ρ is due only to the reduction of the chemical potential.

It deserves mentioning that the effects of charge realignment both on the mobility and on the Seebeck coefficient is underestimated to some extent in these calculations. This is because this particular semiclassical approach is not able to model tunneling through the barriers. Again observing Figure 8.2b, we see that also the shape of the barrier is different at high ρ, in such a way that if electrons were able to tunnel through thin sections of the barrier, then the effective barrier height would be reduced even further. At very high charge carrier concentrations, this could potentially remove almost the entire effect of the barrier.

8.1.1.3 Currents induced by temperature gradients

In order to estimate the electronic component k_e of the thermal conductivity using the direct simulation approach, it is necessary to impose a temperature gradient over the region of simulation. This poses a major problem, since we can then no longer impose periodic boundary conditions. A potential difference can be formulated in terms of an electrical field, which can be periodic even at $V > 0$. Thus, periodic boundary conditions can be imposed, as we have done above. An explicit temperature gradient however, will always explicitly break the periodic translation symmetry, so that this is no longer possible.

Thus, we must instead perform the simulation in a finite region, without periodic boundary conditions, but instead including two leads between which the currents can flow. This poses a problem, since the presence of the leads will introduce contact effects which must be dealt with in some way. As a test of the approach we have calculated the Seebeck coefficient again, using a more

direct approach where we estimate it from the electrical current induced by a temperature gradient. In particular, we have performed a simulation where the charge carrier density as well as the electrostatic potential is equal between the leads, but where the temperature differs by $\Delta T = 0.4$. This will induce a current of $I = \sigma(V + \alpha\Delta T) = \sigma(\alpha\Delta T - e\Delta\mu)$, so that we can estimate the Seebeck coefficient as

$$\alpha = \frac{I/\sigma + e(\mu_1 - \mu_2)}{\Delta T}, \tag{8.5}$$

where the chemical potential is estimated according to the non-degenerate model

$$\mu = T \ln \rho - \frac{3}{2} T \ln T - \frac{1}{2} T \ln 2\pi. \tag{8.6}$$

The result is shown in Figure 8.4a. Comparing this to Figure 8.3c, we see that the results are very similar, but that the result in Figure 8.4a is slightly smaller in absolute magnitude. This can be understood from the fact that the mobility, and thus indirectly other transport coefficients, will be underestimated in a simulation of finite size, due to an additional contact resistance.

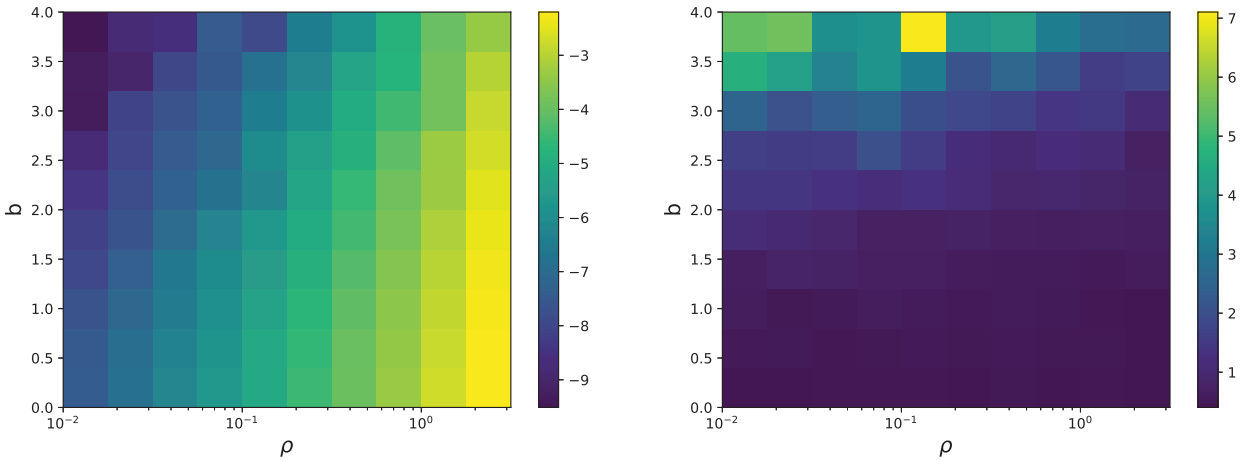

(a) α (b) L

Figure 8.4: Seebeck coefficient α and Lorenz coefficient L of a superlattice structure, as a function of barrier height b and charge carrier concentration ρ. The coefficients are calculated from currents induced by temperature gradients.

In Figure 8.4b we show the Lorenz coefficient, which is estimated as $L = k_e/\sigma T = (q - \Pi I)/\Delta T/\sigma T$. This result appears more noisy than the others, which is probably because more Monte Carlo samples are required to obtain an accurate average. In addition, we observe that the Lorenz coefficient becomes very high for large barriers. To understand the reason for this, we examine Figure 8.5. We observe that at the location of the barrier, the energy average $\langle Ev \rangle / \langle v \rangle$ increases with the barrier height, so that we always have $\langle Ev \rangle / \langle v \rangle > b$. However, in fact it increases even more rapidly in the regions outside of the barrier.

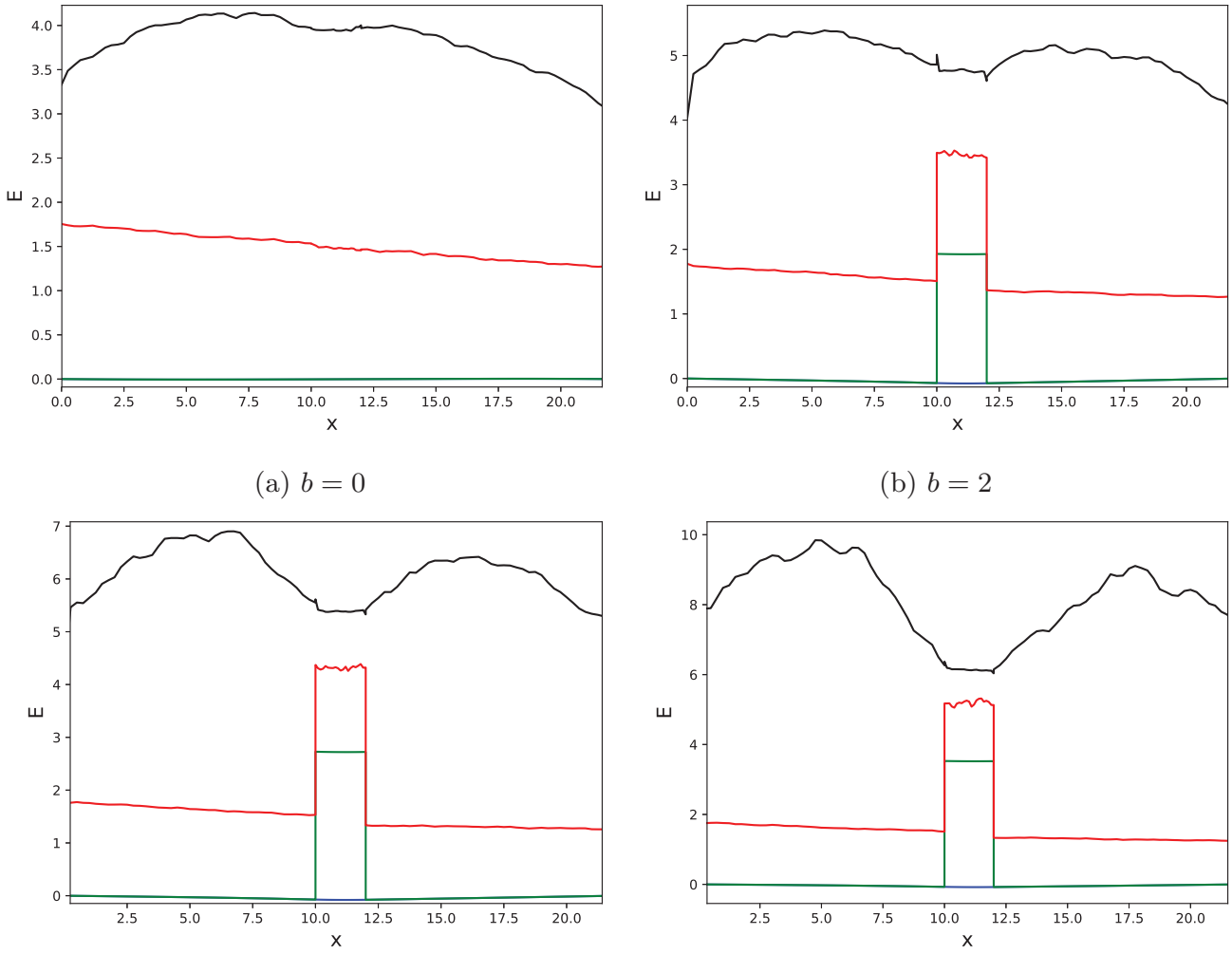

(a) $b = 0$

(b) $b = 2$

(c) $b = 2.8$

(d) $b = 3.6$

Figure 8.5: Transport through superlattice, induced by temperature gradients. b denotes the height of the barrier. The electrostatic potential energy is shown in blue, and the conduction band minimum in green. All four figures are obtained with the charge carrier concentration set to $\rho = 0.01$. The average particle energy $\langle E \rangle$ is shown in red, while the black curve shows $\langle Ev \rangle / \langle v \rangle$, where v is particle velocity. All units are arbitrary.

This is somewhat counter intuitive, and indeed reversed relative to Figure 8.2. However, it can be understood in the following way: The average $\langle Ev\rangle/\langle v\rangle$ is effectively a measure of the electronic component q_e of the heat flow. There is also a lattice contribution q_l to the heat flow, and in stationary state the total heat flow $q = q_e + q_l$ must be conserved throughout the material. The fraction of the total heat flow which is due to electrons will be $q_e/q = k_e/k = k_e/(k_e + k_l)$, where k_e and k_l are respectively the electronic and lattice contributions to the heat conductivity k. Now, since only a small fraction of the electrons is able to pass over the barrier, the electronic heat conductivity k_e is significantly reduced at the location of the barrier. Thus, let us give all quantities a superscript b to signify its value in the barrier region. We then have

$$\frac{q_e}{q_e^b} = \frac{q_e/q}{q_e^b/q} = \frac{k_e}{k_e^b} \cdot \frac{k_e^b + k_l^b}{k_e + k_l}. \tag{8.7}$$

We can in general expect also the lattice contribution to k to be somewhat reduced in the barrier region, but not exponentially like the electronic contribution. Thus, we expect the quantity on right of the equation above to be larger than one, and accordingly q_e and also $\langle Ev\rangle/\langle v\rangle$ will be larger in regions outside of the barriers.

Thus, the discussed effect seen in Figure 8.5 is in fact a real effect. However, the effect is probably overestimated in these calculations, since we are assuming a constant temperature gradient. This implies we are implicitly assuming $k_e^b + k_l^b = k_e + k_l$, so that by the equation above $q_e/q_e^b = k_e/k_e^b \gg 1$. In addition to this, the heat flow is overestimated somewhat due to contact effects in the simulation. This is seen from Figure 8.5a, in which there is no barrier, so that the heat current should be homogeneous in a true bulk system. Accordingly, since the heat flow is being overestimated by two distinct effects, it is unclear whether the behavior of the Lorenz coefficient seen in Figure 8.4b will be seen in real systems. This is particularly the case in superlattices with thin wells, where electrons will not have time to interchange energy with the lattice before reaching the next barrier.

8.1.1.4 Variation of the well thickness

In order to optimize the superlattice for thermoelectric applications, we must study not only how the relevant transport coefficients vary with material properties like charge carrier concentration and barrier height, but also with parameters describing the geometry of the superlattice. In a simple superlattice, like the one above, there are only two such parameters, namely the thicknesses of the two distinct layer types. In the absence of tunneling, it is quite clear that the barrier layer should be as thin as possible, so that it contributes a minimal resistance. However, when tunneling is considered, this conclusion does not hold, since having a to thin barrier could potentially remove the entire effect. Since the transport model considered here is not able to account for tunneling effects, we can thus not correctly optimize the well thickness, and we have accordingly set it arbitrarily to 2.

In the case of the well layer however, significant effects of varying the thickness will be present even in the classical model, so that we can at least illustrate its optimization. Thus, in Figure 8.6 we study how a few thermoelectric transport coefficients depend on the well thickness, which we denote d. In figures 8.6a and 8.6b we show respectively how the mobility and the Seebeck coefficient varies with d, and in 8.6c we show the power factor $\sigma\alpha^2$. The simulations are performed with a charge carrier concentration of $\rho = 0.01$ and a barrier height of $b = 2$. The other parameters are as above. As expected, the mobility increases when the distance between the barriers is increased. However, the absolute value of the Seebeck coefficient tends to drop. The reason for this is illustrated in Figure 8.7. There we see that the energy average $\langle Ev\rangle/\langle v\rangle$ is only raised in a moderately sized region around the barrier. Thus, as the thickness of the wells is increased, the fraction of the material in which $\langle Ev\rangle/\langle v\rangle$ is enlarged drops. Thus, the ratio $\pi = q/I \sim \langle Ev\rangle/\langle v\rangle$ will also drop, as will the Seebeck coefficient $\alpha = \pi/T$.

Examining Figure 8.6c, we see that even though the Seebeck coefficient is largest in the limit $d = 0$, the power factor is actually largest in the bulk limit $d \to \infty$, indicating that the increasing mobility is more important. However, for optimal thermoelectric properties, one must consider not only the power factor, but also the thermal conductivity κ of the material. In fact, if we define z as the ratio between the power factor and κ, one can show that unconstrained by other concerns, the material which is best suited for any thermoelectric application is the material in which zT is higher, where T is absolute temperature. Thus, as was briefly mentioned in the introduction, our goal is not to optimize the power factor, but the dimensionless figure of merit

$$zT = \frac{\sigma\alpha^2}{\kappa}T = \frac{\sigma\alpha^2 T}{\kappa_e + \kappa_l} = \frac{\alpha^2}{L}\left(1 + \frac{\kappa_l}{\kappa_e}\right)^{-1}. \tag{8.8}$$

To optimize this quantity, we will need a model also of the two contributions to the thermal conductivity, κ_e and κ_l. The electronic component may be calculated as $\kappa_e = \rho\mu LT$. As mentioned, it is questionable whether the Monte Carlo simulations discussed here result in values for the Lorenz coefficient that can be trusted. Because of this, we will arbitrarily make use of a constant model with $L = 1$. Further, inspired by the Matthiessen rule[15], we model the lattice contribution to κ as

$$\frac{1}{\kappa_l} = \frac{1}{\kappa_{l0}} + \frac{1}{\kappa_{lB}}, \tag{8.9}$$

where κ_{l0} is the bulk value of κ_l, and κ_{lB} describes a reduction from scattering on the barriers. We expect the barrier contribution $1/\kappa_{lB}$ to be inversely proportional to the well thickness d. Thus, defining the length scale $\lambda_l = d\kappa_{l0}/\kappa_{lB}$, we may write the model as

$$\kappa_l = \kappa_{l0}\left(1 + \frac{\lambda_l}{d}\right)^{-1}. \tag{8.10}$$

In Figure 8.6d we show the figure of merit as a function of d, assuming a lattice contribution to κ given by (8.10), with $\kappa_{l0} = 1$ and $\lambda_l = 100$. Unlike the

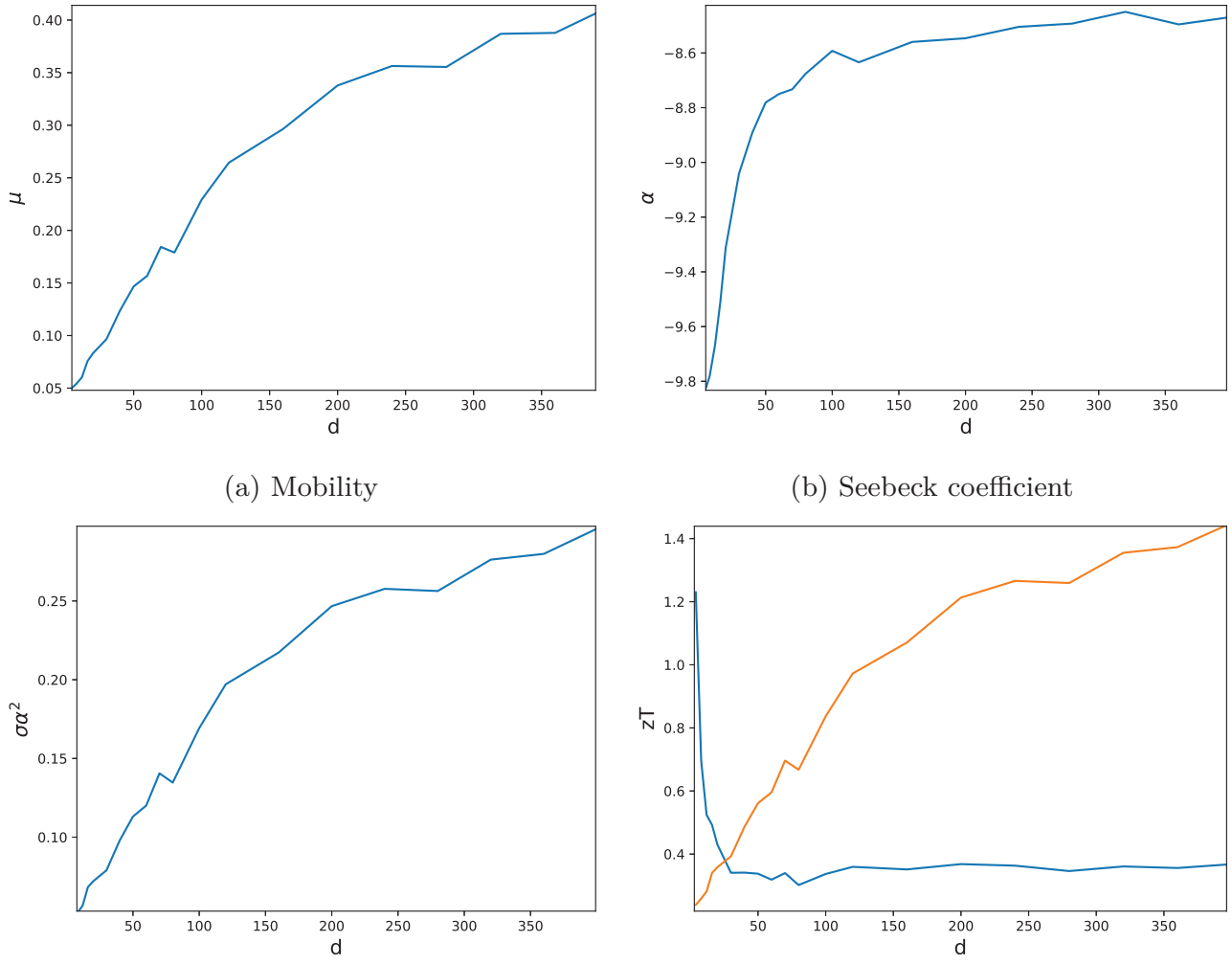

(a) Mobility

(b) Seebeck coefficient

(c) Power factor

(d) Figure of merit

Figure 8.6: Mobility μ, Seebeck coefficient α, power factor $\sigma\alpha^2$, and figure of merit zT of a superlattice structure, as a function of well thickness d. In (d), two different models have been used for the lattice component of the thermal conductivity: The curve in orange assume a constant value $\kappa_l = 0.2$, while the curve in blue assumes $\kappa_l = (1 + 100/d)^{-1}$. All units are arbitrary.

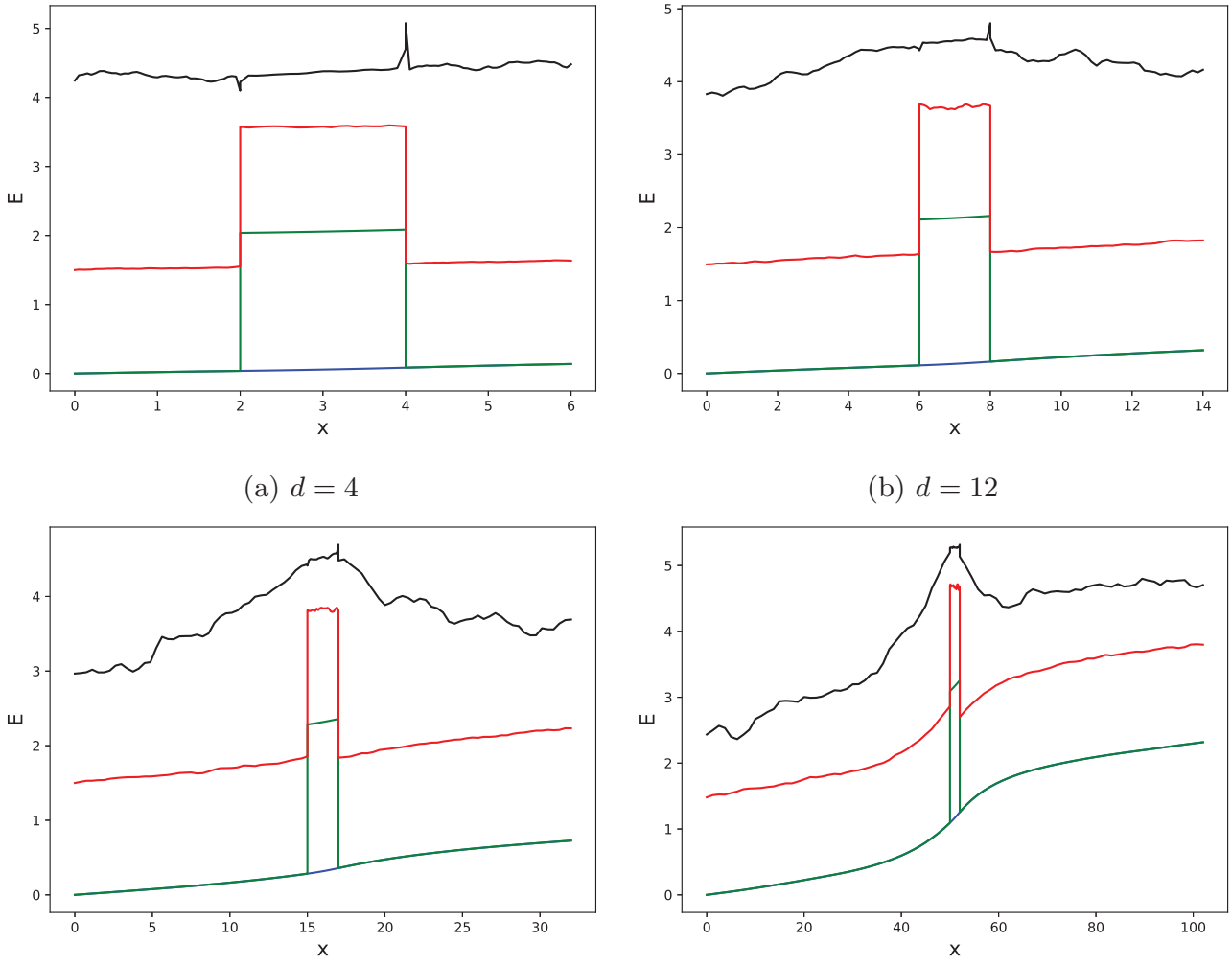

(a) $d = 4$

(b) $d = 12$

(c) $d = 30$

(d) $d = 100$

Figure 8.7: Transport through superlattice. d denotes the thickness of the wells, or equivalently the distance between the barriers. The electrostatic potential energy is shown in blue, and the conduction band minimum in green. All four figures are obtained with the charge carrier concentration set to $\rho = 0.01$, and a barrier height of $b = 2$. The average particle energy $\langle E \rangle$ is shown in red, while the black curve shows $\langle Ev \rangle / \langle v \rangle$, where v is particle velocity. All units are arbitrary.

power factor, this particular model for zT is maximal in the limit $d = 0$, and in fact seems to get a significant boost in the region where $|\alpha|$ is enlarged. However, in reality (8.10) is unlikely to apply all the way down to $d = 0$, since for thin wells we will probably have a transition to coherent transport, as discussed in Section 2.3. Thus, to illustrate the importance of the model for κ_l, Figure 8.6d also include a model for zT where we assume a constant lattice thermal conductivity of $\kappa_l = 0.2$. In this model, the improvement near $d = 0$ is completely gone, and instead the dependence of zT on d resembles that of the power factor, illustrating that the optimization of thermoelectric materials is a nontrivial task.

8.1.1.5 Discussion

The model employed in the simulations above, is too simplified to allow for making conclusions about real materials. Indeed, knowing that this would in any case not be possible, we have not made use of parameters from existing materials, and have made all calculations in arbitrary units. Nevertheless, when it comes to the importance of different physical effects, a few conclusions can still be drawn from the above discussions. Awareness of these effects is important to understand which elements of the model must be generalized to obtain reliable results.

The first important conclusion is drawn from the equation (8.8). We see that in order to obtain a high value of zT, we will typically want the ratio

$$\frac{\kappa_e}{\kappa_l} = \frac{\mu L}{\kappa_l}\rho T \tag{8.11}$$

to be quite high. Thus, we expect that the optimal thermoelectric performance is usually obtained at quite high charge carrier concentrations ρ, so accordingly it is important to be able to model such high charge carrier concentrations. In particular, this means it will be necessary to model a self consistent Poisson potential, since as seen from Figure 8.2 there will be a significant effect of charge realignment at high values of ρ. Figure 8.3 also shows that the Poisson potential can have a significant effect on the transport coefficients.

While a self consistent Poisson potential has been included in the simulations above, there are two important effects of high charge carrier concentrations which are not accounted for. First, the simulations assume non-degenerate statistics, where electrons are distributed according to a Boltzmann distribution. At high ρ, this is not a correct description, and we must instead use degenerate statistics and a Fermi distribution. Secondly, at particularly high values of ρ, we must expect the chemical potential to lie far above the band minimum. In this region, the employed assumption of parabolic bands will not be realistic, so that we must make use of a more accurate description of the band structure.

Next, two important conclusions can be drawn from Figure 8.6d. First of all, in thermoelectric applications, it is impossible to optimize the electronic properties of the material alone, since the model used to describe lattice heat transport will significantly affect the behavior of zT. Thus, a complete model must also include a model of phonons. Secondly, due the effect of κ_l, one can not

apriori know at which value of the well width d one will obtain the optimal zT. Indeed, the two models employed in Figure 8.6d yield completely opposite results, with one having maximal zT at $d = 0$, and the other in the bulk limit $d \to \infty$. Given a more realistic phonon transport model, which correctly accounts for coherent transport at small d, it is entirely possible that the optimal value of d will lie in some intermediate range. Thus, it is important to be able to model the entire range of superlattice geometries, limited neither to small or to large periods.

Another important effect related to the geometry of the superlattice, is of course tunneling through the barrier. As mentioned, it is important to be able model tunneling in order to find the optimal barrier thickness. In addition, we have also mentioned that if tunneling is not accounted for, one may end up underestimating the effects of charge realignment on the effective barrier height.

Finally, the discussion of figures 8.4 and 8.5 illustrates two important points concerning the modeling of heat flows. Firstly, in a wide well super lattice, there will usually be an interchange of energy between electron and lattice contributions to the heat flow, so that these two contributions can not be considered separately, but must actually be modeled self consistently. Secondly, since the direct simulation approach is not able do model currents induced by temperature gradients without breaking the periodic symmetry, one is inevitably stuck with some kind of contact effects, which can be quite severe. In order to remove these effects, one will have to simulate a larger region, containing more than a single superlattice period, which will inevitably increase the computational requirements. This is the approach we have followed in our first two publications, Papers I-II. The alternative is to make use of an indirect approach, such as the Kubo relations.

8.1.2 Green-Kubo relations

As discussed in Section 6.4, the Boltzmann equation is obtained from quantum transport in the limit $\hbar \to 0$. Accordingly, this limit can also be applied to the Kubo relations (4.43)-(4.46). In this limit the integrand of these expressions will be approximately constant in the innermost integration range, so that the innermost integral can be evaluated explicitly, yielding a factor of $\hbar\beta$. Further, in the classical limit $\hbar \to 0$ we can also replace operators such as $\hat{\boldsymbol{j}}(t)$ with classical functions. Thus, (4.43)-(4.46) become

$$\sigma_{ij} = \frac{V}{k_B T} \int_0^\infty \mathrm{d}t \left\langle \bar{j}_j(0) \bar{j}_i(t) \right\rangle , \tag{8.12}$$

$$\mathcal{A}_{ij} = \frac{V}{k_B T^2} \int_0^\infty \mathrm{d}t \left\langle \bar{\phi}_{Qj}(0) \bar{j}_i(t) \right\rangle , \tag{8.13}$$

$$\mathcal{B}_{ij} = \frac{V}{k_B T} \int_0^\infty \mathrm{d}t \left\langle \bar{j}_j(0) \bar{\phi}_{Qi}(t) \right\rangle \quad \text{and,} \tag{8.14}$$

$$\mathcal{C}_{ij} = \frac{V}{k_B T^2} \int_0^\infty \mathrm{d}t \left\langle \bar{\phi}_{Qj}(0) \bar{\phi}_{Qi}(t) \right\rangle . \tag{8.15}$$

These equations represent the classical limit of the Kubo relations (4.43)-(4.46). Relations of this type are often referred to as Green-Kubo relations, since they were independently discovered by Green. The correlation functions in the expressions can be estimated from Monte Carlo simulations at equilibrium, and accordingly these relations can be used to calculate thermoelectric transport coefficients without the need of imposing explicit fields or temperature gradients. As discussed in the previous section, this is a particularly important advantage when modeling the effects of temperature gradients.

In this section, some results are presented which were obtained using the relations (8.12)-(8.15). As in the previous section, we assume parabolic bands and non-degenerate statistics. However, a more realistic scattering mechanism is utilized, compared to the phenomenological model of (8.3), which was employed in the previous section. In particular, the calculations of this section make use of a model of acoustic phonon scattering described by Jacoboni[15]. On the other hand, our implementation has not progressed far enough to model heterostructures like those of the previous section, so it is limited to simple bulk simulations.

The fact that we are assuming non-degenerate statistics allows us to simplify the relations (8.12)-(8.15) even further. This is because under this assumption, and an additional assumption of weak interactions, the particles in the system are uncorrelated. This significantly simplifies the evaluation of the involved correlation functions. Consider for example (8.12). The average current density in the system can be expressed as

$$\bar{\boldsymbol{j}}(t) = \frac{-e}{V} \sum_{n=1}^{N} v_n, \tag{8.16}$$

where we assume that there are N particles within the volume V, and where v_n is the velocity of the n'th particle. Thus, since the particles are uncorrelated, we find

$$\left\langle \bar{j}_j(0)\bar{j}_i(t) \right\rangle = \frac{e^2}{V^2} \sum_{n=1}^{N} \left\langle v_{nj}(0)v_{ni}(t) \right\rangle = \frac{Ne^2}{V^2} \left\langle v_j(0)v_i(t) \right\rangle, \tag{8.17}$$

where we have used that the correlation function is independent of n, since the particles are indistinguishable. Inserting this in (8.12), and using $\rho = N/V$, we obtain

$$\sigma_{ij} = \frac{e^2\rho}{k_B T} \int_0^\infty \mathrm{d}t \left\langle v_j(0)v_i(t) \right\rangle. \tag{8.18}$$

Similarly, the average heat flux in the system can be expressed as

$$\bar{\boldsymbol{j}}(t) = \frac{1}{V} \sum_{n=1}^{N} (E_n - \mu)v_n, \tag{8.19}$$

where μ is the chemical potential, and E_n is the energy of the n'th particle. Repeating the arguments above, we see that (8.13)-(8.15) simplify to

$$\mathcal{A}_{ij} = -\frac{e\rho}{k_B T^2} \int_0^\infty \mathrm{d}t \, \langle (E(0) - \mu) v_j(0) v_i(t) \rangle \,, \tag{8.20}$$

$$\mathcal{B}_{ij} = -\frac{e\rho}{k_B T} \int_0^\infty \mathrm{d}t \, \langle v_j(0) (E(t) - \mu) v_i(t) \rangle \quad \text{and,} \tag{8.21}$$

$$\mathcal{C}_{ij} = \frac{1}{k_B T^2} \int_0^\infty \mathrm{d}t \, \langle (E(0) - \mu) v_j(0) (E(t) - \mu) v_i(t) \rangle \,. \tag{8.22}$$

The correlation functions on the right are easy to estimate in a Monte Carlo simulation. The Seebeck coefficient, Peltier coefficient and the electronic component of the the thermal conductivity, can then be found from $\overleftrightarrow{\mathcal{A}}$, $\overleftrightarrow{\mathcal{B}}$ and $\overleftrightarrow{\mathcal{C}}$ using (4.49)-(4.51).

The scattering mechanism is taken from Ref. [15]. In particular, we make use of model C of chapter 9.3, which describes inelastic scattering on acoustic phonons, assuming spherical and parabolic electron bands. The model is formulated in terms of the integral kernel $\Gamma_{nm}(\boldsymbol{k}, \boldsymbol{k}')$ introduced above (6.89). Since we only have a single band, the band indices n and m are subsumed. The model states

$$\begin{aligned} &\Gamma(\boldsymbol{k}, \boldsymbol{k}') \\ &= \frac{q E_l^2}{8\pi^2 \rho_m c_l} \big(n(q) \delta(E(k') - E(k) + \hbar q c_l) + (n(q) + 1) \delta(E(k') - E(k) - \hbar q c_l) \big), \end{aligned} \tag{8.23}$$

where $E(k) = k^2/2m^\star$,$q = |\boldsymbol{k} - \boldsymbol{k}'|$, E_l is a deformation potential constant, c_l is the speed of sound for longitudinal modes, ρ_m is the mass density of the material, and

$$n(q) = \frac{1}{e^{\beta \hbar q c_l} - 1}. \tag{8.24}$$

The implementation of this model as a Monte Carlo process follows Ref. [16], which describes how to draw new Bloch-vectors $\boldsymbol{k}$ with a probability distribution proportional to (8.23). The simulations were performed with $c_l = 0.1$ and $E_l^2/\rho_m c_l = 100$.

Since (8.23) is a fairly complicated model of scattering, it is important to test the implementation. A particularly important test, is to check whether the particles end up with the correct distribution in $\boldsymbol{k}$-space. Since the simulation coccus at equilibrium, they should be distributed according to the Boltzmann distribution

$$p(\boldsymbol{k}) = \frac{1}{\sqrt{2\pi k_B T m^\star}} e^{-\frac{\boldsymbol{k}^2}{2 k_B T m^\star}}. \tag{8.25}$$

As a very simple test, we can simply simulate a few electrons, plot their position in k-space, and check if the resulting distribution seems reasonable. Figure 8.8 shows a scatter plot of the position in $\boldsymbol{k}$-space of 1000 electrons, after an

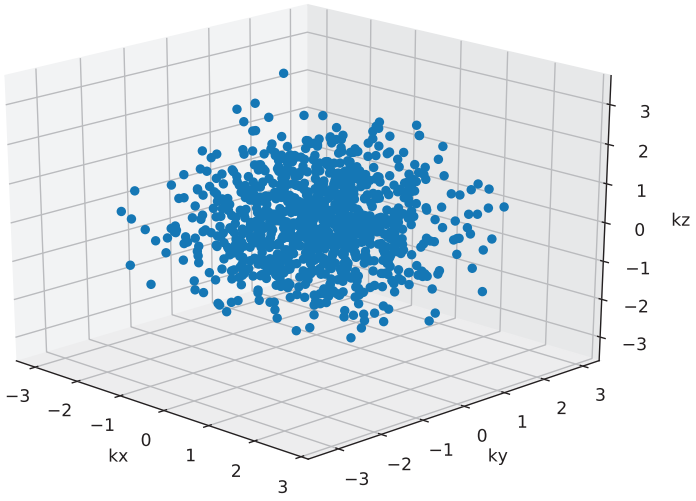

Figure 8.8: $\boldsymbol{k}$-space scatter plot of 1000 electrons after equilibration.

equilibration time of $t = 50$. The result is consistent with a Gaussian distribution centered at the origin.

As a more quantitative test, we study the distribution of energies of the electrons. It is easy to show that the energies $E = k^2/2m^\star$ will have a distribution $\sim \sqrt{E}e^{-\beta E}$, and that the average energy is $\frac{3}{2}k_BT$. Figure 8.9a shows how the energy average of 10 000 electrons develops during a Monte Carlo simulation. The electrons are initialized with $E = 0$, and are equilibrated over a time scale of about $t = 20$. After this the energy average is approximately constant and ≈ 1.5. Since the simulations were performed with $k_BT = 1$, this fits perfectly with the theory. In Figure 8.9b we show the distribution of energies at $t = 50$, where the equilibration should be complete. Again the Monte Carlo result fits perfectly with the analytical result.

Having tested that the simulations yield the correct equilibrium distribution, we turn to time dependent phenomena. First, we estimate the energy- and momentum relaxation times, which are defined respectively as

$$\frac{1}{\tau_E} = \left\langle \frac{E(\boldsymbol{k}') - E(\boldsymbol{k})}{E(\boldsymbol{k}')t} \right\rangle \quad \text{and,} \tag{8.26}$$

$$\frac{1}{\tau_m} = \left\langle \frac{(\boldsymbol{k}' - \boldsymbol{k}) \cdot \boldsymbol{k}'}{|\boldsymbol{k}'|^2 t} \right\rangle, \tag{8.27}$$

where t is the time between scattering events, and $\boldsymbol{k}'$ and $\boldsymbol{k}$ are respectively the momentums before and after a scattering event. These quantities are estimated by averaging over multiple scattering events in a simulation. The averaging starts only after equilibration. We obtain $\tau_E = 4.7$, and $\tau_m = 0.095$. In Figure 8.9a we saw that the electrons are equilibrated over a time scale of about $t = 20 \approx 4\tau_E$. Thus, the energy equilibration time is some small number times τ_E, which seems very reasonable.

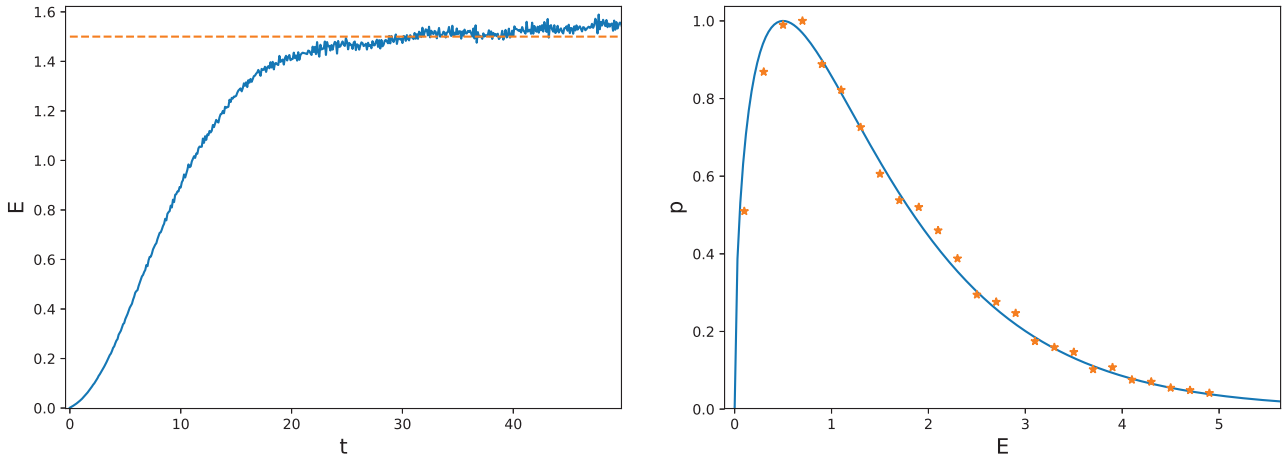

(a) Average energy

(b) Distribution at $t = 50$

Figure 8.9: Electron energy. (a) shows the average energy as a function of time, and (b) shows the distribution of energies at $t = 50$. The orange stars represent a histogram obtained from the Monte Carlo simulation, while the curve in blue represents the analytical Boltzmann distribution (8.25). The distributions have been normalized so that $\max p(E) = 1$.

Next, we turn to the correlation functions of (8.18)-(8.22). These functions are calculated by first equilibrating the simulated particles, and then approximating the expectation values as mixed ensemble and time averages. For instance, the correlation function $\langle v_j(0)v_i(t)\rangle$ is estimated as

$$\langle v_j(0)v_i(t)\rangle \approx \frac{1}{NM}\sum_{n=1}^{N}\sum_{m=1}^{M} v_{nj}(t_0 + m\Delta t)v_{ni}(t_0 + m\Delta t + t), \tag{8.28}$$

where t_0 is larger than the equilibration time, N is the number of simulated particles, and $M\Delta t$ is a sufficiently large range of time. The correlation functions $\langle E(0)v_j(0)v_i(t)\rangle$, $\langle v_j(0)E(t)v_i(t)\rangle$ and $\langle E(0)v_j(0)E(t)v_i(t)\rangle$ are estimated in a similar manor. The results are shown in Figure 8.10. Note that many of these correlation functions are related by exchange of time arguments, and that in those cases they are identical due to time reversal symmetry. For instance, $\langle v_j(0)v_i(t)\rangle = \langle v_i(0)v_j(t)\rangle$, and $\langle v_j(0)E(t)v_i(t)\rangle = \langle E(0)v_i(0)v_j(t)\rangle$. Whenever this is the case, only one of the functions are shown in Figure 8.10.

Examining Figure 8.10, we first observe that all of the non-diagonal results, with $i \neq j$, are essentially zero within the expected accuracy of the calculation. Further, the diagonal results with $i = j$ are identical for all values of i. Both of these facts follow as a consequence of the spherical symmetry of the model. The fact that these symmetries are realized in the simulations is another important consistency check of the implementation. We also observe that the diagonal correlation functions seem to fall of over a time scale ~ 0.1, which fits well with the calculated value of $\tau_m = 0.095$.

As a final consistency check, we may consider the well known fact that the conductivity σ is related to the diffusion constant D by $\sigma = e^2\rho D/k_B T$, which

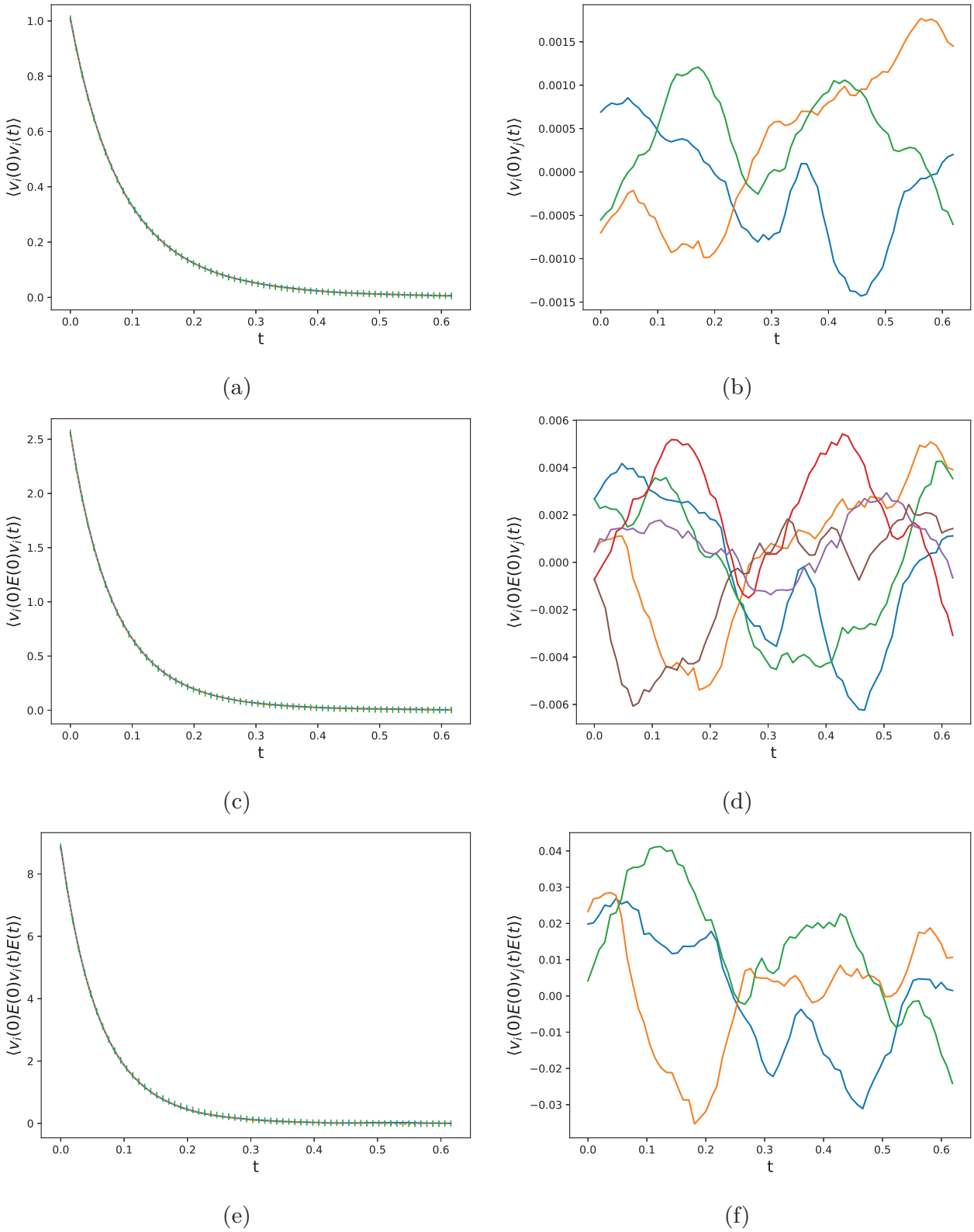

Figure 8.10: Correlation functions. The top, middle and bottom rows respectively show $\langle v_j(0)v_i(t)\rangle$, $\langle v_j(0)E(0)v_i(t)\rangle$, and $\langle v_j(0)E(0)v_i(t)E(t)\rangle$. The figures on the left show results with $i = j$, while those where $i \neq j$ are shown on the right. On the left, results shown in blue, orange and green respectively represent the cases $ii = xx$, yy and zz. On the right, the cases $ij = xy$, xz, yz, yx, zx and zy are respectively shown in blue, orange, green, red purple and brown.

follows from the Einstein relation[7, 15]. Comparing this to (8.18), we see that we must have

$$D = \int_0^\infty \mathrm{d}t \, \langle v_i(0) v_i(t) \rangle \,, \tag{8.29}$$

where i is any of x, y or z. This can be used as a consistency check, since the diffusion constant can also be estimated more directly by considering how the variance of the particles position varies with time. In fact, it is not hard to see that in three dimensions we should have $\sigma_{\boldsymbol{x}}^2 = \langle x^2 \rangle + \langle y^2 \rangle + \langle z^2 \rangle = 6Dt$. Thus, in Figure 8.11 we show Monte Carlo estimates of $\sigma_{\boldsymbol{x}}^2$ as a function of the simulation time t. The dependency of $\sigma_{\boldsymbol{x}}^2$ on t takes on a linear character after $\sim t = 20$. This fits well with the fact that the electrons are equilibrated at about this time, as seen in Figure 8.9a.

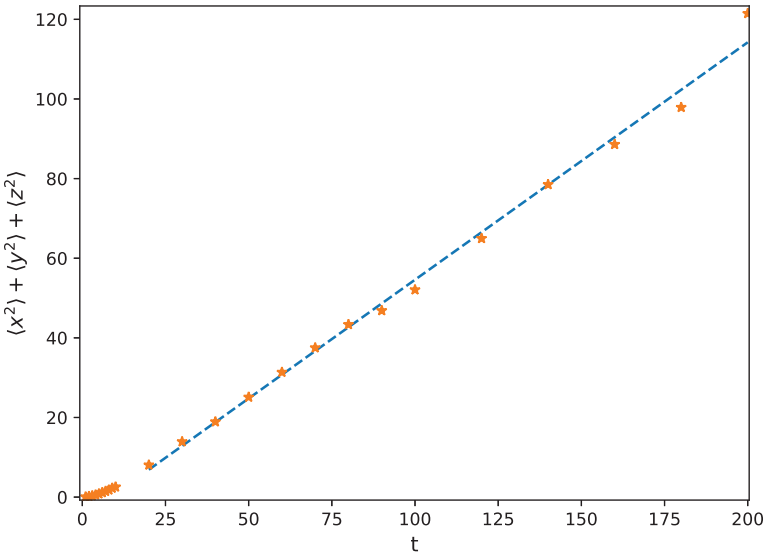

Figure 8.11: Estimation of diffusion constant. The orange stars show estimates of $\sigma_{\boldsymbol{x}}^2 = \langle x^2 \rangle + \langle y^2 \rangle + \langle z^2 \rangle$ after various simulation times t. The dashed line in blue shows a linear fit, fitted only against the points with $t \geq 20$.

Figure 8.11 also includes a linear model, which is fitted against the Monte Carlo results where $t \geq 20$. This model is $-5.04 + 0.596t$. Thus, we estimate the diffusion constant as $D = 0.596/6 = 0.099$. Numerically integrating the function $\langle v_i(0) v_i(t) \rangle$ shown in Figure 8.10a, we obtain $D = 0.095$ by (8.29). Within the expected accuracy, these results are equal, so the implementation passes also this consistency check.

Finally, we calculate the thermoelectric transport tensors $\overleftrightarrow{\sigma}$, $\overleftrightarrow{\alpha}$, $\overleftrightarrow{\pi}$ and $\overleftrightarrow{\kappa_e}$, using (8.18)-(8.22) and (4.49)-(4.51). The simulations are performed with $k_B T = 1$ and $\mu = 0$, which yields a charge carrier density of $\rho = 0.785$. We also assume units where $k_B = e = 1$. The results are shown in table 8.1.

Again we note that the off diagonal results are essentially zero, and that the diagonal elements of each tensor are practically identical. Again, this is a

	σ			α		
	x	y	z	x	y	z
x	0.07451	1.074e-4	8.425e-5	-2.021	-0.002883	-7.182e-04
y	1.074e-4	0.07453	5.231e-5	-3.348e-4	-2.017	0.01105
z	8.425e-5	5.231e-5	0.07474	0.02104	0.008486	-2.024
	π			κ_e		
	x	y	z	x	y	z
x	-2.021	-3.348e-4	0.02104	0.1505	1.002e-5	0.004471
y	-0.002883	-2.017	0.008486	1.002e-5	0.1491	-0.003897
z	-7.182e-4	0.01105	-2.024	0.004471	-0.003897	0.1504

Table 8.1: Thermoelectric transport tensors.

consequence of the spherical symmetry of the system, and indeed follows from the fact that the correlation functions also have these properties. We also note that the conductivity has the expected value given the formula $\sigma = e^2\rho D/k_B T = 0.785 \cdot 0.95 = 0.746$. The Peltier and Seebeck coefficients are identical since $T = 1$, and have a value of $\alpha \approx -2$. We also calculate the Lorenz coefficient to be $L = \kappa_e/\sigma T \approx 0.15/0.075 = 2$.

In the literature[22] we find analytical estimates of α and L within certain approximations. These are $\alpha = -k_B/e(\beta\mu + s + 5/2)$ and $L = k_B^2/e^2(s + 5/2)$, where s is an exponent describing the energy dependence of the scattering rates. For acoustic phonon scattering with parabolic bands[22], $s = -1/2$. Accordingly. we should have $\alpha = -(0 - 1/2 + 5/2) = -2$ and $L = -1/2 + 5/2 = 2$, which fits perfectly with the simulation results.

8.1.2.1 Discussion

Clearly, the application of this method to the simple bulk system above an overkill, since the simple analytical estimates yield the same results. But the application to the bulk system serves as a test of the implementation. Indeed, the agreement with the analytical estimates, together with the other test results, indicates that we can put some trust in the implementation. Thus, the next step would be to apply the method to superlattices, after which we could repeat the studies of the previous section.

The indirect Green-Kubo method described here would be much better suited for that purpose, compared to the direct method made use of there. The fact that we are making use of a more realistic scattering mechanism is only one of the reasons for this. In addition, it is a major advantage that we can perform the simulation at equilibrium, since this entails that we will not have to solve the Poisson equation self consistently with the transport problem, and that we can always apply periodic boundary conditions. Further, when applying the direct method, we always have to make sure the perturbations we apply are small enough for the transport to be within the linear regime. On the other hand, if we choose the perturbations to small, the signal to noise ratio will be

very low, which can also cause erroneous results. This trade-of is something we do not have to consider when using the indirect method presented here.

However, while the implementation is better suited than that of the previous section, it is still lacking important aspects. First of all, like the direct implementation, it is still limited to parabolic bands. This could however be easily remedied, for instance by making use of a tight binding model like the ones we have used in our publications (papers I-II). A larger problem is the limitation to non-degenerate statistics. The derivation of (8.18)-(8.22) assumed that the particles are uncorrelated, which will not be the case if the statistics is degenerate. In addition, the introduction of degenerate corrections to the scattering rates seem to cause a drastic increase in the variance of the correlation functions. However, both of these issues could probably be resolved by more careful consideration.

A more serious problem is the fact that the method is still limited to classical transport, which means we are not able to model quantum transport phenomena such as tunneling and resonance between barriers. Tunneling can probably be dealt with in terms of pre-calculated transmission functions, like we try in our second publication (Paper II). Resonances however, can only be dealt with in a classical transport framework if we assume coherence throughout the super cell, so that the miniband dispersion relation of the superlattice can be utilized. The extent to which that assumption affects the results is the subject in our second publication.

8.2 Perturbative approximations to G^r

This section concerns the evaluation of the retarded Green's function G^r through the solution of (5.81). This is an important step in the evaluation of currents through the NEGF formalism, and indeed in any perturbative transport framework formulated in terms of Green's functions. A major problem when dealing with large systems like those considered in our publications, is the time it takes to solve this equation. Solving the equation through direct inversion would require an amount of time proportional to N^3, where N is the side of the involved matrices. In an atomistic model $N = n_o n_a$, where n_a is the number of atoms in the system, and n_o is the number of states included per atom. Accordingly, direct inversion is fairly intractable in large systems.

In our two first publications (Papers I-II), the solution of (5.81) is done by the external transport framework Kwant[12, 1], which is able to use a variety of different methods. In our third paper (Paper III) we make use of the RGF-algorithm, which is described in detail in the literature[6]. The RGF-algorithm assumes that the system can be divided into a set of n_Z slices, in such a way that there is only nearest neighbor coupling between the slices. It then scales as $n_X^3 n_Z(1 + n_C)$, where n_X is the number of states per slice, and n_C is the number of columns required in the block decomposition of $G^r(E)$. In particular, if only the diagonal of $G^r(E)$ is required, then the RGF-algorithm scales as $n_X^3 n_Z$, while if the full matrix is required it scales as $n_X^3 n_Z^2$. In any case, this is

a significant improvement compared to direct inversion, as long as one is dealing with a quasi-one-dimensional system, where n_X is smaller than n_Z.

Before deciding to use the RGF algorithm, I spent some time considering alternative ways to speed up the solution of (5.81). This section deals in particular with one such approach, which was quite successful. It involves treating states with energies far away from the range of consideration using perturbation theory, rather than the exact expressions. The computational requirements are still cubically scaling with system size, so the approach is not able to compete with the RGF-algorithm in large quasi-one-dimensional systems. However, it may have an advantage over RGF in more general systems.

We begin by considering (5.81) in the absence of scattering, so that it can be written as

$$G^r(E) = \left(E - H - \sum_p \Sigma_p^r(E) \right)^{-1}, \tag{8.30}$$

where Σ_p^r is the retarded lead self energy associated with lead p. Combining (5.105) with (5.86), (5.65) and (5.90) it is easy to see that in the absence of scattering

$$i_p(E) = \frac{1}{h} \sum_q \operatorname{Tr} \Gamma_p^F(E) G^r(E) \Gamma_p^F(E) G^a(E) (f_q(E) - f_p(E)), \tag{8.31}$$

where we have also used that

$$\Gamma(E) = i \left(\Sigma^r(E) - \Sigma^a(E) \right) = \sum_q \Gamma_p^F(E), \tag{8.32}$$

which follows from (5.74), (5.75), (5.65) and (5.66). Comparing (8.31) to (2.16), we see that we must have

$$\bar{\mathcal{T}}_{qp}(E) = \operatorname{Tr} \Gamma_p^F(E) G^r(E) \Gamma_p^F(E) G^a(E), \tag{8.33}$$

an equation which is also derived by Datta[7]. The accuracy of the following approximations will be judged in terms of their ability to reproduce the correct transmission function $\bar{\mathcal{T}}(E)$, where the subscripts qp have been omitted, since we are considering a system with only two leads.

The perturbative procedure requires that the states of our system is divided into two groups based on their energies. One of these groups will be treated exactly, and one perturbatively. However, the states in terms of which a model is formulated, does usually not have a wide range of different energies. For instance, the tight binding model of CdTe employed in our publications (Papers I-II), only has two different types of states: s-orbitals with energy 4.95 eV, and p-orbitals with energy 0.52 eV. This is too coarse grid of energies for us to expect the method to work particularly well.

To introduce a larger variety of different energies, we proceed as follows: First we construct small groups of states localized close to each other. In our

case these groups consist of four neighboring unit cells of CdTe. Indexing these groups by i, the total Hamiltonian of the system can be written as $H = \sum_{ij} H_{ij}$, where H_{ii} represents the Hamiltonian of group i by itself, and the terms with $i \neq j$ represent interactions between the groups. We then diagonalize each of the operators H_{ii} to get a new set of states $|il\rangle$, with energies equal to the corresponding eigenvalues ϵ_{il}. The resulting grid of energies is much denser than that of the original model, as illustrated in Figure 8.12.

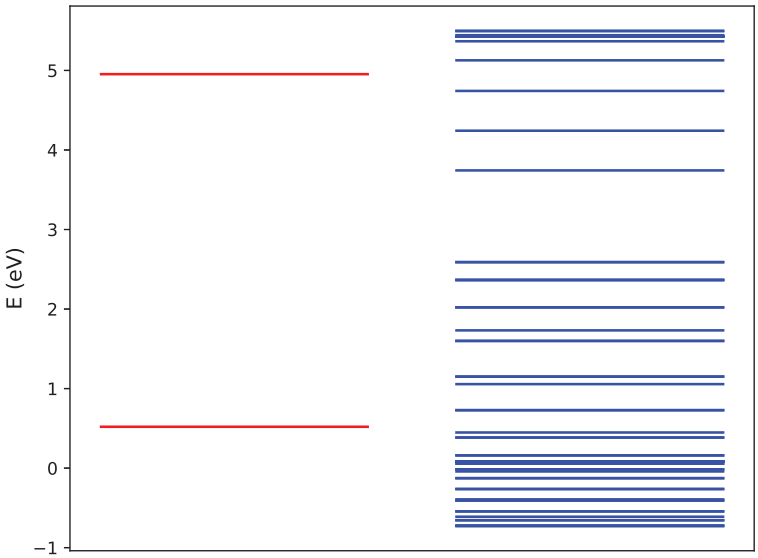

Figure 8.12: Energy levels in a CdTe system. The red lines on the left show the two energy levels of the original tight binding model, while those on the right show the energy levels after applying the procedure described in the text, where four neighboring unit cells of CdTe are grouped together, and the groups isolated Hamiltonian is diagonalized, resulting in a new set of states.

Next, we define an energy range $[E_1, E_2]$, where states $|il\rangle$ such that $E_1 \leq \epsilon_{il} \leq E_2$ will be treated exactly, and the others perturbatively. In the calculations below, we have unless otherwise specified set $E_1 = 0.4$ eV and $E_2 = 5.2$ eV, which results in roughly a third of the energies ϵ_{il} being in the range $[E_1, E_2]$. Following a fairly standard procedure[27], we define a projection operator P such that $P|il\rangle = |il\rangle$ if $E_1 \leq \epsilon_{il} \leq E_2$, and $P|il\rangle = 0$ otherwise. We also define $Q = I - P$. The total Hamiltonian can then be written

$$H = (Q + P)H(Q + P) = H_0 + H^\star + V + V^\dagger, \tag{8.34}$$

where we have defined $H_0 = PHP$, $H^\star = QHQ$, and $V = PHQ$.

The first approximation we will consider involves interaction with the leads. These interactions are described by the matrices Γ_p^F from (8.35), with $p \in \{1, 2\}$ since there are only two leads. The approximation consists of replacing these operators with $P\Gamma_p^F P$, which means we are allowing only states with energy within the range $[E_1, E_2]$ to interact with the leads. The consequences of this approximation is shown in Figure 8.13. There we show the transmission function

of a system consisting of 32 unit cells of CdTe, arranged along the z-axis, and employing the tight bind model of our first publication. Periodic boundary conditions are imposed in the x- and y-directions, and for the lead self energies we use a simple diagonal model $\Sigma_p^r(E) = -iP_p/2\tau$, with $\tau = 2$ eV^{-1}, and P_p a projection operator projecting upon the atoms nearest lead p.

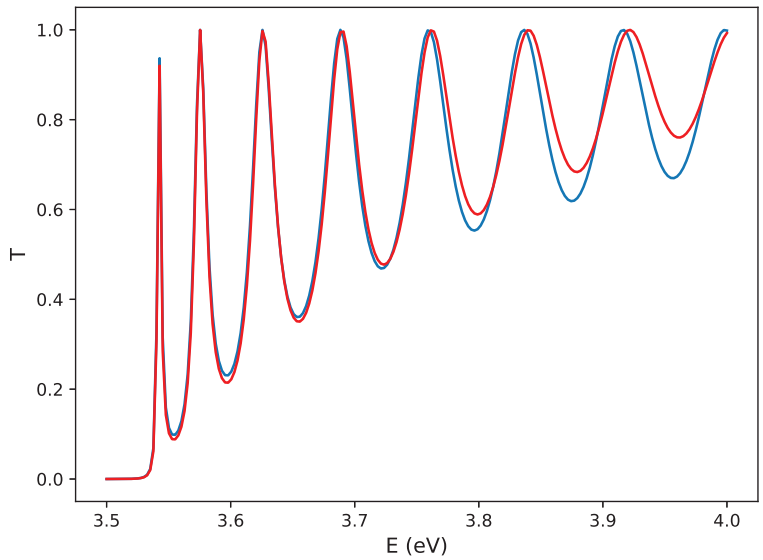

Figure 8.13: Transmission function of a CdTe system. The curve in blue shows the unapproximated transmission function, while the curve in red shows the result after the approximation $\Gamma_p^F = P\Gamma_p^F P$.

Figure 8.13 contains both the exact result, and the result of the approximation $\Gamma_p^F = P\Gamma_p^F P$. We observe that the exact and the approximate results are quite similar in the low lying range $E \sim 3.6$ eV, but that deviations start to become significant at higher energies, closer to the upper limit $E_2 = 5.2$ eV. In the long run we could consider making corrections also to the self energies, which might reduce the deviations seen in Figure 8.13. For now however, such corrections have not been implemented. The model with $\Gamma_p^F = P\Gamma_p^F P$ is thus to be regarded as the target result, to which further approximations will be compared.

Within the approximation $\Gamma_p^F = P\Gamma_p^F P$, we can use the fact that $P^2 = P$ to write (8.31) as

$$\bar{\mathcal{T}}(E) = \mathrm{Tr}\, P\Gamma_1^F(E)PPG^r(E)PP\Gamma_2^F(E)PPG^a(E)P. \tag{8.35}$$

In order to calculate the transmission function, we only need the projected Green's function $PG^r(E)P$. Combining (8.30) with (8.34) we obtain

$$\left(E - H_0 - H^\star - V - V^\dagger - \Sigma_l^r(E)\right) G^r(E) = I, \tag{8.36}$$

where we have defined $\Sigma_l^r(E) = \sum_p \Sigma_p^r(E)$. Multiplying (8.36) on both sides by P, and using that $P^2 = P$, $Q^2 = Q$, and $PQ = QP = 0$, we obtain

$$\left(E - H_0 - \Sigma_l^r(E)\right) PG^r(E)P - VQG^r(E)P = P. \tag{8.37}$$

Similarly, multiplying (8.36) on the left by Q and on the right by P, we get

$$(E - H^\star)\, QG^r(E)P - V^\dagger PG^r(E)P = 0. \tag{8.38}$$

Solving (8.38) for $QG^r(E)P$, we find $QG^r(E)P = (E - H^\star)^{-1} V^\dagger PG^r(E)P$, and upon inserting this in (8.37) we obtain the equation

$$\left(E - H_0 - \Sigma_l^r(E) - V\,(E - H^\star)^{-1}\, V^\dagger\right) PG^r(E)P = P. \tag{8.39}$$

Thus, if we consider inversion only in the subspace spanned by the states $|il\rangle$ with energy in the range $[E_1, E_2]$, we obtain the expression

$$PG^r(E)P = \left(E - H_0 - \Sigma^r(E)\right)^{-1}, \tag{8.40}$$

which is on the same form as (8.30), but where we are using a corrected self energy $\Sigma^r(E) = \Sigma_l^r(E) + \Sigma_R^r(E)$, with

$$\Sigma_R^r(E) = V\,(E - H^\star)^{-1}\, V^\dagger. \tag{8.41}$$

The perturbative approximation consists of approximations to (8.41). We begin by writing $H^\star$ as

$$H^\star = \sum_{il} \epsilon_{il} |il\rangle\langle il| + \sum_{i \neq j} H_{ij}^\star, \tag{8.42}$$

where the first sum is only over l such that $\epsilon_{il} \notin [E_1, E_2]$, and where $H_{ij}^\star = QH_{ij}Q$. We then define $D = \sum_{il} \epsilon_{il} |il\rangle\langle il|$, and $U = \sum_{i \neq j} H_{ij}^\star$, and we write

$$\begin{aligned} (E - H^\star)^{-1} &= (E - D - U)^{-1} = (E - D)^{-1} \left(I - U(E - D)^{-1}\right)^{-1} \\ &= (E - D)^{-1} \sum_{n=0}^{\infty} \left[U(E - D)^{-1}\right]^n, \end{aligned} \tag{8.43}$$

assuming converge of the sum. Finally, we insert (8.43) in (8.41), and obtain

$$\Sigma_R^r(E) = V\,(E - D)^{-1} \sum_{n=0}^{\infty} \left[U(E - D)^{-1}\right]^n V^\dagger. \tag{8.44}$$

Perturbative approximations of various orders are now obtained simply by replacing ∞ by some finite number N. Note that the order of the expansion refers to the total number of interaction factors U or V. Thus, the term with $n = 0$ is a second order term, the term with $n = 1$ a third order term and so on.

Finite order termination of (8.44) are easy to implement using a sparse matrix library, as we have done using Python. In Figure 8.14 we show results of such an implementation, applied to the same system studied in Figure 8.13. The reference result is the result shown in red in Figure 8.13, and is shown in black in Figure 8.14a. The perturbative result of order zero, obtained by setting

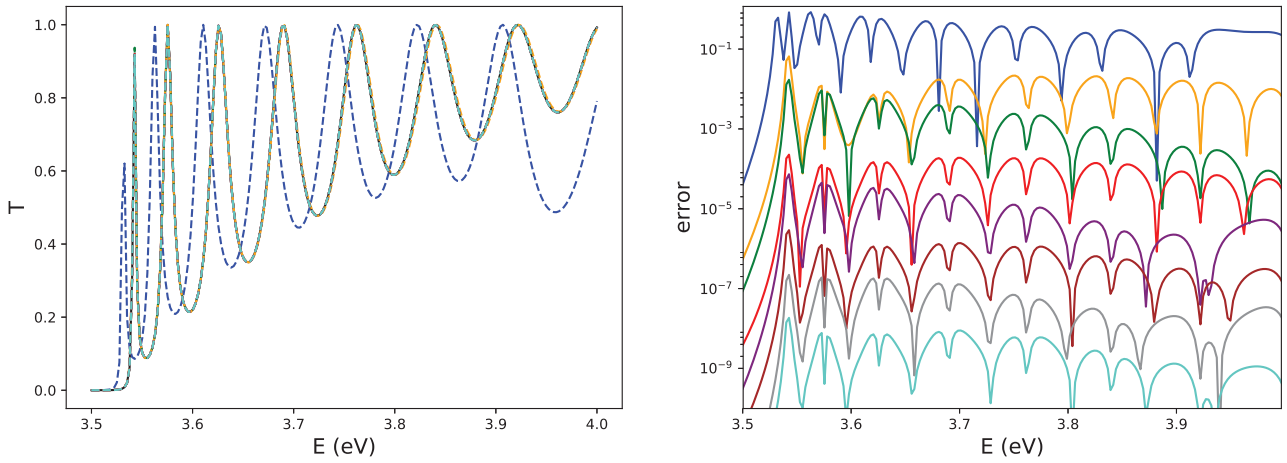

(a) Transmission function

(b) Error of perturbative expansion

Figure 8.14: Transmission function of a CdTe system. (a) shows $\mathcal{T}(E)$ itself, while (b) shows the error $|\mathcal{T}_n(E) - \mathcal{T}(E)|$, where $\mathcal{T}_n(E)$ is a perturbative approximation of order n. In (a) $\mathcal{T}(E)$ is shown as a solid black line, while the perturbative results are shown as dashed lines. In both figures, the blue, orange, green, red, purple, brown, grey and turquoise lines respectively represent perturbative results of order zero, two, three, four, five, six, seven and eight.

$\Sigma_R^r(E) = 0$, lies quite far from the reference. However, already the second order result, with $\Sigma_R^r(E) = V\,(E - D)^{-1}\,V^\dagger$, is almost indistinguishably from the reference result. So are also the higher order results. Thus, in Figure 8.14b we show the errors $|\mathcal{T}_n(E) - \mathcal{T}(E)|$ in a log plot, in order to more clearly illustrate the improvement in accuracy with increasing order.

As one would expect, the error varies quite a bit with energy. To remove this variation, we can consider the maximal error in some range of interest, which we here set arbitrarily to $[3.5, 3.7]$. In Figure 8.15 we show how the maximal error in this range varies both with the perturbation order n, and with the two energy limits E_1 and E_2. Note that the most accurate results are limited by the numerical accuracy, and flatten out at $\sim 10^{-13}$. The dependency of the error on n is seen to fit well with a simple exponential model ar^n. The most important parameter from this fit is the base r, which tells us how fast the perturbative approximation converges towards the correct result. Figure 8.16 shows how this parameter depends on the choice of limits E_1 and E_2. Other than the fact that r decreases when the energy range $[E_1, E_2]$ is increased, the most important thing to note is that we always have $r < 1$, which indicates that we at least in this case, always have convergence in the limit $n \to \infty$.

In addition to the accuracy of the perturbative approximations, we must also compare their computation time requirements to that of the exact solution. Figure 8.17a illustrates how the computation time depends on the perturbation order. It increases close to linearly, which makes sense since for each new order a new term in the expansion (8.44) must be calculated. We note however that the

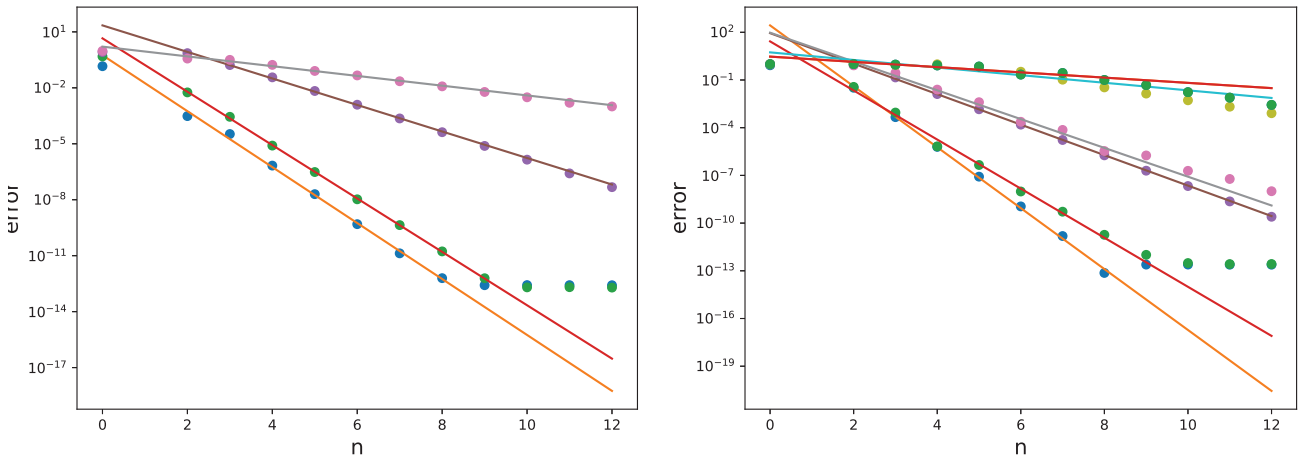

(a) (b)

Figure 8.15: Maximal error $|\mathcal{T}_n(E) - \mathcal{T}(E)|$ of the perturbative approximation in the energy range $[3.5, 3.7]$, as a function of the perturbation order n. In (a) $E_1 = -\infty$, and the results shown in blue, green, purple and pink are obtained respectively with $E_2 = 5.12$, 4.74, 4.24 and 3.74 eV. In (b) $E_2 = \infty$, and results obtained with $E_1 = -0.13$, 0.38, 1.06, 1.60, 2.37, 2.59, and 3.74 eV are shown respectively in blue, green, purple, pink, yellow, blue and green. The solid lines represent exponential models ar^n fitted against the results where $2 \leq n \leq 8$.

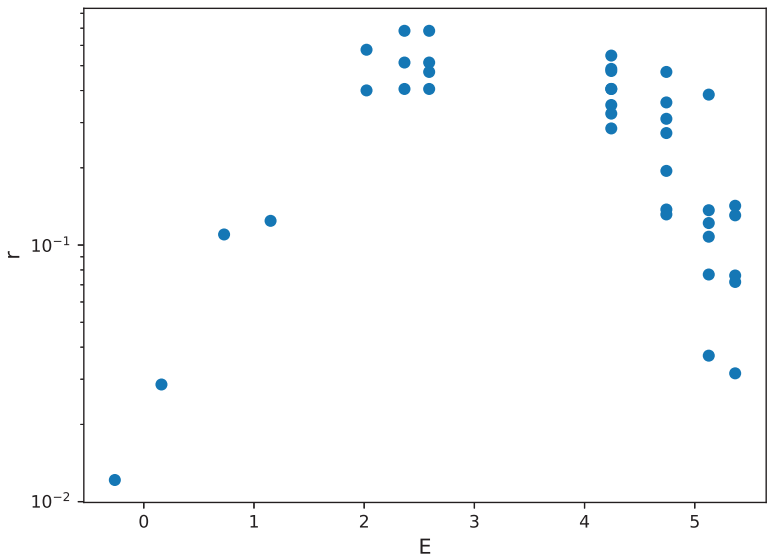

Figure 8.16: Dependency of convergence rate on the energy range $[E_1, E_2]$. We show all possible combinations of $E_2 \in \{5.12, 4.74, 4.24, 3.74, \infty\}$ and $E_1 \in \{-\infty, -0.13, 0.38, 1.06, 1.60, 2.37, 2.59, 3.74\}$. The y-axis shows the parameter r from the exponential fits illustrated in Figure 8.15, and the x-axis shows the energy $\epsilon_{il} \notin [E_1, E_2]$ which is closest to the range $[4.5, 4.7]$, i.e. the closest perturbatively treated energy.

growth rate goes down slightly after $n = 8$. This is probably related to the fact that we have divided the system into 8 groups. Since we have nearest neighbor interaction between these groups, the sparse matrices $[U(D-E)^{-1}]^n$ from (8.44) will be maximally dense after ~ 8 orders.

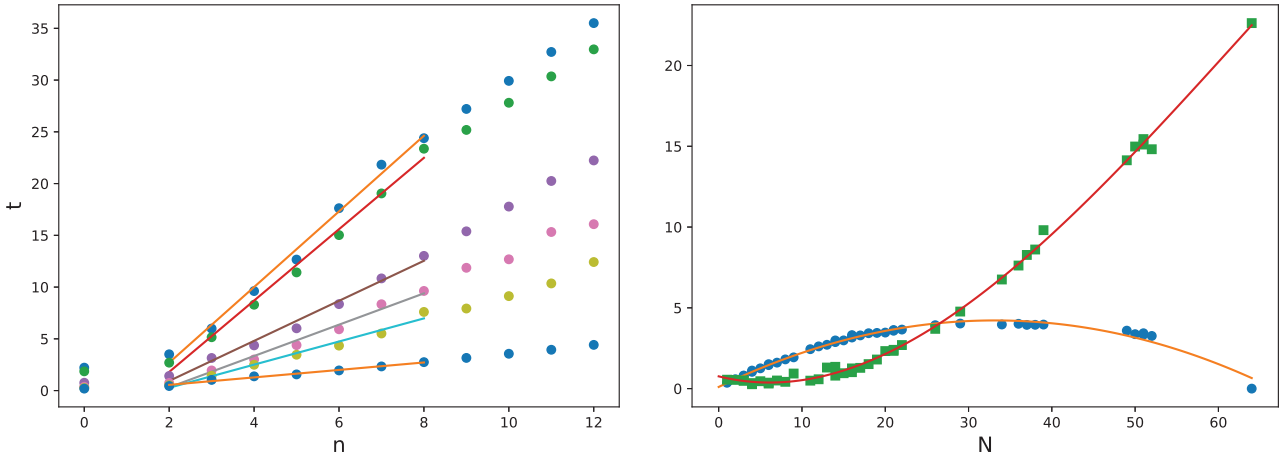

(a) Computation time vs perturbation order

(b) Fit coefficients a and b

Figure 8.17: Computation time of the perturbative method. (a) Shows how the computation time depends on the perturbation order n, for six different arbitrarily chosen energy ranges $[E_1, E_2]$. We also show linear fits $an + b$, fitted in the range $n \in [2, 8]$. (b) shows how the fit coefficients a and b vary with N, the number of states $|0l\rangle$ with energy in $[E_1, E_2]$, i.e. the number of exactly treated states. The constant contribution b is shown in green, while a is shown in blue. We also show a second order polynomial fitted to $a(N)$, and a third order polynomial fitted to $b(N)$.

Figure 8.17a also shows linear fits, obtained in the range $n \in [2, 8]$. Figure 8.17b shows how the fit coefficients depend on the chosen energy range $[E_1, E_2]$. The relevant parameter here is the number of exactly treated states $N = \sum_{E_1 \leq \epsilon_{0l} \leq E_2} 1$, since this determines the size of all dense and sparse matrices involved in the calculation. The exact functional dependency of the computation time on N is determined by internal details of the the sparse matrix library, and is beyond our scope here. We do however note that the coefficient a, describing the order-proportional contribution to the computation time, is roughly proportional to $N(64-N)$. This is probably related to the fact that the matrices $[U(D-E)^{-1}]^n V^\dagger$ from (8.44) have dimension $8(64-N) \times 8N$.

Finally, in Figure 8.18 we compare the computation time requirements to the obtained accuracy. As long as we do not require an accuracy better than 10^{-4}, the fastest calculation is always that shown as grey diagonal crosses. These represent the perturbative approximation where only a single type of state with energy 3.74 eV is treated exactly. This is the least accurate method in terms of convergence with n, but still converges faster in terms of the required computation time, due to the speed of the operations. According to projections based on our fitted models, this trend will continue beyond the twelfth order, so

that the approximation with $N = 1$ will be the fastest method at all levels of accuracy, until it catches up with the exact solution at an accuracy of $\sim 10^{-24}$.

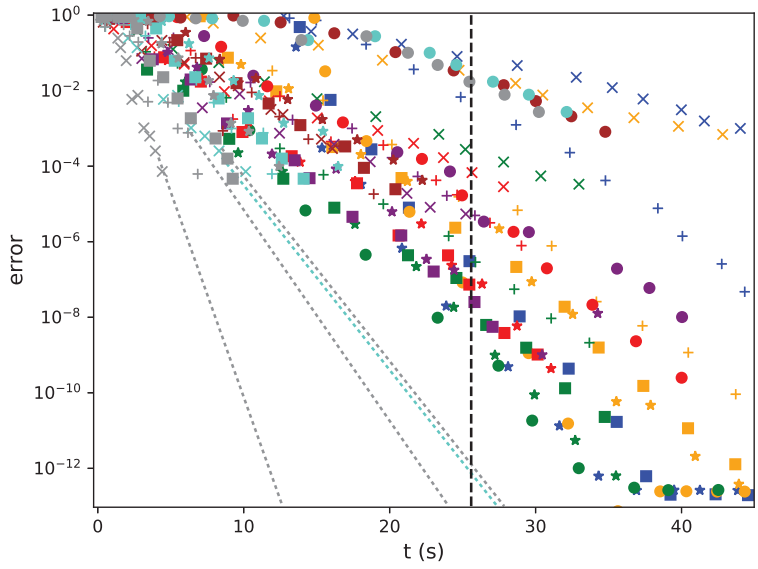

Figure 8.18: Perturbative approximation accuracy as a function of computation time. Results in blue, orange, green, red, purple, brown, turquoise and grey are respectively obtained with $E_1 = -\infty$, -0.13, 0.38, 1.06, 1.60, 2.37, 2.59, and 3.74 eV. Results where $E_2 = \infty$, 5.12, 4.74, 4.24 and 3.74 eV are shown respectively as circles, stars, squares, and horizontal and diagonal crosses. The order of the result always increases towards the right, and goes up to 12 in all cases. For some of the results we also include projections based on the fitted models. These are shown as dotted lines. The vertical dashed line in black represents the average computation time of the exact solution.

8.3 NEGF Monte Carlo

The NEGF Monte Carlo method is described in our third paper (Paper III). Here we just describe some additional results, which were omitted from that work for reasons of brevity. In Section 8.3.1 we use the method to calculate transport coefficients of a small quantum dot. We did this calculation originally as a proof of concept in a small system where the computational requirements are not very large. The quantum dot results also illustrates that the method can be used to calculate thermoelectric coefficients, such as the Seebeck coefficient and the electron contribution to the thermal conductance. In Section 8.3.2 we test the method on a thin film. This was done in order to test the method in a system with k-point dependency.

8.3.1 Quantum dot

In this section we show results of transport calculations in a simple two by two by two unit cells cubic quantum dot of CdTe, employing the tight binding model from our first publication (Paper I). Scattering is implemented within Büttikers approximation, with $\Sigma^r(E) = -i\Gamma I/2$, where $\Gamma = 0.06$ eV. The scattering is assumed elastic and local. As in the previous section, we set $\Sigma_p^r = -i\Gamma_l P_p/2$, but this time with $\Gamma_l = 0.2$ eV. The transmission function is shown in Figure 8.19, which also illustrates that both the error estimates and the spread of the Monte Carlo results converge as $1/\sqrt{n}$, in agreement with theory. The Monte Carlo results of Figure 8.19 are compared to a direct solution approach. This approach involves solving equation (5.86) together with an equation for $\Sigma_s^<(E)$ derived from Büttikers approximation and the elastic criterion. This is described further in Paper III. The direct solution is obtained with and without scattering, in order to show the magnitude of scattering effects and thereby demonstrate that the Monte Carlo approach estimates these effects correctly.

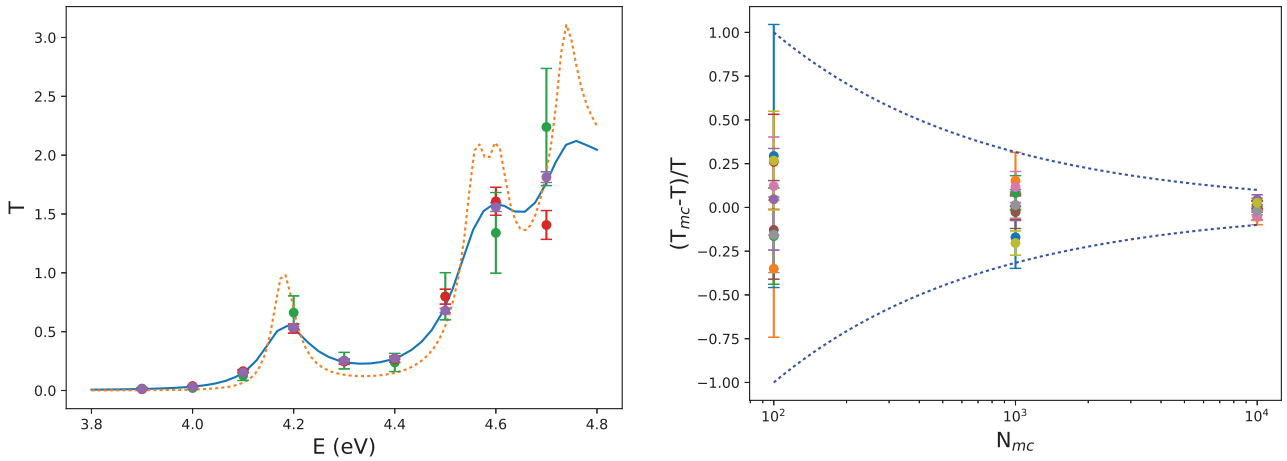

(a) Transmission function

(b) Convergence of Monte Carlo estimates

Figure 8.19: (a) Transmission function $T(E)$. The solid blue line shows the transmission function of the quantum dot, calculated by the direct inversion approach. The dashed orange line shows the transmission function of the same quantum dot without scattering. The green red and purple error bars respectively show Monte Carlo estimates obtained with 100, 1000 and 10000 samples. (b) Relative error $(T_{mc} - T)/T$ as function of the number n of Monte Carlo samples. The nine different colors represent the nine energies in (a). The two dashed blue lines show the functions $\pm 10/\sqrt{n}$.

Figure 8.20 shows the conductance of the quantum dot. The Monte Carlo simulation was set to accumulate samples for 1000 s (17 min) for each value of μ, which resulted in approximately 20000 samples per value. As can be seen from Figure 8.20b, this results in a relative standard deviation $\Delta G/G$ in the range of 1-4 percent. The Monte Carlo results are compared to the direct inversion method, which is integrated over a regular energy grid of 13 points, in the range

$\mu \pm 0.25$ eV. The interpolated method referenced in this figure and the succeeding ones will be explained below.

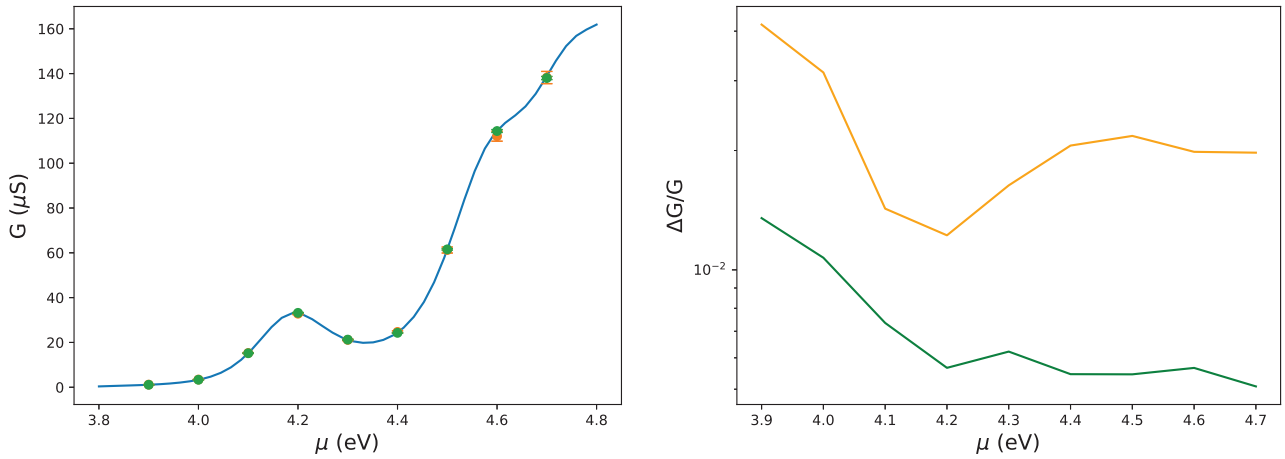

(a) Conductance

(b) Relative error estimate

Figure 8.20: (a) Conductance in Siemens, as function of chemical potential μ in eV. The solid blue line shows the result of the direct inversion approach. The orange and green error bars show results of the Monte Carlo simulations, respectively employing the straight forward and the interpolated method. All of the Monte Carlo results were obtained with an accumulation time of 1000 s. (b) Error estimate of the Monte Carlo calculations in terms of the relative standard deviation $\Delta G/G$. The orange line represents the straight forward method, while the green line represents the interpolated method.

To obtain the other thermoelectric transport coefficients we make use of (2.24)-(2.26), and define

$$\mathcal{S}_n = \int (E-\mu)^n T(E) \mathrm{Th}(E) \mathrm{d}E. \tag{8.45}$$

The thermoelectric coefficients A and B are obtained from $\mathcal{S}_1$, while the coefficient C is obtained from $\mathcal{S}_2$. In the Monte Carlo simulation these coefficients are obtained simultaneously with the conductance calculation, by simply weighting the result respectively with $(E-\mu)$ and $(E-\mu)^2$, E being the energy of the transmitted electron. The thermal conductance k of the quantum dot, and its Seebeck coefficient α can be calculated from A and C using (2.27)-(2.29). In terms of $\mathcal{S}_1$ and $\mathcal{S}_2$, the resulting expressions are

$$\alpha = -\frac{2e\mathcal{S}_1}{hTG}, \quad \text{and} \tag{8.46}$$

$$k_e = \frac{2\mathcal{S}_2}{hT} - \frac{4e^2\mathcal{S}_1^2}{h^2TG}. \tag{8.47}$$

By making use of the general formula

$$\Delta F^2 \approx \sum_i \left(\frac{\partial F}{\partial x_i}\right)^2 \Delta x_i^2, \tag{8.48}$$

we can estimate the standard deviation of the Monte Carlo calculations of α and k as

$$\Delta\alpha = \frac{2e}{hT}\sqrt{\frac{\Delta\mathcal{S}_1^2}{G^2} + \frac{\mathcal{S}_1^2\Delta G^2}{G^4}}, \quad \text{and} \tag{8.49}$$

$$\Delta k = \frac{2}{hT}\sqrt{\Delta\mathcal{S}_2^2 + \left(\frac{2e^2}{h}\right)^2\left(\frac{4\mathcal{S}_1^2\Delta\mathcal{S}_1^2}{G^2} + \frac{\mathcal{S}_1^4\Delta G^2}{G^4}\right)}. \tag{8.50}$$

Monte Carlo calculations of α and k are compared to the direct inversion approach respectively in figures 8.21 and 8.22.

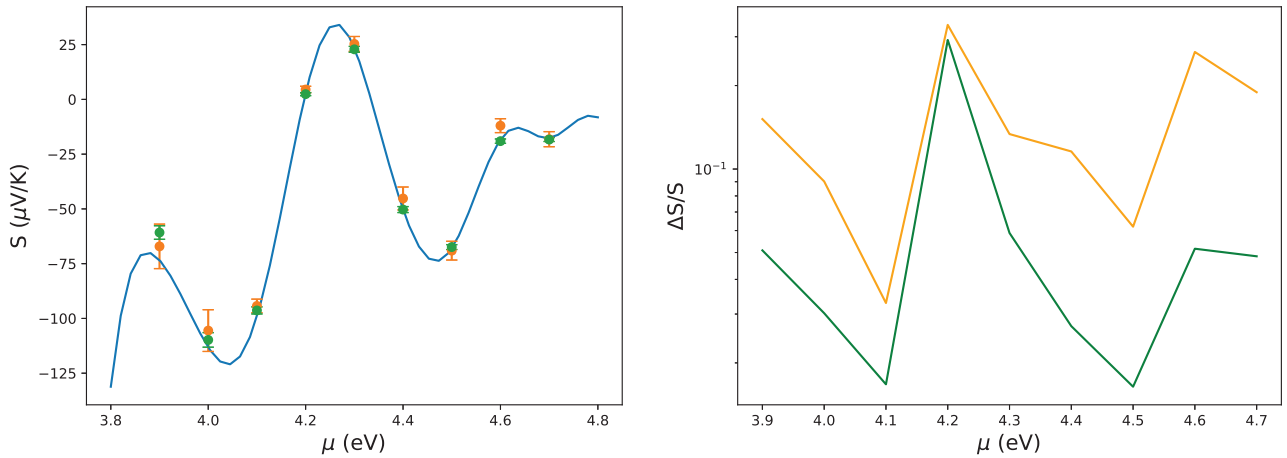

(a) Seebeck coefficient

(b) Relative error estimate

Figure 8.21: (a) Seebeck coefficient $S = V/\Delta T$ in μV/K. The solid blue line shows the result of the direct inversion approach. The orange and green error bars show results of the Monte Carlo simulations, respectively employing the straight forward and the interpolated method. (b) Error estimate of the Monte Carlo calculations in terms of the relative standard deviation $\Delta S/S$. The orange line represents the straight forward method, while the green line represents the interpolated method.

8.3.1.1 Interpolated method

While the transmission function shown in Figure 8.19 is quite fast to calculate using the Monte Carlo technique, calculation of transport coefficients is much slower. This is because in these calculations the electron energy is different in every Monte Carlo sample, which means G^r will have to be recalculated for every such sample. Since calculation of G^r is the most demanding part of the procedure, one could potentially gain a substantial speed improvement if the amount of such recalculations were reduced. One way of obtaining this would be interpolation. That is, instead of always recalculating the scattering probabilities p_{ij} from the Green's function, we sometimes interpolate between previously calculated values of these functions at different energies. One such interpolation scheme is tested here.

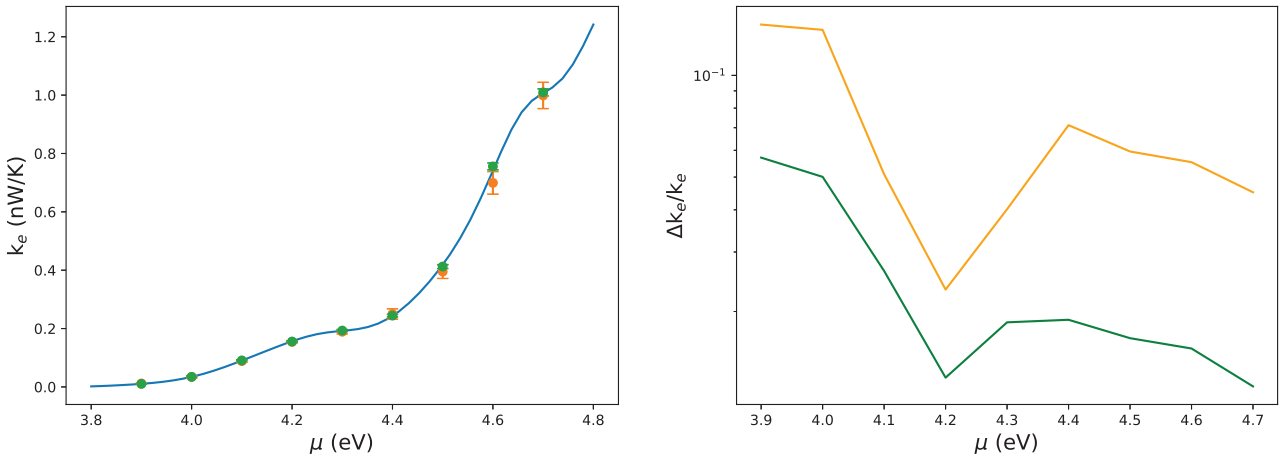

(a) Thermal conductance

(b) Relative error estimate

Figure 8.22: (a) Thermal conductance in W/K. The solid blue line shows the result of the direct inversion approach. The orange and green error bars show results of the Monte Carlo simulations, respectively employing the straight forward and the interpolated method. (b) Error estimate of the Monte Carlo calculations in terms of the relative standard deviation $\Delta k/k$. The orange line represents the straight forward method, while the green line represents the interpolated method.

This interpolation scheme is implemented as follows: Whenever some column of the Green's function is calculated, all corresponding scattering probabilities $p_{ij}(E) = \gamma_i \gamma_j |G_{ij}(E)|^2$ are stored in a table together with their respective energy. Then, whenever transmission functions are required at an energy E between two energies E_1 and E_2 where these probabilities have previously been calculated, we test whether the relevant probabilities differ by more than 5 percent on average between E_1 and E_2. If this is not the case, $p_{ij}(E)$ is interpolated linearly between $p_{ij}(E_1)$ and $p_{ij}(E_2)$. Otherwise, the relevant sections of the Green's function is recalculated, and $p_{ij}(E)$ is obtained from this.

The figures 8.20-8.22 also contain results from the interpolated method. These calculations were executed for 1000 s (17 min), and resulted on average in approximately 200 000 Monte Carlo samples. Relative to the uninterpolated method this is a tenfold improvement. As can be seen from the figures, this has resulted in the relative standard deviation being reduced by approximately a factor of $\sqrt{10} = 3.16$. Figure 8.23 compares the sampling rates of the two methods in a single simulation. The sampling rate of the uninterpolated method stays approximately fixed at 60 samples per second, while the interpolated method starts out at this frequency, but then becomes progressively faster as the interpolation table is filled in. This process saturates after approximately 10000 samples, after which the interpolated method stays fixed at 600-700 samples per second.

Thus, the sampling rate of the interpolated method is seen to saturate at approximately ten times that of the uninterpolated one. However, since the Monte

Carlo method is implemented in Python, it seems likely that this ratio is limited primarily by the Python overhead, and that for instance a C-implementation of the interpolation scheme would be significantly faster still.

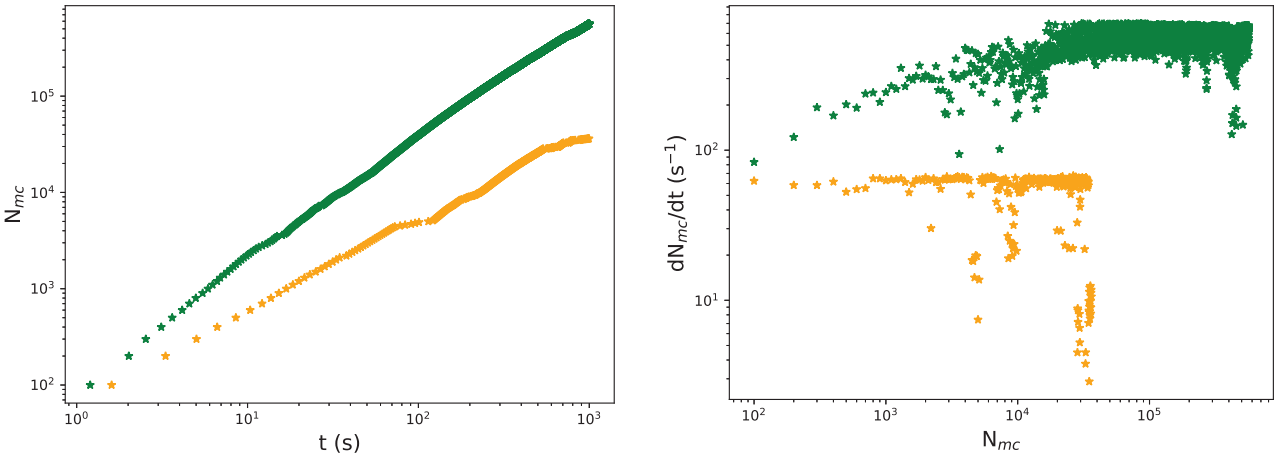

(a) Number of acquired Monte Carlo samples

(b) Sampling rate as a function of the number of samples already acquired

Figure 8.23: Comparison of sampling rate. The uninterpolated method is shown in orange, while the interpolated method is shown in green.

8.3.2 Thin Film

This section includes results of transport calculations in a CdTe thin film with a thickness of two unit cells. Both the CdTe Hamiltonian, the scattering model, and the coupling to the leads make use of the same models as in the previous section. However, this time we set $\Gamma = \Gamma_l = 0.02$ eV.

A major focus of this section is to compare the computational efficiency of the Monte Carlo method to that of alternative approaches, when these have to be integrated over a k-grid. Thus, some effort is put into a study of how the computation time and accuracy of these other methods scale with the grid resolution. We study both the direct solution approach mentioned in the previous section, and in addition an iterative approach. These methods solve the same set of equations, and their only difference is that the first method solves the equations by direct linear inversion, while the second method solves them iteratively. The particular iterative method employed is the Scipy implementation of the gmres method. In both methods, integration over energy is performed over a grid with a quite high resolution of 50 points in the range $\mu \pm 0.25$ eV. This is to assure minimal contribution to the error from energy integration.

8.3.2.1 Results

In Figure 8.24 the direct and iterative methods, employing various k-grid resolutions, are compared to Monte Carlo results. The calculations are performed

both at a chemical potential $\mu = 4.3$ eV, which is quite low in the conduction band, and at $\mu = 5.1$ eV which lies deeply into the conduction band, where the entire Brillouin zone contributes to conduction. In addition, the calculations are performed with two different scattering models. In one of these, scattering does not couple the k-points, i.e. the k-value of an electron is not changed after scattering. In the other model, the electrons are scattered homogeneously between all k-points, i.e. when an electron is scattered, it may end up with any value of $\boldsymbol{k}$ with equal probability.

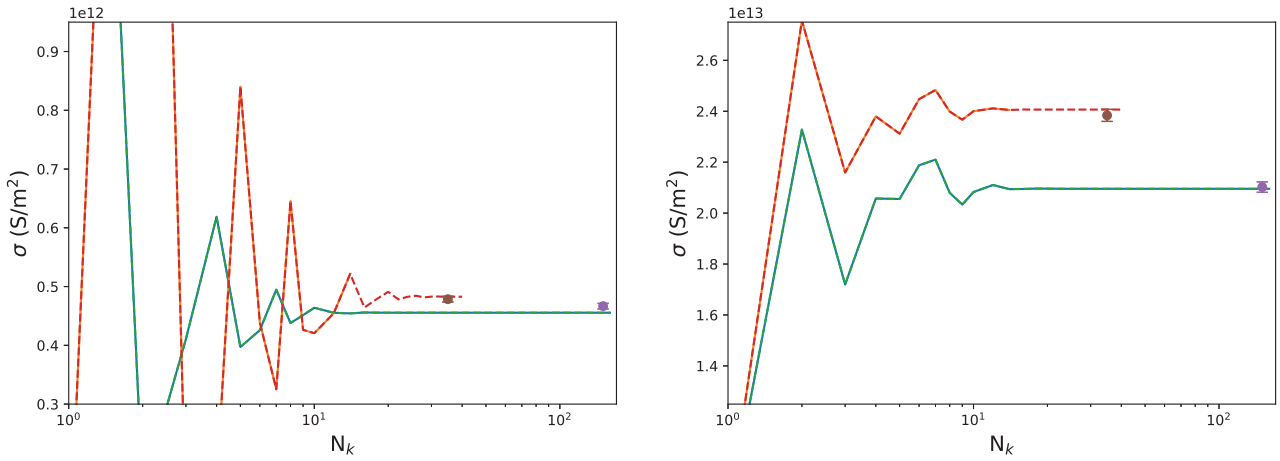

(a) $\mu = 4.3$ eV

(b) $\mu = 5.1$ eV

Figure 8.24: Conductance of thin film in Siemens/m^2, as a function of k-grid resolution. Solid lines employ direct inversion, dashed lines employ the iterative approach, while the error bars represent the Monte Carlo results. Among these, the results shown in green blue and purple employ the k-conserving scattering model, while the results shown in red, orange and brown employ the k-coupling scattering model. The Monte Carlo results do not employ a k-grid, and their position along the horizontal axis is determined simply so as to be convenient in comparing them to the other results.

At the high value om μ, integration is performed over the entire Brillouin zone $k_x, k_y \in [-\frac{1}{2}, \frac{1}{2}]$, wile at the low value of μ it is only performed over the range $k_x, k_y \in [-\frac{1}{4}, \frac{1}{4}]$. This is because the outer extents of the Brillouin zone have no significant contribution to transport this low in the conduction band. In addition, because of the symmetry of the Brillouin zone, values need only be calculated in one quarter of the integration region, for instance that where $k_x, k_y > 0$. The grid resolution N_k referenced in Figure 8.24 and in the following figures, refers to the number of points along one dimension, in the region where values are calculated. That is, in the region $k_x, k_y \in [0, \frac{1}{2}]$ when $\mu = 4.3$ eV, and $k_x, k_y \in [0, \frac{1}{4}]$ when $\mu = 5.1$ eV.

When the k-conserving scattering model is employed, the transport problem can be separated into isolated problems for each k-point. When the k-coupling model is employed however, this is not possible, and as a result the computational demands of the alternative approaches become drastically larger. When

employing the k-conserving model, it was possible to take the grid resolution all the way up to $N_k = 160$ without trouble, but with the k-coupling model, we ran into problems of too little memory at $N_k > 14$ with the direct inversion approach. With the iterative approach such problems did not arise, but after $N_k > 40$ the calculations were just too time consuming.

The Monte Carlo calculations were allowed to accumulate samples until the result was determined with a relative standard deviance of approximately one percent. Relevant information about the results is summarized in table 8.2. The required computation time is determined by the sampling rate, and by the variance ΔX^2 of the estimator. We observe that the sampling rate is roughly 3 times higher when the k-conserving model is employed, compared to the k-coupling model. This is because when the k-coupling model is employed, the diagonal of the Green's function must be recalculated every time an electron is moved, whereas when the k-conserving model is used, this needs only be calculated once per sample.

μ (eV)	4.3	4.3	5.1	5.1
scattering model	k-conserving	k-coupling	k-conserving	k-coupling
G (S/m^2)	$4.5552{\cdot}10^{11}$	$4.8270{\cdot}10^{11}$	$2.0955{\cdot}10^{13}$	$2.4066{\cdot}10^{13}$
G_{mc} (S/m^2)	$4.6667{\cdot}10^{11}$	$4.7856{\cdot}10^{11}$	$2.1022{\cdot}10^{13}$	$2.3839{\cdot}10^{13}$
ΔG_{mc} (S/m^2)	$4.7897{\cdot}10^{9}$	$4.8657{\cdot}10^{9}$	$2.0424{\cdot}10^{11}$	$2.3668{\cdot}10^{11}$
ΔX (S/m^2)	$2.9387{\cdot}10^{12}$	$6.6054{\cdot}10^{12}$	$8.9526{\cdot}10^{13}$	$9.3588{\cdot}10^{13}$
num. samples	376451	1842945	192140	156351
comp. time (s)	6411.1	102406.	2565.9	6405.8
t_s (s)	0.01703	0.05557	0.01335	0.04097

Table 8.2: Monte Carlo results. G is the result of the standard methods, G_{mc} is the Monte Carlo result, ΔG_{mc} is the standard deviance of the Monte Carlo result, ΔX is the standard deviance of the estimator X which is sampled to calculate $G_{mc} = \bar{X}$, and t_s is the computation time per sample.

In addition, we observe that the ratio $\Delta X/G$ is higher at the low value of μ. This is because a large fraction of the samples are then drawn from k-points which do not contribute significantly to conduction. In the k-conserving case, this problem is mitigated by drawing the k-points from a probability distribution proportional to the k-projected density of states of bulk CdTe, so that most of them are drawn from the region contributing to conduction. In the k-coupled case however, this technique is not effective, and in fact leads to a significant increase in the variance of X. Accordingly, we have not made use of this technique in the k-coupled case.

8.3.2.2 Analysis of computational scaling

In Figure 8.25a we study how the relative error of the direct solution and iterative method depends on the k-grid resolution. The relative error is estimated as $\Delta G/G$, where ΔG is calculated as the difference between each result and the same

result with maximal grid size. The first thing to note is that for the k-conserving $\mu = 4.3$ eV case, the direct solution and iterative results are coinciding until an error of less than about 10^{-6} is reached. We thus conclude that the separation point 10^{-6} represents the accuracy of the iterative method. Similar conclusions hold for the other three cases, so in order to simplify the figure we include only the direct inversion result in the other k-conserving case, and only the iterative results for the two k-coupling cases.

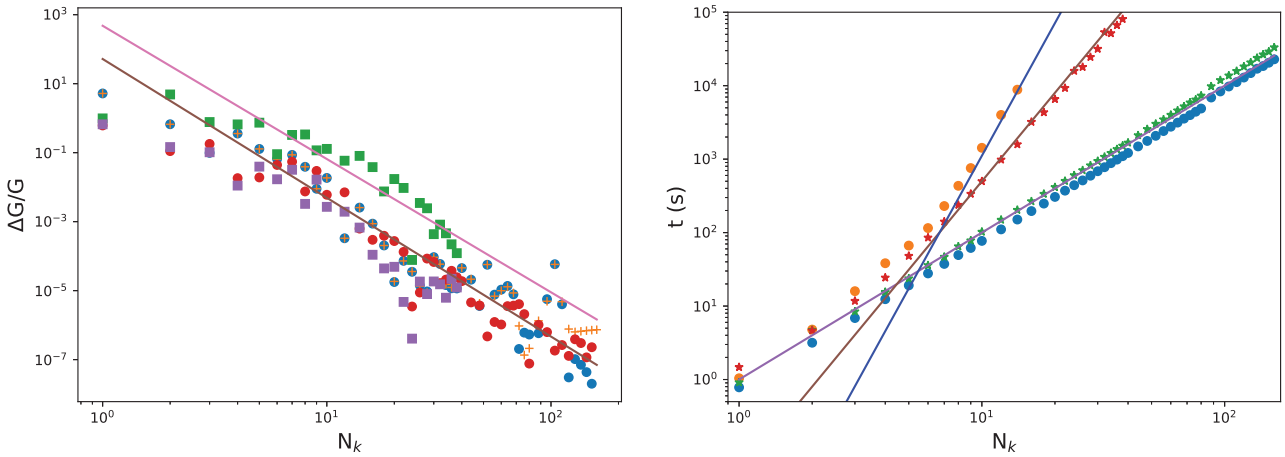

(a) Accuracy (b) Computation time

Figure 8.25: Accuracy and computation time of direct and iterative solution. (a) Error estimate as function of grid size. Circles represent results with k-conserving scattering, employing the direct solution approach. Squares represent results with k-coupling scattering, employing the iterative approach. The blue circles and green squares are obtained with $\mu = 4.3$ eV, while the red circles and purple squares are obtained with $\mu = 5.1$. The orange crosses are obtained with the same parameters as the blue circles, but using the iterative approach. The brown and pink line are power functions fitted respectively to the k-conserving and k-coupling results at $\mu = 4.3$ eV. (b) Computation time as function of grid size. Direct inversion results are shown as circles, and iterative results as stars. The blue circles and green stars were obtained using the k-conserving scattering model, while the orange circles and red stars were obtained using the k-coupling model. The results are from the calculation at $\mu = 4.3$ eV, but the results at $\mu = 5.1$ eV are almost identical. The solid lines in purple, brown and blue show respectively the power functions N_k^2, $0.05 \cdot N_k^4$ and $0.00111 \cdot N_k^6$.

The solid line shown in brown in Figure 8.25a represents a power function fitted to the k-conserving $\mu = 4.3$ eV case. The first six points are ignored in this fit, and the result is $\epsilon = 51.931 \cdot N_k^{-4.0235}$. We observe that the asymptotic behavior of the two cases with $\mu = 5.1$ eV also agree fairly well with this function. The k-coupling $\mu = 4.3$ eV case however, lies a little higher than the other results, and we thus make a separate fit of that case. The result is $\epsilon = 477.44 \cdot N_k^{-3.8633}$, and is shown as a solid line in pink in Figure 8.25a. Both of the fitted functions have an exponent fairly close to 4, and we thus conclude that the integration accuracy is of fourth order in these cases.

In Figure 8.25b we study how the computation time of the direct solution and iterative methods scale with k-grid resolution. The results are compared to appropriate power functions. We see that in the k-conserving case, both the direct inversion and iterative approach lies close to the function $t = N_k^2$. This is reasonable, since in that case the problem can be divided into isolated problems for each k-point, so that the total computation time should be proportional to the total number of k-points N_k^2.

In the k-coupled case, we see that the iterative computation time asymptotically approaches the function $t = 0.05 \cdot N_k^4$, while the direct inversion time approaches $0.00111 \cdot N_k^6$. This is also reasonable, since we are then solving a linear equation set with a number of equations proportional to the number of k-points. It is well known that direct inversion scales as N^3 and an iterative method as $N_{itt} \cdot N^2$, where N is the number of equations and N_{itt} the required number of iterations.

At small grid sizes all of the methods lie close to the function N_k^2. We conclude that this function describes the time required to calculate G^r, which will always be proportional to the number of k-points.

Summarizing, the error ϵ of both the direct solution and the iterative method scales with N_k^{-4}, the computation time t of the k-conserving cases with N_k^2, while in the k-coupled cases the computation time of the iterative method scales with N_k^4, and the computation time of direct inversion method with N_k^6. Combining all this, we find that the error scales with t^{-2} in the k-conserving cases, while in the k-coupled cases the iterative and direct inversion errors scale respectively as t^{-1} and $t^{-\frac{2}{3}}$.

For the case of the Monte Carlo calculations, corresponding expressions for the relative deviation $\epsilon = \Delta G/G$, with ΔG now being the standard deviation, can be found from the general relation

$$\epsilon = \frac{\Delta X}{G\sqrt{N_s - 1}} \approx \frac{\sqrt{t_s}\Delta X}{G} t^{-\frac{1}{2}}, \tag{8.51}$$

where t_s is the average computation time per Monte Carlo sample. Thus, the error of the Monte Carlo method always scales as $t^{-\frac{1}{2}}$. Concrete expressions for the relation between ϵ and t in the four cases we have tested can be found by inserting the numbers from table 8.2 into (8.51). In the k-conserving cases, we obtain respectively $\epsilon \approx 0.84 \cdot t^{-\frac{1}{2}}$ and $\epsilon \approx 0.94 \cdot t^{-\frac{1}{2}}$ in the $\mu = 4.3$ eV and $\mu = 5.1$ eV cases, while in the k-coupling cases, we obtain respectively $\epsilon \approx 3.2 \cdot t^{-\frac{1}{2}}$ and $\epsilon \approx 0.79 \cdot t^{-\frac{1}{2}}$ in the same two cases. All of these scaling relations are compared in Figure 8.26, where the error and computation time of the actual results is also included. We observe that even the worst scaling of the alternative approaches, the k-coupled direct solution, has an error which scales better with computation time than the Monte Carlo method.

However, it remains a question how general the fourth order scaling of the error seen in Figure 8.25a actually is. Further, the Monte Carlo method can be parallelized much more efficiently than the other methods, and has smaller memory requirements. It should also be mentioned that the k-coupled Monte

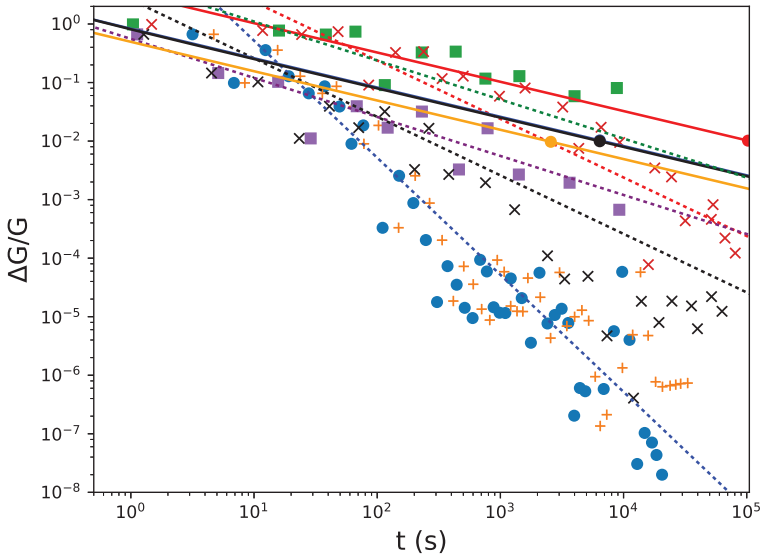

Figure 8.26: Relative error as a function of computation time in seconds. The blue circles and orange crosses show respectively the direct and iterative solutions in the k-conserving $\mu = 4.3$ eV case. The other results assume k-coupled scattering. Among these, the green and purple squares show respectively the direct solution in the $\mu = 4.3$ eV and $\mu = 5.1$ eV cases, while the red and black crosses show respectively the iterative solutions for the same values of μ. The dotted lines show scaling estimates obtained in the text. These are in the same colors as the results they are obtained from. The solid lines show the scaling of the relative deviation in the Monte Carlo calculations. The blue and red lines represent respectively the k-conserving and k-coupled $\mu = 4.3$ eV cases, while the orange and black lines represent respectively the k-conserving and k-coupled $\mu = 5.1$ eV cases. The Monte Carlo results from our simulations obtained a relative deviation of 10^{-2}. These points are marked on the scaling relation as overlying circles.

Carlo calculations are slowed down quite significantly by the unnatural scattering mechanism, where all k-points are drawn with equal probability. This causes the electrons to spend most of the simulation in regions of the Brillouin zone where they are almost immobile, and accordingly causes the calculation to be very inefficient. In more realistic scattering models, the probability of scattering to a particular k-point is proportional to the k-projected density of states, meaning that the electrons would spend most of the simulation time in regions contributing more to the conductivity. This could significantly improve the efficiency of the simulation.

Chapter 9

Conclusions

During the course of this thesis, I have pursued a series of different methods for performing transport calculations. All of these have been lacking important aspects, by not employing sufficiently accurate models of band structure and scattering, and by ignoring important physical effects. Because of this, none of my results are useful as predictions concerning values of transport coefficients in real materials. Nevertheless, my experimentation with these methods has allowed me to make a few conclusions concerning the appropriate way forward for implementing a general transport framework. In particular, I would like to share some conclusions concerning how the appropriate method varies between different regimes of heterostructure transport.

The first parameter I will use to distinguish different regimes, is the typical size scale of structures in the heterostructure. In a superlattice, this size scale would typically be the superlattice period, while in a disordered three dimensional structure it could be the average grain size, or some similar parameter. Whenever this size scale is considerably larger than the coherence length of the transported particles, which is usually similar to their mean free path, the transport problem is well described by the Boltzmann equation, and the Boltzmann Monte Carlo method seems best suited to solve this. In high field applications, one must use the method described in Section 8.1.1, while for the calculation of linear transport coefficients, the method of Section 8.1.2 seems much better suited, assuming it is appropriately generalized.

A second important parameter which distinguishes different regimes, is the effective dimensionality of the problem. In particular, I will distinguish between quasi-one-dimensional systems, and systems that have fully three-dimensional structures. All of my own calculations have been limited to the quasi-one-dimensional case, so my discussion of the fully three-dimensional case will be limited to a discussion merely of what seems intuitive. In fully three-dimensional systems, there seems to have been some success in modeling heterostructure transport using the Boltzmann equation, even when the heterostructure size scale is small. In a sense, it also seems intuitive that this approach should work better in such systems than in quasi-one-dimensional systems, since failure of the Boltzmann equation is due to interference effects, which will be reduced by the inverse square law in fully three-dimensional systems.

On the other hand, peculiar transport phenomena like Anderson localization have been predicted to occur also in three-dimensionally disordered systems. Since such effects are not predicted by the Boltzmann equation, it is clear that Boltzmann based approaches are not always applicable to three-dimensional heterostructures. All in all this indicates that in the fully three-dimensional case, more study is required in order to understand precisely which cases are

treatable by the Boltzmann equation, and which ones are not. In the mean time, Boltzmann Monte Carlo methods seems like a good starting point for doing practical calculations. Again, the choice between the methods described in 8.1.1 and 8.1.2 will depend on whether the problem is in the linear or high field regimes.

In the quasi-one-dimensional case, we must distinguish between the periodic case of superlattices, and the non-periodic case, which is sometimes referred to as disordered superlattices. The regimes of high field transport in superlattices is well described by Wacker[28], so the discussion here will be limited to the regimes of linear transport, which was investigated in our second publication (Chapter II). Assuming a simple superlattice, with a single well and barrier layer, our results show that semiclassical approaches are applicable when the superlattice period is ether considerably larger, or considerably smaller than the coherence length. However, when the period is large, one must use the band structure of the composing materials, while in the regime of small superlattice period, the minibands of the superlattice should be used. In the first of these cases, the Monte Carlo method of Section 8.1.2 seems like the best suited method. In the second case, the Boltzmann equation can be solved directly as long as the scattering model is not too complicated. Given a more complicated scattering model, the method of Section 8.1.2 again seems like the appropriate choice.

The results in our second publication also show that one can expect the existence of an intermediate regime, where neither of the two semiclassical approaches work particularly well. Based upon the discussion of Section 6.4, the failure of the miniband approach in this regime is due to the step from (6.82) to (6.88) not being justified. Thus, the fairly specialized regime of superlattices with a period comparable to the coherence length, can probably be handled by applying (6.82) directly.

The final regime to be discussed, is that of non-periodic quasi-one-dimensional heterostructures. It is probably in this regime that the Monte Carlo method described in our third paper (Chapter III) is most useful. This is both because there are few other methods capable of handling this regime, at least when accurate scattering models are required, and also because it is precisely in quasi-one-dimensional systems where one can expect Monte Carlo methods to have a major advantage, since they do not require explicit integration over the crystal momentum.

Thus, the NEGF Monte Carlo method could have potential applications within several different areas, among which our original application of thermoelectric effect in quasi-one-dimensional heterostructures is only one. However, before this can be realized, considerable amounts of additional testing is required to determine the actual utility of the method. In particular, we must perform more appropriate tests of how competitive the method is performance wise, and perform tests with more realistic scattering mechanisms. In addition, additional investigations are needed into the linear limit, and the range of applicability of the positivity assumption.

Finally, in retrospect it seems that the choice to base our calculations on the NEGF formalism rather than the Kubo relations was a mistake. The main

reason for this has to do with the numerical derivative of the NEGF currents. As it happens, all methods for solving the NEGF equations we have encountered, have some problems with numerical noise. Often, this noise will be insignificant in the currents themselves, but the numerical derivative can severely magnify the effect. Thus, to obtain stable results, it is best to calculate these derivatives analytically, in which case we will in any case obtain expressions similar to the Kubo relations. In addition to this, there is no reason to assume four point functions to be considerably much harder to handle in a perturbative framework, where everything is in any case expressed in terms of unperturbed Green's functions. Thus, the perceived advantage of the NEGF formalism, in that one does not need to handle four point functions, seems not to be that relevant.

Papers

Paper
I

Thermoelectric transport calculations using the Landauer approach, ballistic quantum transport simulations, and the Buttiker approximation

I

Computational Materials Science 132 (2017) 146–157

Contents lists available at ScienceDirect

Computational Materials Science

journal homepage: www.elsevier.com/locate/commatsci

Thermoelectric transport calculations using the Landauer approach, ballistic quantum transport simulations, and the Buttiker approximation

Lars Musland [a], Espen Flage-Larsen [b,*]

[a] University of Oslo, P.O. Box 1048 Blindern, NO-0316 Oslo, Norway
[b] SINTEF Materials and Chemistry, P.O. Box 124 Blindern, NO-0314 Oslo, Norway

ARTICLE INFO

Article history:
Received 27 July 2016
Received in revised form 20 January 2017
Accepted 12 February 2017
Available online 10 March 2017

Keywords:
Thermoelecric
CdTe
Seebeck coefficient
Conductivity
Thermal conductivity
Charge carrier transport
Landauer approach
Tight binding
Buttiker approximation
Greens functions

ABSTRACT

An implementation of the Landauer approach utilizing the ballistic quantum transport package Kwant to calculate thermoelectric transport properties is presented. Incoherent scattering is included by an approach suggested by Buttiker, where scattering is mimicked by virtual contacts (Buttiker probes). In this paper we present the implementation and provide a simple validation by comparing results to the Boltzmann transport equation (BTE) for bulk CdTe and a simple short period superlattice. The electronic structure, serving as a base for fitting a tight-binding model, is calculated from first-principles. From there, the electronic structure on a dense k-point grid is generated and passed to the BTE routines, while the transmission coefficients in the Landauer approach are calculated from Green's functions based on the tight-binding model. Our results show good agreement between the results from the Buttiker and the BTE calculations, which indicates a successful initial implementation. We discover significant performance bottlenecks tied to the density of the Buttiker probes and as such the implementation needs additional optimization to be viable for production work.

1. Introduction

Improvements in the conversion efficiency of thermoelectric materials have been proposed to be possible by the use of controlled heterostructures, such as superlattices [1–17]. Such improvements would be a consequence both of reduced heat conductivity, and from effects on electron transport. These effects include quantum confinement, tunnelling, and band offsets between the different layers. The idea is that these effects may limit the energy range contributing to electron transport, which is an approach commonly referred to as energy filtering [5,9,14,17–23]. Because of the complexity of such materials, modelling will form an important part in testing whether this proposal holds true, and if so to guide synthesis and assist interpretation of measurements.

In thermoelectric research, the usual modelling approach is to solve the semi-classical Boltzmann Transport Equation (BTE) within the Relaxation-time Approximation (RTA) [24–26], an approach which has proven successful for the modelling of bulk materials [26–36]. However, it has long been known that when the mesoscale geometry of the material is complicated, the Boltzmann equation is no longer strictly valid [27,28,37]. For certain applications this fact has been shown to have significant consequences in superlattices [38,39]. More specifically, the BTE does not reproduce resonances at high fields, and even at low fields it can be quantitatively different from calculations that include quantum effects [38,39]. In view of the recent focus on the concept of energy filtering, investigations of such effects on the thermoelectric transport coefficients of these structures is thus of great importance.

For the modelling of systems where both quantum and scattering effects are important, the Nonequilibrium Green's functions (NEGF) method [28,37] is becoming increasingly popular. This approach is also the only widely applicable method that is close to being rigorously correct. It has already been applied to the modelling of thermoelectric superlattices [40–43], and was found to give insight to why the predicted improvements are difficult to realize experimentally [43]. However, no argument was given as to whether the same conclusions could have been found by utilizing the BTE.

In other work [41] some difference between NEGF and BTE results was found, but as stated by the authors, this difference was probably mainly due to the small total thickness of the super-

* Corresponding author.
E-mail address: espen.flage-larsen@sintef.no (E. Flage-Larsen).

http://dx.doi.org/10.1016/j.commatsci.2017.02.016
0927-0256/

lattice (6 nm) causing quantum confinement effects. At this length scale transport is still in the semi-ballistic regime, and is not comparable to the BTE.

An approach to quantum transport that is related to NEGF, but which is conceptually simpler, is one that has been referred to as the Buttiker approximation [42]. The central idea of this approach is that scattering processes can be modelled by so called Buttiker probes [37,42,44–50], which are a set of virtual floating contacts attached to the system. Since the probes are floating their only net effect on the system is to randomize the momentum and phase of the carriers, thus effectively acting like a simple scattering mechanism. The Buttiker approximation can also be applied to phonon transport [42,51].

By the use this approach, the transport problem is transformed into a ballistic problem, and is thus treatable within a ballistic formalism, and can be solved with a ballistic solver. Here we report on an implementation of the Buttiker approximation within the Landauer formalism, utilizing the ballistic quantum transport package Kwant [52,53], which is used to calculate the transmission function T. Within the Landauer framework both the conductivity and the other thermoelectric transport coefficients are expressed in terms of the transmission function.

The purpose of this paper is primarily to present and to validate our implementation. Our approach to validation is to compare our results to those of the BTE in a regime where the BTE is expected to be valid. This is the case in bulk materials, and also in short period superlattices. Accordingly, we present transport calculations on bulk CdTe, as well as on a super lattice with a period consisting of four unit cells of CdTe followed by four unit cells of $Hg_{.25}Cd_{.75}Te$. Kwant requires a tight-binding model of electrons in the material. We acquire this model by fitting its parameters to the band-structures of CdTe and $Hg_{.25}Cd_{.75}Te$ obtained by DFT calculations using VASP [54–56].

This paper is organized as follows:

In Section 2 we describe some of the theory behind the approach: In Section 2.1 we discuss thermoelectric transport properties and how these are expressed in the Landauer formalism. Then, in Section 2.2 we describe the Buttiker approximation in more detail. In Section 2.3 we discuss in which cases the semiclassical BTE can be expected to agree with our implementation based on quantum transport.

Following, in Section 3 we describe the details of our implementation: In Section 3.1 we describe in detail the fitting procedure we used to obtained the tight-binding model that was used in our calculations. Then, in Section 3.2 we describe the implementation of the Buttiker approximation, and how we use this together with Kwant to calculate the transmission function and the backscattering mean free path [57], while in Section 3.3 we describe the numerical integrals needed to calculate the thermoelectric transport coefficients.

In Section 4 we present our results: In Section 4.1 we present the tight-binding models obtained by our fitting procedure, while in Sections 4.2 and 4.3 we present transport calculations on bulk CdTe and on the short period superlattice $4x$CdTe-$4x$$Hg_{.25}Cd_{.75}Te$, respectively. Finally, in Section 5 we summarize and conclude.

2. Theory

2.1. Thermoelectric transport coefficients and Landauer framework

The most relevant thermoelectric transport properties are the electrical conductivity σ, the thermal conductivity κ and the Seebeck coefficient α. These are the three transport coefficients that enter the thermoelectric figure-of-merit: $zt = \sigma\alpha^2 t/\kappa$, which determines the conversion efficiency of the material [58–60]. The thermal conductivity has contributions from electrons and lattice vibrations: $\kappa = \kappa_e + \kappa_l$ respectively. In this work, we focus on electron transport, and will thus be exclusively concerned with κ_e, commonly written as $\kappa_e = \sigma L t$, t being absolute temperature and L being the Lorenz coefficient [61,62]. L reduces to $2.44 \cdot 10^{-8}\,\mathrm{V}^2/\mathrm{K}^2$ in highly degenerate systems, such as simple metals [59–63].

We will restrict this work to elastic scattering, in which case these coefficients can be expressed within Landauer formalism as [57,64]

$$\sigma = \int \mathrm{d}E\,\Sigma(E)F_T(E), \tag{1a}$$

$$\alpha = -\frac{1}{\sigma e t}\int \mathrm{d}E\,\Sigma(E)F_T(E)(E-\mu), \tag{1b}$$

$$\kappa_e = \frac{1}{e^2 t}\int \mathrm{d}E\,\Sigma(E)F_T(E)(E-\mu)^2 - t\sigma\alpha^2. \tag{1c}$$

These expressions are identical to the ones obtained from the RTA BTE formalism, where $\Sigma(E)$ is often referred to as the transport distribution function. $F_T(E)$ is the thermal broadening function [37] or Fermi window, defined by

$$F_T(E) = -\frac{\partial f(E)}{\partial E} = \frac{\beta}{4\cosh^2\beta(E-\mu)/2}, \tag{2}$$

where $f(E)$ is the Fermi function and $\beta = 1/kt$.

Within Landauer formalism the transport distribution function can generally be expressed as [57]

$$\Sigma(E) = \frac{l}{A}\frac{2e^2}{h}\overline{T}(E). \tag{3}$$

Here l is the length of the sample, A is the cross sectional area and $\overline{T}(E)$ is the transmission function $T(E)$ integrated over all final and initial modes. The factor 2 comes from assumed spin degeneracy.

In this work we will also assume that the initial and final modes are always the same. This amounts to the assumption that scattering is not only elastic, but also conserves $\boldsymbol{k}$-components orthogonal to the transport direction. This is not an assumption that is in any way physically justified, and is made only for reasons of numerical efficiency. However, the approach should produce a reasonable effective description. This is similar to the relaxation time approximation of the BTE, which is also not physically justified in general. In addition, since our present concern is mainly to compare our approach to the BTE, a realistic description of scattering is not important as long as the same form of scattering is assumed in both formalisms.

The assumption of identical initial and final modes, together with the fact that the transmission is expressed as $T = \lambda/L$ in the diffusive limit [57], allows us to express the transport distribution function as

$$\Sigma(E) = \frac{2e^2}{h}\int \frac{\mathrm{d}^2\boldsymbol{k}_\perp}{(2\pi)^2}\lambda(E,\boldsymbol{k}_\perp). \tag{4}$$

Here $\boldsymbol{k}_\perp$ is the component of the Bloch vector that is orthogonal to the transport direction (transverse component), and λ is the backscattering mean free path [27,57].

The backscattering mean free path λ may be calculated from its relationship with T. However, in practical calculations where the size of the system is limited, we cannot expect to reach the diffusive limit $T = \lambda/l$. But assuming that we can at least reach the incoherent limit, the literature derivation [27] of this expression can be generalized to give

$$\frac{1}{T} = \frac{1}{T_C} + \frac{l}{\lambda}, \tag{5}$$

where T_C is the total transmission of the two contacts.

2.2. Scattering within the Buttiker approximation

As mentioned, we treat scattering within the so-called Buttiker approximation [42,45–50], where the effects of scattering is mimicked by a set of virtual contacts known as Buttiker probes. That is, the simulated region has several contacts attached, but only two of them represent real contacts. These model the emitter and collector contacts between which currents would be measured in an actual experiment. The other contacts are Buttiker probes, which are left floating so that no net current is emitted or absorbed. Thus, the only net effect of the Buttiker probes is the randomization of momentum and phase coherence. They thus mimic a simple but rather flexible scattering mechanism.

The absorption of carriers by the Buttiker probes can generally be described by the retarded self energy functions Σ^r [37]. This functionality is already implemented in Kwant. In the case of real contacts, an expression of the self energy can be derived from considerations of modes in the leads [37]. However, since we are interested in an effective description of scattering, and not in physical contacts, we will take a simpler approach. We will instead assume the simplest form the self energy could have, while still causing the correct relaxation of momentum. Thus, we will assume Σ^r proportional to the identity. In addition, we observe that only anti-hermitian self energies cause relaxation, since any hermitian part would effectively just be an energy dependent addition to the Hamiltonian. Thus, we assume the retarded self energy of the Buttiker probes to be anti-hermitian, and write it as $\Sigma^r = -i\xi(E, \boldsymbol{k}_\perp)I$, with ξ a real function.

To find the actual value of ξ, we consider the fact that carriers moving through the simulated region will effectively obey the modified Schrödinger equation $\hbar i\dot{\psi} = (H + \Sigma^r)\psi$. Knowing that the Bloch momentum k commutes with the single particle Hamiltonian H, we derive

$$\begin{aligned}\hbar\frac{\mathrm{d}k}{\mathrm{d}t} &= \hbar\frac{\mathrm{d}}{\mathrm{d}t}\psi^\dagger k\psi \\ &= i\psi^\dagger(H + \Sigma^{r\dagger})k\psi - i\psi^\dagger k(H + \Sigma^r)\psi \\ &= -2\xi(E, \boldsymbol{k}_\perp)k. \end{aligned} \tag{6}$$

In addition we should consider the momentum injected through the Buttiker probes, but in the case of k_z this is entirely randomized, and averages to zero. We thus obtain the solution $k_z(t) = k_z(0)e^{-2\xi t/\hbar}$ and a momentum relaxation time of $\tau = \hbar/2\xi$. Thus, we may express the Buttiker probe self energies as

$$\Sigma^r(E, \boldsymbol{k}_\perp) = -\frac{\hbar i}{2\tau(E, \boldsymbol{k}_\perp)}I. \tag{7}$$

Since we are at this point only concerned with validating our implementation, we will assume a constant relaxation time $\tau(E, \boldsymbol{k}_\perp) = \tau$ in our calculations. We need to emphasize that concerns about the representative nature of this assumption is not the focus of this work, it is only introduced in order to make an as equal as possible footing where the transport distribution function $\Sigma(E)$ can be compared to the BTE calculations. By the assumption of elastic scattering, $\Sigma(E)$ will in each formalism and at each individual energy depend only on the relaxation time at that energy.

The retarded self energy describes the way in which carriers are absorbed by the Buttiker probes [37]. In addition it is necessary to describe the way in which carriers are re-emitted. Within the NEGF formalism emission is described by the lesser self energies $\Sigma^<$ [37], but within our underlying ballistic framework, there is no way of explicitly defining these. Instead, the re-emission process is simply defined in the following way: Carriers are re-emitted from the same probe at which they were absorbed, they have the same energy, and the same transverse momentum as they had before absorption, and finally, as a consequence of the probes being local, the momentum component parallel to the transport direction is fully randomized. Thus the scattering process conserves charge, energy and transverse momentum.

2.3. Agreement with the BTE

Our approach to validate the implementation and method is to compare it to the BTE in systems where the BTE is expected to be valid. Thus, we need a simple criterion by which to determine when the BTE is valid. The relationship between the BTE and Landauer approach have been studied in previous work [57], where it was found that the two formalism are mathematically equivalent if one makes the substitution

$$\langle\langle\lambda\rangle\rangle = \frac{2\langle v_z^2\tau\rangle}{\langle|v_z|\rangle}. \tag{8}$$

Here v is the group velocity $v = \partial E/\partial k/\hbar$, and the averages are taken over different modes [57]. In the case of one dimensional conductors the authors find that this expression reduces to $\lambda = 2v_z\tau$, where only one mode in the one dimensional conductor is assumed. Because of our assumption that scattering conserves transverse momentum, $\Sigma(E)$ can be expressed by Eq. (4), which is essentially an integral over multiple independent one dimensional channels. Thus we may in our case also make use of the simple expression $\lambda = 2v_z\tau$.

Intuitively this expression makes sense, except for the factor of two. We can however understand this factor by considering that τ is a relaxation time, representing the time it takes before the expected momentum of a particle is relaxed to zero. On the other hand, λ is the length the particle moves before it is reflected, and has the opposite momentum. Intuitively, this takes twice as long as the relaxation to zero, which explains the factor of two.

With this in mind we now argue that since the BTE is equivalent to setting $\lambda = 2v_z\tau$, it is the validity of this expression that determines the validity of the BTE. At first this expression seems universal, but due to the quantum nature of charge carriers, their velocity is not sharply defined. Although the group velocity of each Bloch state is well defined, an actual particle moving through the sample will generally be in a superposition of several Bloch states, and will thus not have a sharp velocity. In order for a sharply defined velocity to be a good approximation, the uncertainty in velocity must satisfy $\Delta v \ll v$, which can be written as

$$\frac{\partial v}{\partial k}\Delta k \ll v. \tag{9}$$

From the uncertainty principle, $2\Delta k\Delta x \geqslant 1$. By combining this inequality with Eq. (9) we get $\partial v/\partial k/\Delta x \ll v$. Finally $\partial v/\partial k$ should be of order $\partial v/\partial k \sim av$, where a is the lattice parameter, so that the condition becomes

$$a \ll \Delta x. \tag{10}$$

Thus, the BTE is only strictly justified when the carriers are delocalized over a scale much larger than the lattice period. It is physically reasonable to assume that the carriers are localized when they scatter, and delocalize when they move between scattering events. Thus Δx should be of order $\Delta x \sim \lambda \sim v\tau$, which finally lets us write the condition as

$$a \ll v\tau. \tag{11}$$

This condition is also equivalent to the one described in the work on superlattices by Wacker et al. [38,39]. They found that the miniband-transport-model, i.e. applications of the BTE to superlat-

tices, is valid when $\Gamma \simeq \hbar/\tau \ll u$, where u is the coupling between the wells. We can realize this equivalence by comparing two reasonable estimates of the transfer time t_T between the wells:

$$\frac{a}{v} \sim t_T \sim \frac{\hbar}{u}. \tag{12}$$

Semiconductor scattering rates typically lie in the range [28] $\Gamma \simeq 1/\tau \simeq 10^{12}$–$10^{14}$ s^{-1}, or 100 fs after a geometric average. For the group velocity we base our estimate on simple dimensional analysis and pick $\hbar v \sim$ eV Å, since this is a typical unit of this quantity. From this we obtain the estimate $v\tau \sim 10$ nm, which if used together with Eq. (11) suggests that the BTE should be applicable for bulk materials where $a \sim$ a few Å, and for superlattices with a short period. These two cases are tested in this work to demonstrate a working implementation.

3. Implementation

3.1. Fitting of tight-binding model

Kwant relies on a tight-binding description of the system of interest, which allows for the inclusion of atomistic detail for very large systems. Thus, as the first step, it is necessary to obtain tight-binding models of the materials of interest, which in our case are alloys of HgTe and CdTe. These alloys were chosen due to the fact that they can be combined to produce super lattices of very high quality [65].

Our parametrized tight-binding model can be described as follows: We combine each Te atom with one of the nearby Hg or Cd atoms to form larger units consisting of two atoms. These effective units can be seen to be organized in an fcc structure rather than in the slightly more complex Zinkblende structure of the atomic lattice. This together with the electronic configuration of these materials allows us to make use of a simple nearest neighbour model described in the literature [66], where hybridized sp^3 states are associated to each atom in an fcc-structure.

Among the parameters of this model are clearly the energy levels of the s and p states of both the HgTe and CdTe units. In addition there are 5 hopping parameters $E_{ss}, E_{sp}, E_{xx}, E_{xy}$ and E_{zz}, the meanings of which are described in the literature [66]. In our case we have hopping both between HgTe and HgTe, between CdTe and CdTe and between HgTe and CdTe, so that the number of such hopping parameters is increased by a factor of three. This means that the total number of parameters in our model is 19.

However, since our present calculations only concern systems that are Hg sparse, the HgTe-HgTe hopping parameters are not needed. The remaining 14 parameters were determined by fitting against density functional theory (DFT) calculations of the band structure of CdTe as well as the alloy $Hg_{.25}Cd_{.75}Te$. These calculations made use of VASP [54–56] and were based on the Perdew-Burke-Ernzerhof (PBE) exchange correlation functional. A plane-wave energy cutoff of 650 eV with a k-point sampling of $31 \times 31 \times 31$ was used. We are not in this work concerned with how well these DFT calculations reproduce the actual electronic structure, as generalization to more accurate methods is straight forward.

The fitted model is obtained by use of a numerical minimization routine, minimizing the quantity

$$\sum_{n\boldsymbol{k}} \left(E^{DFT}_{n\boldsymbol{k}} - E^{TB}_{n}(\boldsymbol{k})\right)^2 \left[w\left(E^{DFT}_{n\boldsymbol{k}}\right) + w\left(E^{TB}_{n}(\boldsymbol{k})\right)\right]$$

by varying the 14 remaining tight-binding parameters. Here the index n is chosen to run over the 12 highest valence bands and the 4 lowest conduction bands, $E^{DFT}_{n\boldsymbol{k}}$ and $E^{TB}_{n}(\boldsymbol{k})$ are the DFT and tight-binding results respectively, while $w(E)$ is a weighting function used to make the fitting prioritize energy regions where agreement is desired. For transport calculations, a good fit close to the band gap is essential, while other regions are unimportant. Without a weighting function the fit would overall be better, but less accurate in the interesting region. In our minimization we put $w(E) = F_T(E)$, which is defined in Eq. (2). The parameters μ and β were chosen so that μ lies in the middle of the band gap and $1/\beta = 0.15$ eV.

3.2. Calculation of the transmission function and backscattering mean free path

In the following we give details of our implementation, which employs the quantum transport package Kwant [52,53]. For additional details related to Kwant consult its documentation [53].

3.2.1. Definition of the system

Kwant needs a system definition. The current available implementation of Kwant is tailored for systems of finite size, and there is no native support for translational symmetry in two directions. We circumvent this by Fourier transforming the tight-binding model in the x and y directions, and treating the resulting Bloch momenta k_x and k_y as parameters of a one-dimensional model. This transformation to a k-dependent model is straight forward, and we have thus chosen to not include these details here. The resulting system, consisting simply of a long chain of unit cells, is declared and set up in Kwant, together with the resulting k-dependent tight-binding model.

We attach a set of contacts, or leads as they are referred to in Kwant, to this system. Two of these are the real contacts, and are attached to the end points of the chain. The other leads are Buttiker probes, and these are distributed evenly along the chain. The most correct approach would be to attach these Buttiker probes to every single atom in the system. However, the calculation time scales strongly with the size of the region to which contacts are attached. Such an approach is thus not feasible. Instead the Buttiker probes are only connected to an evenly distributed subset of the unit cells, and their density is controlled by a numerical parameter d_{sc}. More specifically, the Buttiker probes are attached at regular intervals between the end points, with one single probe per d_{sc} unit cells.

The leads are declared in Kwant by defining their self energies. For the Buttiker probes we make use of the model defined in Eq. (7), but scale the magnitude of Σ^r by a factor d_{sc} in order to compensate for the lower density of Buttiker probes. Since by construction our calculations are independent of contact effects, the self energies of the two real contacts do not matter, and we choose them simply as $\Sigma^r = -iI \cdot 1$ eV.

3.2.2. Ballistic transmission functions

For each combination (k_x, k_y, E) of transverse k-points and energies in the integration grid, we calculate the ballistic transmission functions between all leads. This is done in the following manner:

(i) first we update the tight-binding model by updating the transverse momenta (k_x, k_y), which are treated as parameters of the model,
(ii) then we ask Kwant to calculate the Greens function of the system at energy E, and
(iii) finally we ask Kwant to calculate all transmission functions given this Greens function.

This yields the ballistic transmission functions T_{pq} between the two real contacts, $T_{p\phi}$ between the real contacts and the Buttiker probes, and $T_{\phi\psi}$ between different Buttiker probes.

3.2.3. The effective transmission function

The next step is the calculation of the effective transmission function T. This can be interpreted as the probability that a carrier injected at one end eventually ends up at the other end, possibly taking a path via multiple Buttiker probes. In the case that there is only a single Buttiker probe, an expression for the effective transmission is derived in the literature [37] as

$$T = T_{pq} + \frac{T_{p\phi}T_{\phi q}}{T_{\phi p} + T_{\phi q}}. \tag{13}$$

The derivation is easily generalized, and we obtain

$$T = T_{pq} + \sum_{\phi\psi} T_{p\phi}\left(R^{-1}\right)_{\phi\psi} T_{\psi q}, \tag{14a}$$

where the matrix R is given by

$$R_{\phi\psi} = \left(\sum_{\psi} T_{\phi\psi} + T_{\phi p} + T_{\phi q}\right)\delta_{\phi\psi} - T_{\phi\psi}. \tag{14b}$$

This is the expression we use to calculate the effective transmission. It is essentially the solution of a random walk problem.

3.2.4. The backscattering mean free path

Finally, for each point in the integration grid we calculate the backscattering mean free path $\lambda(E, \boldsymbol{k}_\perp)$. We approach this by evaluating the effective transmission of two systems differing only in their lengths l_1 and l_2. These two systems will have different effective transmissions T_1 and T_2, respectively, and utilizing Eq. (5) we obtain

$$\frac{1}{T_2} - \frac{1}{T_1} = \frac{l_2}{\lambda} - \frac{l_1}{\lambda}. \tag{15}$$

This gives us an estimate of λ as

$$\lambda = \frac{l_2 - l_1}{1/T_2 - 1/T_1}, \tag{16}$$

which is used in our implementation. The lengths l_1 and l_2 are chosen in such a way that l_1 is always an even number of fundamental periods, while $l_2 = 3l_1/2$.

As mentioned, Eq. (5) is only valid in the incoherent regime, and both systems thus need to be large enough to be in that regime. We made sure this was the case by a simple process of trial and error, where l_1 was increased until the linear relationship of Eq. (5) was obtained. In the case of our CdTe model we found that we are well within this regime at $l_1 = 512a = 337$ nm, where $a = 6.59$ Å is the lattice constant of CdTe.

However, this concrete number is clearly related to the particular material, and to the model that we use. Thus, a more general criterion should be formulated. We approach this by relating the system size to the coherence length l_ϕ [28,37]. With our simplified treatment of scattering, where both momentum and phase is completely randomized at each scattering event, the coherence length is equal to the momentum relaxation length: $l_\phi = l_p = v\tau$. As mentioned we use a constant relaxation time of $\tau = 100$ fs, while at the highest energy in our integration grid $E = 4.1$ eV, the group velocity of our CdTe model is $\hbar v \approx 6$ eV Å. This gives $v\tau = 91$ nm, and the required system size corresponds to $l_1 = 3.7\, l_\phi$.

In other words, we are in the incoherent regime when the system size is about four times the coherence length. This also makes sense heuristically, since coherent effects should decrease exponentially with l/l_ϕ.

3.3. Integration and calculation of transport coefficients

3.3.1. The transport distribution function

By utilizing the approach of the previous section, we can now calculate $\lambda(E, \boldsymbol{k}_\perp)$ for any value of E and $\boldsymbol{k}_\perp$, which allows us to calculate the transport distribution function by Eq. (4). The integral extends over the transverse part of the Brillouin zone, and can be re-expressed as

$$\begin{aligned}\Sigma(E) &= \frac{2e^2}{h}\int_{-\pi/a}^{\pi/a}\frac{\mathrm{d}k_x}{2\pi}\int_{-\pi/a}^{\pi/a}\frac{\mathrm{d}k_y}{2\pi}\,\lambda(E, k_x, k_y) \\ &= \frac{2e^2}{a^2h}\int_{-1/2}^{1/2}\mathrm{d}k_x\int_{-1/2}^{1/2}\mathrm{d}k_y\,\lambda\left(E, \frac{2\pi}{a}k_x, \frac{2\pi}{a}k_y\right).\end{aligned} \tag{17}$$

In both CdTe and the alloy $Hg_{.25}Cd_{.75}Te$, the materials considered in this work, the band edges lie at the Gamma point. Because of this, the regions where $\boldsymbol{k}_\perp > 2\pi/a$ will have non-zero contributions only when E is far from the band gap. Thus, these regions will not contribute significantly to transport, and we can allow ourselves to ignore these regions. We can then write the integral in circular coordinates as

$$\begin{aligned}\Sigma(E) &= \frac{2e^2}{a^2h}\int_0^{1/2}\mathrm{d}k\int_0^{2\pi}k\mathrm{d}\theta\,\lambda\left(E, \frac{2\pi}{a}k\cos\theta, \frac{2\pi}{a}k\sin\theta\right) \\ &= \frac{16e^2}{a^2h}\int_0^{1/2}\mathrm{d}k\,k\int_0^{\pi/4}\mathrm{d}\theta\,\lambda\left(E, \frac{2\pi}{a}k\cos\theta, \frac{2\pi}{a}k\sin\theta\right),\end{aligned} \tag{18}$$

where the last equality comes from the square symmetry of the transverse Brillouin zone. When circular integration is not possible, one would instead use Eq. (17). This would however be at an increased computational cost.

To evaluate Eq. (18) numerically, we divide both the θ and k intervals into regular subintervals, and use simple midpoint integration. The number of points N_k along the radial direction is kept fixed, while the number of points N_θ^n in the angular direction varies with the radial coordinate. N_θ^n is chosen in such a way that the arc distance between neighbouring points in the angular direction is smaller than some minimal step:

$$\frac{\pi k_n}{4N_\theta^n} < \frac{2\pi}{a}\delta_\theta. \tag{19}$$

If $\delta_\theta \geqslant \pi/8 = 0.393$ then $N_\theta^n = 1$ for all n.

3.3.2. Thermoelectric transport coefficients

Given the transport distribution function $\Sigma(E)$, we calculate the transport coefficients by Eqs. (1a)–(1c). All of these expressions can be written as integrals of the form

$$Y = \int \mathrm{d}E X(E)\Sigma(E)F_T(E). \tag{20}$$

We approximate these as integrals over the range $[E_{min}, E_{max}]$, and evaluate them by the same simple midpoint technique, using N_E regularly spaced points. This approach is used to evaluate the conductivity σ, the Seebeck coefficient α, and the Lorenz coefficient $L = \kappa_e/\sigma t$.

In the calculations of this work, we always have $E_{min} = 2$ eV, $E_{max} = 4.1$ eV and normally $N_E = 200$. The chemical potential μ in our calculations is in the range between 2.5 and 3.6 eV, while the temperature is chosen to be 300 or 700 K. This results in a buffer of 0.5 eV $\geqslant 8\,kt$ between the chemical potential and the integration limits. Outside of this buffer we have $F_T(E)/F_T(\mu) \approx 4e^{-\beta E} < 4e^{-8} \approx 10^{-3}$, so that the contributions from these ranges are in any case very small. In addition we always have $kt/(\Delta E/N_E) \geqslant 2.5$, meaning that there will always be at least 5 energy points within an interval of $2kt$. This assures a quite reasonable sampling of the function $F_T(E)$ of Eq. (2).

4. Results

4.1. Fitted tight-binding model of the HgCdTe system

In this section we present and validate the tight-binding model we will use for the rest of our calculations. The model was obtained by use of the fitting procedure described in Section 3.1.

In Fig. 1 band structures of CdTe and the alloy $Hg_{.25}Cd_{.75}Te$ are compared to the fitted models. The gray shaded area shows where good agreement has been achieved. This is in a reasonably sized region around the band gap. The parameters of the resulting models are shown in Table 1. The CdTe and CdTe-CdTe parameters are obtained from the fit against the CdTe band structure shown in Fig. 1a. The HgTe and CdTe-HgTe parameters are obtained from the fit against the $Cd_{0.75}Hg_{.25}Te$ band structure of Fig. 1b. The meaning of the parameters are explained in the literature [66].

To verify that the resulting model captures the physics relevant to describing electronic structure in hetero-structures, we also calculate the band structures of two superlattices and compare these to DFT calculations. The results are shown in Fig. 2. Fig. 2a shows the band structure of a super lattice made up of two unit cells of HgTe followed by two unit cells of $Hg_{.25}Cd_{.75}Te$, while Fig. 2b shows that of a super lattice with a period of four unit cells of CdTe followed by four unit cells of $Hg_{.25}Cd_{.75}Te$. We stress that this model also makes use of the parameters of Table 1, and is not fitted to the DFT calculations of Fig. 2. Given this, the agreement within the included region is quite impressive, although it is not perfect. Perfect agreement would in any case not be expected, since there are

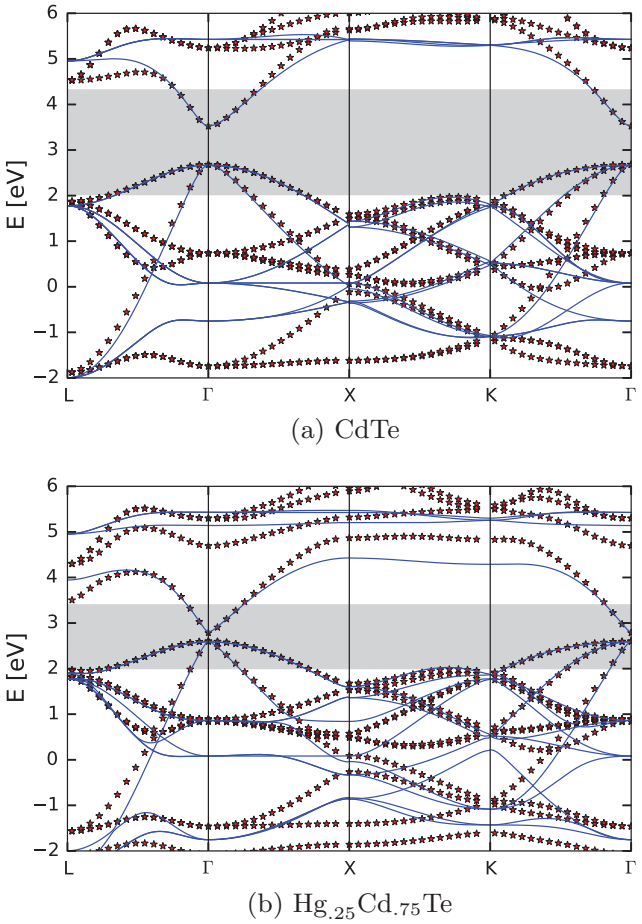

(a) CdTe

(b) $Hg_{.25}Cd_{.75}Te$

Fig. 1. Fitted models. Blue lines are tight-binding results, while the red stars are DFT results. In (a) the results have been shifted to better match the band alignment between the two materials. (For interpretation of the references to colour in this figure legend, the reader is referred to the web version of this article.)

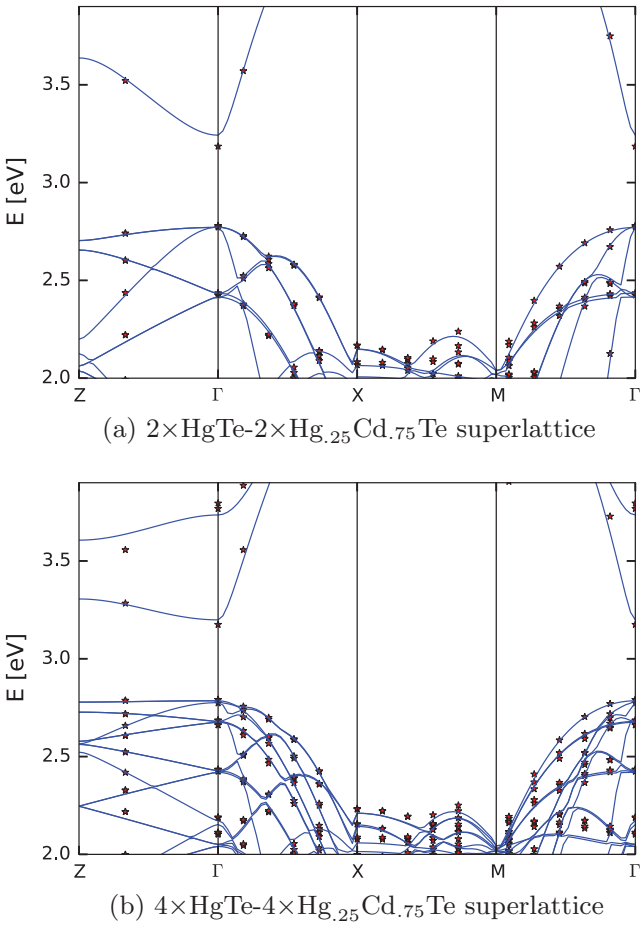

(a) $2\times HgTe\text{-}2\times Hg_{.25}Cd_{.75}Te$ superlattice

(b) $4\times HgTe\text{-}4\times Hg_{.25}Cd_{.75}Te$ superlattice

Fig. 2. Superlattice band structures. Blue lines are tight-binding results, while the red stars are DFT. (For interpretation of the references to colour in this figure legend, the reader is referred to the web version of this article.)

Table 1
Fitted parameters of the HgCdTe model. E_s and E_p are the energy level of s and p states respectively. $E_{ss}, E_{sp}, E_{xx}, E_{xy}$ and E_{zz} are hopping parameters, the meanings of which can be found in the literature [66].

CdTe		CdTe-CdTe		CdTe-HgTe	
E_s:	4.9530 eV	E_{ss}:	−0.11853 eV	E_{ss}:	−0.16814 eV
E_p:	0.51990 eV	E_{sp}:	0.25609 eV	E_{sp}:	0.23259 eV
HgTe		E_{xx}:	0.21377 eV	E_{xx}:	0.30393 eV
E_s:	3.9439 eV	E_{xy}:	0.31457 eV	E_{xy}:	0.37341 eV
E_p:	0.21829 eV	E_{zz}:	0.10939 eV	E_{zz}:	−0.11725 eV

several microscopic details that are not captured by our tight-binding model. In particular these include strain effects and partial charge transfers.

4.2. Transport in bulk CdTe

Here we present transport coefficients in bulk CdTe calculated by our implementation, and compare these to BTE calculations, the implementation of which is covered in a separate work [67]. The results are shown in Fig. 3, where figures a–d show, respectively the transport distribution function, the electrical conductivity, the Seebeck coefficient and the Lorenz coefficient. The transport coefficients are calculated with two different temperatures of 300 and 700 K.

The BTE result in Fig. 3a is in reality the electrical conductivity at 10 K as a function of μ. At this low temperature the integral of Eq. (1a) samples only a very small region around μ, so that the calculated function should be almost identical to the transport distribution function. The small oscillations in this function are likely due to the expected poor convergence in the integrals at such low temperatures.

In the calculations employing the Buttiker approximation, the function $\tau(E)$ was set to a constant value of 100 fs, the simulated region had a thickness of $l_1 = 675$ nm, corresponding to 1024 unit cells of CdTe, while the various numerical parameters defined in Sections 3.2 and 3.3 were set to $E_{min} = 2.0$ eV, $E_{max} = 4.1$ eV, $N_E = 200$, $N_k = 100$, $\delta_0 = 0.03$ and $d_{sc} = 32$.

The BTE calculations made use of the same constant relaxation time $\tau = 100$ fs, and used the band structure obtained from the same tight-binding model that was used by Kwant to calculate the Green's functions. For the purpose of making a convergence study, we did the BTE calculations with several different integration grids, having sampling sizes of $N_k^B \times N_k^B \times N_k^B$, with $N_k^B = 11, 51, 101$ and 201. The results of the convergence study are shown more explicitly in Fig. 4, where the relative difference between the two methods is shown as a function of N_k^B for some selected values of μ. These values are indicated as vertical lines in Fig. 3.

As expected the Boltzmann results converge towards the Landauer results with increasing N_k^B, and in most of the results, the difference seems to saturate somewhere between $N_k^B = 51$ and $N_k^B = 201$. The saturated value is in almost all cases on the order of a few percent or smaller, which gives a strong indication that we have a successful implementation. One exception is the Lorenz coefficient at $t = 700$ K and $\mu = 3.6$ eV, where the saturated differ-

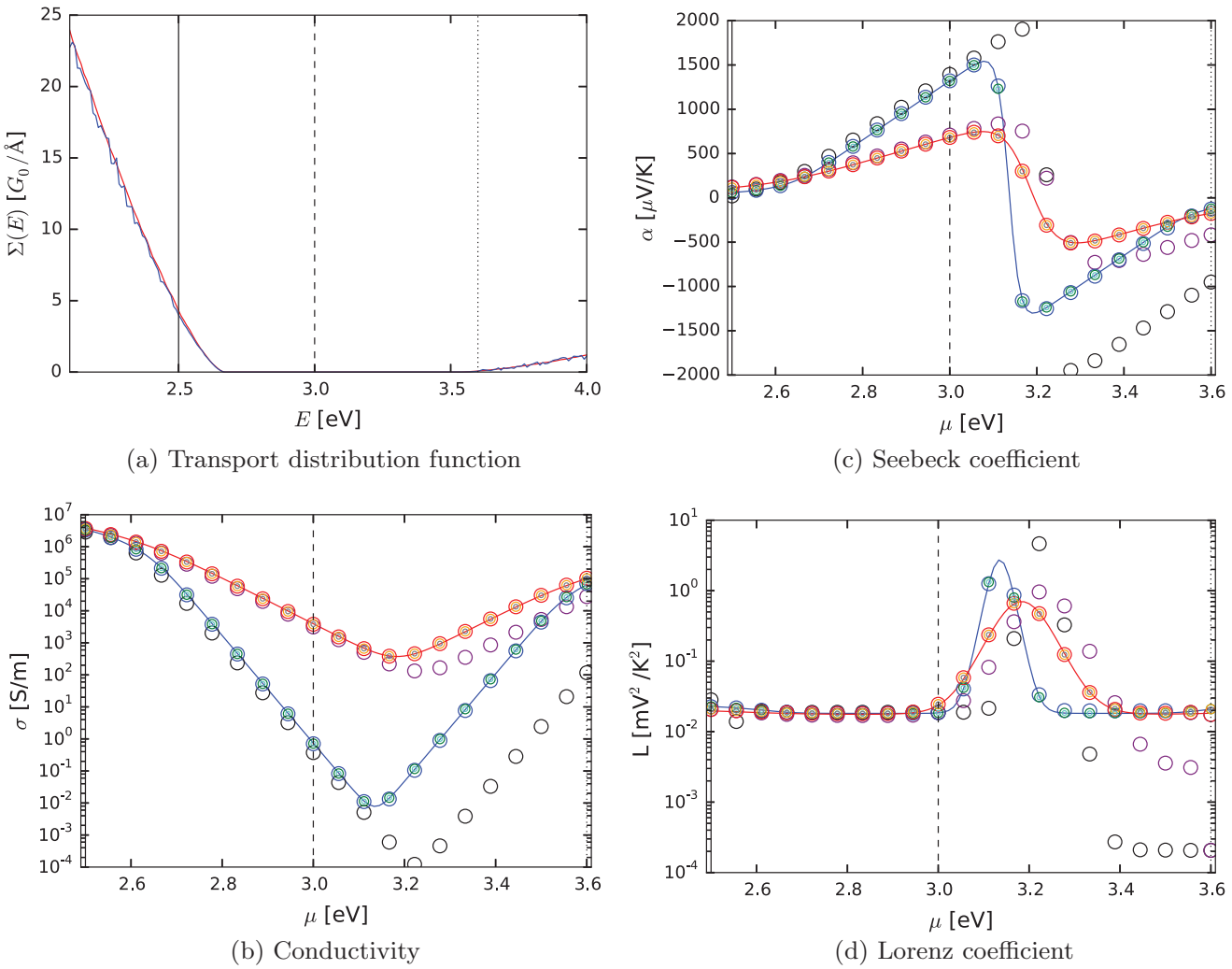

(a) Transport distribution function (c) Seebeck coefficient

(b) Conductivity (d) Lorenz coefficient

Fig. 3. Comparison of BTE and Buttiker approximation results in bulk CdTe. (a) The blue curve is calculated by the BTE while and red curve by the Buttiker approximation. (b-d) The solid lines are Buttiker approximation results while the circles are BTE results. The black, blue, green and turquoise results are calculated with $T = 300$ K, while purple, red, orange and grey are at 700 K. Among the BTE results black and purple is with an $11 \times 11 \times 11$ k-grid, red and blue with $51 \times 51 \times 51$, turquoise and orange with $101 \times 101 \times 101$ and green and grey with $201 \times 201 \times 201$. The black vertical lines show values of μ where the convergence with grid density is shown more explicitly in Fig. 4. (For interpretation of the references to colour in this figure legend, the reader is referred to the web version of this article.)

ence is as high as 7%. This is probably because the Lorenz coefficient is extra sensitive to the integration interval over energy, and a clearing of $8kt$ from the chemical potential is too small.

As for the remaining few percent difference, this could have several different sources. The fact that the relative difference saturates at the higher $\boldsymbol{k}$-point densities in Fig. 4, shows that it is unlikely that this difference comes from the integration density used in the BTE. It could in principle come from any of the numerical parameters E_{Max}, E_{Min}, N_E, N_k, δ_θ, d_{sc} and L used in our implementation of the Buttiker approximation. In addition to this, part of the difference could come from a true physical difference between the two methods, which according to Eq. (11) are only fully in agreement in the limit $v\tau/a \to \infty$. We are in any case more interested in using this method on heterostructures, where the answers to these questions could be completely different from the case of bulk materials. Therefore, we address these issues more carefully in the next section, where we study transport in a short period superlattice.

4.3. Transport in a 4xCdTe-4x$Hg_{.25}Cd_{.75}Te$ superlattice

In this section, we present transport calculations on the short period super lattice whose band structure is shown in Fig. 2b. As mentioned, this structure consists of four unit cells of CdTe followed by four unit cells of $Hg_{.25}Cd_{.75}Te$. It has a total period of $a_{sl} = 5.3$ nm, and according to the considerations of Section 2.3, should still be within the regime where the BTE is valid given reasonable values of $v\tau \sim 10$—100 nm.

The numerical parameters related to the integration grid were set to $N_E = 200$, $N_k = 100$ and $\delta_\theta = 0.03$. Most of the calculations are carried out using a material region with a total thickness of $l_1 = 337$ nm, containing 64 superlattice periods and a total of 512 unit cells of CdTe and $Hg_{.25}Cd_{.75}Te$. To verify convergence with respect to these parameters, we performed calculations where the integration densities in the energy, radial k and angular k-directions, as well as the simulation thickness L were respectively doubled. This caused only minor changes to the results, significantly smaller than the changes observed when d_{sc} and τ are varied. We thus conclude that the results are sufficiently converged at the lower values of N_E, N_k, δ_θ and l_1, and focus the more detailed convergence study on the two remaining parameters d_{sc} and τ.

The results of the calculations are shown in Fig. 5. Fig. 5a, b, c and d shows the transport distribution function, the conductivity and the Seebeck and Lorenz coefficients, respectively. The calculations are performed with different constant relaxation times of $\tau = 100$, 200 and 400 fs. Calculations with higher values of τ also simulate a thicker region of material. This is because higher values of τ result in higher values of l_ϕ, so that the material region must be larger in order to remain in the incoherent regime.

In order for the results to be more directly comparable, Fig. 5a shows the transport distribution function divided by τ. For the same reason the conductivities in figure b with $\tau = 200$ and 400 fs have been scaled down by a factor of two and four, respectively. Also, the Buttiker approximation calculations employ different values of the parameter d_{sc}. These are $d_{sc} = 8$, 4, 2 and 1, where $d_{sc} = 1$ corresponds to the "exact" case, where Buttiker probes are attached to every single unit cell. In addition, Fig. 5b–d shows results at two different temperatures of 300 and 700 K.

Results calculated by the BTE are also included in Fig. 5. The BTE calculations make use of a regular cubic integration grid with a resolution of 51×51 points in the inplane directions of $\boldsymbol{k}$-space and 13 points in the crossplane direction. They make use of the same tight-binding model as the Buttiker approximation to calculate the superlattice band structures, and also uses the same values of τ for the momentum relaxation time. The BTE result included in Fig. 5a is actually the conductivity calculated at 50 K. Again, the conductivity is very similar to the transport distribution function $\Sigma(E)$ at such low temperatures. Both the BTE and Buttiker approx-

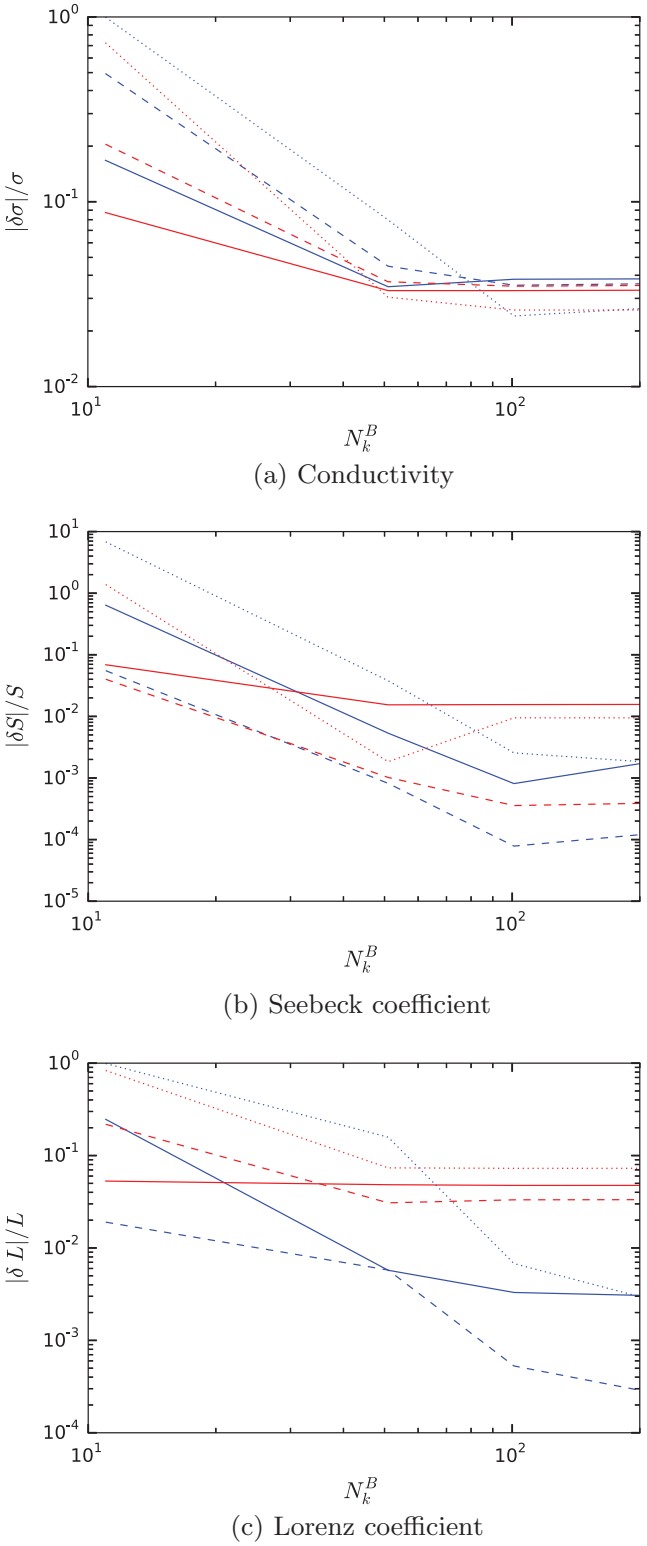

Fig. 4. Relative difference between the BTE and Buttiker approximation results of Fig. 3. The results are shown as function of the BTE integration grid, which has a cubic sampling of $N_k^B \times N_k^B \times N_k^B$. The blue curves are at $T = 300$ K while the red curves are at $T = 700$ K. Also, the solid, dashed and dotted lines are calculated respectively with $\mu = 2.5$, 3.0 and 3.6 eV. (For interpretation of the references to colour in this figure legend, the reader is referred to the web version of this article.)

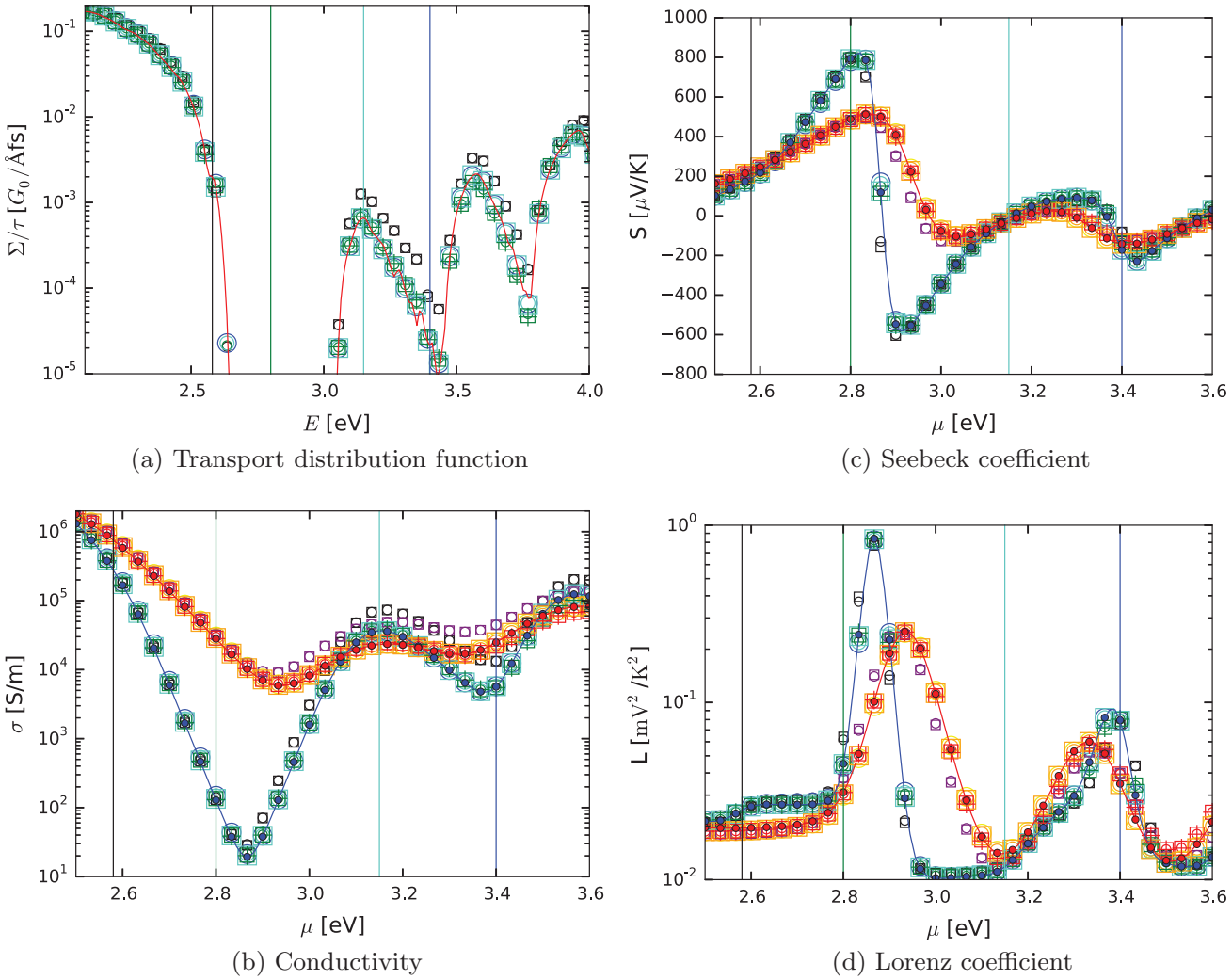

Fig. 5. Transport coefficients in a 4-4 CdTe-$Hg_{.25}Cd_{.75}Te$ super lattice as function of chemical potential μ. (a) The single red curve is the BTE result while the other curves are calculated using the Buttiker approximation. Circles, squares and crosses are for $\tau = 100$, 200 and 400 fs, respectively, while black, green, turquoise and blue represent respectively results with $d_{sc} = 8$, 4, 2 and 1. (b-d) BTE results are included as lines and filled circles, in blue at 300 K and red at 700 K. Buttiker approximation results are shown in the same styles as in figure a, and in the same colours at 300 K. At 700 K the results with $d_{sc} = 8$, 4, 2 and 1 are shown in purple, red, orange and yellow, respectively. The four vertical lines represent the values of μ at which explicit convergence studies are shown in Fig. 6. Note that the results of figure b with $\tau = 200$ and 400 fs have been scaled down by a factor of two and four, respectively. (For interpretation of the references to colour in this figure legend, the reader is referred to the web version of this article.)

imation results show oscillations in $\Sigma(E)$, and also in the three transport coefficients. This is a consequence of the formation of minibands, which can be seen in Fig. 2b.

For reasons of clarity we make a more explicit convergence study in Fig. 6, where we show how the relative difference between the BTE and Buttiker results varies with d_{sc} and τ. The study is done at four different values of the chemical potential. These values are indicated as vertical lines in Fig. 5.

In Fig. 6, we observe two trends: At the higher values of μ of 3.15 eV (in turquoise and orange) and 3.4 eV (in blue and grey) the agreement between the models generally improves greatly as d_{sc} is decreased. At the lower values of μ of 2.58 eV (in black and purple) and 2.8 eV (in green and red) this trend is much less clear. However, for these low values of μ, the agreement instead tends to improve greatly when τ is increased, which is an effect much less noticeable at the higher μ-values. Both of these trends are more clear in Fig. 6b than in the others. In particular the improvement with τ is close to absent in Fig. 6d. In fact it tends to oscillate as we increase τ, which might be an indication that the Lorenz coefficient is highly sensitive to numerical noise stemming from the finite resolution of the $\boldsymbol{k}$-space integration grid.

The different behaviour between the low values of $\mu = 2.58$ and 2.8 eV and the high values of $\mu = 3.15$ and 3.4 eV can be understood from the fact that transport at the lower values of μ is dominated by the valence band, while transport at the higher values is dominated by the conduction band. As seen from the band structure of Fig. 2b the valence band contains several minibands that are much flatter than those of the conduction band. This means that the group velocity $v = \partial E_k/\partial k/\hbar$ will be lower, and accordingly that higher values of τ are required for Eq. (11) to be satisfied. Thus, the results at $\mu = 2.58$ and 2.8 eV may not be fully within the regime of validity of the BTE when $\tau = 100$ fs. This explains why the agreement is not improved with decreasing d_{sc}, but instead improves much when τ is increased.

Our results are thus seen to be fully in agreement with theoretical expectations. In addition we obtain quite small relative differences in the transport coefficients on the order of 10^{-2} between the Buttiker approximation and the BTE at low values of d_{sc}. This is on the order of magnitude of the error we expect from our integration methods, and also what we obtained in the previous section. We thus conclude once more that we have a successful implementation, and that it produces results that are comparable to the BTE

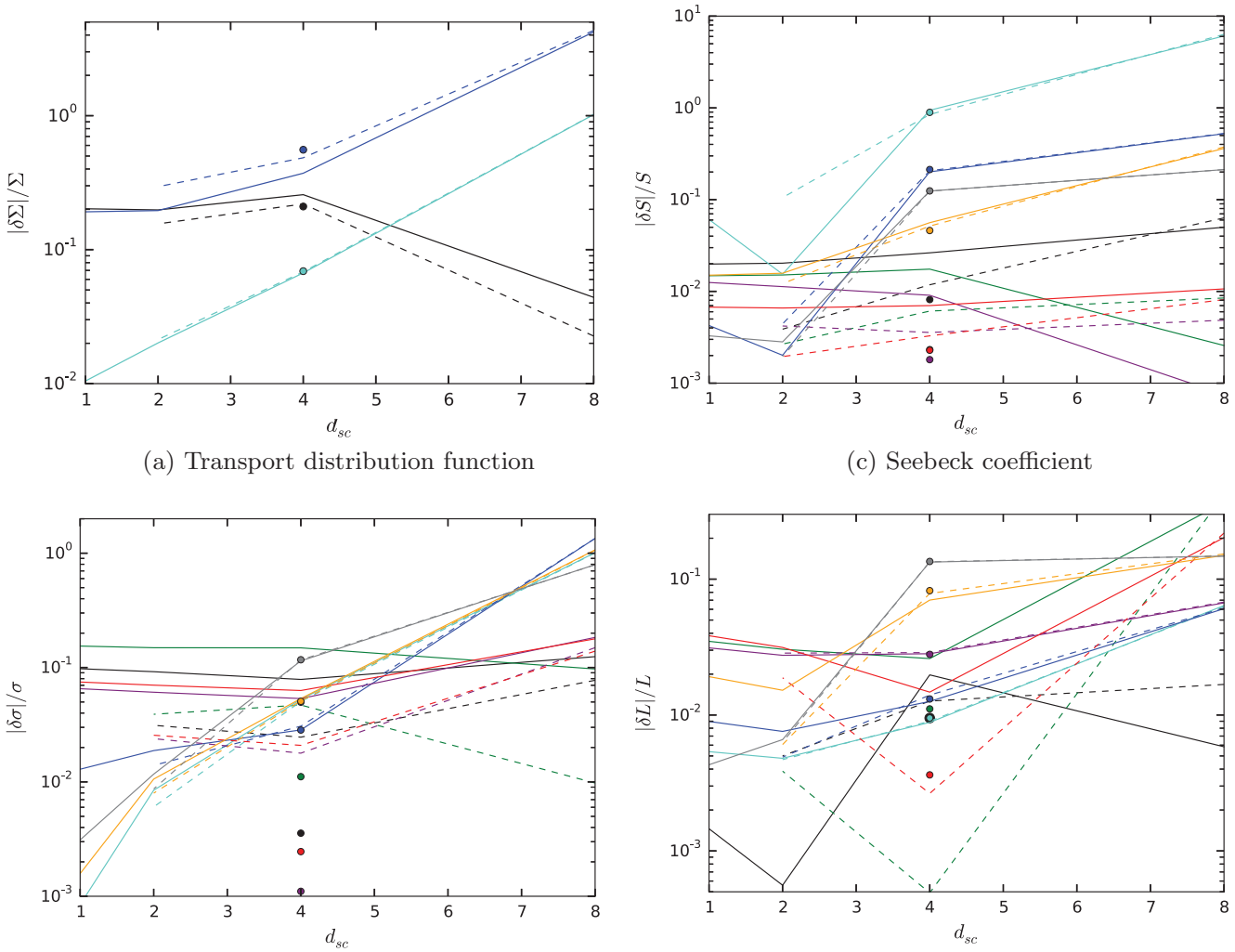

Fig. 6. Relative difference between the Buttiker approximation and BTE results of Fig. 5, and its dependence on d_{sc} and τ. The black, green, turquoise and blue curves are calculated respectively at the values of $\mu = 2.58$, 2.8, 3.15 and 3.4 eV indicated in Fig. 5, and at 300 K in figures b-d. The purple, red, orange and grey curves are calculated at 700 K and respectively at the same values of μ. The solid and dashed curves and the circles are calculated respectively with $\tau = 100$, 200 and 400 fs. The $d_{sc} = 1$ results are only calculated for one value of τ, and the $\tau = 400$ fs results only for one value of d_{sc}. This is because of the high computational cost of these two cases. In (a) the result at $\mu = 2.8$ eV is omitted since $\Sigma(E) = 0$ in the band gap. (For interpretation of the references to colour in this figure legend, the reader is referred to the web version of this article.)

in such a degree that it can be used to study physical differences between these models for a more general set of systems.

5. Conclusions

The primary purpose of this paper was to describe and verify a particular implementation of the Buttiker approximation applied to the calculation of thermoelectric transport coefficients. The agreement between the implemented approach and an existing implementation using the BTE is very good in the regime where this is expected, indicating a successful implementation of this method. In particular, in bulk CdTe the small difference that remains is only of order a few percent, and is likely due mostly to finite accuracy in the numerical integration.

In the short period superlattice studied in Section 4.3, the situation is more complex. There, the agreement between the Buttiker approximation and the BTE shows a strong dependence on d_{sc} and on the relaxation time τ. However, our results show a strong indication of convergence between these two methods in the limit $d_{sc} \to 1$ and $\tau \to \infty$, thereby giving further credence to our implementation. In our bulk calculations, we obtained very good agreement with the BTE already for $d_{sc} = 32$, while in Fig. 6, for our example short period superlattice, d_{sc} must be at least as low as 2–4 to obtain acceptable convergence. The poor convergence in superlattices probably originates from varying carrier densities within the superlattice period. These variations will not be sampled correctly for large values of d_{sc}.

An important point that should be emphasized is the computational cost of this implementation. The most important factor determining the efficiency of the calculations is the parameter d_{sc}, which describes the density of Buttiker probes. The computational time scales quite poorly with d_{sc}. In the calculation where d_{sc} was set to 2 and the system size was $l = 337$ nm, the calculation of one single transport distribution function took a total of 9200 CPU hours. Mainly because of the poor convergence in d_{sc}, we find that this implementation is probably too inefficient for general purpose calculations. Possibly steps can be taken to improve this convergence, for instance by in some way weighting the relaxation time with electron density. Alternatively, one could employ a more efficient inversion algorithm, such as the RGF algorithm [68], which might not require $d_{sc} > 1$.

Acknowledgements

We would like to acknowledge the Research Council of Norway (NANO2021 project Thelma, 228854) for providing funding and the Norwegian Metacenter for Computational Resources (NOTUR) for providing computational resources. Also, we are grateful to Mathias Schrade and Kristian Berland for proofreading and advice on language.

References

[1] L.D. Hicks, M.S. Dresselhaus, Effect of quantum-well structures on the thermoelectric figure of merit, Phys. Rev. B 47 (1993) 12727.
[2] L.W. Whitlow, T. Hirano, Superlattice applications to thermoelectricity, J. Appl. Phys. 78 (1995) 5460.
[3] A. Shakouri, J.E. Bowers, Heterostructure integrated thermionic coolers, Appl. Phys. Lett. 71 (9) (1997) 1234.
[4] G.D. Mahan, L.M. Woods, Multilayer thermionic refrigeration, Phys. Rev. Lett. 80 (1998) 4016, http://dx.doi.org/10.1103/PhysRevLett.80.4016. <http://link.aps.org/doi/10.1103/PhysRevLett.80.4016>.
[5] Z. Bian, M. Zebarjadi, R. Singh, Y. Ezzahri, A. Shakouri, G. Zeng, J.-H. Bahk, J.E. Bowers, J.M.O. Zide, A.C. Gossard, Cross-plane Seebeck coefficient and Lorenz number in superlattices, Phys. Rev. B 76 (2007) 205311, http://dx.doi.org/10.1103/PhysRevB.76.205311. <http://link.aps.org/doi/10.1103/PhysRevB.76.205311>.
[6] D. Vashaee, Y. Zhang, A. Shakouri, G. Zeng, Y.-J. Chiu, Cross-plane Seebeck coefficient in superlattice structures in the miniband conduction regime, Phys. Rev. B 74 (2006) 195315, http://dx.doi.org/10.1103/PhysRevB.74.195315. <http://link.aps.org/doi/10.1103/PhysRevB.74.195315>.
[7] J.-H. Bahk, R.B. Sadeghian, Z. Bian, A. Shakouri, Seebeck enhancement through miniband conduction in III–V semiconductor superlattices at low temperatures, J. Electron. Mater. 41 (2012) 1498, http://dx.doi.org/10.1007/s11664-012-1917-9. <http://dx.doi.org/10.1007/s11664-012-1917-9>.
[8] V.M. Fomin, P. Kratzer, Thermoelectric transport in periodic one-dimensional stacks of InAs/GaAs quantum dots, Phys. Rev. B 82 (2010) 045318, http://dx.doi.org/10.1103/PhysRevB.82.045318. <http://link.aps.org/doi/10.1103/PhysRevB.82.045318>.
[9] E. Flage-Larsen, O.M. Løvvik, Materials, preparation, and characterization in thermoelectrics, in: D.M. Rowe (Ed.), Band Structure Guidelines for Higher Figure-of-Merit: Analytic Band Generation and Energy Filtering, CRC Press, 2012 (Chapter 10).
[10] R. Venkatasubramanian, E. Siivola, T. Colpitts, B. O'quinn, Thin-film thermoelectric devices with high room-temperature figures of merit, Nature 413 (6856) (2001) 597.
[11] H. Ohta, S. Kim, Y. Mune, T. Mizoguchi, K. Nomura, S. Ohta, T. Nomura, Y. Nakanishi, Y. Ikuhara, M. Hirano, Giant thermoelectric Seebeck coefficient of a two-dimensional electron gas in $SrTiO_3$, Nat. Mater. 6 (2) (2007) 129.
[12] P. Komar, T. Jaeger, C. Euler, E. Chávez Angel, U. Kolb, M.M. Müller, B. Balke, M. H. Aguirre, S. Populoh, A. Weidenkaff, Half-Heusler superlattices as model systems for nanostructured thermoelectrics, Phys. Status Solidi (a) 213 (2016) 732.
[13] A.J. Karttunen, T. Tynell, M. Karppinen, Layer-by-layer design of nanostructured thermoelectrics: first-principles study of ZnO:organic superlattices fabricated by ALD/MLD, Nano Energy 22 (2016) 338, http://dx.doi.org/10.1016/j.nanoen.2016.02.028. <http://www.sciencedirect.com/science/article/pii/S2211285516000793>.
[14] X.H. Yang, X.Y. Qin, J. Zhang, D. Li, H.X. Xin, M. Liu, Enhanced thermopower and energy filtering effect from synergetic scattering at heterojunction potentials in the thermoelectric composites with semiconducting nanoinclusions, J. Alloy. Compd. 558 (2013) 203.
[15] H. Böttner, G. Chen, R. Venkatasubramanian, Aspects of thin-film superlattice thermoelectric materials, devices, and applications, MRS Bull. 31 (03) (2006) 211.
[16] G. Chen, M.S. Dresselhaus, G. Dresselhaus, J.-P. Fleurial, T. Caillat, Recent developments in thermoelectric materials, Int. Mater. Rev. 48 (2003) 45.
[17] M.F. ODwyer, R.A. Lewis, C. Zhang, T.E. Humphrey, Electronic efficiency in nanostructured thermionic and thermoelectric devices, Phys. Rev. B 72 (20) (2005) 205330.
[18] K. Berland, X. Song, P.A. Carvalho, C. Persson, T.G. Finstad, O.M. Løvvik, Enhancement of thermoelectric properties by energy filtering: theoretical potential and experimental reality in nanostructured ZnSb, J. Appl. Phys. 119 (12) (2016) 125103.
[19] D. Narducci, S. Frabboni, X. Zianni, Silicon de novo: energy filtering and enhanced thermoelectric performances of nanocrystalline silicon and silicon alloys, J. Mater. Chem. C 3 (47) (2015) 12176.
[20] J.-H. Bahk, Z. Bian, A. Shakouri, Electron energy filtering by a nonplanar potential to enhance the thermoelectric power factor in bulk materials, Phys. Rev. B 87 (2013) 075204, http://dx.doi.org/10.1103/PhysRevB.87.075204. <http://link.aps.org/doi/10.1103/PhysRevB.87.075204>.
[21] D. Narducci, E. Selezneva, G. Cerofolini, S. Frabboni, G. Ottaviani, Impact of energy filtering and carrier localization on the thermoelectric properties of granular semiconductors, J. Solid State Chem. 193 (2012) 19.
[22] S.V. Faleev, F. Léonard, Theory of enhancement of thermoelectric properties of materials with nanoinclusions, Phys. Rev. B 77 (21) (2008) 214304.
[23] J.P. Heremans, C.M. Thrush, D.T. Morelli, Thermopower enhancement in lead telluride nanostructures, Phys. Rev. B 70 (11) (2004) 115334.
[24] A. Cantarero, F.X. Àlvarez, Nanoscale Thermoelectrics. Thermoelectric Effects: Semiclassical and Quantum Approaches from the Boltzmann Transport Equation, Springer International Publishing, Cham, 2014 (Chapter 1).
[25] N.W. Ashcroft, N.D. Mermin, Solid State Physics, Thomson Learning, 1976.
[26] G.K.H. Madsen, D.J. Singh, Boltztrap. A code for calculating band-structure dependent quantities, Comput. Phys. Commun. 175 (1) (2006) 67.
[27] M. Lundstrom, Fundamentals of Carrier Transport, second ed., Cambridge University Press, 2000. <http://dx.doi.org/10.1017/CBO9780511618611>.
[28] C. Jacoboni, Theory of Electron Transport in Semiconductors: A Pathway from Elementary Physics to Nonequilibrium Green Functions, Springer Series in Solid-State Sciences, Springer, Berlin, Heidelberg, 2010. <https://cds.cern.ch/record/1339135>.
[29] B.-L. Huang, M. Kaviany, Ab initio and molecular dynamics predictions for electron and phonon transport in bismuth telluride, Phys. Rev. B 77 (12) (2008) 125209.
[30] J. Yang, H. Li, T. Wu, W. Zhang, L. Chen, J. Yang, Evaluation of half-Heusler compounds as thermoelectric materials based on the calculated electrical transport properties, Adv. Funct. Mater. 18 (19) (2008) 2880.
[31] G.K.H. Madsen, Automated search for new thermoelectric materials: the case of LiZnSb, J. Am. Chem. Soc. 128 (37) (2006) 12140.
[32] D.J. Singh, Doping-dependent thermopower of PbTe from Boltzmann transport calculations, Phys. Rev. B 81 (19) (2010) 195217.
[33] K.P. Ong, D.J. Singh, P. Wu, Analysis of the thermoelectric properties of n-type ZnO, Phys. Rev. B 83 (11) (2011) 115110.
[34] Y. Wang, X. Chen, T. Cui, Y. Niu, Y. Wang, M. Wang, Y. Ma, G. Zou, Enhanced thermoelectric performance of PbTe within the orthorhombic P nma phase, Phys. Rev. B 76 (15) (2007) 155127.
[35] A.F. May, D.J. Singh, G.J. Snyder, Influence of band structure on the large thermoelectric performance of lanthanum telluride, Phys. Rev. B 79 (15) (2009) 153101.
[36] J.J. Pulikkotil, D.J. Singh, S. Auluck, M. Saravanan, D.K. Misra, A. Dhar, R.C. Budhani, Doping and temperature dependence of thermoelectric properties in Mg2(Si, Sn), Phys. Rev. B 86 (15) (2012) 155204.
[37] S. Datta, Electronic Transport in Mesoscopic Systems, Cambridge Studies in Semiconductor Physics, Cambridge University Press, 1997. <https://books.google.no/books?id=28BC-ofEhvUC>.
[38] A. Wacker, A.-P. Jauho, Quantum transport: the link between standard approaches in superlattices, Phys. Rev. Lett. 80 (1998) 369, http://dx.doi.org/10.1103/PhysRevLett.80.369. <http://link.aps.org/doi/10.1103/PhysRevLett.80.369>.
[39] A. Wacker, Semiconductor superlattices: a model system for nonlinear transport, Phys. Rep. 357 (1) (2002) 1, http://dx.doi.org/10.1016/S0370-1573(01)00029-1. <http://www.sciencedirect.com/science/article/pii/S0370157301000291>.
[40] A. Bulusu, D.G. Walker, Modeling of thermoelectric properties of semiconductor thin films with quantum and scattering effects, J. Heat Transfer 129 (4) (2007) 492.
[41] A. Bulusu, D.G. Walker, Quantum modeling of thermoelectric properties of Si/Ge/Si superlattices, IEEE Trans. Electron. Dev. 55 (1) (2008) 423.
[42] T. Musho, Predicting the figure of merit of nanostructured thermoelectric materials, J. Mater. Res. 30 (17) (2015) 2628.
[43] M. Thesberg, M. Pourfath, N. Neophytou, H. Kosina, The fragility of thermoelectric power factor in cross-plane superlattices in the presence of nonidealities: a quantum transport simulation approach, J. Electron. Mater. 45 (3) (2016) 1584.
[44] M. Buttiker, Coherent and sequential tunneling in series barriers, IBM J. Res. Dev. 32 (1) (1988) 63, http://dx.doi.org/10.1147/rd.321.0063.
[45] S. Birner, T. Zibold, T. Andlauer, T. Kubis, M. Sabathil, A. Trellakis, P. Vogl, Nextnano: general purpose 3-D simulations, IEEE Trans. Electron. Dev. 54 (9) (2007) 2137.
[46] V.K. Lamba, R.S. Sawhney, D. Engles, A.B. Garg, R. Mittal, R. Mukhopadhyay, Treatment of scattering in nano-films, AIP Conference Proceedings-American Institute of Physics, vol. 1349, 2011, p. 671.
[47] S. Wang, N. Mingo, Tailoring interface roughness and superlattice period length in electron-filtering thermoelectric materials, Phys. Rev. B 79 (2009) 115316.
[48] H. Li, Y. Yu, G. Li, Computational modeling and analysis of thermoelectric properties of nanoporous silicon, J. Appl. Phys. 115 (12) (2014) 124316.
[49] J. Li, T.C.A. Yeung, C.H. Kam, Influence of electron scatterings on thermoelectric effect, J. Appl. Phys. 112 (3) (2012) 034306.
[50] A. Bulusu, D.G. Walker, Review of electronic transport models for thermoelectric materials, Superlattice. Microst. 44 (1) (2008) 1.
[51] K. Sääskilahti, J. Oksanen, J. Tulkki, Thermal balance and quantum heat transport in nanostructures thermalized by local Langevin heat baths, Phys. Rev. E 88 (2013) 012128.
[52] C.W. Groth, M. Wimmer, A.R. Akhmerov, X. Waintal, Kwant: a software package for quantum transport, New J. Phys. 16 (6) (2014) 063065.
[53] http://kwant-project.org/.
[54] G. Kresse, J. Hafner, Ab initio molecular dynamics for liquid metals, Phys. Rev. B 47 (1) (1993) 558.
[55] G. Kresse, J. Hafner, Ab initio molecular-dynamics simulation of the liquid-metal–amorphous-semiconductor transition in germanium, Phys. Rev. B 49 (20) (1994) 14251.

[56] http://cms.mpi.univie.ac.at/vasp.
[57] C. Jeong, R. Kim, M. Luisier, S. Datta, M. Lundstrom, On Landauer versus Boltzmann and full band versus effective mass evaluation of thermoelectric transport coefficients, J. Appl. Phys. 107 (2) (2010) 023707.
[58] C. Wood, Materials for thermoelectric energy conversion, Rep. Prog. Phys. 51 (4) (1988) 459.
[59] E. Maciá, Thermoelectric Materials: Advances and Applications, Pan Stanford Publishing, 2015. <https://books.google.no/books?id=PuM_CQAAQBAJ>.
[60] H.J. Goldsmid, Introduction to Thermoelectricity, Springer Series in Materials Science, Springer, Berlin Heidelberg, 2009. <https://books.google.no/books?id=LYN3nDy0FccC>.
[61] E. Flage-Larsen, Ø. Prytz, The Lorenz function: its properties at optimum thermoelectric figure-of-merit, Appl. Phys. Lett. 99 (20) (2011) 202108.
[62] H.-S. Kim, Z.M. Gibbs, Y. Tang, H. Wang, G.J. Snyder, Characterization of Lorenz number with Seebeck coefficient measurement, APL Mater. 3 (4) (2015) 041506.
[63] A.H. Wilson, The Theory of Metals, Cambridge University Press, 2011. <https://books.google.no/books?id=cX8U_gAACAAJ>.
[64] U. Sivan, Y. Imry, Multichannel Landauer formula for thermoelectric transport with application to thermopower near the mobility edge, Phys. Rev. B 33 (1986) 551, http://dx.doi.org/10.1103/PhysRevB.33.551. <http://link.aps.org/doi/10.1103/PhysRevB.33.551>.
[65] Y. Selamet, Y.D. Zhou, J. Zhao, Y. Chang, C.R. Becker, R. Ashokan, C.H. Grein, S. Sivananthan, HgTe/HgCdTe superlattices grown on CdTe/Si by molecular beam epitaxy for infrared detection, J. Electron Mater. 33 (6) (2004) 503, http://dx.doi.org/10.1007/s11664-004-0038-5. <http://dx.doi.org/10.1007/s11664-004-0038-5>.
[66] Y.-C. Chang, Bond-orbital models for superlattices, Phys. Rev. B 37 (1988) 8215, http://dx.doi.org/10.1103/PhysRevB.37.8215. <http://link.aps.org/doi/10.1103/PhysRevB.37.8215>.
[67] E. Flage-Larsen, T4ME - transport properties for materials: The Boltzmann Transport Equation for electrons in the relaxation time approximation, 2017 (in preparation).
[68] S. Cauley, M. Luisier, V. Balakrishnan, G. Klimeck, C.-K. Koh, Distributed non-equilibrium greens function algorithms for the simulation of nanoelectronic devices with scattering, J. Appl. Phys. 110 (4) (2011) 043713.

Paper II

Thermoelectric effect in superlattices; applicability of coherent and incoherent transport models

II

Computational Materials Science 153 (2018) 88–96

Contents lists available at ScienceDirect

Computational Materials Science

journal homepage: www.elsevier.com/locate/commatsci

Thermoelectric effect in superlattices; applicability of coherent and incoherent transport models

Lars Musland[a], Espen Flage-Larsen[b,c,*]

[a] University of Oslo, Department of Physics, P.O. Box 1048 Blindern, NO-0316 Oslo, Norway
[b] SINTEF Industry, Material Physics, P.O. Box 124 Blinder, NO-0314 Oslo, Norway
[c] University of Stavanger, Department of Mechanical and Structural Engineering and Materials Science, Ullandhaug, NO-4036 Stavanger, Norway

ARTICLE INFO

Keywords:
Electron transport
Thermal transport
Landauer
Buttiker approximation
Heterestructure
Superlattice

ABSTRACT

Calculations of thermoelectric transport coefficients including quantum effects are performed on superlattices using the Buttiker approximation. The results are compared to the Boltzmann transport equation with minibands present, and to an incoherent transport model. Comparisons are performed in the linear regime for the electrical conductivity, Seebeck and Lorenz coefficients. We show that at superlattice periods smaller than the typical electron mean free path, the former model and the calculations including quantum effects are in agreement. However, for longer superlattices the incoherent model is shown to be more correct.

1. Introduction

The thermoelectric properties are often improved by nano structuring [1] materials. This improvement stems mostly from a reduction of the thermal conductivity due to a reduced phonon mean free path. However, such modifications could also have a positive impact on the transport of charge carriers. Inclusion of nanoscale structures affects both the electronic structure and the scattering properties of carriers, and if tailored properly, these effects could increase the thermoelectric conversion efficiency.

An approach to nanostructuring that is motivated by this, is the concept of energy filtering [2–6]. In this approach the contributions to the electrical conductivity at different carrier energies are modified [7,3]. These contributions are contained in what is usually referred to as the transport distribution function. For applications of thermoelectricity, it is beneficial that the transport distribution function is asymmetric and sharply peaked close to the chemical potential. Previously it has been shown that the ideal shape of the transport distribution function is a delta function [7,8]. Unfortunately this can never be achieved, but by utilizing the flexibility of nano structuring it might be possible to approach this ideal case.

The concept of energy filtering rely on the possibility to tune the alignment of the charge carrier energy levels between different layers of materials. A model system where such effects can be studied is for instance periodic heterostructures, also known as superlattices. Consequentially, an extensive literature has appeared that address how the thermoelectric effect behaves in superlattices. Some of these suggest there is a large potential for improving the conversion efficiency by this approach [9–12,3]. Apart from isolated cases [13,14], experimental demonstration of such improvement is largely absent. This discrepancy could have several different sources. In fact, the synthesis and measurement phases are inherently difficult. However, it has also been suggested that the discrepancies between experiment and theory are mainly due to the approximations employed in the applied theoretical models [15].

Thus, there is a need too investigate less approximate models. For this purpose, several considerations are important. It might be necessary to: (i) include multiple bands past the effective mass approximation. (ii) include electrostatic interactions due to charge redistribution, as well as strain effects in the heterostructure. (iii) explicitly consider both the correct atomistic structure of the superlattice that is targeted, and also how close the synthesis process actually gets to that ideal case: Both interface roughness and deviations from the ideal periodic structure should be accounted for in the model. (iv) use better models for the carrier scattering. This applies in particular to the constant relaxation time approximation which is often employed. In order for the model to have predictive power, scattering models should either be developed from ab initio, or be based on empirical models that have been rigorously demonstrated to hold in a large number of different heterostructures. And finally, (v) consider the validity of the applied transport formalism.

The latter topic will be the subject of this work. The transport formalism that is usually applied to bulk thermoelectric materials is the semiclassical Boltzmann transport equation (BTE) [16–19]. Commonly,

* Corresponding author at: SINTEF Industry, Material Physics, P.O. Box 124 Blinder, NO-0314 Oslo, Norway.
E-mail address: espen.flage-larsen@sintef.no (E. Flage-Larsen).

https://doi.org/10.1016/j.commatsci.2018.05.044
Received 4 January 2018; Received in revised form 2 May 2018; Accepted 21 May 2018
Available online 26 June 2018

the BTE is linearized and used within the relaxation time approximation (RTA), thus making calculations particularly tractable [18]. The BTE is also applied to heterostructures.

However, it is not clear how the heterostructural properties of a superlattice should be treated in the BTE. One possibility is to assume a position dependent charge carrier energy dispersion relation upon solving the BTE itself. However, according to the uncertainty principle a position dependent dispersion relation is ill defined at the nanoscale. Another possibility is to use the band structure of the dominant material, and to treat the interfaces and barriers as a scattering mechanism. This approach has been pursued utilizing tractable, but not necessarily realistic models of interface scattering [10,20–23]. It is also possible to use the BTE within individual layers of the heterostructure, and treat transport of carriers between layers as an instance of thermionic emission [24,11,25,26]. Finally, in the case of superlattices, the periodicity of the structure allow to apply Bloch's theorem to the heterostructure itself. The effect of heterostructuring is then included in the band structure [27–31,2,32–34]. Since the energy bands of the bulk material are split into smaller subbands known as minibands, this model has been referred to as the miniband transport model [35]. The miniband transport model also has a limited regime of validity [35].

Recently the thermoelectric effect in superlattices have been studied by the application of non-equilibrium Green's functions (NEGF) [36–44,15,45–52]. The advantage of NEGF, is that it is derived directly from quantum mechanics and does not rely on a semi-classical model like the variety of BTE that is usually applied. Information dependent on position can thus be included in the calculations without violating the uncertainty principle. Due to its computationally demanding nature, applications of NEGF to thermoelectric materials usually rely on the effective mass approximation and simplified scattering models. NEGF has however been applied beyond these approximations [53–56] in other fields, but usually only to ordered structures. Recently new techniques has appeared to tackle also disordered structures, typically by employing non-equilibrium coherent potential approximation (NECPA) [57,58].

Studies of the range of validity of the BTE and the NEGF approach are thus of great interest. For the case of superlattices, Wacker [35,59–61] have made a significant contribution. In particular Wacker concludes that the miniband transport model is in agreement with NEGF when the superlattice wells are strongly coupled in comparison both to the scattering rate and to the electric field. Furthermore, he describes two other approximate schemes, valid when the scattering rate or the electric field is strong, respectively. These approximate models are justified in three different ways: by heuristic arguments, by formal derivation from NEGF, and finally by direct comparison of numerical calculations. Thus, Wacker demonstrates quite thoroughly the existence of three regimes where approximations to the NEGF formalism are valid.

However, Wacker's work was exclusively concerned with electrical conductivity σ. For thermoelectric applications, the Seebeck coefficient α [17,18] and the Lorenz coefficient L [62,63] are equally important. In addition, Wacker was mostly concerned with transport at high fields. In thermoelectric applications we are mostly concerned with low fields, or linear transport. A comparison of this kind was made in one recent work employing NEGF [37]. However, this work was limited to heterostructures with a total spatial extent of 6 nm. Since the bulk BTE expressions only apply in the diffusive regime, the sample should be considerably thicker in order for the results to be comparable.

The purpose of this study is to extend the work of Wacker to include also the Seebeck and Lorenz coefficient at low field for superlattices with different thickness. This work is not about obtaining experimental accuracy or reproducibility, but to investigate how quantum effects modify the themoelectric transport coefficient and how these results differ from the results from the BTE.

In this work we consider the most important quantum effects to include to be the wave nature of carriers, and the momentum and coherence loss caused by scattering. Accordingly, we have chosen to use a ballistic quantum transport simulator, which inherently captures the wave nature of carriers, and to incorporate the effects of momentum and coherence loss by the use of Buttiker probes [64,65,54,49–52,39,36]. The Buttiker probes are a set of virtual floating contacts attached to the ballistic system. Since these probes are floating, their only effect on the system is to randomize the momentum and phase of the carriers similar to a scattering mechanism. This approach is often referred to as the Buttiker approximation [36]. It is related to NEGF, but is less general and usually bears a lower computational cost. The Buttiker probes are described by self energies, in the same way as scattering processes are in NEGF. However, a key difference between the two methods is that the Buttiker approximation does not allow for the explicit definition of lesser self energies [64,66]. In practice this yields less control of the assignation of new states to carriers after scattering [64].

This work is organized as follows: The theoretical aspects are described and discussed in Section 2, where our quantum transport approach is described in Section 2.1. Sections 2.2 and 2.3 describes respectively the miniband transport model, and a second semiclassical approach that assumes incoherent transport between barriers. In Section 3 we show the results of our calculations. There we make two separate studies where we compare the electrical conductivity, the Seebeck and the Lorenz coefficient, as calculated by the Buttiker approximation, the miniband transport model, and by the incoherent model of Section 2.3. In Section 3.1 we study how the agreement between the models depend on the scattering rate, while in Section 3.2 we study how this agreement is affected by the size of the superlattice period. Finally, in Section 4 we provide final discussion and conclusions.

2. Theory and models

2.1. The Buttiker approximation

We utilize a ballistic quantum transport simulator with Buttiker probes [64,65]. The employed simulator is Kwant [67,68], which requires the definition of a tight binding model in the transport region, and a set of attached leads. Kwant efficiently solves the resulting quantum mechanical scattering problem, using either a wave function or a Green's function based approach. On completion, the ballistic transmission functions between the leads are obtained.

Only two of the leads attached to the transport region represent real contacts. These are the emitter and collector, between which currents would be measured in an experiment. The remaining leads are Buttiker probes, which are included to emulate scattering processes. For reasons of computational efficiency, the Buttiker probes are only connected to a subset of the sites in the transport region, and the density of Buttiker probes are controlled by the parameter d_{sc}. More specifically, the Buttiker probes are attached at regular intervals between the two real contacts, with one single probe per d_{sc} unit cells of the materials composing the heterostructure.

The interactions between the leads and the scattering region are described by retarded self energy functions [64,68]. In this work, the retarded self energies of the Buttiker probes are defined as $\Sigma^r = -i\hbar/2\tau$, which result in the relaxation of carrier momentum with a characteristic relaxation time τ [69,50]. This allows for a particularly simple comparison to the BTE within the RTA. When $d_{sc} > 1$, the scattering self energies are modified to $\Sigma^r = -d_{sc} \cdot i\hbar/2\tau$, to compensate for the lower density of Buttiker probes. The magnitude of the self energies of the contacts are not of significance, since our calculations are made in such a way as to be independent of contact effects. Please consult our previous work for additional details [69].

The retarded self energy functions describe how carriers are absorbed by the Buttiker probes [64]. In addition, it is necessary to describe how carriers are emitted. Within the NEGF formalism, carriers

that enter the system are described by the lesser self energies $\Sigma^<$ [64]. However, within our ballistic framework, these cannot be explicitly defined. Instead, we define the re-emission of carriers after absorption by a Buttiker probe as follows: Carriers are re-emitted from the same probe at which they were absorbed with the same energy and momentum orthogonal to the transport direction as before absorption. The momentum component parallel to the transport direction is randomized. The scattering process thus conserves charge, energy and transverse momentum. The conservation of energy is by choice, since we want to model elastic scattering. On the other hand, the conservation of transverse momentum is only introduced for reasons of computational efficiency.

By extending the expression for transmission [64,69], we use Kwant together with the scheme described earlier to calculate the effective transmission between the two real contacts. Since only elastic scattering is present, we make use of the Landauer transport formalism to connect the effective transmission function to the relevant transport coefficients. These are in our case the electrical conductivity σ, the Seebeck coefficient [17,18] α and the Lorenz coefficient L. The latter is defined as $\kappa_e = \sigma L T$ [62,63]. Here κ_e is the electron contribution to the thermal conductivity. In the linear regime, the magnitude of these coefficients in the cross plane direction can be expressed as [69–71]

$$\sigma = \int \mathrm{d}E\, \Sigma(E) F_T(E), \tag{1a}$$

$$\alpha = -\frac{1}{\sigma e T} \int \mathrm{d}E\, \Sigma(E) F_T(E)(E-\mu), \tag{1b}$$

$$L = \frac{1}{\sigma e^2 T^2} \int \mathrm{d}E\, \Sigma(E) F_T(E)(E-\mu)^2 - \alpha^2. \tag{1c}$$

where $\Sigma(E)$ is the transport distribution function, and $F_T(E)$ is the thermal broadening function or Fermi window $F_T(E) = -\partial f/\partial E$, where f is the Fermi-function.

2.2. The miniband transport model

Following Wacker's nomenclature [35], we refer to the application of the BTE, using the band structure of the superlattice, as the miniband transport model. The superlattice band structure may be obtained by schemes of varying approximation, ranging from the introductory Kronig Penney model [27,28,72] to ab initio approaches such as DFT [30,34]. In this study we use the band structure resulting from the solutions of the same tight binding model used in the Kwant simulations discussed above as input to the BTE. This allows for a direct comparison of the results, without considering differences in electronic structure between the models. In addition, the tight binding model allows calculations on superlattices with very large periods with acceptable accuracy.

The validity of the miniband transport model have been extensively investigated by Wacker [35,59]. He describes two conditions $t \gg \hbar\Gamma$ and $t \gg eFa$, both of which must be satisfied for the miniband model to be valid. Here t is the coupling energy between neighboring wells of the superlattice, Γ is the scattering rate, F is the applied electric field, and a is the superlattice period. In this work we study linear transport and the latter condition is satisfied by definition. The former may be heuristically rewritten as follows: within a simple nearest neighbor tight binding description, the miniband energy dispersion along the growth direction is given by $E(k) = 2t\cos ka$. Thus, the velocity is $v = \partial E_k/\partial k/\hbar \sim ta/\hbar$. Given this, we may rewrite Wacker's first condition as

$$a \ll v\tau. \tag{2}$$

Here $\tau = 1/\Gamma$ is the average scattering time, which in the case of our simple scattering model is equal to the momentum relaxation time. In our previous work [69], Eq. (2) was also derived by a heuristic argument involving Heisenberg's uncertainty relations.

The product $v\tau$ will generally be similar to the coherence length [64] l_ϕ. As such Eq. (2) is thus equivalent to a condition stated in previous work [10,2], namely that the superlattice period should be shorter than l_ϕ for the miniband model to apply. This condition is intuitive, since the minibands always arise from the solution of some wave equation. When $a > l_\phi$, the electron behavior is not coherent within the unit cell, and accordingly no wave equation is applicable.

2.3. The sequential transmission model

In addition to the case $t \gg \hbar\Gamma$, Wacker also describes an approximate model that applies in the opposite limit $t \ll \hbar\Gamma$ [35,59], here given by $a \gg v\tau$. This model, which he refers to as the sequential tunneling model, is extensive and involves scattering theory beyond Fermi's golden rule. The reason why this is necessary, is that the applied field misaligns the energy levels of the different wells, so that first order scattering expressions result in zero current due to energy conservation [35]. However, since we here only study linear transport, we express the currents in terms of transmission functions at zero bias [64], where this does not pose a problem.

Thus, we make use of another model employed in previous work [20], which we will refer to as the sequential transmission model. It is derived here again for consistency. A central assumption for proceeding is that transport between different wells in the superlattice is incoherent [35]. We then use incoherent transmission functions [73] in series, expressed as

$$\frac{1}{T} = \frac{1}{T_1} + \frac{1}{T_2} - 1. \tag{3}$$

The transmission through a single superlattice period can be found from this by substituting the well transmission T_w for T_1, and the barrier transmission T_b for T_2. The transmission through N periods can then be found by applying the addition formula inductively to get

$$\begin{aligned} \frac{1}{T} - 1 &= N\left(\frac{1}{T_w} + \frac{1}{T_b} - 2\right) \\ &= N\left(\frac{1}{T_w} - 1\right) + \frac{L}{a}\left(\frac{1}{T_b} - 1\right), \end{aligned} \tag{4}$$

where L is the total length of the N periods.

In the case where there are no barriers present we obtain by the same procedure

$$\frac{1}{T_{bulk}} - 1 = N\left(\frac{1}{T'_w} - 1\right), \tag{5}$$

where T'_w is the transmission function of the well sections. Since these sections are thicker in absence of barriers, $T'_w \neq T_w$. However, if the well sections are considerably thicker than the barriers, then the change in thickness will be small and $T_w = T'_w$ is a good approximation. In this case, we may combine Eqs. (4) and (5) such that

$$\frac{1}{T} - 1 = \frac{1}{T_{bulk}} - 1 + \frac{L}{a}\left(\frac{1}{T_b} - 1\right). \tag{6}$$

In the literature, we also find the back scattering mean free path λ defined through the expression $1/T - 1 = L/\lambda$ [73,70]. Inserting this, Eq. (6) becomes

$$\frac{1}{\lambda} = \frac{1}{\lambda_{bulk}} + \frac{1}{a}\left(\frac{1}{T_b} - 1\right), \tag{7}$$

which applies in the limit where both $a \gg v\tau$ and $a \gg b$, with b being the thickness of the barriers. If we also assume $b \ll v\tau$, we can approximate T_b to be ballistic, which allows for more efficient calculations.

Within the Landauer transport formalism, the transport distribution function $\Sigma(E)$ is determined by the back scattering mean free path [70] and Eq. (7) is thus sufficient to determine the thermoelectric transport

coefficients σ, α and L. One can also use the derived expressions for the transport in the Landauer approach and the BTE [70,69] to express Eq. (7) in terms of relaxation times in the RTA. The resulting expression becomes

$$\frac{1}{\tau} = \frac{1}{\tau_{bulk}} + \frac{2v}{a}\left(\frac{1}{T_b} - 1\right), \tag{8}$$

and must be used in the BTE together with the band structure of the well material. This expression is an instance of Matthiessen's rule [66]: The first term on the right is the relaxation rate of the bulk well material, while the last term is the relaxation rate of scattering on barriers.

3. Results

The transport distribution function is calculated from the transmission function [64] by utilizing the Landauer formalism. Please consult our previous work [69], where this approach is explained in detail. Additional details can also be found in the literature [73,64,70,71]. In this work we again utilize CdTe and CdHgTe alloys as a model system. Their only role of this work is to provide a somewhat realistic system from which the band structure can be constructed. Details of the tight-binding model and fitting procedure from first-principle calculations, as well as the resulting parameters, can be found in our previous work [69].

3.1. Dependence on the scattering time.

According to the discussion of Section 2.2 we expect agreement between the Buttiker and the miniband model for large values of τ. At smaller values this agreement should disappear, and the quantum transport model should eventually agree with an incoherent model. In this section, the calculations are performed on a superlattice containing at total of 16 unit cells, eight of CdTe followed by eight of $Cd_{0.75}Hg_{0.25}Te$. The resulting spectral function and transport properties are shown in Fig. 1 for different values of τ, ranging from 1 fs to 0.1 ps. At larger values of τ, the thickness L of the simulated region must be larger in order for the transport process to remain incoherent. Accordingly, L is chosen respectively as 337, 169, 84.5 and 42.3 nm for $\tau = 100$, 50, 20 and 10 fs, and as 21.1 nm (two superlattice periods) for $\tau = 5$, 2 and 1 fs. Similarly, at smaller values of τ the coherence length is shorter, so that d_{sc} must be smaller in order to sample structures at smaller length scales. Thus, we choose $d_{sc} = 2$ when $\tau = 100$, 50 or 20 fs, and $d_{sc} = 1$ when $\tau = 10$, 5, 2 or 1 fs.

The operating principles behind these choices are that we always have $L \gtrsim 4v\tau$, while d_{sc} satisfies both $d_{sc} \leqslant 2$ and $d_{sc}a < v\tau/4$. The first two of these conditions originate from our previous work [69], while the latter is a heuristic condition based on the desire to have a reasonable sampling of the coherence length. The group velocity v is estimated to $\hbar\langle v\rangle = \langle \partial E/\partial \boldsymbol{k}\rangle \approx 0.6$ eVÅ, from the band structure of the $Cd_{0.75}Hg_{0.25}Te$ model [69].

Our implementation of the Buttiker approximation calculates the transport distribution function as an integral over the transverse component of k-space. This integration makes use of the midpoint method, and is performed in cylindrical coordinates. The integration grid has an evenly distributes sampling of $N_k = 100$ points in the radial $\boldsymbol{k}$-direction, and a distance of $\delta_\theta = 0.03$ between points in the angular direction in direct $\boldsymbol{k}$-space [69]. Calculation of transport coefficients requires integration over energy, which also utilize the midpoint method on a regular sampling of $N_E = 200$ points between $E_{min} = 2.0$ eV and $E_{max} = 4.0$ eV. This interval surrounds the band gaps of the involved materials, as can be seen in our previous work [69].

The routines to perform the BTE calculations required by the miniband transport model, are explained in detail in a separate work [74]. In summary a regular cubic integration grid was used, employing a resolution of $N_k^{xy} = 51$ points in the k_x and k_y directions, and $N_k^z = 13$ points in the k_z direction, which is the transport direction and the cross plane direction of the super lattice. These choices were again based on convergence studies performed in our previous work [69]. The tight binding model was used to generate the band structure on this grid followed by a step of numerical differences to extract the velocities. Finally, a trapezoidal integration scheme was performed. The relaxation time was fixated at 1 fs to be compatible with the model used for the Buttiker model.

In Fig. 1a, we present the results of $\Sigma(E)/\tau$ for different values of τ. Since evaluating $\Sigma(E)$ using the BTE is demanding, we show only results of the Buttiker approximation and the sequential transmission model. However, in our previous work we demonstrated that our implementation of the Buttiker approximation is in agreement with the miniband transport model for short period superlattices and large values of τ, in agreement with Section 2.2. We thus expect the miniband transport result to largely agree with results from the Buttiker approximation at $\tau = 100$ fs. Since the BTE expression for $\Sigma(E)$ is proportional to τ [18,17], the miniband results with smaller values of τ would also be identical to this curve. The calculated results from the miniband model contains numerical noise, which originates from a too course integration grid. As we approach a very low temperature which is required to produce $\Sigma(E)$ an extremely dense integration grid is needed. In the calculation of transport coefficients, this noise is smeared by the finite temperature, and is thus not of particular significance. In order not to confuse readers we thus opted not to show these results in Fig. 1a.

The sequential transmission model does not agree with the Buttiker approximation, even for small values of τ. However, such agreement is not to be expected here. In addition to the requirement $v\tau \ll a$, $a \gg b$ also need to be satisfied. This is not the case, since $b = a/2 = 5.3$ nm. The sequential transmission model is by design more suited for large superlattice periods than small values of τ. Small values of τ may instead require a more sophisticated sequential model, such as the one described by Wacker [35,59].

Figs. 1b–d compare the electrical conductivity, Seebeck and Lorenz coefficients calculated using the Buttiker approximation and the miniband transport model. The sequential transmission model is not shown, since its failure is demonstrated already in Fig. 1a. In Fig. 1b the electrical conductivities are normalized by the magnitude of τ. This makes the miniband transport results independent of τ in all three figures, due to the cancellation of a constant relaxation time in the α and L [18,17]. The miniband transport results are in good agreement with those of the Buttiker approximation when $\tau = 100$ fs, but when τ is reduced the agreement gradually disappears. This effect is in agreement with the discussion concerning Eq. (2).

In all four Figs. 1a-d, we see clear oscillations in the transport coefficients as a function of the chemical potential μ. This effect originates when the chemical potential is varied, and the contributions from the minibands are picked up. When τ is decreased, the oscillations are gradually smeared, indicating that the miniband structure disappears. For the smallest values of τ, even variation in transport properties originating in the bulk band gap is beginning to smooth out. However, the disappearance of the band gap is probably an artifact of the crudeness of our scattering model. One can show that a scattering model of the type described in Section 2.1 will cause a Lorenzian broadening of eigenstates [64], which given sufficiently small values of τ will smooth out any structures in the transport properties. However, in the more realistic case of a non-constant relaxation time, the broadening of eigenstates can have a more complicated shape [64], allowing for the band gap to be maintained.

3.2. Dependence on the superlattice period

The question of dependence on the superlattice period is experimentally relevant to a larger extent than that of the previous section, since the scattering time tends to fall in the range τ=10–1000 fs, while

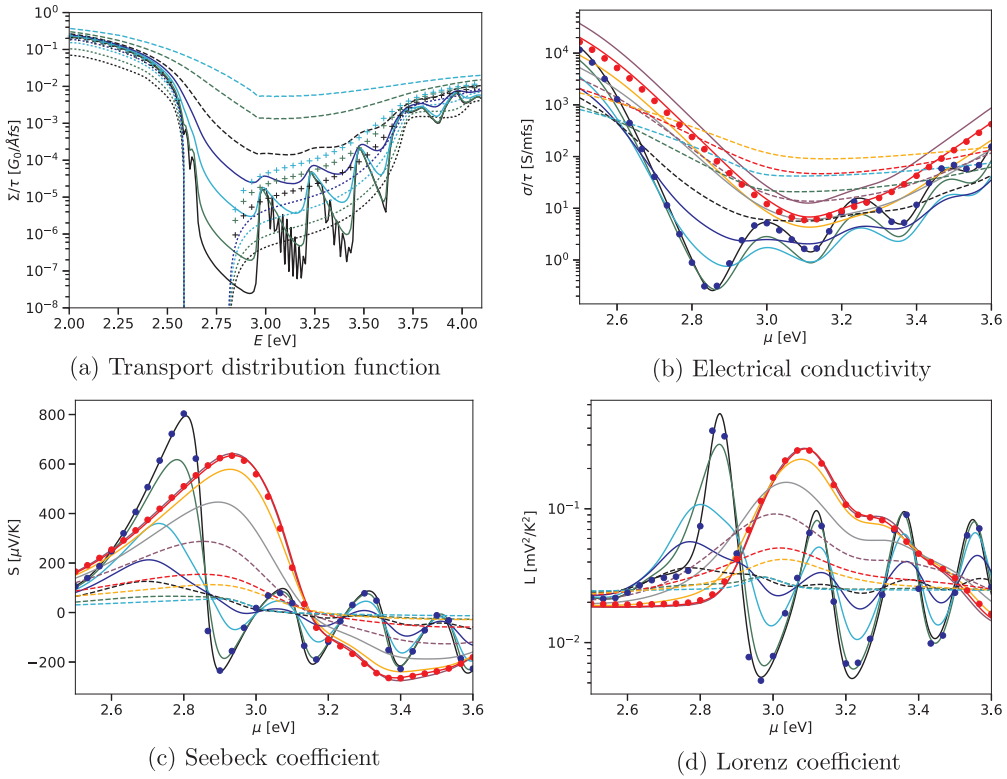

Fig. 1. Transport coefficients for electrons in an 8-8 CdTe-$Hg^{0.25}Cd^{0.75}Te$ superlattice as function of the chemical potential μ. The solid and dashed lines are calculated by the Buttiker approximation, the circles by the miniband transport model, and the dotted lines and crosses by the sequential transmission model. For the solid and doted lines, the black, green, turquoise and blue results are from calculations with $\tau = 100$, 50, 20 and 10 fs, respectively. For the dashed lines and the crosses, the black, green and turquoise lines are from calculations with $\tau = 5$, 2 and 1 fs, respectively. Furthermore, in panel (b–d) results in black, green, turquoise and blue are calculated at 300 K, while the purple, red, orange and gray lines are calculated at 700 K. Among the solid and dashed lines, the purple, red, orange and gray lines respectively have $\tau = 100$, 50, 20 and 10 fs. Among the dashed lines and crosses the purple, red and orange lines have $\tau = 5$, 2 and 1 fs respectively. The miniband results are shown as blue and red dots at 300 K and 700 K, respectively. (For interpretation of the references to colour in this figure legend, the reader is referred to the web version of this article.)

the superlattice period can be tailored during synthesis.

In Figs. 2 and 3, results are shown for several different superlattices, having periods ranging from 11 to 340 nm. All of the supercells are composed of a single barrier layer composed of eight unit cells of CdTe, and a single well layer composed of $Cd^{0.75}Hg^{0.25}Te$. The results from the Buttiker approximation were obtained at $\tau = 100$ fs, with $d_{sc} = 2$,

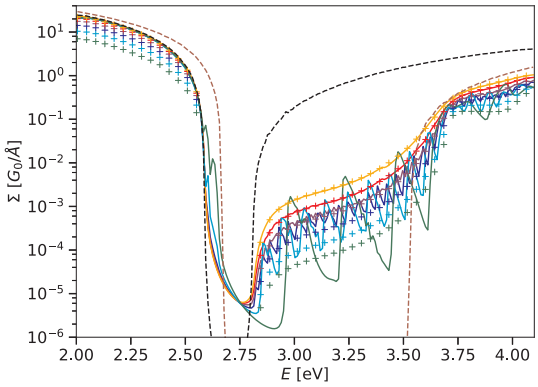

Fig. 2. Transport distribution function in multiple superlattices. Results shown in green, turquoise, blue, purple red and orange are calculated respectively with superlattice periods of 16, 32, 64, 128, 256 and 512 unit cells of the composing materials. Among these, solid lines represent the Buttiker approximation, while crosses represent the sequential transmission model. The brown and black dashed lines are respectively the transport distribution function of bulk CdTe and $Cd^{0.75}Hg^{0.25}Te$. (For interpretation of the references to colour in this figure legend, the reader is referred to the web version of this article.)

and using the same integration grid as in the previous section. The BTE calculations also use the same integration grid as in the previous section.

Fig. 2 shows the transport distribution function, which is compared to that of pure CdTe and $Cd^{0.75}Hg^{0.25}Te$. Only results from the Buttiker approximation and the sequential transmission model are shown. Comparison to the miniband transport model is left for Fig. 3 where we show respectively the conductivities, Seebeck coefficients and Lorenz coefficients of the mentioned superlattices, calculated at 300 and 700 K. Fig. 3 includes results from the Buttiker approximation, the sequential transmission model, and the miniband transport model.

At short superlattice periods, the Buttiker approximation is in reasonable agreement with the miniband transport model, while for large superlattice periods it agrees more closely with the sequential transmission model. Consequently, the expectation that Eq. (7) is valid for large periods is confirmed, also for the Seebeck and Lorenz coefficient. The transition between the two regimes is better illustrated in Fig. 4, which shows the calculated transport coefficients as a function of the superlattice period a at the three values of $\mu = 2.6$, 3.0 and 3.35 eV. These chemical potentials are also illustrated by vertical lines in Fig. 3.

In all results where significant difference can be seen between the models, the Buttiker approximation changes from agreeing with the miniband model to the sequential transmission model at around $a = 100$ nm. As discussed above, the average group velocity of $Cd^{0.75}Hg^{0.25}Te$ in the conduction band is approximately 0.6 eVÅ. Since $\tau = 100$ fs, $\langle v \rangle \tau \approx 90$ nm. The transition at $a \sim 100$ nm is thus confirmed to be close to the relaxation length $v\tau$, which gives confidence that the mean free path is a reasonable estimate of the transition point between the two regimes. In fact, within the accuracy to which this can be

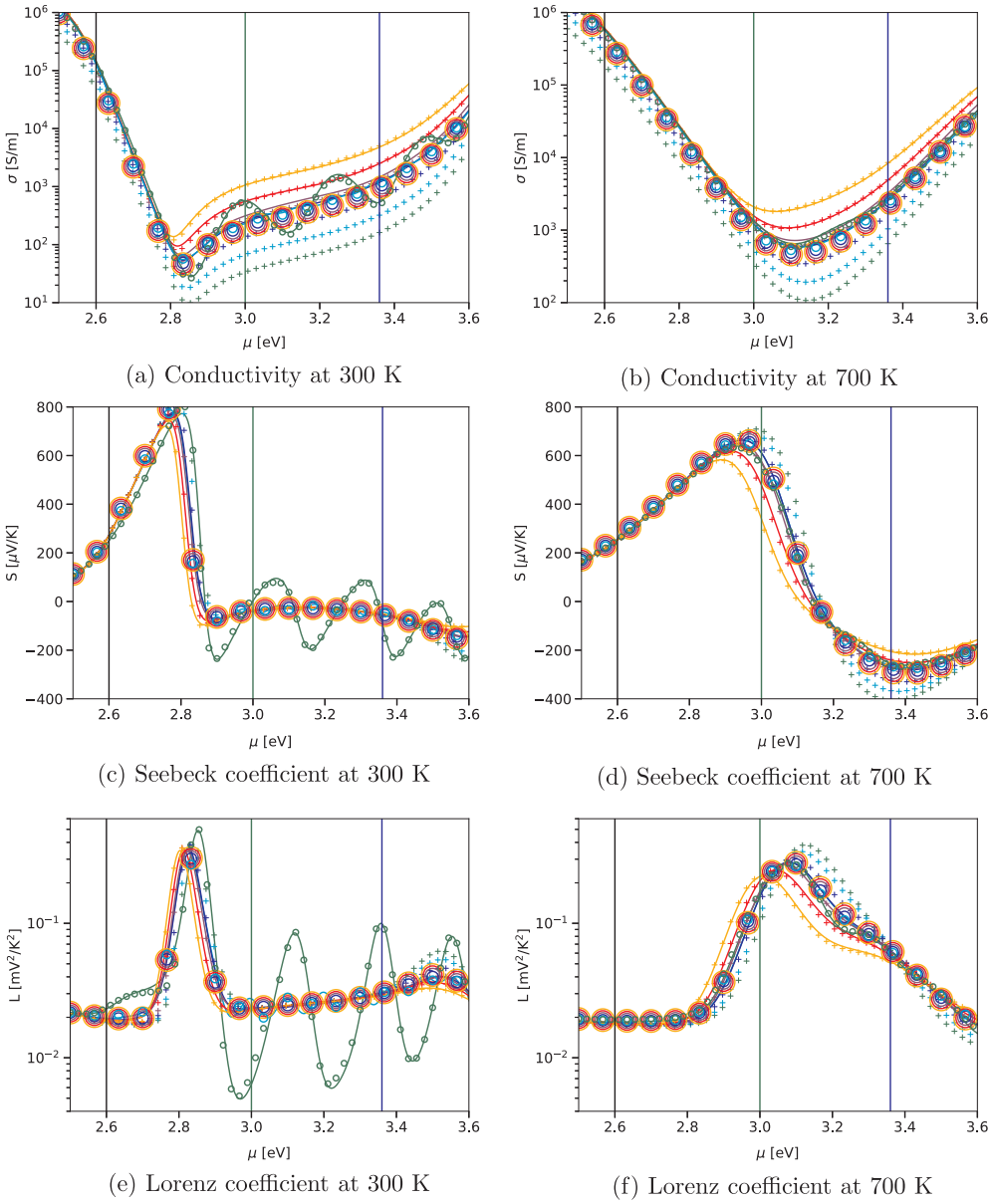

(a) Conductivity at 300 K (b) Conductivity at 700 K

(c) Seebeck coefficient at 300 K (d) Seebeck coefficient at 700 K

(e) Lorenz coefficient at 300 K (f) Lorenz coefficient at 700 K

Fig. 3. Transport coefficients in multiple superlattices as function of the chemical potential μ of electrons. Results shown in green, turquoise, blue, purple red and orange are calculated respectively with superlattice periods of 16, 32, 64, 128, 256 and 512 unit cells of the composing materials. Solid lines represent the Buttiker approximation, crosses represent the sequential transmission model, while circles represent the miniband transport model. The three vertical lines represent values of μ at which the dependence on period is examined more closely in Fig. 4. (For interpretation of the references to colour in this figure legend, the reader is referred to the web version of this article.)

judged, the transition seems to happen exactly at $a = v\tau$. However, this is likely to be an artifact of our simplified scattering model, where the momentum relaxation time is by construction equal to the coherence time [69]. In general we should expect the transition to happen near the phase relaxation length, of which the momentum relaxation length $v\tau$ is usually only a rough estimate [64].

We would also like to emphasize that the transition region in Fig. 4 appears to be quite small. If this fact generalizes, then the respective conditions $v\tau \gg a$ and $v\tau \ll a$ of the miniband transport and sequential transmission regimes, can be modified to $v\tau \gtrsim a$ and $v\tau \lesssim a$. The thermoelectric effect in superlattices can thus possibly always be studied using semiclassical approaches, and that the only role of quantum transport is to determine the transition point between the coherent and incoherent regimes. In order to confirm this, further studies are needed, which include different material systems and more realistic scattering mechanisms.

4. Summary and conclusion

The purpose of this work was to provide demonstrations of validity regimes of semiclassical treatment of electron transport in superlattices, extend earlier work [35,59–61] to also include thermoelectric transport coefficients, and to perform an exclusive treatment of the linear regime. Our approach utilized the Buttiker approximation, and performed explicit comparisons between the resulting transport coefficients and two different semiclassical models described in Sections 2.2 and 2.3.

We showed that the miniband transport model is better fit to reproduce the results of the Buttiker approximation for large values of the scattering time τ. We also compared the results of the Buttiker approximation to the sequential transmission model, and in the case of the structure with a short period discussed in Section 3.1, we found a poor match for all values of τ. However, as we showed, this is expected. In Section 3.2, we showed that the miniband transport model and the

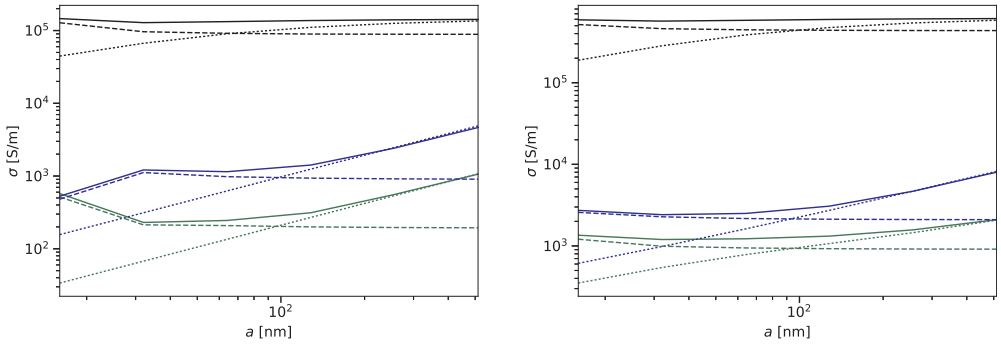

(a) Conductivity at 300 K

(b) Conductivity at 700 K

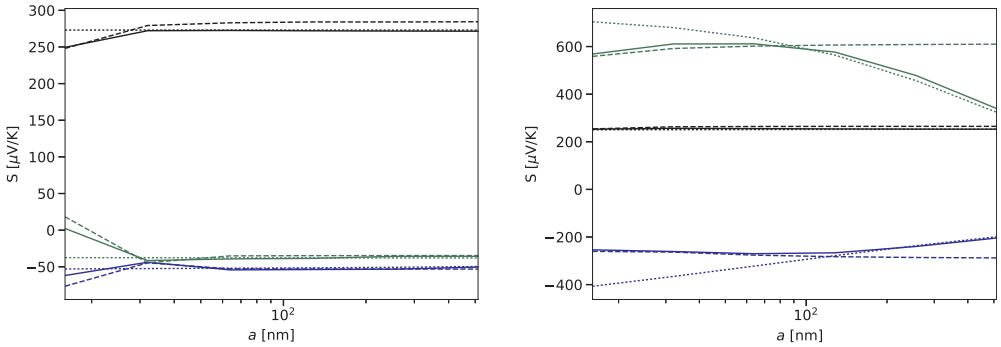

(c) Seebeck coefficient at 300 K

(d) Seebeck coefficient at 700 K

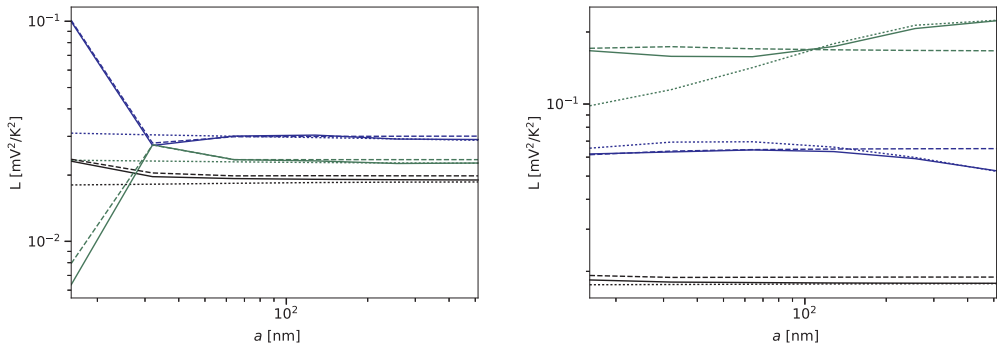

(e) Lorenz coefficient at 300 K

(f) Lorenz coefficient at 700 K

Fig. 4. Transport coefficients as function of the superlattice period a. Results shown in black, green and blue are calculated respectively with a chemical potential of $\mu = 2.6$ eV, $\mu = 3.0$ eV and $\mu = 3.36$ eV. The different line styles represents different models. The solid lines represent the Buttiker approximation, the dashed lines the miniband transport model, while the dotted lines represent the sequential transmission model. (For interpretation of the references to colour in this figure legend, the reader is referred to the web version of this article.)

Buttiker approximation are in good agreement for superlattice periods shorter than ~ 100 nm, while the sequential transmission model and Buttiker approximation are in agreement for periods larger than ~ 100 nm. To summarize, our results are in excellent agreement with the expectations discussed in Sections 2.2 and 2.3, and with those stated in earlier works for the case of conductivity [35,59–61]. We can conclude that these observations should also hold for the Seebeck and Lorenz coefficient.

It has been argued that superlattices with high thermoelectric efficiency should have a short period to inhibit phonon transport [2]. Consequently they should then fall into the miniband regime which would simplify future interpretation and calculations significantly. However, a good thermoelectric material also requires a high electrical conductivity, which suggests that the superlattice period should be large, so as not to inhibit the motion of carriers. Increased focus on the electrical properties is also becoming increasingly important due to the fact that several bulk materials already possess a very low thermal conductivity below 1 W/m K. Secondly, there could be other ways of reducing phonon transport than having a short period. For instance, one could let the superlattice period itself have a complex structure. Accordingly, we conclude that the question of coherent versus incoherent transport models may in fact be important to the design of thermoelectric heterostructures, and that some special cases may even require a full quantum transport approach, such as the Buttiker approximation or NEGF.

Acknowledgments

We would like to acknowledge the Research Council of Norway (NANO2021 project Thelma, number 228854) for providing funding, and the Norwegian Metacenter for Computational Resources (NOTUR) for providing computational resources.

References

[1] E. Maciá, Thermoelectric Materials: Advance and Applications, Pan Stanford Publishing, 2015.
[2] Z. Bian, M. Zebarjadi, R. Singh, Y. Ezzahri, A. Shakouri, G. Zeng, J.-H. Bahk, J.E. Bowers, J.M.O. Zide, A.C. Gossard, Cross-plane Seebeck coefficient and Lorenz number in superlattices, Phys. Rev. B 76 (2007) 205311.
[3] E. Flage-Larsen, O.M. Løvvik, Materials, Preparation, and Characterization in Thermoelectrics, in: D.M. Rowe (Ed.), Band Structure Guidelines for Higher Figure-of-Merit: Analytic Band Generation and Energy Filtering, CRC Press, 2012 (Chapter 10).
[4] K. Berland, X. Song, P.A. Carvalho, C. Persson, T.G. Finstad, O.M. Løvvik, Enhancement of thermoelectric properties by energy filtering: theoretical potential and experimental reality in nanostructured ZnSb, J. Appl. Phys. 119 (12) (2016) 125103.
[5] D. Narducci, S. Frabboni, X. Zianni, Silicon de novo: energy filtering and enhanced thermoelectric performances of nanocrystalline silicon and silicon alloys, J. Mater. Chem. C 3 (47) (2015) 12176.
[6] X.H. Yang, X.Y. Qin, J. Zhang, D. Li, H.X. Xin, M. Liu, Enhanced thermopower and energy filtering effect from synergetic scattering at heterojunction potentials in the thermoelectric composites with semiconducting nanoinclusions, J. Alloy. Compd. 558 (2013) 203.
[7] Z. Fan, H.-Q. Wang, J.-C. Zheng, Searching for the best thermoelectrics through the optimization of transport distribution function, J. Appl. Phys. 109 (7) (2011) 073713.
[8] G.D. Mahan, J.O. Sofo, The best thermoelectric, Proc. Natl. Acad. Sci. USA 93 (1996) 7436–7439.
[9] L.D. Hicks, M.S. Dresselhaus, Effect of quantum-well structures on the thermoelectric figure of merit, Phys. Rev. B 47 (1993) 12727.
[10] L.W. Whitlow, T. Hirano, Superlattice applications to thermoelectricity, J. Appl. Phys. 78 (1995) 5460.
[11] G.D. Mahan, L.M. Woods, Multilayer thermionic refrigeration, Phys. Rev. Lett. 80 (1998) 4016.
[12] F. Zahid, R. Lake, Thermoelectric properties of Bi2Te3 atomic quintuple thin films, Appl. Phys. Lett 97 (21) (2010) 212102.
[13] R. Venkatasubramanian, E. Siivola, T. Colpitts, B. O'quinn, Thin-film thermoelectric devices with high room-temperature figures of merit, Nature 413 (6856) (2001) 597.
[14] J.M.O. Zide, D. Vashaee, Z.X. Bian, G. Zeng, J.E. Bowers, A. Shakouri, A. Gossard, Demonstration of electron filtering to increase the seebeck coefficient in In0.53Ga0.47 As/In0.53Ga 0.28Al 0.19 As superlattices, Phys. Rev. B 74 (20) (2006) 205335.
[15] M. Thesberg, M. Pourfath, N. Neophytou, H. Kosina, The fragility of thermoelectric power factor in cross-plane superlattices in the presence of nonidealities: a quantum transport simulation approach, J. Electron. Mater. 45 (3) (2016) 1584.
[16] A. Cantarero, F.X. Àlvarez, Nanoscale Thermoelectrics. Thermoelectric Effects: Semiclassical and Quantum Approaches from the Boltzmann Transport Equation, Springer International Publishing, Cham, 2014 Chapter 1.
[17] G. Grosso, G.P. Parravicini, Solid State Physics, Elsevier Science, 2013.
[18] N.W. Ashcroft, N.D. Mermin, Solid State Physics, Thomson Learning, 1976.
[19] G.K.H. Madsen, D.J. Singh, Boltztrap. A code for calculating band-structure dependent quantities, Comput. Phys. Commun. 175 (1) (2006) 67.
[20] A. Popescu, L.M. Woods, J. Martin, G.S. Nolas, Model of transport properties of thermoelectric nanocomposite materials, Phys. Rev. B 79 (20) (2009) 205302.
[21] C. Bera, M. Soulier, C. Navone, G. Roux, J. Simon, S. Volz, N. Mingo, Thermoelectric properties of nanostructured Si1- xGex and potential for further improvement, J. Appl. Phys. 108 (12) (2010) 124306.
[22] V. Brinzari, D.L. Nika, I. Damaskin, B.K. Cho, G. Korotcenkov, Thermoelectric properties of nano-granular indium-tin-oxide within modified electron filtering model with chemisorption-type potential barriers, Phys. E: Low-Dimen. Syst. Nanostruct. 81 (2016) 49–58.
[23] J.-H. Bahk, A. Shakouri, Minority carrier blocking to enhance the thermoelectric figure of merit in narrow-band-gap semiconductors, Phys. Rev. B 93 (16) (2016) 165209.
[24] A. Shakouri, J.E. Bowers, Heterostructure integrated thermionic coolers, Appl. Phys. Lett. 71 (9) (1997) 1234.
[25] D. Vashaee, A. Shakouri, Improved thermoelectric power factor in metal-based superlattices, Phys. Rev. Lett 92 (10) (2004) 106103.
[26] D. Vashaee, A. Shakouri, Electronic and thermoelectric transport in semiconductor and metallic superlattices, J. Appl. Phys. 95 (3) (2004) 1233–1245.
[27] Y.-M. Lin, M.S. Dresselhaus, Thermoelectric properties of superlattice nanowires, Phys. Rev. B 68 (7) (2003) 075304.
[28] D.A. Elhabti, P. Vasipoulos, J.F. Currie, Impact of impurities on superlattice transport-coefficients in the absence of a magnetic-field, Can. J. Phys. 69 (3-4) (1991) 465–473.
[29] G. Fiedler, L. Nausner, Y. Hu, P. Chen, A. Rastelli, P. Kratzer, Thermoelectric properties of Ge/Si heterostructures: a combined theoretical and experimental study, Phys. Stat. Solidi (a) 213 (3) (2015) 524.
[30] M. Salimi, S.J. Hashemifar, First-principles calculation of semiclassical thermoelectric properties of (agsbse 2) n (agsbte 2) n superlattices, J. Alloy. Compd. 650 (2015) 143.
[31] R.J. Radtke, H. Ehrenreich, C.H. Grein, Multilayer thermoelectric refrigeration in Hg1-xCdxTe superlattices, J. Appl. Phys. 86 (1999) 3195.
[32] J.-H. Bahk, R.B. Sadeghian, Z. Bian, A. Shakouri, Seebeck enhancement through miniband conduction in III–V semiconductor superlattices at low temperatures, J. Electron. Mater. 41 (2012) 1498.
[33] V.M. Fomin, P. Kratzer, Thermoelectric transport in periodic one-dimensional stacks of InAs/GaAs quantum dots, Phys. Rev. B 82 (2010) 045318.
[34] N. Hinsche, I. Mertig, P. Zahn, Lorenz function of Bi2Te3/Sb2Te3 superlattices, J. Electron. Mater. 42 (7) (2013) 1406.
[35] A. Wacker, Semiconductor superlattices: a model system for nonlinear transport, Phys. Rep. 357 (1) (2002) 1.
[36] T. Musho, Predicting the figure of merit of nanostructured thermoelectric materials, J. Mater. Res. 30 (17) (2015) 2628.
[37] A. Bulusu, D.G. Walker, Quantum modeling of thermoelectric properties of Si/Ge/Si superlattices, IEEE T. Electron Dev. 55 (1) (2008) 423.
[38] A. Bulusu, D.G. Walker, Modeling of thermoelectric properties of semi-conductor thin films with quantum and scattering effects, J. Heat Transf. 129 (4) (2007) 492.
[39] A. Bulusu, D.G. Walker, Review of electronic transport models for thermoelectric materials, Superlatt. Microst. 44 (1) (2008) 1.
[40] A. Bulusu, D.G. Walker, Quantum modeling of thermoelectric performance of strained Si/Ge/Si superlattices using the nonequilibrium greens function method, J. Appl. Phys. 102 (7) (2007) 073713.
[41] T. Musho, D.G. Walker, Scalability of quantum simulations of thermoelectric superlattice devices, Comp. Mater. Sci. 50 (11) (2011) 3265–3269.
[42] T. Musho, D.G. Walker, Quantum simulation of nanocrystalline composite thermoelectric properties, Nanosc. Microsc. Therm. 16 (4) (2012) 288.
[43] A. Bulusu, D.G. Walker, Effect of quantum confinement on the thermoelectric properties of semiconductor 2d thin films and 1d wires, in: Thermal and Thermomechanical Proceedings 10th Intersociety Conference on Phenomena in Electronics Systems, 2006. ITHERM 2006., IEEE, 2006, p. 1299.
[44] A. Bulusu, D.G. Walker, Modeling of electron transport in thin films with quantum and scattering effects, in: ASME 2005 Pacific Rim Technical Conference and Exhibition on Integration and Packaging of MEMS, NEMS, and Electronic Systems collocated with the ASME 2005 Heat Transfer Summer Conference, American Society of Mechanical Engineers, 2005, p. 1427.
[45] M. Thesberg, M. Pourfath, N. Neophytou, H. Kosina, A non-equilibrium green functions study of energy-filtering thermoelectrics including scattering, International Conference on Large-Scale Scientific Computing, Springer, 2015, p. 301.
[46] M. Thesberg, M. Pourfath, H. Kosina, N. Neophytou, Thermoelectric power factor optimization in nanocomposites by energy filtering using negf, in: Proceedings of the 2015 International Workshop on Computational Electronics IWCE.
[47] R. Kim, M.S. Lundstrom, Computational study of the seebeck coefficient of one-dimensional composite nano-structures, J. Appl. Phys. 110 (3) (2011) 034511.
[48] R. Kim, M.S. Lundstrom, Computational study of energy filtering effects in one-dimensional composite nano-structures, J. Appl. Phys. 111 (2) (2012) 024508.
[49] V.K. Lamba, R.S. Sawhney, D. Engles, A.B. Garg, R. Mittal, R. Mukhopadhyay, Treatment of scattering in nano-films, in: AIP Conference Proceedings-American Institute of Physics, vol. 1349, 2011, p. 671.
[50] S. Wang, N. Mingo, Tailoring interface roughness and superlattice period length in electron-filtering thermoelectric materials, Phys. Rev. B 79 (2009) 115316.
[51] H. Li, Y. Yu, G. Li, Computational modeling and analysis of thermoelectric properties of nanoporous silicon, J. Appl. Phys. 115 (12) (2014) 124316.
[52] J. Li, T.C.A. Yeung, C.H. Kam, Influence of electron scatterings on thermoelectric effect, J. Appl. Phys. 112 (3) (2012) 034306.
[53] S. Cauley, M. Luisier, V. Balakrishnan, G. Klimeck, C.-K. Koh, Distributed non-equilibrium greens function algorithms for the simulation of nanoelectronic devices with scattering, J. Appl. Phys. 110 (4) (2011) 043713.
[54] S. Birner, T. Zibold, T. Andlauer, T. Kubis, M. Sabathil, A. Trellakis, P. Vogl, Nextnano: general purpose 3-D simulations, IEEE T. Electron Dev. 54 (9) (2007) 2137.
[55] Y.-M. Niquet, V.-H. Nguyen, F. Triozon, I. Duchemin, O. Nier, D. Rideau, Quantum calculations of the carrier mobility: methodology, Matthiessen's rule, and comparison with semi-classical approaches, J. Appl. Phys. 115 (5) (2014) 054512.
[56] J.E. Fonseca, T. Kubis, M. Povolotskyi, B. Novakovic, A. Ajoy, G. Hegde, H. Ilatikhameneh, Z. Jiang, P. Sengupta, Y. Tan, et al., Efficient and realistic device modeling from atomic detail to the nanoscale, J. Comput. Electron. 12 (4) (2013) 592.
[57] A.V. Kalitsov, M.G. Chshiev, J.P. Velev, Nonequilibrium coherent potential approximation for electron transport, Phys. Rev. B 85 (2012) 235111.
[58] M. Filoche, M. Piccardo, Y.-R. Wu, C.-K. Li, C. Weisbuch, S. Mayboroda, Localization landscape theory of disorder in semiconductors. I. Theory and modeling, Phys. Rev. B 95 (2017) 144204.
[59] A. Wacker, A.-P. Jauho, Quantum transport: the link between standard approaches in superlattices, Phys. Rev. Lett. 80 (1998) 369.
[60] A. Wacker, A.-P. Jauho, S. Rott, A. Markus, P. Binder, G.H. Döhler, Hot electrons in superlattices: quantum transport versus boltzmann equation, Physica B 272 (1) (1999) 157.
[61] A. Wacker, A.-P. Jauho, S. Rott, A. Markus, P. Binder, G.H. Döhler, Inelastic quantum transport in superlattices: success and failure of the boltzmann equation, Phys. Rev. Lett. 83 (4) (1999) 836.
[62] E. Flage-Larsen, Ø. Prytz, The Lorenz function: its properties at optimum thermoelectric figure-of-merit, Appl. Phys. Lett. 99 (20) (2011) 202108.
[63] H.-S. Kim, Z.M. Gibbs, Y. Tang, H. Wang, G.J. Snyder, Characterization of Lorenz number with Seebeck coefficient measurement, APL Mater. 3 (4) (2015) 041506.
[64] S. Datta, Electronic transport in mesoscopic systems, Cambridge Studies in Semiconductor Physics, Cambridge University Press, 1997.
[65] M. Buttiker, Coherent and sequential tunneling in series barriers, IBM J. Res. Dev. 32 (1) (1988) 63.
[66] C. Jacoboni, Theory of Electron Transport in Semiconductors: A Pathway from

Elementary Physics to Nonequilibrium Green Functions, Springer Series in Solid-State Sciences, Springer, Berlin, Heidelberg, 2010.
[67] C.W. Groth, M. Wimmer, A.R. Akhmerov, X. Waintal, Kwant: a software package for quantum transport, New J. Phys. 16 (6) (2014) 063065.
[68] http://kwant-project.org/.
[69] L. Musland, E. Flage-Larsen, Thermoelectric transport calculations using the Landauer approach, ballistic quantum transport simulations, and the Buttiker approximation, Comput. Mater. Sci. 132 (2017) 146–157.
[70] C. Jeong, R. Kim, M. Luisier, S. Datta, M. Lundstrom, On Landauer versus Boltzmann and full band versus effective mass evaluation of thermoelectric transport coefficients, J. Appl. Phys. 107 (2) (2010) 023707.
[71] U. Sivan, Y. Imry, Multichannel Landauer formula for thermoelectric transport with application to thermopower near the mobility edge, Phys. Rev. B 33 (1986) 551.
[72] R.L. Kronig, W.G. Penney, Quantum mechanics of electrons in crystal lattices, in: Proceedings of the Royal Society of London A: Mathematical, Physical and Engineering Sciences, Vol. 130, The Royal Society, 1931, pp. 499–513.
[73] M. Lundstrom, Fundamentals of Carrier Transport, 2nd ed., Cambridge University Press, 2000.
[74] E. Flage-Larsen, T4ME – Transport Properties for Materials: The Boltzmann Transport Equation for electrons in the relaxation time approximation. < https://espenfl.github.io/t4me > , 2017 (in preparation).

Paper III

A Monte Carlo method for solving the NEGF equations for electron transport

III

Bibliography

[1] http://kwant-project.org/.

[2] A. Altland and B. D. Simons. *Condensed matter field theory*. Cambridge University Press, 2010.

[3] L. Barletti. Wigner envelope functions for electron transport in semiconductor devices. *Transport Theory and Statistical Physics*, 32(3-4):253, 2003.

[4] MG Burt. The justification for applying the effective-mass approximation to microstructures. *Journal of Physics: Condensed Matter*, 4(32):6651, 1992.

[5] M. Buttiker. Coherent and sequential tunneling in series barriers. *IBM J. Res. Dev.*, 32(1):63, Jan 1988.

[6] S. Cauley, M. Luisier, V. Balakrishnan, G. Klimeck, and C-K. Koh. Distributed non-equilibrium greens function algorithms for the simulation of nanoelectronic devices with scattering. *J. Appl. Phys.*, 110(4):043713, 2011.

[7] S. Datta. *Electronic Transport in Mesoscopic Systems*. Cambridge Studies in Semiconductor Physics. Cambridge University Press, 1997.

[8] J. E. Fonseca, T. Kubis, M. Povolotskyi, B. Novakovic, A. Ajoy, G. Hegde, H. Ilatikhameneh, Z. Jiang, P. Sengupta, Y. Tan, et al. Efficient and realistic device modeling from atomic detail to the nanoscale. *Journal of Computational Electronics*, 12(4):592, 2013.

[9] H. J. Goldsmid. *Introduction to Thermoelectricity*. Springer Series in Materials Science. Springer Berlin Heidelberg, 2009.

[10] H. J. Groenewold. On the principles of elementary quantum mechanics. In *On the Principles of Elementary Quantum Mechanics*, pages 1–56. Springer, 1946.

[11] G. Grosso and G. P. Parravicini. *Solid State Physics*. Elsevier Science, 2013.

[12] C. W. Groth, M. Wimmer, A. R. Akhmerov, and X. Waintal. Kwant: a software package for quantum transport. *New J. Phys.*, 16(6):063065, 2014.

[13] Brian C Hall. *Quantum theory for mathematicians*, volume 267. Springer, 2013.

[14] P. C. Hemmer. *Kvantemekanikk*. Tapir akademisk forlag, 2005.

[15] C. Jacoboni. *Theory of Electron Transport in Semiconductors: A Pathway from Elementary Physics to Nonequilibrium Green Functions*. Springer Series in Solid-State Sciences. Springer, Berlin, Heidelberg, 2010.

[16] C. Jacoboni and L. Reggiani. The monte carlo method for the solution of charge transport in semiconductors with applications to covalent materials. *Reviews of modern Physics*, 55(3):645, 1983.

[17] C. Jeong, R. Kim, M. Luisier, S. Datta, and M. Lundstrom. On Landauer versus Boltzmann and full band versus effective mass evaluation of thermoelectric transport coefficients. *J. Appl. Phys.*, 107(2):023707, 2010.

[18] Pathria R. K. *Statistical Mechanics*. Butterworth-Heinemann, 1996.

[19] R. Kubo. Statistical-mechanical theory of irreversible processes. i. general theory and simple applications to magnetic and conduction problems. *Journal of the Physical Society of Japan*, 12(6):570, 1957.

[20] R. Kubo, M. Yokota, and S. Nakajima. Statistical-mechanical theory of irreversible processes. ii. response to thermal disturbance. *Journal of the Physical Society of Japan*, 12(11):1203, 1957.

[21] M. Le Bellac. *Quantum physics*. Cambridge University Press, 2011.

[22] M. Lundstrom. *Fundamentals of Carrier Transport*. Cambridge University Press, second edition, 2000.

[23] F. Mandl and G. Shaw. *Quantum field theory*. John Wiley & Sons, 2010.

[24] A. Messiah. *Quantum Mechanics*. John Wiley & Sons Canada, Limited, 1961.

[25] J. E. Moyal. Quantum mechanics as a statistical theory. *Mathematical Proceedings of the Cambridge Philosophical Society*, 45(1):99, 1949.

[26] L. Onsager. Reciprocal relations in irreversible processes. i. *Phys. Rev.*, 37:405, Feb 1931.

[27] I. Shavitt and R. J. Bartlett. *Many-body methods in chemistry and physics: MBPT and coupled-cluster theory*. Cambridge university press, 2009.

[28] A. Wacker. Semiconductor superlattices: a model system for nonlinear transport. *Phys. Rep.*, 357(1):1, 2002.

[29] E. Wigner. On the quantum correction for thermodynamic equilibrium. *Phys. Rev.*, 40:749, Jun 1932.

[30] E. Y. Wilner, T. J. Levy, and E. Rabani. Analytical continuation approaches to electronic transport: The resonant level model. *The Journal of chemical physics*, 137(21):214107, 2012.

[31] R. Zwanzig. Time-correlation functions and transport coefficients in statistical mechanics. *Ann. Rev. Phys. Chem.*, 16(1):67, 1965.